

Magnetic field effects in topologically nontrivial systems

Inaugural-Dissertation

zur Erlangung des Doktorgrades
der Mathematisch-Naturwissenschaftlichen Fakultät
der Heinrich-Heine-Universität Düsseldorf

vorgelegt von

Tim Yannik Bauer
aus Essen, Deutschland

Düsseldorf, Dezember 2024

aus dem Institut für Theoretische Physik IV
der Heinrich-Heine-Universität Düsseldorf

Gedruckt mit der Genehmigung
der Mathematisch-Naturwissenschaftlichen Fakultät
der Heinrich-Heine-Universität Düsseldorf

Berichterstatter:

1. Prof. Dr. Reinhold Egger
2. PD Dr. Hermann Kampermann
3. Prof. Dr. Volker Meden

Tag der mündlichen Prüfung: 13. Februar 2025

Abstract

The influence of a magnetic field on quantum states of matter gives rise to a wealth of phenomena that are at the heart of modern condensed matter research. The theoretical description of these fascinating effects typically involves the notion of topology, which has captivated researchers of solid-state physics for over five decades. A defining property of topologically nontrivial states of matter is the existence of characteristic energy excitations, which either are localized near the boundary of the system or constitute exotic quasiparticles in the bulk.

This thesis investigates three phenomena induced by magnetic fields in solid-state systems, which are either intrinsically topological or acquire topological properties in the presence of magnetic fields. The majority of this work is devoted to unconventional phases of two-dimensional magnets, called *quantum spin liquids* (QSLs), which defy description within the paradigmatic Ginzburg-Landau theory of phase transitions and exhibit striking quantum effects. In the specific QSL studied in this thesis, an external magnetic field induces the formation of energy excitations termed *Ising anyons*. These exotic quasiparticles exhibit fractional exchange statistics and are intriguing beyond the viewpoint of fundamental physics due to potential applications in quantum information processing. The objective of my Publications **P2** and **P3** is to design novel experiments that detect and manipulate Ising anyons in the QSL using local electric probes, such as scanning tunneling microscopy. These studies are based on a microscopic description of specific transition metal compounds which, according to theoretical predictions, might stabilize the QSL phase.

A major difficulty faced by previous experiments on these candidate materials is given by trivial effects that obscure the unambiguous interpretation of results. To validate our predictions in Publications **P2** and **P3**, we therefore studied a more conventional field-induced state of matter, namely, the (partially) polarized phase of two-dimensional magnets. The elemental excitations of this phase are magnons and, in the case of the aforementioned transition metal compounds, acquire topological properties. We find that magnetic impurities in the sample can trap *magnon bound states* and thereby generate low-energy signatures reminiscent of the predictions for Ising anyons. However, in Publication **P4**, we detail how these magnon bound states are associated with a local spin flip transition and can, therefore, be fully characterized using the proposed experimental set-up. This result strongly suggests that local electric probes can distinguish Ising anyons in the putative QSL phase from trivial excitations in the polarized state. Moreover, the discovered mechanism is generic in polarized magnets and holds promise for applications in spintronic or magnonic devices involving van der Waals materials.

During my doctoral research, I did not only study low-dimensional magnets. In Publication **P1**, my collaborators and I investigated a class of topological semimetals called *Weyl semimetals*. These three-dimensional conductors are characterized by low-energy excitations which formally behave as ultrarelativistic chiral fermions. This fact entails the solid-state realization of various phenomena studied in theoretical high-energy particle physics, such as the anomalous response of massless fermions to external electromagnetic fields. On the other

hand, Weyl semimetals host localized surface states which reflect the nontrivial topology of these compounds and form a remarkable open energy contour termed *Fermi arc*. The interplay of Fermi arcs and the anomalous response of bulk excitations in a magnetic field gives rise to an exotic cyclotron motion which manifests intriguing non-local effects. In Publication **P1**, we provide the full quantum mechanical description of this phenomenon and thereby go beyond previous theoretical works which relied on a semiclassical approximation.

My thesis is structured as follows. Chapter **1** provides an extensive introduction to topology in condensed matter physics and the phenomenology of Weyl semimetals and QSLs. Subsequently, Chapter **2** details the putative QSL phase in the transition metal compounds and sets the stage for my publications listed in Chapter **3**.

Kurzfassung

Der Einfluss eines Magnetfelds auf Quantenzustände der Materie erzeugt eine Vielzahl von Phänomenen, die von zentraler Bedeutung für die moderne Forschung der kondensierten Materie sind. Die Beschreibung dieser faszinierenden Effekte basiert in der Regel auf Konzepten der Topologie, die im Rahmen der Festkörperphysik die Wissenschaft seit über fünfzig Jahren begeistern. Eine definierende Eigenschaft von topologisch nichttrivialen Materiezuständen ist die Existenz charakteristischer Anregungen, die entweder nahe dem Rand einer Probe lokalisiert sind oder exotischen Quasiteilchen im Inneren des Systems entsprechen.

Diese Thesis erforscht drei durch Magnetfelder induzierte Phänome in Festkörpern, die entweder von topologischer Natur sind oder in einem Magnetfeld topologische Eigenschaften erhalten. Die Mehrheit dieser Arbeit widmet sich unkonventionellen Phasen von zweidimensionalen Magneten namens *Quanten-Spin-Flüssigkeiten* (QSF), die nicht im Rahmen der Ginzburg-Landau-Theorie der Phasenübergänge beschrieben werden können und bemerkenswerte Quanteneffekte aufweisen. In der spezifischen QSF, die hier betrachtet wird, generiert ein externes Magnetfeld Anregungen namens *Ising-Anyonen*. Diese exotischen Quasiteilchen besitzen fraktionierte Austauschstatistiken und sind nicht nur für die Grundlagenforschung interessant, sondern möglicherweise für Anwendungen in der Quanteninformationsverarbeitung geeignet. Das Ziel meiner Publikationen **P2** und **P3** ist die Konzipierung neuartiger Experimente, die Ising-Anyonen in der QSF mithilfe lokaler elektrischer Proben, wie z.B. mit einem Rastertunnelmikroskop, detektieren und manipulieren können. Diese Arbeiten basieren auf einer mikroskopischen Beschreibung bestimmter Übergangsmetallverbindungen, die der Theorie zufolge eine QSF stabilisieren können.

Eine wesentliche Schwierigkeit, die in bisherigen Experimenten zu diesen Materialien aufgetreten ist, besteht in trivialen Effekten, die eine eindeutige Interpretation der Messergebnisse verhindern können. Um unsere Vorhersagen in den Publikationen **P2** und **P3** zu validieren, haben wir daher auch einen gewöhnlicheren, durch ein Magnetfeld induzierten Zustand erforscht, nämlich die polarisierte Phase von zweidimensionalen Magneten. Die elementaren Anregungen in dieser Phase sind Magnonen, die im Falle der genannten Übergangsmetallverbindungen topologische Eigenschaften besitzen. Es stellt sich heraus, dass magnetische Verunreinigungen Magnonen binden und dadurch experimentelle Signale erzeugen können, die den Vorhersagen für Ising-Anyonen ähneln. Allerdings zeigen wir in der Publikation **P4**, wie gebundene Magnonzustände mit einem lokalen Spin-Flip zusammenhängen und daher in unserem vorgeschlagenen Aufbau charakterisiert werden können. Dieses Ergebnis legt nahe, dass lokale elektrische Proben zwischen Ising-Anyonen in der QSF und gewöhnlicheren Anregungen in der polarisierten Phase unterscheiden können. Außerdem sollte der erwähnte Effekt in einer Vielzahl von polarisierten Magneten auftreten und könnte sich daher als nützlich für Anwendungen in der auf van-der-Waals-Materialien basierenden Spintronik erweisen.

Ich habe mich in meiner Promotion nicht nur mit niedrigdimensionalen Magneten beschäftigt, sondern in der Publikation **P1** auch sogenannte Weyl-Semimetalle erforscht. Die charak-

teristischen Anregungen dieser dreidimensionale Leiter verhalten sich formal wie ultrarelativistische, chirale Fermionen. Es ist daher möglich, eine Reihe von Phänomenen der theoretischen Teilchenphysik in diesen Festkörpern zu untersuchen, wie zum Beispiel der Einfluss durch externe elektromagnetische Felder. Andererseits besitzen Weyl-Semimetalle nahe der Ränder gebundene Zustände, die die nichttriviale Topologie dieser Materialien demonstrieren und eine besondere Dispersionsrelation namens *Fermi-Arc* aufweisen. Das Zusammenspiel von elektromagnetischen Feldern und der Fermi-Arc erzeugt eine exotische Zyklotronbewegung, die nichtlokale Effekte verursacht. In der Publikation **P1** beschreiben wir dieses Phänomen im Rahmen der Quantenmechanik und ohne semiklassische Näherungen.

Diese Thesis ist wie folgt aufgebaut. Kapitel **1** bietet eine ausführliche Einleitung zu topologischen Konzepten in dem Feld der kondensierten Materie und zu der Phänomenologie von Weyl-Semimetallen und QSF. Das nachfolgende Kapitel **2** erläutert die vermeintliche QSF in den genannten Übergangsmetallverbindungen und bereitet auf meine Publikationen vor, die in Kapitel **3** angehängt sind.

Preface

This doctoral thesis is based on articles that I co-authored, and which have been published in peer-reviewed scientific journals. All articles are reproduced in Chapter 3 and listed below in topical order. My contributions to these articles are also specified in Chapter 3.

- P1** **T. Bauer**, F. Bucchieri, A. D. Martino, and R. Egger
Quantum description of Fermi arcs in Weyl semimetals in a magnetic field
 Physical Review Research, vol. 6, no. 4, p. 043201 (2024)

- P2** L. R. D. Freitas, **T. Bauer**, R. Egger, and R. G. Pereira
Electric polarization near vortices in the extended Kitaev model
 npj Quantum Materials, vol. 9, no. 1, p. 33 (2024)

- P3** **T. Bauer**, L. R. D. Freitas, R. G. Pereira, and R. Egger
Scanning tunneling spectroscopy of Majorana zero modes in a Kitaev spin liquid
 Physical Review B, vol. 107, no. 5, p. 054432 (2023)

- P4** **T. Bauer**, L. R. D. Freitas, E. C. Andrade, R. Egger, and R. G. Pereira
Local spin-flip transitions induced by magnetic quantum impurities in two-dimensional magnets
 Physical Review B, vol. 110, no. 22, p. L220403 (2024).

Acknowledgements

This thesis is an accomplishment of many people. First and foremost, I want to thank Reinhold Egger for his continuous supervision and support. During my time in Düsseldorf, I learned a lot from his experience and his pragmatic approach to scientific research and other aspects of life. I also want to thank Rodrigo G. Pereira for the fruitful collaborations, for his hospitality and for introducing me to the cuisine of Minas Gerais. My visits to Natal were tremendously beneficial for me as a person and as a scientist. One reason for this is my time in a joint office with Lucas R. D. Feitas, who I want to thank for our discussions and his friendship. I also want to express my gratitude towards my other collaborators, Eric C. Andrade, Alessandro De Martino and Francesco Buccheri. In particular, I want to thank the latter for sticking to our project for such a long time. All former and present members of our group were also of much help in difficult times. On my personal side, I want to thank my family, my friends and Sophia for their patience and unconditional support. Finally, I want to thank Christina, Alex, Samuel and Anna for proofreading my thesis.

Contents

1	Introduction	1
1.1	New universality in condensed matter	1
1.1.1	Band topology	2
1.1.2	Topological order	4
1.2	Band topology of Weyl semimetals	8
1.2.1	Monopoles of Berry curvature	9
1.2.2	Fermi arcs	11
1.2.3	Poor man's chiral anomaly	13
1.3	Topological order in \mathbb{Z}_2 quantum spin liquids	17
1.3.1	Frustrated magnetism	17
1.3.2	Coulomb phase of the classical Kitaev honeycomb model	21
1.3.3	Resonating valence bond liquid	23
2	Realization of the Kitaev spin liquid	30
2.1	Kitaev honeycomb model	30
2.1.1	Majorana fermion representation	32
2.1.2	Flux-free ground state and Majorana zero modes	36
2.1.3	Ising anyons for topological quantum computation	40
2.2	Jackeli-Khaliullin mechanism	41
2.2.1	Low-energy description of Mott insulators	41
2.2.2	Spin-orbit assisted Mott insulators	43
2.2.3	Bond-directional superexchange	44
2.2.4	Kitaev materials	47
2.3	Experimental status of RuCl_3	48
2.3.1	Proximate spin liquid	48
2.3.2	Quantum thermal Hall effect of the field-induced state	50
2.3.3	Topological magnons in the partially polarized phase	52
2.4	Electrical probes for magnetic insulators	55
2.4.1	Electric polarization of Mott insulators	56
2.4.2	Scanning tunneling spectroscopy of local magnetic moments	57
3	Scientific publications	59
P1	Quantum description of Fermi arcs in Weyl semimetals in a magnetic field . . .	60
P2	Electric polarization near vortices in the extended Kitaev model	77
P3	Scanning tunneling spectroscopy of Majorana zero modes	92
P4	Local spin-flip transitions induced by magnetic quantum impurities	106
	References	121

Chapter 1

Introduction

The theoretical description underpinning all Publications listed in Chapter 3 involves topology. This chapter gives a brief introduction to topology in condensed matter. To this end, Section 1.1 starts with a broad overview of the general phenomenology of topologically nontrivial systems and concludes by stating the main objective of my doctoral research. Subsequently, Sections 1.2 and 1.3 use simple models for more detailed discussions on Weyl semimetals and quantum spin liquids, respectively. The latter section also sets the stage for Chapter 2.

1.1 New universality in condensed matter

Many-body physics seeks not only to describe specific systems but to uncover universality. According to the paradigmatic Ginzburg-Landau theory, phase transitions are associated with symmetry breaking, and the universality of continuous phase transitions is reflected in the critical behavior of thermodynamic observables, that is, their independence of the microscopic details close to the transition. In the last century of condensed matter research,¹ this notion of universality proved remarkably successful in describing both thermal phase transitions - an archetypal example is the spontaneous magnetization of Ising ferromagnets at the Curie temperature - and quantum phase transitions at zero temperature. It was in 1980, however, that Klaus von Klitzing experimentally observed the *integer quantum Hall effect (IQHE)* [116] and thereby discovered a new type of universality, which is not associated with any symmetry breaking.

The original IQHE is the quantized Hall effect of a (weakly interacting) two-dimensional (2D) electron gas as realized in a metal-oxide-semiconductor heterostructure subjected to a strong perpendicular magnetic field. Von Klitzing found that, with astonishing accuracy (up to one part per billion [147]), the quantized transverse conductivity is given by

$$\sigma_{xy} = \frac{e^2}{h} \nu, \quad (1.1)$$

where $\nu \in \mathbb{Z}$ is an integer and roughly corresponds to the (floor) filling factor of the quantized Landau levels in the confined electron gas. It is now well-established that the current giving rise to σ_{xy} is transported by $|\nu|$ gapless, propagating edge states localized near the boundary of the sample. As pointed out by Laughlin in his qualitative description of charge pumping in the

¹While the Ginzburg-Landau theory was formulated conclusively only in the 1970s [147], it is based on the seminal work [126] of Lev Landau from 1937.

integer quantum Hall phase, the existence of these edge states is a consequence of gauge invariance in the bulk. As a result, the quantization of the macroscopic observable σ_{xy} in terms of the ratio of the fundamental constants e^2 and h is largely independent of microscopic details such as the purity, size and host material of the electron gas. It is this striking new universality that inspired extensive and ongoing research of condensed matter systems with nontrivial *topology*. For the purpose of this introduction, let us trace the trajectory of these efforts in terms of a short non-chronological (and rather incomplete) summary distinguishing between two central concepts - *band topology* and *topological order*.

1.1.1 Band topology

In solid-state systems, the description of the IQHE in terms of Landau levels formed by free electrons is only valid at energies near the minimum of the full band structure. The IQHE, however, is also supported by lattice models. An elegant description of itinerant electrons hopping on a 2D lattice penetrated by a perpendicular magnetic field is provided by the Hofstadter model [83], which retains translational invariance for an extended magnetic unit cell, given that the magnetic flux through the plaquettes of the lattice is commensurate, i.e., a rational multiple of the flux quantum $\Phi_0 = h/e$. A second model with no external but an *intrinsic* staggered magnetic field was proposed by Haldane [77] for the honeycomb lattice.² Both models support an IQHE, which can most remarkably be understood in terms of an integer number associated with the bulk band structure. This number is a *topological invariant* and called *Chern number* or sometimes TKNN integer (acknowledging the seminal work [204] by Thouless, Kohmoto, Nightingale and den Nijs). To define the Chern number, let us assume a nondegenerate band structure and the knowledge of the single-particle eigenstates $|u_j(\mathbf{k})\rangle$ of the j th energy band in momentum space parametrized by \mathbf{k} . The Chern number $\mathcal{C}_j \in \mathbb{Z}$ of the j th energy band expressed in terms of the projector $P_j = |u_j\rangle \langle u_j|$ is given by

$$\mathcal{C}_j = \frac{i}{2\pi} \iint_{\text{BZ}} dk_x dk_y \text{Tr} \left[\left(\partial_{k_x} P_j \right) P_j \left(\partial_{k_y} P_j \right) - \left(\partial_{k_y} P_j \right) P_j \left(\partial_{k_x} P_j \right) \right], \quad (1.2)$$

where integration runs over the first Brillouin zone (BZ) [7, 147]. One can show [147] that in the case of the IQHE of lattice models, the integer ν in Eq. (1.1) is the sum of the Chern numbers of all filled bands. This result manifests two hallmark features of systems with nontrivial band topology. First, it shows that the topological invariant is a physical quantity that is observable in magnetotransport experiments such as measurements of the transverse conductivity σ_{xy} . Second, since σ_{xy} arises due to edge channels, we find that a nontrivial topological invariant of the bulk band structure is associated with the emergence of edge or surface states localized near the system's boundary [79]. The latter feature is an instance of the celebrated *bulk-boundary correspondence* in condensed matter systems and enables an alternative scheme of detecting *band topology* in terms of surface-sensitive probes. We give examples of such techniques below. Going back to Eq. (1.2), let us also note that in Section 1.2, we detail an equivalent definition of the Chern number \mathcal{C}_j in terms of the *Berry curvature* associated with the eigenstates $|u_j(\mathbf{k})\rangle$. This makes clear that a topological invariant is invariant under adiabatic transformations of the Hamiltonian (which keep the bulk system gapped) and, therefore, suggests an intrinsic *topological protection* against perturbations which do not close the energy gap. Typically, in the case of

²More precisely, the effective magnetic field in the Haldane model varies spatially on the two sublattices of the honeycomb lattice and averages to zero. The resulting ground state is called *Chern insulator*.

band topology, however, this line of arguments only holds under specific symmetry constraints, as exemplified in what follows.

The above description in terms of the Chern number (1.2) requires nondegenerate energy bands. So far, however, our discussion did not consider the internal spin degree of freedom of the electrons. In the case of spinful electrons, or more precisely, systems of particles with half-integer spin, energy bands exhibit a two-fold Kramer's degeneracy at specific points in the BZ if *time-reversal symmetry* (TRS) is present.³ A necessary ingredient for the IQHE is therefore the breaking of TRS due to either intrinsic magnetism or an external magnetic field. In the latter case, Kramer's degeneracy is typically lifted by a Zeeman coupling of the spins. In fact, in all systems studied in my research articles in Chapter 3, an external magnetic field is present, and TRS is broken. The Chern number (1.2) thus provides a valuable concept to probe the topology of these systems.

Let us briefly discuss electronic systems with good TRS. Such states can also be topologically nontrivial, if subject to strong spin-orbit coupling. Jumping ahead roughly 20 years, this was first noticed by Kane and Mele, who generalized Haldane's model [77] by including the spin degree of freedom (thereby retaining spinful TRS) and spin-orbit coupling [101, 102]. They found that the resulting ground states can be classified in terms of a \mathbb{Z}_2 topological invariant which distinguishes between trivial band insulators and *2D topological insulators*. A nontrivial invariant again implies the existence of metallic edge states, which, in contrast to the IQHE, are counter propagating for opposite spin projections and protected against hybridization due to backscattering as long as TRS is present.⁴ As a result, the edge states give rise to a theoretically proposed *quantum spin Hall effect* (QSHE) as analogue of the IQHE for spin transport (without external magnetic field). While the QSHE is only realized under idealized conditions [147], related charge transport phenomena were predicted [23] and experimentally observed [123] in quantum wells.

Another important development in the study of topological insulators was the theoretical generalization of the \mathbb{Z}_2 invariant to three spatial dimensions [67, 154]. The boundary of a *3D topological insulator* does not host edge states but surface states, which, at low energies, can be typically described as ultra-relativistic, massless fermions (upon substituting the speed of light by the Fermi velocity). While no quantized observable is expected in these systems and magnetotransport signatures are somewhat elusive [147], it is possible to measure the resulting Dirac cones of the surface-state dispersion using angle-resolved photoemission spectroscopy (ARPES) [87] and thereby confirm the bulk topology via the bulk-boundary correspondence. Indeed, ARPES has proven a powerful technique to detect band topology in the absence of an external magnetic field, and guided the discovery of a by now large number of material realizations. Notably, topological insulators continue to attract the attention of the condensed matter community in the context of *topological superconductivity* - a potential platform for *topological quantum computation*, see below.

An alternative route to realize nontrivial band topology in three dimensions (without necessarily requiring TRS) is provided by *topological semimetals*. Semimetals are gapless electronic systems with characteristic points or lines in momentum space at which energy bands cross

³By "nondegenerate energy bands" we mean energy bands that do not coincide with other bands at any point \mathbf{k} in momentum space. In systems with spinful TRS, energy bands corresponding to opposite spin projections coincide at the *time-reversal invariant momenta*, i.e., points \mathbf{k} of the BZ with $\mathbf{k} = -\mathbf{k}$ (modulo reciprocal lattice vectors).

⁴This is why, according to the theoretical classification of condensed matter in two dimensions, topological insulators represent a *symmetry-protected topological phase* [216]. This does not contradict the fact that there can be a phase transition from a trivial to a topological insulator without any symmetry breaking.

close to the Fermi energy, thereby giving rise to a low-dimensional Fermi surface. While generic band crossings are typically unstable and easily gapped out by perturbations [6], in some instances, they are protected by present symmetries or band topology. Due to the absence of an energy gap, however, it is impossible to define a topological invariant of the full 3D band structure within the theoretical framework of adiabatic dynamics. Instead, one can compute topological invariants, namely the Chern number (1.2), for gapped 2D slices of the 3D band structure which exclude the band crossings [6]. The resulting value of the invariant is then associated with the exact nature of the band crossing, and like above encodes information about topological surface states and magnetotransport signatures. We illustrate this fact in Section 1.2, where we focus on a particular class of topological semimetals, so-called *Weyl semimetals* (WSMs), to set the stage for my Publication P1. Moreover, generally speaking, an expansion near the band crossings yields a low-energy description in terms of massless ultra-relativistic fermions with, typically, definite *chirality*. The anomalous response of these particles to electromagnetic fields is well studied in theoretical high-energy physics and allows an alternative explanation of magnetotransport [162, 34] experimentally observed in real materials [244, 164]. Notably, the existence of a Fermi surface enables other magnetotransport probes such as measurements of Shubnikov-de Haas oscillations [84, 244]. Besides this, surface-sensitive probes such as ARPES [159, 133, 231] and, more recently, quasi-particle interference measurements [155] proved tremendously helpful in detecting a large number of topological semimetals.

By now, a myriad of confirmed topological insulators and nonmagnetic topological semimetals are collected in large data bases [29, 202, 250, 209]. Making theoretical predictions for magnetic compounds is somewhat harder [22], but recent high-throughput calculations report non-trivial band topology in more than 20 percent of all studied magnetic materials [232]. These efforts show that band topology is a generic property of solid state systems and an essential concept in the modern toolbox of condensed matter theory. Apart from the long term goal of realizing topological quantum computation, proposed applications include novel electronic [68] and spintronic [170] devices. But our compressed summary of topology in condensed matter should not end here.

1.1.2 Topological order

So far, we have discussed non-interacting electrons in clean crystalline systems, and defined topological invariants in terms of single-particle Bloch wavefunctions assuming translational invariance. This was justified, since for finite but weak interaction between electrons, the IQHE is still observable and the Chern number remains a well-defined concept [147]. Moreover, in the presence of disorder, local topological markers in real-space and the entanglement spectrum can probe the topology of a system without the necessity of translational invariance [175, 25]. Despite these results, however, roughly a decade after the discovery of the IQHE, experiments showed that the above framework is insufficient to describe specific strongly correlated states of condensed matter.⁵ At the time new fabrication technique permitted higher quality of semiconductor heterostructures hosting 2D electron gases [147], and led to the observation of the *fractional quantum Hall effect* (FQHE) by Tsui, Störmer and Gossard [207].

The FQHE resembles a generalization of the IQHE, in that under appropriate conditions, the transverse conductivity σ_{xy} in Eq. (1.1) forms quantized plateaus not only at integer filling factors ν but also at specific fractional values $\nu \in \mathbb{Q}$, e.g. at $\nu = 1/3$. The explanation of these plateaus is not possible within a non-interacting single-particle picture but requires con-

⁵Much of this theoretical framework was, of course, developed only after the discovery of the FQHE.

sideration of the Coulomb interactions and the extensive degeneracy of states that minimize the kinetic energy at fractional filling [147]. Notably, for a filling factor of the form $\nu = 1/m$, where $m \in \mathbb{Z}$ is an odd integer, the theoretical description (within the lowest Landau level) is facilitated by a variational ground state proposed in a seminal work by Laughlin [127].⁶

The study of *Laughlin's wavefunction* revealed fascinating new physics beyond band topology and led to the introduction of a concept termed *topological order* by Wen and Niu [217]. Rather than giving a general definition [216], let us discuss two hallmark features of topological order based on Laughlin's wavefunction. First, we note that depending on the system's geometry, the ground state might not be unique but an element of a degenerate multiplet. More precisely, the *topological ground-state degeneracy* on a manifold of genus g is 3^g [147], i.e., 1 for a sphere and 3 for a torus.⁷ Typically, the degenerate ground states cannot be distinguished by local operators, and are, in that sense, protected against local perturbations. This fascinating fact might enable nonlocal encoding of quantum information for robust quantum memory, as proposed in a seminal work by Kitaev [114].

The second feature we discuss here does not concern Laughlin's wavefunction itself but its *emergent* quasiparticle excitations. Most remarkably, at filling factor $\nu = 1/m$, these quasiparticles carry only the fraction $1/m$ of the electron charge. The discovery of this fact constitutes the historically first instance of *fractionalization* in more than one spatial dimension, that is, the impossibility of representing the emergent (low-energy) degrees of freedom in terms of sums of the microscopic (high-energy) degrees of freedom [147].⁸ We note that the fractional charge of edge states, which emerge due to the bulk-boundary correspondence, was experimentally observed in shot-noise measurements [184]. Moreover, besides the appearance of fractional quantum numbers, fractionalization is typically accompanied with *anyonic exchange statistics* of quasiparticles. To schematically illustrate this fascinating concept, let us consider a many-body wavefunction $\Psi(\mathbf{r}_1, \dots, \mathbf{r}_N)$ of N identical particles with real-space dependencies \mathbf{r}_j . We are interested in the effect of exchanging two particles. Generally, this should accumulate a phase $\theta \in [0, 2\pi)$ and resemble a transformation of the form

$$\Psi(\dots, \mathbf{r}_j, \dots, \mathbf{r}_k, \dots) \rightarrow e^{i\theta} \Psi(\dots, \mathbf{r}_k, \dots, \mathbf{r}_j, \dots). \quad (1.3)$$

In a four dimensional space-time and under the assumption Lorentz invariance, the spin-statistics theorem permits only two possible values for the phase θ , namely, $\theta = 0$ in the case of bosonic particles and $\theta = \pi$ for fermions. The confinement to two spatial dimensions, however, gives rise to more generality and allows, in principle, any value for θ in $[0, 2\pi)$.⁹ Roughly speaking, this is because in 2D, the phase is generally sensitive to the way the particles are rearranged and, in particular, the winding number of the exchange [196, 147]. If this is the case, i.e., if $e^{i\theta} \neq \pm 1$, the particles are called *Abelian anyons*. And indeed, in the FQHE at $\nu = 1/m$, elemental quasiparticle excitations correspond to a statistical angle $\theta = 2\pi/m$. We note that the theoretical description of anyons is based on braid groups, and permits a generalization of Eq. (1.3), which describes processes that are sensitive to the order of the particle exchange. These corresponding excitations are called *non-Abelian anyons* and expected in the FQHE at

⁶The symmetry of Laughlin's wavefunction requires that m is odd for fermions and even for bosons.

⁷For finite system size, the energy splitting of the degenerate multiplet is exponentially small in the linear system size [217].

⁸Fractionalization in the bulk of 1D systems is not due to topological order but typically associated with symmetry breaking [147], as in the case of the Peierl's instability of elastic electronic chains.

⁹Stability requires that θ is a rational multiple of 2π though [112]. We also note that for a more rigorous discussion of this exchange statistics we should clarify what we mean by particle exchange. We do this in Chapter 2.

specific filling factors not captured by Laughlin's wavefunction, e.g. $\nu = 5/2$ [153]. Moreover, it was recognized that the manipulation of non-Abelian anyons (in terms of *braiding* and *fusing*) could potentially enable robust quantum information processing in a *topological quantum computer* [114, 112, 158], as discussed in Chapter 2.

The long-term prospect of topological quantum computing makes topological order intriguing beyond the perspective of fundamental physics. To gain a deeper understanding of this physics and the difference to band topology, it is helpful to study electronic systems, in which the kinetic energy is frozen out and the electrons are effectively decoupled from the lattice. This is the case in Mott insulators, which, for strong Coulomb repulsion and at low energies, are typically described by a model of localized spins, see Chapter 2. The study of 2D spin models takes up the majority of my Publications **P2**, **P3** and **P4**. In this context, the *toric code model* resembles the hydrogen atom of topological order [114]. The model describes spin-1/2 moments (i.e., qubits) on (the edges of) a square lattice coupled by specific interactions, and, most remarkably, gives rise to an extensive number of conserved operators, which are each associated with a square plaquette of the lattice. This extensive symmetry allows an exact solution for the spectrum, and a comprehensive study of its topological properties. As first discussed by Kitaev [114], the system exhibits topological ground state degeneracy on a torus, and three different species of Abelian anyonic excitations¹⁰ - both consequences of a \mathbb{Z}_2 topological order. However, while the toric code model proved a tremendously helpful toy model in the fields of condensed matter and quantum error correction, it is not realized in real-world solid state systems.

Instead, in a conventional electronic material, upon cooling to low temperatures, the spins form long-range patterns and enter a *magnetically ordered* phase with lower symmetry than the Hamiltonian, e.g. a ferromagnetic state. The resulting phase transition is captured by the aforementioned Ginzburg-Landau theory and is associated with symmetry breaking. However, in some instances, either the lattice geometry or specific exchange anisotropy give rise to *frustration*, i.e., the obstruction of the concurrent minimization of all exchange interactions and, therefore, the ordering of spins. In this scenario, spins can maintain rotation symmetry and give rise to a *quantum spin liquid* (QSL). Generally speaking, QSLs are exotic nonmagnetic states of frustrated magnets characterized by large quantum entanglement, fractionalization and, typically, topological order.¹¹ We discuss this phase of matter in more detail in Section 1.2 and study a specific type of QSL in Chapter 2 as preparation for my Publications **P2**, **P3** and **P4**. At this point, however, we can infer that topological order is an essential organizing mechanism of many-body quantum systems in the absence of symmetry breaking. This is a sharp difference from nontrivial band topology, which can exist in a conventionally ordered phase under specific symmetry constraints.¹²

The realization and detection of QSLs are major goals of modern condensed matter research. While there is no universally accepted *smoking-gun* measurement of a QSL, a variety of experimental evidence of different QSL phases in real material candidates is available [187, 206]. In this context, inelastic neutron scattering (INS) provided a considerably successful technique which probes the dynamical spin structure factor, i.e., the Fourier transform of the spin correlations. While the INS signal of magnetically ordered states typically involves sharp Bragg

¹⁰One excitation is fermionic and one is bosonic. Albeit they are typically referred to as anyons due to their nontrivial braiding relations.

¹¹Gapless QSLs do not host topological order [216] nor are they described by a topological quantum field theory. There is no agreed-upon definition of QSLs that includes all instances, where the term is used, and goes beyond the absence of magnetic order as a defining property [187].

¹²For example, the integer quantum Hall state at integer filling is a *flat-band ferromagnet* [147].

peaks reflecting long-range correlations, QSLs give rise to smooth features in INS data, indicating broad continua of nonlocal fractional excitations [187]. We note in passing that INS also enabled the experimental confirmation of spin fractionalization in three dimensions. This was accomplished for *spin ice*, a class of (classical) 3D magnets on a pyrochlore lattice, which, due to frustration, exhibit an extensive degeneracy of classical low-energy spin configurations and stabilize the *Coulomb phase*. The latter is an instance of a *classical spin liquid*, which, as we discuss in Section 1.2, gives rise to an emergent $U(1)$ *gauge field* reminiscent of classical electrodynamics [37]. A strong indication of the emergent gauge field as well as classical fractional excitations were observed in INS [30, 61], albeit that spin ice is not topologically ordered in the above sense [37].

While INS and other measurement techniques probing global observables of the sample's bulk might yield consistent indication of genuine topological order and fractional excitations, they do not provide smoking guns in that they do not reveal our new notion of universality. Notably, in some instances, theoretical calculations for QSLs [112] and other topologically nontrivial phases [165, 134] predict universally quantized transport signatures, which are associated either with emerging boundary modes or with local probes of fractional bulk excitations. However, beyond idealized conditions and the well-controlled realm of quantum Hall physics, the richness of these interacting systems commonly allows topologically trivial (or at least more conventional) excitations that mimic the predictions in terms of non-quantized but finite transport signals. The most prominent instance of such an ambiguity is the zero-bias anomaly in topological superconductors. Topological superconductivity is an exotic form of superconductivity, which, roughly speaking, is predicted in semiconductors (or topological insulators) with strong spin-orbit coupling and proximity to a conventional superconductor [113, 66]. This phase hosts fractional fermionic excitations termed *Majorana zero modes* (MZMs) at the edge and, under specific conditions, in vortices of the superconductor [66]. In the latter case, the bound MZMs form non-Abelian *Ising anyons*, thereby qualifying the system as a platform for topological quantum computation [92, 158]. In any case, theoretical calculations for electronic transport through a junction or a local tunneling probe predict a quantized conductance peak of $2e^2/h$ at zero bias voltage inside the bulk gap [165, 134, 240]. While experimental claims of this quantized zero-bias anomaly attracted massive attention, it is now understood that these measurements are not sufficient to distinguish MZMs from trivial in-gap states [106], such as Andreev bound states [19]. The search for MZMs is, therefore, still on-going. As we discuss in Chapter 2, a similar situation might arise for quantized thermal transport signatures in the QSL type of interest.

Given these considerations, we can finally formulate the main objective of my doctoral research. It is the design of feasible experiments that allow the unambiguous detection (and potential manipulation) of non-Abelian anyons in quantum spin liquids using local electrical probes and external magnetic fields. This effort is the subject of my Publications P2 and P3. While the resulting experimental predictions are not quantized, we discuss how to distinguish them from a more trivial explanation, which is further elucidated in my Publication P4. Notably, the effect described in P4 is novel and promises relevance outside the context of QSL research. The successful detection of anyons in QSLs in terms of local probes would be of great interest to the condensed matter community, and their manipulation could be an essential step on the long path to a topological quantum computer.

To conclude this account of topology in condensed matter systems, let us emphasize its incompleteness. Here, we focused on experimental phenomenology and theoretical concepts, which play a crucial role in the following chapters. We thereby neglected important aspects

of the present theoretical understanding in this field, such as the overall classification in terms of quantum field theory, the role of disorder and defects, and a description outside of equilibrium. Another subject we did not touch upon is nontrivial band topology of bosonic systems. We encounter such a scenario in Chapter 2, when we briefly discuss the magnonic modes of polarized QSL candidate materials to set the stage for my Publications P3 and P4.

1.2 Band topology of Weyl semimetals

Let us turn to a more detailed discussion of band topology in the state of matter which is the subject of my Publication P1, that is, *Weyl semimetals* (WSMs). On the non-interacting level, WSMs are characterized by gapless energy bands, which, close to the Fermi level, are nondegenerate with the exception of a discrete number of points, where two bands touch or cross [6]. These band crossings are called *Weyl nodes* for reasons that become clear below. Since the concurrent presence of time-reversal symmetry (TRS) and spatial inversion symmetry ensures the degeneracy of bands at every point in the Brillouin zone (BZ), we can classify WSMs into two families, namely systems with broken TRS and systems with broken inversion symmetry. In the latter case, the breaking of inversion symmetry is either caused or accompanied by strong spin-orbit coupling, which lifts the spin degeneracy.¹³ The required symmetry breaking in WSMs can be provided by intrinsic mechanisms, such as a magnetization texture or a non-centrosymmetric crystal structure, respectively, but can also be achieved by external influence, such as strain [6]. The crossing points, i.e., the Weyl nodes, of the resulting energy bands do not necessarily occur at high-symmetry points in the BZ but typically resemble *accidental degeneracies* at arbitrary points [82]. Notably, such band crossings in 3D systems are more stable than in one or two dimensions, since, roughly speaking, a 3D momentum space provides more parametric freedom to tune an energy gap to zero. Thus small perturbations should merely move the Weyl node in momentum space [6].

Given all these considerations, it might seem that Weyl nodes are generic in crystals and that WSMs should be common in nature. Indeed, what actually restricts this material class are the constraints that the Weyl nodes are located close to the Fermi energy, and that additional structures in the Fermi surface, such as Fermi pockets and nodal lines, are insubstantial enough to justify the following low-energy description. Given a band crossing of two nondegenerate bands, we can expand in its vicinity to obtain an effective two-band model. Up to an overall constant, we find at linear order in the momentum (setting $\hbar = c = 1$)

$$H(\mathbf{k}) \simeq \mathbf{k} \cdot \mathbf{v}_0 \sigma^0 + \sum_{j=1}^3 \mathbf{k} \cdot \mathbf{v}_j \sigma^j, \quad (1.4)$$

where \mathbf{k} is the momentum measured with respect to the Weyl node and the \mathbf{v}_μ are velocity vectors obtained from the dispersion relation. The identity σ^0 and the Pauli matrices $\sigma^1 = \sigma^x$, $\sigma^2 = \sigma^y$ and $\sigma^3 = \sigma^z$ act on a pseudospin, which typically is a mix of spin and orbital degrees of freedom. Notably, within the formalism of relativistic quantum mechanics, the above Hamiltonian describes massless particles with conic dispersion and definite chirality $\chi = \text{sign}[\mathbf{v}_1 \cdot (\mathbf{v}_2 \times \mathbf{v}_3)]$. This fact becomes more evident when we consider an isotropic

¹³In this case, if spinful TRS is preserved, there is still a Kramer's degeneracy at the time-reversal invariant momenta, see Footnote 3. However, in well-defined WSMs, the energy at these points is typically large compared to the Fermi level and the following arguments still apply.

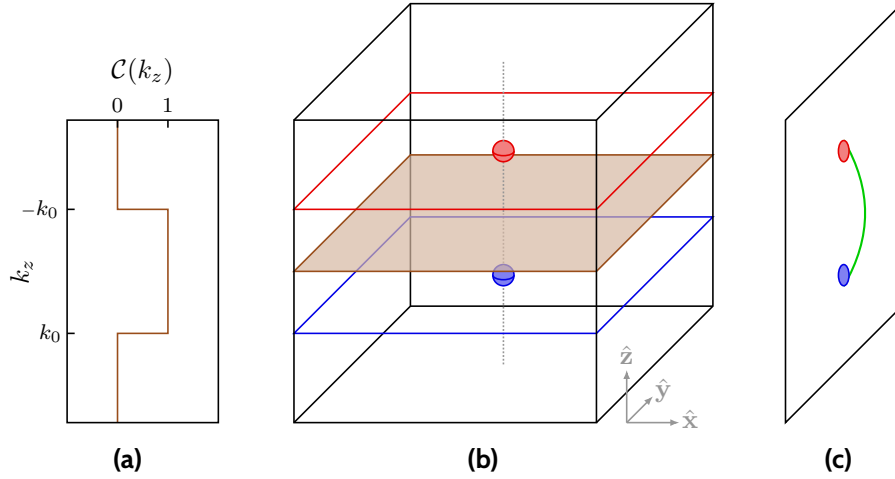


FIG. 1.1: Band topology of the WSM lattice model (1.9). **(a)** Chern number $\mathcal{C}(k_z)$ of the upper band corresponding to the horizontal 2D cuts indicated in the center. $\mathcal{C}(k_z)$ is not defined at $k_z = \pm k_0$. **(b)** Cubic bulk Brillouin zone hosting two Weyl nodes indicated by the blue ($\chi = 1$) and red ($\chi = -1$) spheres. **(c)** Quadratic surface Brillouin zone for a surface in the yz -plane. The Weyl node projections (blue and red circles) are connected by a schematic Fermi arc (green curve).

cone, i.e., $|\mathbf{v}_1| = |\mathbf{v}_2| = |\mathbf{v}_3| = v_F$, and negligible values of $|\mathbf{v}_0|$.¹⁴ For an appropriate choice of the coordinate system, we then arrive at the Hamiltonian

$$H_\chi(\mathbf{k}) = \chi v_F \mathbf{k} \cdot \boldsymbol{\sigma}. \quad (1.5)$$

Upon replacing the speed of light by the Fermi velocity v_F , this is the Hamiltonian of the Weyl equation describing Weyl fermions with chirality $\chi = \pm 1$, as obtained from the massless limit of the 3D Dirac equation and a convenient representation of the Clifford algebra. While Weyl fermions do not appear in the standard model of fundamental particles, they are realized naturally in solid state physics. Before stressing the analogy to high-energy physics further, however, let us illustrate the nontrivial band topology of WSMs in terms of the continuum Hamiltonian (1.5) and a simple lattice model.

1.2.1 Monopoles of Berry curvature

In Section 1.1, we introduced the Chern number (1.2) as the topological invariant for lattice models supporting the integer quantum Hall effect and other gapped systems with broken TRS. Despite the absence of an energy gap, we can also employ this concept to describe WSMs. To this end, we note that the Chern number is related to the geometrical properties of energy eigenstates in the parameter space and, therefore, to the *Berry phase*. Initially introduced by Berry in the context of adiabatic dynamics [24], the Berry phase constitutes the geometric phase a state accumulates when a nondegenerate Hamiltonian is adiabatically varied in a general parameter space, and it is formally defined as the line integral of the *Berry connection*. To define the Berry connection for our purposes, let us assume a 3D system with translational invariance and let $|u_j(\mathbf{k})\rangle$ be the eigenstate of the j th energy eigenvalue at momentum \mathbf{k} . The corresponding

¹⁴The vector \mathbf{v}_0 tilts the Weyl cone in momentum space. Finite but small values of $|\mathbf{v}_0|$ do not change the topological and physical properties on a qualitative level. The corresponding systems are called *type-I* WSMs. Beyond a critical value of $|\mathbf{v}_0|$, however, the cone crosses the Fermi level and forms Fermi pockets. The resulting system is called *type-II* WSM [6] and is not further discussed here.

Berry connection is then given by

$$\mathcal{A}_j(\mathbf{k}) = i \langle u_j(\mathbf{k}) | \nabla_{\mathbf{k}} u_j(\mathbf{k}) \rangle. \quad (1.6)$$

Roughly speaking, this quantity measures the similarity of states at different momenta somewhat like parallel transport measures the similarity of different tangent vectors on a curved manifold [147]. The name stems from the fact that the Berry connection transforms like a vector potential under gauge transformations $|u_j(\mathbf{k})\rangle \rightarrow e^{i\alpha(\mathbf{k})} |u_j(\mathbf{k})\rangle$ for scalar $\alpha(\mathbf{k})$ [230]. Thus, the corresponding Berry phase is only gauge invariant for a closed path in momentum space. More specifically, in three dimensions, the formal similarity to electromagnetic fields motivates the definition of the Berry curvature $\mathcal{B}_j(\mathbf{k}) = \nabla_{\mathbf{k}} \times \mathcal{A}_j(\mathbf{k})$ of the j th energy band. Based on the Gauss-Bonnet theorem [147], we can then define the Chern number $\mathcal{C}_j \in \mathbb{Z}$ of the j th band as the quantized flux of Berry curvature through a closed 2D manifold \mathcal{S} (in units of 2π), i.e.,

$$\mathcal{C}_j(\mathcal{S}) = \frac{1}{2\pi} \int_{\mathcal{S}} d\mathbf{S} \cdot \mathcal{B}_j(\mathbf{k}). \quad (1.7)$$

In the context of 2D models, when integrating over the whole BZ (which is a closed manifold), this definition is equivalent to Eq. (1.2) [7]. Let us apply this concept to Weyl semimetals, and, in particular, to the simple Hamiltonian $H_{\chi}(\mathbf{k})$ in Eq. (1.5) describing an isotropic Weyl node with chirality χ and eigenvalues $E_{\pm}(\mathbf{k}) = \pm v_F k$, where $k = |\mathbf{k}|$. While the Berry curvature is not defined at the Weyl node $\mathbf{k} = \mathbf{0}$ itself, it is straightforward to show that the Berry curvature of the upper band is given by [35]

$$\mathcal{B}_+(\mathbf{k}) = \frac{\chi \mathbf{k}}{2k^3}. \quad (1.8)$$

Based on the formal similarity to classical electrodynamics, we can therefore identify the Weyl nodes as sources or sinks or, more generally, *monopoles* of Berry curvature. As we discuss below, this gives rise to anomalous magnetotransport which can be captured by modifying the semiclassical equations of motion [199, 147]. Moreover, we note that the Chern number of the upper band associated with a sphere enclosing the Weyl node is $C_+ = \chi$, i.e., the chirality.

While the definition of a global topological invariant in terms of a Chern number is impossible due to the three spatial dimensions and the absence of an energy gap, we still encounter nontrivial band topology in the vicinity of Weyl nodes. Consequently, we can apply the concepts from Section 1.2 to explain the emerging physics in WSMs and, in particular, the appearance of topological surface states. However, to fully characterize the energy contour of surface states in the whole surface Brillouin zone (sBZ), we have to revert to a lattice model. For simplicity, we consider a two-band model on a cubic lattice with unit lattice constant given by

$$H_{\text{cubic}}(\mathbf{k}) = t_x \sigma^x \sin k_x + t_y \sigma^y \sin k_y + t_z \sigma^z (\cos k_0 - \cos k_z), \quad (1.9)$$

where we assume $k_0 \in (0, \pi/2]$ for concreteness [28]. Given an appropriate choice of the parameters t_x , t_y and t_z , this model describes a WSM with broken TRS and two Weyl nodes of opposite chirality located at $\mathbf{k} = \pm k_0 \hat{\mathbf{z}}$. The isotropic continuum description (1.5) is recovered for $t_x = t_y = v_F$ and $t_z = v_F / \sin k_0$ upon shifting the Weyl node with chirality ± 1 to $k_z = \mp k_0$.¹⁵

To probe the band topology of this Hamiltonian, let us consider 2D cuts of the cubic BZ, such as the horizontal planes at different values of k_z that are illustrated in Fig. 1.1(b). As long as

¹⁵Formally speaking, the expansion at $\mathbf{k} = k_0 \hat{\mathbf{z}}$ should be accompanied by the unitary transformation σ^z , i.e., $H_{\text{cubic}}(\mathbf{k} - k_0 \hat{\mathbf{z}}) \simeq \sigma^z H_-(\mathbf{k}) \sigma^z$ for $k_0 \gg k$.

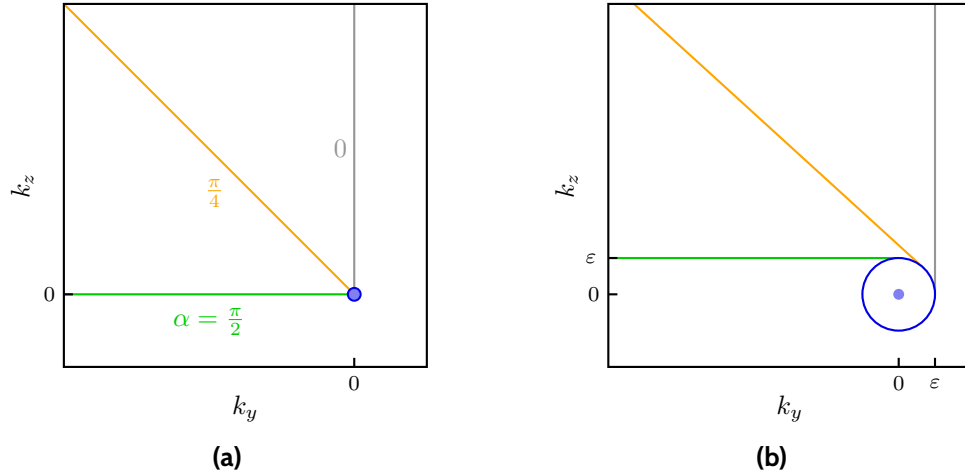


FIG. 1.2: Energy contour of the surface-state dispersion (1.12) for $\chi = +1$ and different values of the angle α . **(a)** At zero energy ($\varepsilon = 0$), the contour terminates at the projection of the Weyl node (blue point). **(b)** At finite energy ($\varepsilon > 0$) the contour is tangential to and terminates at the projection of the bulk cone (blue circle).

a plane does not contain a Weyl node, the associated cut of the band structure resembles a 2D insulator and we can use Eq. (1.7) to compute the associated Chern number $\mathcal{C}(k_z)$ of the upper band. Results are shown in Fig. 1.1(a). We find that, upon varying the position of the plane k_z , the Chern number jumps at the Weyl nodes and, in our case, assumes finite values only between the nodes, i.e., for $|k_z| < k_0$. In this region, the 2D cut of the bulk band structure resembles a *Chern insulator*, as mentioned in Footnote 2.

Moreover, due to the required periodicity of $\mathcal{C}(k_z)$ as function of k_z , we can infer that Weyl nodes must appear in pairs of opposite chirality [6]. This is formally ensured by the famous no-go theorem by Nielsen and Ninomiya [161], which states that the number of left-handed ($\chi = -1$) particles must equal the number of right-handed ($\chi = +1$) particles in any lattice realization. It follows that Weyl nodes can only be gapped in terms of pairwise annihilation, and therefore hints at intrinsic protection of nodes against weak perturbations [6]. Moreover, we can discern how the Nielsen-Ninomiya theorem manifests in both aforementioned hallmark features of band topology, namely magnetotransport signatures and the emergence of topological boundary states. Let us begin with the discussion of the latter.

1.2.2 Fermi arcs

A 2D Chern insulator with a unit Chern number hosts exactly one topological edge mode at a given boundary [147]. This is also the case for the 2D cuts presented in Fig. 1.1(c). From the reiteration of this argument for planes with different orientation, we can then infer that the zero-energy contour formed of the surface states must terminate at the projection of the Weyl nodes on the sBZ [6]. As illustrated in Fig. 1.1, the contour thus forms an open and disjoint segment of a curve - the so-called Fermi arc.

For a more explicit description of these unconventional surface states and as a preparation for the calculation in my Publication P1, let us again consider the low-energy Hamiltonian (1.5) of a single Weyl node, and let us derive the Fermi arc for a system which fills the positive half-space $x > 0$ and shares a boundary with vacuum at $x = 0$. While the in-plane momentum $\mathbf{k}_\perp = (k_y, k_z)^T$ remains a good quantum number, we account for the breaking of translational invariance along the x -direction in terms of the substitution $k_x \rightarrow -i\partial_x$. An appropriate

boundary condition is then obtained by imposing Hermiticity of the Hamiltonian H_χ for the half-space geometry [225, 78, 203], i.e., $\langle \Psi_1 | H_\chi \Psi_2 \rangle - \langle H_\chi \Psi_1 | \Psi_2 \rangle = 0$ for all states Ψ_1 and Ψ_2 in the Hilbert space. Physically, this constraint prohibits any net current flow through the surface.¹⁶ As further discussed in my Publication **P1**, Hermiticity is ensured by the sufficient boundary condition

$$M_\alpha \Psi(x=0) = \Psi(x=0) \quad \text{for} \quad M_\alpha = \sigma^y \cos \alpha + \sigma^z \sin \alpha, \quad (1.10)$$

where α is a free parameter. Up to overall normalization, evanescent energy eigenstates which satisfy the boundary condition are thus of the form

$$\Psi(x) \propto e^{-\kappa x} \begin{pmatrix} 1 + \sin \alpha \\ i \cos \alpha \end{pmatrix}, \quad (1.11)$$

where we use the standard representation of Pauli matrices. Inserting our ansatz in the eigenproblem $H_\chi \Psi = \varepsilon \Psi$ yields for the energy dispersion and the inverse decay length

$$\varepsilon(\mathbf{k}_\perp) = \chi k_y \cos \alpha + \chi k_z \sin \alpha, \quad \kappa(\mathbf{k}_\perp) = -k_y \sin \alpha + k_z \cos \alpha, \quad (1.12)$$

respectively [78, 203]. We note that physical solutions in the positive half-space are restricted by the normalization constraint $\kappa > 0$. Thus, the energy contour is a semi-infinite line with a single termination point and oriented at an angle α with respect to the k_z -axis. This is illustrated in Fig. 1.2. At zero energy, $\varepsilon = 0$, this termination point is exactly given by the Weyl node projection at $\mathbf{k}_\perp = \mathbf{0}$, while at finite energy, the contour is tangential to the Weyl cone.

Here, we find a semi-infinite precursor of the full finite Fermi arc, since we consider only a single Weyl node, thereby ignoring the Nielsen-Ninomiya theorem. A more appropriate continuum model should consider two Weyl nodes, which are either coupled by a mass term or described by a quadratic dispersion [28, 36]. In our case, the latter can be obtained by expanding H_{cubic} in Eq. (1.9) up to second order. Alternatively, in my Publication **P1**, we study a continuum model of two decoupled Weyl nodes and, notably, still find physical finite Fermi arcs for boundary conditions which mix the two chiral sectors.¹⁷ The shape and curvature of the resulting arc is then controlled by free parameters of the boundary condition like above. Generally speaking, the parametric freedom granted by imposing Hermiticity of relativistic continuum models has drastic physical implications on the boundary spectrum, and allows us to implement symmetries of real materials and their microscopic boundaries [3, 4]. This is certainly helpful for modeling, since in typical WSM realizations, Fermi arcs are not straight lines connecting isolated pairs of Weyl nodes but exhibit a much richer *connectivity* [218, 88].

The experimental observation of Fermi arcs enabled the first experimental confirmation of a WSM, and was based on angle-resolved photoemission spectroscopy (ARPES) measurements on the transition metal compound TaAs [231, 135]. TaAs and the related WSMs TaP, NbAs and NbP crystallize in a non-centrosymmetric tetragonal lattice structure and thereby break inversion symmetry [218, 88, 6]. Due to additional strong spin-orbit coupling, the band structure is nondegenerate with the exception of 24 Weyl nodes. As revealed by careful symmetry analysis and confirmed by soft X-ray photons in ARPES, specific surfaces of TaAs host 16 curved Fermi

¹⁶In our case, since \mathbf{k}_\perp is conserved, the current through the surface also vanishes locally. In general, however, it is possible to formulate boundary conditions which break translational invariance in the yz -plane and require treatment of the full real-space Hamiltonian $-i\chi v_F \nabla_{\mathbf{r}} \cdot \boldsymbol{\sigma}$.

¹⁷The model in Publication **P1** is justified since internode scattering is typically small in real materials [6].

arcs.¹⁸ A smaller number of Weyl nodes and a more comprehensible surface state dispersion can be typically found in magnetic WSMs with broken TRS [22]. Although it is generally harder to grow sufficiently large samples of this material class [6], ARPES and quasi-particle interference measurements confirmed a WSM phase and topological surface states in the ferromagnets Co₂MnGa [21] and Co₃Sn₂S₂ [131, 155]. Notably, Co₃Sn₂S₂ is a layered material, and the Fermi-arc connectivity of the projections of the six Weyl nodes depends on the surface termination as it differs for surface layers of Co and Sn atoms [155]. Another mechanism which controls the connectivity was recently proposed in studies of twisted WSM interfaces [56, 1, 31] and tunnel junctions [43]. Both the recent experimental progress on magnetic WSMs and the theoretical studies on novel Fermi-arc states were motivation for the research which is presented in my Publication P1 and which investigates the interplay of a Fermi arc and bulk magnetotransport. Let us discuss the latter next.

1.2.3 Poor man's chiral anomaly

Shortly after Paul Dirac proposed his eponymous equation and thereby set the foundation of relativistic quantum mechanics and quantum field theory [54], Hermann Weyl introduced an important simplification of the Dirac equation in the massless limit and for three spatial dimensions [219]. While, so far, Weyl fermions have not been observed in high-energy physics experiments, in the context of condensed matter, they naturally emerge as the low-energy excitations of WSMs. Notably, this allows to probe the unconventional response of Weyl fermions to electromagnetic fields, which, according to theory, is governed by the *chiral anomaly*. In quantum field theory, anomalies are the failure of a classical symmetry in the corresponding quantum theory. The first quantum anomaly was discovered by Adler, Bell and Jackiw in the context of the dominant decay of a pion into two photons [20, 2]. Here, we schematically discuss the phenomenology of the chiral anomaly for Weyl fermions and how it manifests on the level of the band structure of real materials.

To this end, let us consider the Dirac action for massless fermions in a four-dimensional spacetime (using Einstein notation)

$$S(\psi) = i \int d^4x \psi^\dagger(x) \gamma^0 \gamma^\mu \partial_\mu \psi(x), \quad (1.13)$$

where γ^μ are gamma matrices with $\{\gamma^\mu, \gamma^\nu\} = 2\eta^{\mu\nu}$ and $\eta = \text{diag}(1, -1, -1, -1)$ is the Minkowski metric. It is well established that the action has an U(1) symmetry, which corresponds to the conservation of electric charge. More intriguingly, due to the absence of a mass term, the action is also invariant under

$$\psi \rightarrow e^{i\theta\gamma^5} \psi, \quad (1.14)$$

where θ is a scalar and $\gamma^5 = i\gamma^0\gamma^1\gamma^2\gamma^3$. It is this symmetry which, given an appropriate choice of the gamma matrices, permits the decomposition of a Dirac fermion into two Weyl fermions with different chirality, as discovered by Weyl [219]. Moreover, according to Noether's theorem, as a continuous symmetry of the action, it corresponds to the conservation of a *chiral charge*. Variation of the action manifests this fact in terms of the continuity equation $\partial_\mu j_5^\mu = 0$ of the chiral current

$$j_5^\mu = \psi^\dagger \gamma^0 \gamma^5 \gamma^\mu \psi, \quad (1.15)$$

¹⁸The situation in TaAs is even more subtle. In the case of the specific surface orientation, some Weyl nodes of equal chirality are projected onto the same points in the sBZ, giving rise to effective Chern numbers of magnitude two. These Weyl node projections are thus each connected to two Fermi arcs [218, 88, 6].

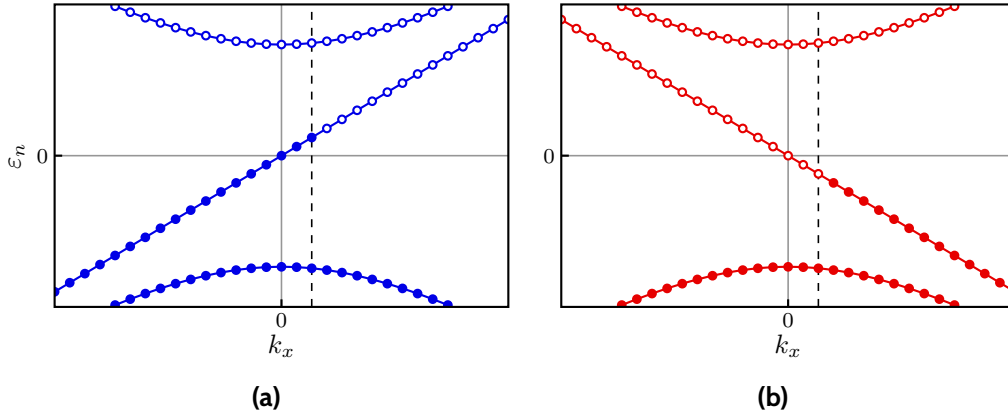


FIG. 1.3: Dispersion of Landau levels (1.17) for **(a)** $\chi = -1$ and **(b)** $\chi = +1$. An electric field along x displaces the manifold of occupied states (filled circles) and generates chiral fermions. Adapted from Ref. [162]

which holds both for the classical and quantized theory. The situation changes when we switch on a static electromagnetic field and couple the fermion ψ to an $U(1)$ gauge field a_μ . Upon the substitution $\partial_\mu \rightarrow \partial_\mu + ie a_\mu$, the action (1.13) remains invariant under the transformation (1.14) and Noether's theorem still applies on a classical level. In the renormalized quantum theory, however, the continuity equation is violated as one finds [162]

$$\partial_\mu j_5^\mu = \frac{e^2}{2\pi^2} \mathbf{E} \cdot \mathbf{B}, \quad (1.16)$$

where, as per usual, the electric field \mathbf{E} and the magnetic field \mathbf{B} are obtained from the field strength tensor $F_{\mu\nu} = \partial_\mu a_\nu - \partial_\nu a_\mu$. Within the path integral formalism of quantum field theory, this surprising result arises due to the fact that the integral measure does not share the symmetry of the action and is not invariant under the transformation (1.14). We do not present a derivation of Eq. (1.16) within this formalism, but instead discuss how the anomaly and the violation of chiral charge conservation arises on the level of the energy bands.

Landau quantization of a Weyl node

For this purpose, let us revisit the simple two-band model (1.5) of a single Weyl node with chirality χ and consider the presence of a homogeneous magnetic field $\mathbf{B} = B\hat{\mathbf{x}}$ with $B > 0$. As a standard approximation [162, 34], we neglect Zeeman coupling of the spin and only consider the orbital effect of the magnetic field, that is, the Landau quantization obtained from minimal coupling. A detailed derivation of the bulk spectrum is included in my Publication P1. Here, we just present results for the Landau levels (LLs) ε_n , which are labeled by an integer $n \in \mathbb{Z}$ and given by

$$\varepsilon_0(k_x) = -\chi k_x, \quad \varepsilon_n(k_x) = \text{sign}(n) \sqrt{\frac{2|n|}{\ell_B^2} + k_x^2} \quad \text{for } n \neq 0, \quad (1.17)$$

where $\ell_B = 1/\sqrt{eB}$ is the magnetic length and we set $v_F = c = 1$ for consistency with the above expressions and with my Publication P1. This energy spectrum is shown in Fig. 1.3. Notably, the LLs only disperse along the x -direction parallel to the magnetic field.¹⁹ While the

¹⁹When choosing a gauge of the vector potential which retains translational invariance along an additional direction, e.g. the Landau gauge $\mathbf{A} = By\hat{\mathbf{z}}$, the dispersion along this direction is flat and thereby accounts for the extensive degeneracy of LLs.

higher order LLs or $n \neq 0$ exhibit a typical massive relativistic dispersion, the 0th LL is chiral and gapless. The chirality of the 0th LL manifests both in the direction of the dispersion, which is determined by χ , as well as the *spin-momentum locking* of the corresponding eigenstates, as detailed in Publication **P1**.

The chiral anomaly emerges, if we adiabatically switch on a homogeneous electric field. For simplicity, we consider an electric field $\mathbf{E} = E\hat{\mathbf{x}}$ parallel to \mathbf{B} , thereby reducing the problem to one spatial dimension. Since the density of states in the 0th LL per unit volume is $eB/(4\pi^2)$, the electric field generates fermions at a rate [162]

$$\dot{N}_\chi = \frac{\chi e}{4\pi^2} \mathbf{E} \cdot \mathbf{B}, \quad (1.18)$$

where N_χ is the total number of fermions with chirality χ . The particle generation is also indicated in Fig. 1.3. To connect to results for a massless Dirac fermion described by Eq. (1.13), we should consider two Weyl nodes of opposite chirality and, for now, at the same position in momentum space. Notably, total electric charge is then conserved since $\dot{N}_+ + \dot{N}_- = 0$. In case of the chiral charge, however, we find

$$\partial_\mu j_5^\mu = \partial_0 j_5^0 = \dot{N}_+ - \dot{N}_- = \frac{e^2}{2\pi^2} \mathbf{E} \cdot \mathbf{B}, \quad (1.19)$$

where we used that the spatial contraction $\partial_k j_5^k = 0$ (for $k \in \{1, 2, 3\}$) vanishes for homogeneous fields \mathbf{E} and \mathbf{B} . This agrees with the result (1.16) from quantum field theory, and consequently, constitutes the chiral anomaly on the level of the Landau quantization.

Notably, the above derivation also holds if the two Weyl nodes are separated in momentum space, as it is the case in WSMs. We briefly discuss how to attain this separation in the action (1.13) down below. At this point, however, we can already infer important subtleties of the low-energy description in terms of quantum field theory. To this end, we note that the generation of fermions according to Eq. (1.18) is only possible due to the infinitely deep Fermi sea of the free continuum. As we can easily see by means of the simple model (1.9), however, this is not given in lattice realizations of Weyl nodes. In particular, in a lattice model, the energy bands that yield the low-energy description (1.5) for $\chi = \pm 1$ must either be identical or cross at higher energies. As the equal numbers of Weyl nodes with positive and negative chirality are ensured by the Nielsen-Ninomiya theorem, it follows that the overall electric and chiral charge is conserved. Conversely, we might say that the total charge conservation manifests in the Nielsen-Ninomiya theorem [161, 162], and that WSMs merely realize a *poor man's chiral anomaly*. Besides this, the Lorentz invariance of Eq. (1.13) is, if at all, a feature of the low-energy description but not of the full lattice model. We conclude that, even under idealized conditions, the description of the chiral anomaly in condensed matter systems is subtle and somewhat elusive [75, 34]. From this perspective, my Publication **P1** resembles a study on how the chiral anomaly is further modified in the presence of a boundary.

Experimental signatures of anomalous magnetotransport

It is nevertheless possible to predict characteristic magnetotransport signatures of WSMs using a low-energy description. To separate the two Weyl fermions in momentum and energy, we can perform the substitution $\partial_\mu \rightarrow \partial_\mu + ib_\mu \gamma^5$ in the Dirac action (1.13). It is straightforward to show that the resulting Hamiltonian describes two Weyl nodes at $\mathbf{k} = \pm \mathbf{b}/2$ with energy $\pm b_0$. More notably, upon promoting Eq. (1.14) to a local symmetry with $\theta(x) = -x^\mu b_\mu$, the above substitution resembles a coupling between the fermion ψ and a *chiral gauge field* $b_\mu \gamma^5$ [259].

If we further include an electromagnetic gauge field a_μ like above, the present symmetries of the action then allow for an additional term $\propto \theta(x)\mathbf{E} \cdot \mathbf{B}$, which couples the fields a_μ and b_μ [259, 195, 208]. Such a term is familiar from the study of *axion electrodynamics* [72] and plays an important role in the description of topological insulators [147]. As per usual, the (classical) electric current can then be obtained by variation of the total action [34, 259]

$$\mathbf{j} = \frac{e^2}{2\pi^2}(\mathbf{E} \times \mathbf{b} + b_0 \mathbf{B}). \quad (1.20)$$

Given the aforementioned caveats of the low-energy description, let us not go into further detail but motivate a consistent expression using the cubic lattice model (1.9). As discussed above and illustrated in Fig. 1.1, 2D slices of the band structure in the $k_x k_y$ -plane at fixed k_z resemble Chern insulators with nontrivial band topology if $|k_z| < k_0$ (for the specified parameters). Such Chern insulators host exactly one gapless edge mode and, therefore, support an integer quantum Hall effect with transverse conductivity $\sigma_{xy}^{2D} = e^2/h$. The effective stack of Chern insulators between the Weyl nodes should then amount to a transverse conductivity [6]

$$\sigma_{xy} \propto \frac{e^2}{h} k_0, \quad (1.21)$$

which is consistent with Eq. (1.20) for $\mathbf{b} = 2k_0 \hat{\mathbf{z}}$. This result constitutes a non-quantized *anomalous Hall effect (AHE)* in WSMs. As confirmed by Burkov [33], the overall prefactor of the conductance quantum e^2/h is robust as long as the Fermi energy is close to the Weyl nodes and, in that sense, universal and intrinsic. This is different to the AHE of generic ferromagnetic metals [156, 230], which can exhibit a strong dependency on microscopic details [33]. The discrimination of extrinsic and intrinsic contributions is crucial for an unambiguous explanation of experiments on the AHE and the chiral anomaly.

The first successful observation of the chiral anomaly was reported in measurements of *longitudinal magnetoresistance (LMR)* in the first confirmed WSM TaAs [244]. The LMR is the change in longitudinal resistance due to the presence of a finite magnetic field. While typically small and positive in nonmagnetic materials [6, 244], a negative and large (in magnitude) LMR is expected to arise in WSMs due to the chiral anomaly. Moreover, since the generation rate in Eq. (1.18) is proportional to $\mathbf{E} \cdot \mathbf{B}$, the LMR should exhibit a strong dependency on the field direction. The expected signatures were observed in TaAs and, importantly, alternative explanations of the measured LMR were eliminated by additional techniques such as ARPES, *ab initio* calculations and measurements of the *Shubnikov de-Haas (SdH)* oscillations [244]. The latter are an instance of quantum oscillations, that is, the periodicity of an observable as a function of the inverse magnetic field strength $1/B$ due to Landau quantization and the existence of a Fermi surface.

Quantum oscillations proved a powerful technique to probe WSMs and other topological semimetals [6]. Measurements of SdH oscillations in the WSM TaP, for example, enabled the observation of the annihilation of Weyl nodes due to the mixing of chiralities from magnetic internode tunneling [245]. Moreover, a semiclassical description predicts the appearance of exotic quantum oscillations in thin films (or similar nanostructures) of WSMs due to exotic cyclotron orbits which involve both the Fermi-arc surface state and chiral LLs in the bulk - so-called *Weyl orbits* [174, 251, 243]. The nonlocal nature of Weyl orbits inspired various theoretical studies [70, 167, 18, 86, 160, 258], and was experimentally reported in related topological semimetals [152, 241, 253] and non-centrosymmetric WSMs [242, 129, 157]. The comparison of the semiclassical approximation and a full quantum mechanical description of Weyl orbits in

magnetic WSMs is subject of my Publication **P1**. There, we give a detailed introduction to Weyl orbits and employ many of the technical concepts presented in this section.

1.3 Topological order in \mathbb{Z}_2 quantum spin liquids

Let us familiarize ourselves with the states of matter which occupy the majority of this thesis, that is, *quantum spin liquids* (QSLs). This effort is somewhat obscured by the fact that there is no generally accepted definition of a QSL which includes all instances, where the term is used [187, 118, 147]. A minimal requirement for a QSL which is agreed upon, however, states that a QSL is neither a conventional high-temperature paramagnet nor a *magnetically ordered* phase which arises due to spontaneous symmetry breaking. This is at odds with the conventional scenario for magnetic systems, in which, upon cooling the system to low temperatures, spin degrees of freedom spontaneously form long-range patterns which break symmetries of the underlying theory and give rise to a thermal phase transition from a paramagnetic to an ordered state with long ranged correlations. Typically, the critical temperature of this transition is well estimated by the Curie-Weiss temperature Θ_{CW} as determined by the strength of the spin exchange. Below the critical temperature, the Ginzburg-Landau theory provides a comprehensible description of the magnetically ordered phase in terms of an effective field theory for a local order parameter [213]. Due to the tremendous success of this paradigm, we may first discuss the microscopic mechanism which suppresses magnetic ordering. To this end, we focus on Mott insulating systems at commensurate filling to justify the use of effective models which only involve localized spin degrees of freedom, see Chapter 2. Our considerations eventually guide us to spin models which do not exhibit spontaneous symmetry breaking both on the classical level and in the quantum theory, but which instead host topological order as described above. Two comments are appropriate about these results. First, we note some QSLs can spontaneously break symmetries of the underlying theory, such as *chiral spin liquids* which obstruct the time-reversal symmetry of the system [187, 147]. Second, albeit that topological order was introduced as the organizing mechanism in the absence of conventional local order, gapless QSLs do not host topological order as a strict definition of this concept requires a finite energy gap [216, 187]. While we briefly encounter a gapless QSL in Chapter 2, the majority of this thesis and, in particular, my Publications **P2** and **P3** are devoted to a specific gapped QSL. We thus employ the concept of topological order to introduce a phenomenon which is common in all QSLs and distinguishes these exotic states of matter from conventional paramagnets. This phenomenon is the fractionalization of the microscopic spin degrees of freedom and manifests in exotic quasiparticle excitations.

1.3.1 Frustrated magnetism

To understand the microscopic mechanism that prohibits the formation of long-range order, we consider a variety of simple toy models, starting with arguably the most studied model in the fields of condensed matter and statistical physics. The classical Ising model is given by

$$H_{\text{I}} = J \sum_{\langle jk \rangle} \sigma_j \sigma_k, \quad (1.22)$$

where the $\sigma_j = \pm 1$ are Ising spins and $\langle jk \rangle$ denotes the bond connecting the neighboring sites j and k on a given lattice. Here, we focus on two-dimensional (2D) lattice geometries

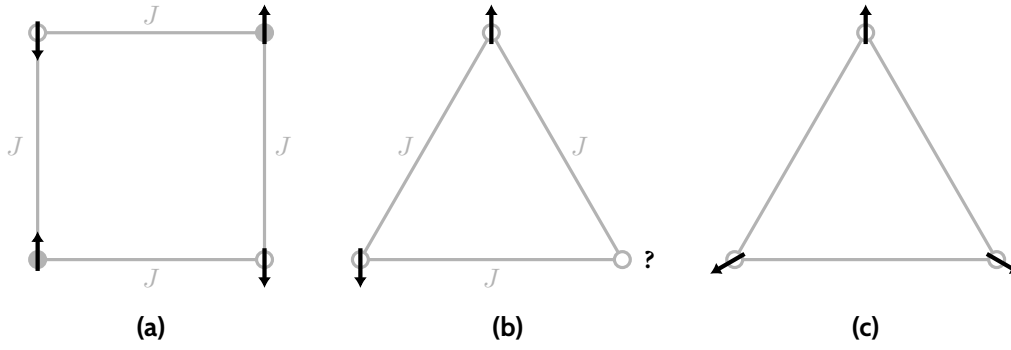


FIG. 1.4: Geometric frustration for antiferromagnetic spin exchange. **(a)** The Néel state on the frustration-free square lattice minimizes both H_I in Eq. (1.22) and H_H in Eq. (1.23). **(b)** The Néel state is incompatible with the frustrated triangular lattice. **(c)** The 120° order of Heisenberg spins on the triangular lattice minimizes H_H .

and antiferromagnetic coupling $J > 0$. On a square lattice (or any other bipartite lattice), the low-energy physics of this model is well established and comprehensible. Starting with a high-temperature disordered paramagnet, upon cooling to low temperatures, the system exhibits a second-order phase transition to a Néel state. The antiferromagnetic ground state configuration is then unique upon global symmetry transformations and breaks the \mathbb{Z}_2 symmetry of the Hamiltonian H_I , as shown in Fig. 1.4(a). While this description applies to any bipartite lattice, the situation changes dramatically for non-bipartite geometries such as the triangular lattice. As illustrated in Fig. 1.4(b), the antiparallel spin alignment on a given triangle of the lattice is not possible and the formation of a Néel state is suppressed. As a consequence, the competing interaction terms corresponding to the bonds on a triangle cannot be minimized simultaneously. In any low-energy configuration, every triangle thus involves exactly one bond interaction which is not minimized. Comparing to the simple results for the square lattice, we can then infer that the antiferromagnetic order is obstructed by the lattice geometry. This mechanism is termed *geometric frustration*. As first described in a seminal work by Wannier [215], the large number of low-energy configurations on the triangular lattice gives rise to an extensive ground state degeneracy and a residual entropy at zero temperature.²⁰ We further discuss the resulting low-energy physics of the model below, while, for now, it is sufficient to know that the classical antiferromagnetic Ising model on the triangular lattice does not host a magnetically ordered phase at low temperatures.

Notably, despite the name, geometric frustration still contains a dependency on the specific spin interaction. This becomes evident when describing an antiferromagnet in terms of another hallmark model of magnetism, the classical Heisenberg model (again assuming $J > 0$)

$$H_H = J \sum_{\langle jk \rangle} \mathbf{S}_j \cdot \mathbf{S}_k, \quad (1.23)$$

where the \mathbf{S}_j are Heisenberg spins as formally obtained from quantum spins for $S \rightarrow \infty$. While, like above, the triangular lattice does not support a Néel state, the continuous symmetry of H_H permits other configurations with low energy. Namely, at low temperature, the neighboring spins align at an angle of 120° with respect to each other and thereby give rise to

²⁰In our discussion of frustrated magnetism, we sometimes use the term *ground state* to describe the classical spin configuration with the lowest energy. Moreover, we say that a degeneracy is extensive, if it scales with the system size [213]. We note that only degenerate configurations with finite statistical weight contribute to the zero-point entropy [215].

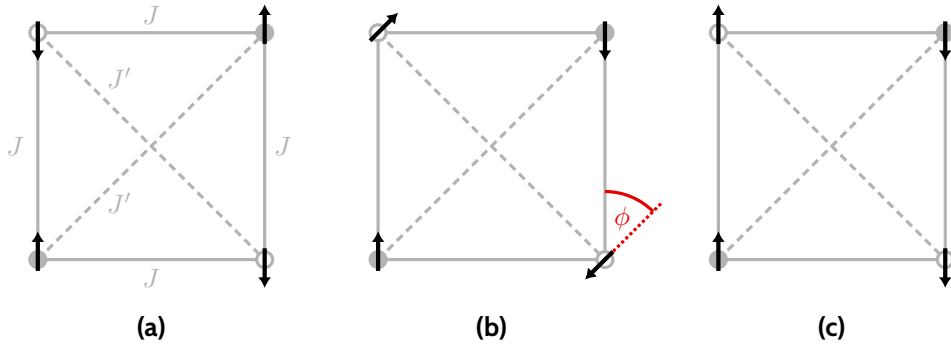


FIG. 1.5: Order by disorder in the J_1 - J_2 model in Eq. (1.24). **(a)** The Néel state is the classical configuration with minimum energy for $J' < 2J$. **(b)** For $J' > 2J$, the large degeneracy of classical configurations with antiparallel next-nearest neighbors is parametrized by the angle ϕ . **(c)** Quantum fluctuations select the ground state with either $\phi = 0$ or $\phi = \pi$. Adapted from Ref. [118].

an antiferromagnetic phase after all, see Fig. 1.4(c). We might infer that, in the case of Heisenberg spins, changing the lattice geometry cannot suppress magnetic order but only select a different ordered state. However, it is also possible to obscure spontaneous symmetry breaking of Heisenberg spins, if, instead of the lattice geometry, we modify the spin exchange. To this end, let us revert to the square lattice for simplicity, and include an antiferromagnetic next nearest-neighbor coupling

$$H'_H = H_H + J' \sum_{\langle\langle jk \rangle\rangle} \mathbf{S}_j \cdot \mathbf{S}_k, \quad (1.24)$$

where $\langle\langle jk \rangle\rangle$ denotes a next nearest-neighbor bond connecting j and k , i.e., a diagonal crossing a square plaquette of the lattice, see Fig. 1.5. The Hamiltonian H'_H then constitutes the famous J_1 - J_2 model (for $J = J_1$ and $J' = J_2$) [41]. The model is generally frustrated for $J' \geq 2J$, but, as we further detail below, we can distinguish different degrees of magnetic frustration. Of particular interest is the *highly-frustrated* point $J' = 2J$, which gives rise to an extensive degeneracy of low-energy configurations [41, 39]. This degeneracy stems from the competition of different exchange terms in the Hamiltonian which cannot be minimized simultaneously. Accordingly, we term this mechanism *exchange frustration*. And, indeed, it is currently debated whether the quantum version of the J_1 - J_2 model at the highly-frustrated point describes a QSL or a valence bond crystal [179, 118].

For a more comprehensible illustration of exchange frustration, let us discuss another example which does not require fine tuning and, notably, involves ferromagnetic spin coupling. This model is defined on a honeycomb lattice and involves a specific anisotropic spin exchange. To define this interaction, we note that the honeycomb lattice is tricoordinated and therefore comprises three different types of bonds, which we label by x , y and z as done in Fig. 1.6(a). We then consider Heisenberg spins $\mathbf{S}_j = (S_j^x, S_j^y, S_j^z)^T$ coupled by an anisotropic Ising-like exchange according to

$$H_K = K \sum_{\langle jk \rangle_x} S_j^x S_k^x + K \sum_{\langle jk \rangle_y} S_j^y S_k^y + K \sum_{\langle jk \rangle_z} S_j^z S_k^z = K \sum_{\langle jk \rangle_\alpha} S_j^\alpha S_k^\alpha, \quad (1.25)$$

where $\langle jk \rangle_\alpha$ refers to a bond of type $\alpha \in \{x, y, z\}$ connecting the neighboring sites j and k . This is our first encounter of the (isotropic) *Kitaev model* [112].²¹ The QSL phase captured by this

²¹The model is sometimes referred to as *Kitaev's honeycomb model* to distinguish from other seminal models by Alexei Kitaev [113, 114].

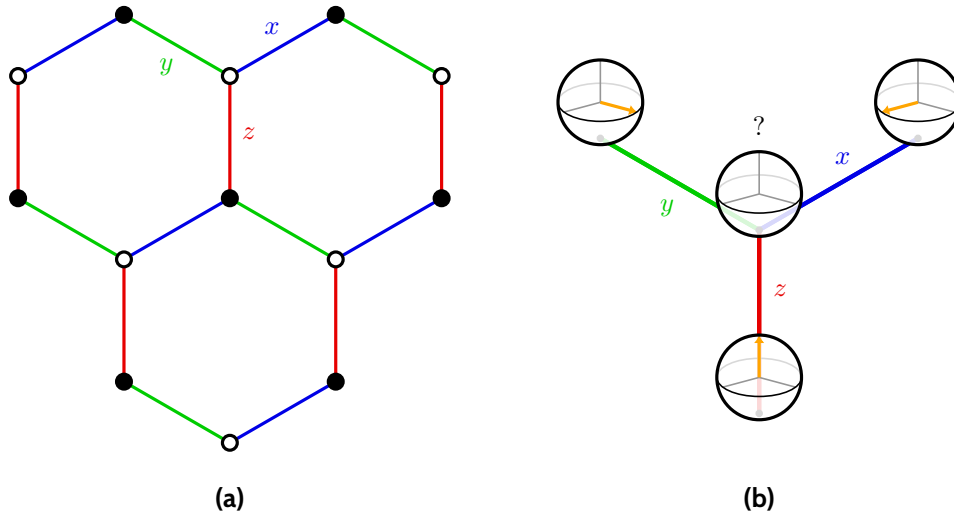


FIG. 1.6: Exchange frustration of Kitaev model (1.25) due to exchange anisotropy. **(a)** Tricoordinated honeycomb lattice with three different bond types x (blue), y (green) and z (red). **(b)** Simultaneous minimization of the bond-dependent interaction $K S_j^\alpha S_k^\alpha$ for $\alpha \in \{x, y, z\}$ is not possible. Adapted from Ref. [206].

model for quantum spins with $S = 1/2$ is the focus of a detailed analysis in Chapter 2 as well as my Publications **P2** and **P3**. Here, we discuss the exchange frustration of H_K on the classical level (for $S \rightarrow \infty$). As illustrated in Fig. 1.6(b), even for ferromagnetic coupling $K > 0$, the simultaneous minimization of all three interactions coupled to a given site is impossible. As a consequence, we again obtain a large manifold of minimum-energy configurations leading to residual entropy at zero temperature [17, 205]. We further discuss the low-energy physics of the classical Kitaev model below. Moreover, in my Publication **P4**, we numerically determine the classical ground state of the polarized Kitaev model in the presence of impurities. Such inhomogeneities in frustrated systems typically tip the sensitive energy balance in favor of a local distortion of the configuration, thereby acting as a so-called local *relief of frustration* [210, 227, 226]. In the case considered in Publication **P4**, this distortion is associated with a vorticity of the classical spins near the impurity that reflects the frustration of the model [144].

Summarizing our discussion until now, we identified both the geometry and spin exchange of the system as possible sources of magnetic frustration, which energetically penalizes magnetically ordered states. We did not, however, weigh in the effects of thermal or quantum fluctuations on the appearance of a phase transition. To do so, we first note that the extensive ground state degeneracy of highly-frustrated classical magnets is not associated with a global symmetry but seemingly accidental. The effect of fluctuations can therefore vary drastically for different ground state configurations and thereby select a specific state to maximize entropy [118]. This counter-intuitive ordering mechanism is called *order by disorder* [211]. Due to thermal fluctuations, for example, a frustrated system might order in a range of finite temperatures, but remain paramagnetic or disordered at low and zero temperature.

Similarly, quantum fluctuations can stabilize magnetic order at low temperatures. A simple example of this is provided by the aforementioned J_1 - J_2 model H_H' in Equation (1.24) on a square lattice. For sufficiently large next-nearest neighbor coupling $J' > 2J > 0$, the antiparallel alignment of next-nearest neighbors is energetically preferred and results in two interpenetrating Néel patterns [118], see Fig. 1.5(b). On a purely classical level, the angle ϕ between neighboring spins is completely arbitrary and gives rise to a sub-extensive ground state degeneracy. However, when we include bosonic quantum fluctuations in terms of a standard

Holstein-Primakoff expansion in S^{-1} , where S is the length of the quantum spins, the energy up to order S^{-1} is minimized for collinear states, i.e., $\phi \in \{0, \pi\}$ [190, 118]. The resulting spin configuration is illustrated in Fig. 1.5(c) and represents a typical instance of order by disorder.

Given that some frustrated magnets exhibit long-range order for sufficiently strong fluctuations while some do not at all, we should describe frustration quantitatively. A rough measure of the degree of frustration in real materials is given by the *frustration ratio*

$$f = \frac{|\Theta_{\text{CW}}|}{T_c}, \quad (1.26)$$

where Θ_{CW} is the aforementioned Curie-Weiss temperature and T_c is the (potentially suppressed) critical temperature of the magnetically ordered phase. While conventional magnets correspond to $f \approx 1$, systems with $f \gtrsim 10$ are typically referred to as highly frustrated [205]. Notably, magnets which do not exhibit any magnetic phase transitions upon cooling to zero temperature correspond to $f \rightarrow \infty$. We focus on such systems in what follows, starting with a more detailed classical description of the instances we encountered so far.

1.3.2 Coulomb phase of the classical Kitaev honeycomb model

Above we identified two highly-frustrated models which do not stabilize magnetic order at any finite temperature, namely, the antiferromagnetic Ising model on the triangular lattice and the (ferromagnetic) Kitaev model on the honeycomb lattice. Let us investigate the phenomenology, which emerges in the absence of order at low temperatures, and introduce the concept of a *classical spin liquid*. Due to its exceptional role in this thesis, we here focus on the Kitaev model H_K in Eq. (1.25) but note that the description of the Ising model is analogous. In fact, the close relation of antiferromagnetic coupling on the triangular lattice to ferromagnetism on its dual, the honeycomb lattice, was already recognized by Wannier [215]. While we ultimately want to include quantum fluctuations for $S = 1/2$, we stick to the classical limit $S \rightarrow \infty$ in what follows. Notably, since order by disorder due to thermal fluctuation is absent in the latter regime, we can identify remarkable (albeit limited) similarities to the quantum limit that can guide our discussion for the case $S = 1/2$, in particular, on the role of perturbations to H_K . We note, however, that the situation for large but finite S is more subtle [42, 189].

As a first step, we characterize the manifold of low-energy configurations of H_K in terms of a set of local constraints reflecting the exchange frustration. To this end, we consider the set of constraints stating that every spin has to align with one nearest neighbor along the Cartesian axis corresponding to the bond type [17].²² To compute the energy of a configuration meeting these constraints, we note that for every spin exactly one nearest-neighbor coupling is minimized while the remaining two coupling terms vanish identically. For a lattice with N sites, the energy then amounts to $KN/2$, which is indeed the global minimum of H_K for $K < 0$ [42]. Fig. 1.7 shows a spin configuration which meets the constraints and, therefore, constitutes a classical ground state. However, as expected, this is not the only possible configuration. To rationalize this, it is convenient to visualize the pairs of aligned spins which minimize their coupling as *dimers* consisting of two neighboring sites. We can then identify a one-to-one correspondence between ground state configurations and *dimer coverings* of the honeycomb

²²More formally, for a selected pair of sites j and k connected by a bond of type α , the local constraint is $\mathbf{S}_j = \mathbf{S}_k = \pm \hat{\alpha}$, where $\hat{\alpha} \in \{\hat{\mathbf{a}}, \hat{\mathbf{b}}, \hat{\mathbf{c}}\}$ is a unit vector along a crystallographic direction. The arbitrary sign \pm has to be accounted for in the ground state degeneracy [17]. Here, we assumed $K < 0$ and normalized the Heisenberg spins. The modification for antiferromagnetic Kitaev coupling $K > 0$ is straightforward.

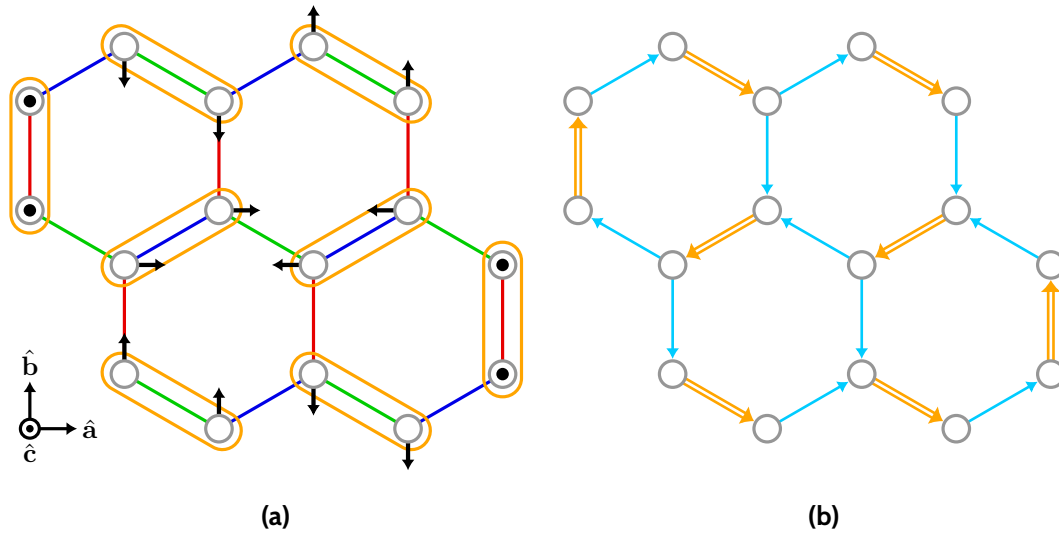


FIG. 1.7: Coulomb phase of the classical Kitaev model (1.25). **(a)** Minimum-energy spin configuration satisfies local constraints and corresponds to a dimer covering (orange) of the honeycomb lattice. Adapted from Ref. [183]. **(b)** Emergent artificial magnetic field (cyan and orange) with zero divergence at the lattice sites (except at a boundary). Adapted from Ref. [189].

lattice.²³ Counting all possible dimer coverings estimates the ground state degeneracy to be 1.662^N [17] and implies a finite residual entropy at zero temperature [205].

The theoretical description of the classical Kitaev model is further facilitated by the following abstraction. Given a specific dimer covering, we can map the bonds to an *artificial magnetic field* \mathbf{b} , which is twice as strong on bonds covered by dimers than on bonds not covered by dimers and which is directed by the bond types [189]. This is illustrated for the exemplar configuration in Fig. 1.7. As visible there, this specific mapping ensures that the artificial magnetic field is *divergence-free* at the sites of the lattice, i.e., $\text{div } \mathbf{b} = 0$ for a suitable lattice divergence [213]. Due to this emergence of magnetostatics, the low-energy state of the system is termed *Coulomb phase* [80]. As mentioned in Section 1.1, the Coulomb phase is an instance of a classical spin liquid and is clearly distinguishable from a conventional paramagnet in terms of its theoretical description [205].²⁴ This is evident in the spin correlations, which, for the Coulomb phase, drop according to a power law [189]. Moreover, the system hosts fascinating elemental excitations. These are given violations of local constraints and, since this corresponds to a finite divergence of \mathbf{b} , resemble *magnetic monopoles* of the artificial magnetic field [147]. We do not go into further detail but note that, in this sense, fractionalization of H_K is already observable on the classical level. In particular, the emerging description of the classical limit is roughly comparable to the emergence of the fractional quantum Hall effect, where, at fractional filling, electronic configurations in the lowest Landau level minimizing the kinetic energy are also extensively degenerate [147], see Section 1.1. We might therefore expect that the Kitaev model H_K for $S = 1/2$ provides an ideal incubator for fractional anyonic excitations and the accumulation of large quantum entanglement. As discussed in Chapter 2, this is indeed the case and subject of intensive investigation in my Publications P2 and P3.

We note, however, that the description of the Coulomb phase in the Kitaev model and the drawn conclusions have to be approached with caution. Besides general conceptual subtleties

²³Actually, it is a two-to-one correspondence, see Footnote 22.

²⁴Notably, however, between the spin liquid and the paramagnetic phase, there is no thermal phase transition but a thermal crossover [42, 189].

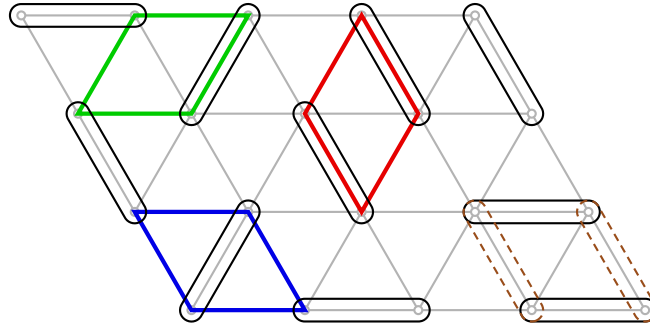


FIG. 1.8: Hardcore dimer covering of the triangular lattice. The three different types of rhombohedral plaquettes are indicated by blue, red and green. The red plaquette is flippable, while the blue and green plaquettes are not. The brown dashed lines indicate the configuration obtained by resonant dimer move as induced by the kinetic term of Eq. (1.27).

not mentioned here [147], the ground state degeneracy of the Kitaev model and the associated Coulomb phase are considerably sensitive to both lattice distortions and perturbations of the Hamiltonian [189], see Chapter 2. Instead, as discussed in Section 1.1, the prime example of the Coulomb phase is realized in *spin ice* on the three-dimensional pyrochlore lattice [147]. The pyrochlore lattice resembles a network corner-sharing tetrahedra and requires a modification of the set of local constraints defining the ground state manifold.²⁵ The emerging Coulomb phase is similar to above nevertheless, and was successfully confirmed in (inelastic) neutron scattering experiments on the pyrochlore oxides $\text{Dy}_2\text{Ti}_2\text{O}_7$ and $\text{Ho}_2\text{Ti}_2\text{O}_7$ [30, 61]. We do not further discuss the rich physics of spin ice here but, instead, proceed with the quantum limit. To this end, the above concept of dimer covering permits a straightforward generalization and the explicit construction of a QSL state.

1.3.3 Resonating valence bond liquid

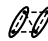

So far, our discussion of frustrated magnetism assumed classical spins with length $S \rightarrow \infty$. For a transparent characterization of quantum effects, let us now consider the opposite limit, i.e., $S = 1/2$, and let us attempt to build on our acquired understanding of classical spin liquids. As a first step, we should ensure that quantum fluctuations do not stabilize magnetic order by disorder as in the case of the J_1 - J_2 model, see Fig. 1.5. To this end, let us construct a many-body state which preserves $\text{SU}(2)$ symmetry. It is evident that such a state cannot be given by a simple product state of individual spin states. Instead, we should use the singlet representation of $\text{SU}(2)$ and, with realistic local exchange in mind, we consider a state composed of singlets formed by neighboring spins [147]. Identifying a singlet with a dimer and imposing the *hard-core* constraint that every site is part of exactly one dimer, then again guides our search for a disordered ground state to the study of hardcore dimer coverings of the respective lattice.²⁶ Although we can recognize an analogy to classical spin liquids at this point, our construction of a disordered state, and in particular a QSL, is not complete. This is because, as we will see below, emergence of long-range order is still possible if specific dimer coverings correspond to ground states, and instead, we expect a QSL to be a specific superposition of dimer coverings.

²⁵Namely, out of the four effective Ising spins on the corners of every tetrahedron, two spins have to point into and two spins have to point out of the tetrahedron [37]. The name *spin ice* stems from the fact that the resulting configurations are reminiscent of the proton positions in ice.

²⁶Notably, the mapping from a singlet to a dimer is not unique. This fact implies technical subtleties when considering dimer coverings as low-energy states of spin models [148].

The search for this state and a Hamiltonian which is minimized by this state leads us to the formal study of *quantum dimer models*.

Quantum dimer model on the triangular lattice

The first quantum dimer model was introduced by Rokhsar and Kivelson for the square lattice [181] to facilitate the description of a peculiar phase of matter proposed by Anderson and collaborators [58] and termed *resonating valence bond (RVB) liquid*. Notably, the RVB liquid was initially put forward by Anderson as a nonmagnetic parent state of high-temperature superconductivity in cuprates [5]. While this effort ultimately failed, the fascinating properties of this state inspired intensive on-going research, and it is now appreciated as the historically first description of a QSL. Here, we do not discuss the quantum dimer model for the square or the honeycomb lattice, but instead turn to the triangular lattice for reasons that become clear below. Possible dimer coverings of the triangular lattice are depicted in Fig. 1.8. We launch our quantum description by promoting all possible hardcore dimer coverings c to orthonormal quantum states $|c\rangle$ that span our Hilbert space. Subsequently, we introduce coherent quantum dynamics by defining a Hamiltonian in terms of operators that act on the rhombohedral plaquettes of the triangular lattice. As shown in Fig. 1.8, there are three different types of rhombohedral plaquettes, which are equivalent up to rotations by $\pm 60^\circ$. If a plaquette hosts exactly two dimers, we call it *flippable* and distinguish the two possible configurations by the symbols  and . The quantum dimer model is then given by [150]

$$H_{\text{QDM}} = -t \sum_{\Delta} (|\text{flippable symbol 1}\rangle \langle \text{flippable symbol 2}| + |\text{flippable symbol 2}\rangle \langle \text{flippable symbol 1}|) + v \sum_{\Delta} (|\text{flippable symbol 1}\rangle \langle \text{flippable symbol 1}| + |\text{flippable symbol 2}\rangle \langle \text{flippable symbol 2}|), \quad (1.27)$$

where summation runs over all possible rhombohedral plaquettes, including plaquettes obtained by rotation of the shape Δ . The first term resembles the kinetic energy of the dimers since its action induces *resonant* dimer moves on flippable plaquettes as indicated in Fig. 1.8.²⁷ The second term is the potential energy and simply counts the number of flippable plaquettes.

For a qualitative discussion of the Hamiltonian family H_{QDM} parametrized by v/t , we assume $t > 0$ and again employ a graphical analysis. Starting with limiting cases, we note that for $v/t \rightarrow -\infty$, it is energetically favorable to maximize the number of flippable plaquettes. As illustrated in Fig. 1.9(a), this is achieved for a columnar configuration of dimers. Notably, such states break translational and rotational symmetries of H_{QDM} and, therefore, indicate *crystallization* of dimers. Perturbation theory verifies, that this phenomenon persists for large but finite $-v/t$ and gives rise to an ordered phase [150]. This phase is termed *columnar phase* and constitutes an instance of an *RVB crystal*.²⁸ We encounter a similar situation for the opposite limit $v/t \rightarrow \infty$. In this case, it is preferred to minimize the number of flippable plaquettes. As depicted in Fig. 1.9(b), flippable plaquettes are entirely avoided when dimers are placed in a staggered pattern. Notably, these staggered states are annihilated by both the kinetic and potential term in Eq. (1.27). Thus, they provide zero-energy ground states as long as the Hamiltonian is positive semi-definite. Since this is the case for $v/t \geq 1$ [148], we can identify another extended crystalline phase. This phase is termed *staggered phase* and, on the triangular lattice for $v/t > 1$, is characterized by a unique ground state up to global symmetry transformations.

²⁷The names of the resonating valence bond phases stem from the analogy to the resonance of the two possible dimer configurations of three valence electrons on the six sites of a benzene ring [147].

²⁸We note that despite being ordered, the columnar phase is nontrivial on the triangular lattice as the number of columnar configurations, i.e., states with maximum number of flippable plaquettes, grows exponentially with the linear system size [150]. Monomer excitations are confined in the columnar phase [148].

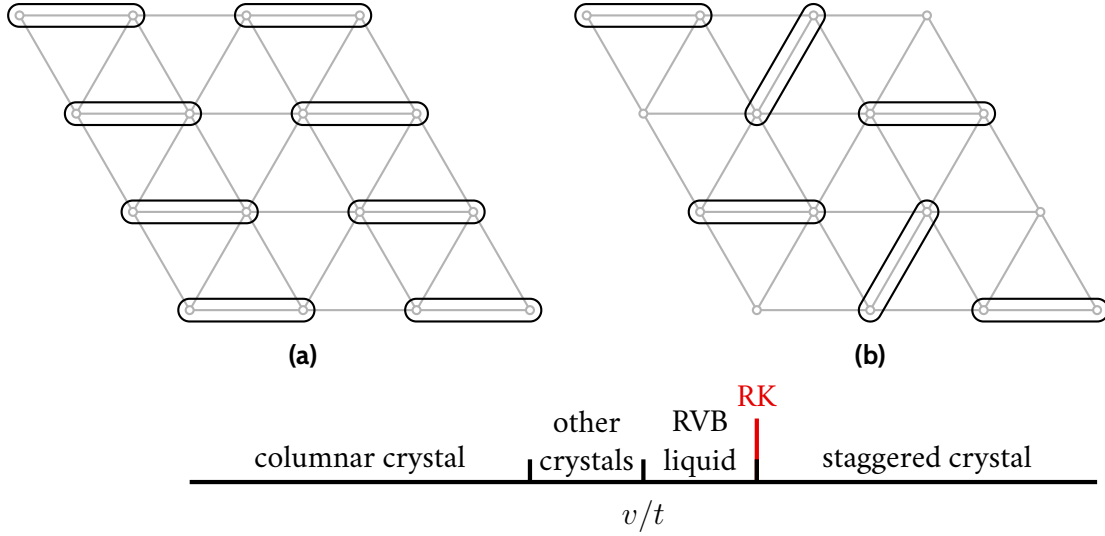


FIG. 1.9: Quantum phase diagram of the quantum dimer model on the triangular lattice parametrized by v/t . **(a)** Columnar state. **(b)** Staggered state for $v/t \geq 1$. The hardcore constraint is violated at the boundary. Adapted from Ref. [150].

Given these considerations, we might only expect a disordered phase for $v/t \lesssim 1$. To this end, it is helpful to study the case $v = t > 0$. This parameter choice is termed *Rokhsar-Kivelson (RK) point* and allows to rewrite the Hamiltonian (1.27) to a sum of projectors,

$$H_{\text{RK}} = t \sum_{\Delta} (|\text{empty}\rangle - |\text{dimer}\rangle) (|\text{empty}\rangle - |\text{dimer}\rangle). \quad (1.28)$$

The RK point is of particular interest as it yields an exact solution for the ground states [181]. Up to normalization, these states are equal-weight superpositions of the form [148]

$$|\Phi_s\rangle \propto \sum_{c_s} |c_s\rangle, \quad (1.29)$$

where summation runs over all dimer coverings c_s in the *dynamical sector* s , that is, the set of dimer coverings closed under repeated action of the kinetic term in Eq. (1.27). As the staggered states are annihilated by the kinetic term, it is evident that they are of the above form and constitute ground states of H_{RK} .²⁹ There exist, however, also nontrivial solutions with an arbitrary number of flippable plaquettes. To show this, let us consider a general superposition

$$|\Psi\rangle = \sum_c A_c |c\rangle, \quad (1.30)$$

where A_c are complex coefficients and the summation runs over all possible dimer coverings c . From the specific shape of H_{RK} in Eq. (1.28), we can infer that $|\Psi\rangle$ is annihilated by H_{RK} , if and only if the coefficient A_c of any dimer covering c with at least one flippable plaquette is equal to the coefficients $A_{c'}$ of all dimer coverings c' that are obtained from c by a resonant dimer move, i.e., a transformation of the form $\text{empty} \longleftrightarrow \text{dimer}$. Notably, this set of coverings constitutes a dynamical sector, and we then arrive at solutions of the form (1.29) [148]. Obviously, any superposition of our degenerate ground state solutions is also a ground state. In particular, this

²⁹Since H_{RK} is a sum of projectors, i.e., terms with eigenvalues 0 and 1, it is clear that the ground state energy must vanish identically.

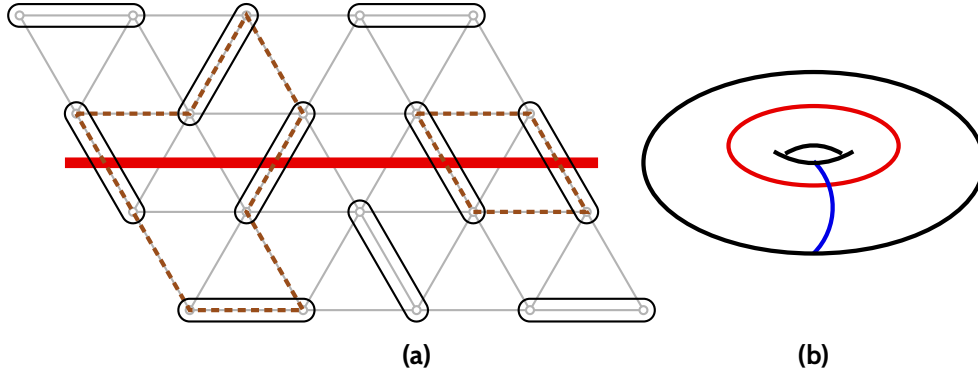


FIG. 1.10: Topological order of the RVB liquid. **(a)** The winding number is the number of dimers crossing a non-contractible reference line (red). Its parity is invariant under dimer flips along loops (brown) with alternating covered and uncovered bonds. **(b)** Two non-contractible lines (blue and red) winding around a torus permit the definition of two non-equivalent winding numbers.

is the case for $\sum_s |\Phi_s\rangle$, that is, the equal-weight superposition of all possible dimer coverings. From this result, we infer that with the exception of staggered states, the ground states of the RK point are disordered. In the case of such states, the dimers do not crystallize but, instead, form the RVB liquid as initially proposed by Anderson [58, 5].

Numerical results away from the exactly solvable RK point $v/t = 1$ indicate that a gapped RVB liquid on the triangular lattice is stabilized in an extended phase for $0.8 < v/t < 1$ [177]. This phase is characterized by exponentially decaying dimer correlations and, as we demonstrate below, \mathbb{Z}_2 topological order [150]. Our qualitative discussion of the phases of the quantum dimer model (1.27) is summarized in Fig. 1.9. Notably, between the columnar phases and the RVB liquid, more intricate crystalline phases are expected, which, however, are challenging numerical methods due to remarkably large unit cells [151, 148].³⁰ We also emphasize that the phase diagram of quantum dimer models crucially depends on the lattice geometry. In particular, it is currently believed that the RK point for any 2D bipartite lattice is not part of an extended liquid phase but constitutes a critical point between two crystalline phases [147]. Some of the exotic properties of the RK point, which we discuss in the following for the triangular lattice, however, persist for bipartite geometries, such as the square and honeycomb lattice [181, 148].

Topological order in the resonating valence bond liquid

Given our first explicit encounter of a QSL, let us demonstrate the hallmark features of its topological order based on the general discussion in Section 1.1, starting with its *topological ground-state degeneracy*. To visualize this concept at the RK point (1.28), let us assume a system with periodic boundary conditions in both spatial directions, that is, a system on a torus. As exemplified in Fig. 1.10, we then consider a non-contractible reference line winding around the torus with an arbitrary hardcore dimer covering, and count the dimers crossing this line to define the *winding number* \mathcal{W}_1 . The key step is to notice that no local resonant dimer move can change the parity of this winding number \mathcal{W}_1 . Since the equal-weight superposition (1.29) of the dimer coverings obtained from such moves is a ground state at the RK point (1.28), it follows that the parity of \mathcal{W}_1 is a quantum number or, put differently, a topological invariant of the ground state. Repeating this argument for a reference line along the other toroidal direction

³⁰We note that an exact solution of such a crystalline state exists for $v = 0$ [151]. The corresponding unit cell involves 12 sites.

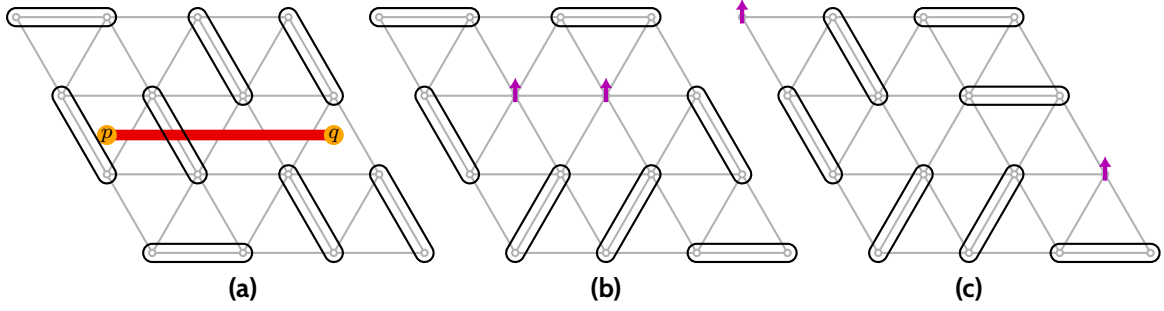


FIG. 1.11: Elemental excitations of the RVB liquid at the RK point (1.28). **(a)** Two \mathbb{Z}_2 vortices in triangular plaquettes p and q (orange) separated by a reference line (red). **(b)** Two monomers violating the hardcore constraint. **(c)** Dimer flips separate the two monomers without energy cost. Adapted from Ref. [148].

yields a second winding number \mathcal{W}_2 and permits the full characterization of a multiplet of four degenerate ground states in terms of the parities of \mathcal{W}_1 and \mathcal{W}_2 .³¹ More generally speaking, for a system geometry with genus g we can define $2g$ non-equivalent winding numbers and expect a degenerate multiplet of size 4^g [148]. This is the topological ground-state degeneracy of the RVB liquid [150]. It is fundamentally different to the degeneracy of ordered ground states, as it depends on the geometry of the system and, more importantly, cannot be characterized by any local order parameter. Instead of the latter, we have to perform a nonlocal operation to compute the topological invariants associated with the non-contractible lines to identify the ground state. This reflects the fact that the winding-number parities remain unaffected not only by resonant dimer moves described by the kinetic term in Eq. (1.27) but any local operation. To see this, we note that under the hardcore dimer constraint, such operations are associated with dimer flips along a closed loop with alternating covered and uncovered bonds [148] called *Wilson loop*, see Fig. 1.10. Any local Wilson loop intersects a reference line an even number of times and thus cannot change the parity. We might think of this result as an instance of *topological protection*.

The second hallmark feature of topological order is *fractionalization* of the microscopic degrees of freedom. This phenomenon typically manifests in elemental excitations with unconventional properties and, in particular, anyonic exchange statistics. The first excitations of the RK point (1.28) that we discuss are called \mathbb{Z}_2 *vortices* (or sometimes *visons*). They live on the dual lattice, namely, a honeycomb lattice connecting neighboring triangular plaquettes, and are captured by the variational wavefunction (in a given sector s) [147]

$$|p, q\rangle \propto \sum_{c_s} (-1)^{n_{c_s}(p,q)} |c_s\rangle, \quad (1.31)$$

where p and q label triangular plaquettes hosting \mathbb{Z}_2 vortices and $n_c(p, q)$ is the number of dimers crossing a reference line connecting p and q for the dimer covering c , as exemplified in Fig. 1.11(a). \mathbb{Z}_2 vortices are subject of my Publications P2 and P3, and their phenomenology is detailed in Chapter 2. For now, we are interested in their fractional character and this becomes evident when we study the interplay with a second type of excitations of the RK point (1.28).³²

To define these excitations, we have to revert to the initial spin system, which realizes the

³¹This statement is only exact in the thermodynamic limit, see Footnote 7. Moreover, we note that the winding numbers define *topological sectors*, which each might include multiple dynamical sectors [148].

³²We note, however, that numerical results indicate that vortex-like excitations are the lowest-energy excitations of the gapped RVB liquid away from the critical RK point (1.28) [91].

considered dimer coverings by forming nearest-neighbor singlet bonds.³³ An elemental excitation is then provided by exciting an $SU(2)$ singlet to a triplet state. Similarly to the classical spin liquid discussed above and as illustrated in Fig. 1.11(b), we can understand this excitation as two local monomer defects that violate the hardcore dimer constraint. As both monomers carry a spin of $1/2$ and zero charge, they are called *spinons*. Most remarkably, at the RK point (1.28), spinons can be separated to large distances without energy cost by moving dimers appropriately [148, 147], and are, therefore, said to be *deconfined* [216]. Before employing this result to study the relative statistics of spinons and \mathbb{Z}_2 vortices, we note that a second type of monomer excitation can be obtained by extracting an electron from the system, thereby leaving an unpaired spin and a hole behind [150, 147]. At the RK point (1.28) but also within the RVB liquid phase, these monomers can again be separated without energy cost and behave like independent particles, namely, a spinon and a so-called *holon* [148]. As the holon carries electric charge and no spin, this procedure manifests *spin-charge separation* - a typical phenomenon in QSLs reflecting fractionalization [187].

Let us now study the relative statistics of the two elemental excitations, i.e., \mathbb{Z}_2 vortices and monomers. To this end, we consider an isolated \mathbb{Z}_2 vortex connected to a distant partner by a reference line, see Fig. 1.12(a), and envision the following protocol assuming fine-tuning to the RK point (1.28). First, we replace a nearby dimer by two monomers as described above. Then, we move one monomer around the \mathbb{Z}_2 vortex along a closed trajectory at no energy cost to, finally, re-merge the two monomers and form a dimer. As indicated in Fig. 1.12(b), this process corresponds to flipping the dimers along a Wilson loop, which intersects the reference line an odd number of times, and therefore changes the sign of the wavefunction (1.31) [148]. Notably, this change of phase is equivalent to the Aharonov-Bohm phase for a π flux through the triangular plaquette that hosts the \mathbb{Z}_2 vortex. While this result hints at anyonic exchange statistics, a more elaborate discussion requires the consideration of the energies associated with alternative processes. In particular, it might be energetically favorable to bind a monomer to a \mathbb{Z}_2 vortex in terms of *flux attachment* and thereby change the relative statistics of monomers [147]. Namely, the above considerations imply that the particle composed of a monomer and \mathbb{Z}_2 vortex is a fermion while free monomers are bosons with respect to themselves [115].³⁴ Flux attachment plays an important role in my Publication P3 as it permits the detection of \mathbb{Z}_2 vortices by observing the attached excitations. We note that more exotic and even non-Abelian exchange statistics are enabled by modifications of the Hamiltonian or the lattice [143, 148].

Realization in spin systems

So far, we assumed dimerized spin systems to define a Hamiltonian on the manifold of hardcore dimer coverings, and eventually fine tuned the energy constants at the RK point to describe the RVB liquid. Let us now briefly discuss what microscopic spin models yields an effective description in terms of the quantum dimer model (1.27). Albeit that the RVB liquid was initially proposed as a ground state for antiferromagnetic Heisenberg models [58], this endeavor is nontrivial. Besides aforementioned subtleties of the mapping from a singlet representation to a dimer covering, see Footnote 33, this is because it is difficult to ensure that the manifold of configurations formed by singlet bonds is sufficiently gapped with respect to other states

³³Notably, this procedure enlarges our Hilbert space and introduces technical issues regarding the orthogonality of different dimer coverings, which we do not touch upon in our introductory discussion [148].

³⁴The RVB liquid belongs to the same universality class as the aforementioned toric code model due to their mutual \mathbb{Z}_2 topological order [216, 112]. The exact solution of the toric code therefore facilitates the description of the anyonic exchange statistics also present in the RVB liquid [114].

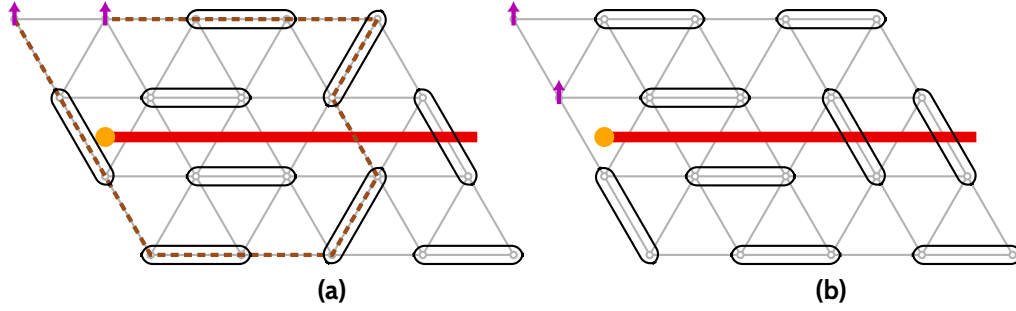


FIG. 1.12: (a) Two monomers replacing a dimer. One monomer can move along a closed loop (brown) around \mathbb{Z}_2 vortex (orange) connected to a reference line (red) (b) Dimer covering after the process has a different number of dimers crossing the reference line. Adapted from Ref. [148].

[148]. In the case of Ising models, however, it is possible to show that the kinetic term of H_{QDM} in Eq. (1.27) can be generated by various types of spin interaction terms, such as a transverse exchange, a ring exchange or the coupling to a transverse field [149, 148]. In particular, there is an exact correspondence between the strong coupling limit of the fully-frustrated transverse field Ising model on the honeycomb lattice and the kinetic term of H_{QDM} on the triangular lattice [151, 148]. The potential term of H_{QDM} , on the other hand, typically corresponds to an additional multi-spin interaction [148]. Realizing quantum dimer models from $\text{SU}(2)$ invariant models is more involved and typically employs perturbed Klein models constructed from appropriate projectors [148, 147]. The resulting models are elusive and the stabilization of the RVB liquid in real magnets remains to be observed in experiments.

In Chapter 2, we therefore choose a different path to realize QSLs with topological order in a spin system. From the view point of quantum dimer physics, this path is paved by a relaxation of the hardcore dimer constraint. Instead of imposing the number of dimers which have to include a given site, we can merely impose the parity of this number [148]. We thereby arrive at a \mathbb{Z}_2 gauge field which associates every bond with a bond variable $u_{ij} = \pm 1$. Notably, for these relaxed constraints, any plaquette is flippable, and we might, therefore, expect much richer physics from local exchange. In Chapter 2, an emergent \mathbb{Z}_2 gauge field is crucial for the description of the Kitaev model on the honeycomb lattice [112]. There, specific violations of the local constraints in terms of open gauge strings again turn out to be quasiparticle excitations, namely, \mathbb{Z}_2 vortices. More generally speaking, we note that emergent gauge fields are characteristic of QSLs and allow a rough classification [187]. Besides gapped \mathbb{Z}_2 QSLs, an important family is given by gapless QSLs with emergent $\text{U}(1)$ gauge fields which are reminiscent of electrodynamics. In the following, however, we stick to \mathbb{Z}_2 gauge fields and focus on a gapped non-Abelian phase of the Kitaev model. Like the RVB liquid, this phase gives rise to nontrivial topological order.

Chapter 2

Realization of the Kitaev spin liquid

My Publications **P2** and **P3** study a specific type of quantum spin liquid and its solid-state realization. This chapter provides a broad overview of the relevant research fields. To this end, Section 2.1 starts with a schematic discussion of the quantum spin liquid phase described by the Kitaev honeycomb model. The microscopic Jackeli-Khaliullin mechanism which realizes the characteristic spin exchange of this model in candidate materials is outlined by Section 2.2. Subsequently, Section 2.3 summarizes experimental results for the candidate material α - RuCl_3 and concludes with a discussion of the polarized phase of this compound to set the stage for my Publication **P4**. Finally, Section 2.4 motivates the experimental set-up studied in my Publications **P2** and **P3**. We note that this chapter employs many concepts introduced in Chapter 1 and, oftentimes, does so without explicit reference.

2.1 Kitaev honeycomb model

In Chapter 1, we encountered the *Kitaev (honeycomb) model* (1.25) for classical spins and identified its anisotropic spin coupling as a source of large exchange frustration that suppresses magnetic ordering at low and zero temperature, and instead gives rise to a classical spin liquid and zero-point entropy. These results motivate us to study the quantum description of the model for $S = 1/2$ as initially done in the seminal work by Kitaev [112]. A slightly more general version of the model is given by¹

$$H = -K_x \sum_{\langle jk \rangle_x} \sigma_j^x \sigma_k^x - K_y \sum_{\langle jk \rangle_y} \sigma_j^y \sigma_k^y - K_z \sum_{\langle jk \rangle_z} \sigma_j^z \sigma_k^z = - \sum_{\langle jk \rangle_\alpha} K_\alpha \sigma_j^\alpha \sigma_k^\alpha, \quad (2.1)$$

where σ_j^x , σ_j^y and σ_j^z are Pauli matrices and the summation runs over bonds $\langle jk \rangle_\alpha$. To avoid double counting, we assume that $\langle jk \rangle_\alpha$ denotes a bond of type $\alpha \in \{x, y, z\}$ connecting a site j on a specified sublattice \mathcal{A} to a nearest neighbor k on the other sublattice \mathcal{B} , as illustrated in Fig. 2.1(a).

The Kitaev model is integral to this thesis and the research of topologically ordered systems because it constitutes a rare instance of an interacting quantum model that is exactly solvable and describes a *quantum spin liquid* (QSL). As we detail below, the solution for the spectrum of H involves a spin representation in terms of Majorana fermion operators that reflects *spin fractionalization* in the QSL phase. However, we can already infer on the level of the spin degrees

¹The generality relative to Eq. (1.25) is given by potential anisotropy of the exchange constants K_x , K_y and K_z . Below, however, we focus on the isotropic limit $K = K_x = K_y = K_z$. Moreover, note that we changed sign convention with respect to Chapter 1 as ferromagnetic spin coupling now corresponds to $K_\alpha > 0$.

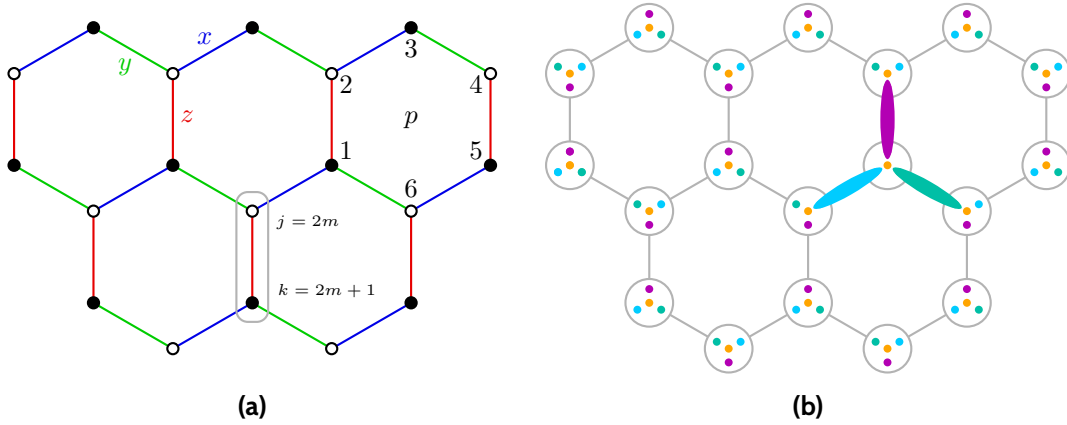


FIG. 2.1: (a) Honeycomb lattice with three different bond types x (blue), y (green) and z (red) and two sublattices \mathcal{A} (white) and \mathcal{B} (black). p labels a hexagon plaquette with adjacent sites 1-6. The gray box indicates a unit cell with two sites $j \in \mathcal{A}$ and $k \in \mathcal{B}$. (b) The spin representation in terms of four Majoranas (green, magenta, blue and orange). Three Majoranas are paired with neighboring sites while one Majorana is itinerant. Adapted from Ref. [206].

of freedom that the model has a rich structure that facilitates its theoretical description. A first indication of this is the *conservation of all Wilson loops* [112, 76]. In the present context, the Wilson loop is the product of all spin interactions corresponding to the bonds along a closed loop. We are particularly interested in the smallest possible loop winding around a single hexagonal plaquette. The corresponding Wilson loop is termed *plaquette operator* and given by

$$W_p = \sigma_1^x \sigma_2^y \sigma_3^z \sigma_4^x \sigma_5^y \sigma_6^z, \quad (2.2)$$

where the spins around a specified plaquette p are labeled according to Fig. 2.1(a). It is straightforward to show that a given plaquette operator W_p commutes with the Hamiltonian and all other plaquette operators. It follows that the Kitaev model has an extensive number of constants of motion. We can therefore partition the Hilbert space \mathcal{L} into mutual eigenspaces of all plaquette operators, and in a specific eigenspace, replace the operators W_p by their eigenvalues $w_p = \pm 1$. Below we find that a plaquette p with $w_p = -1$ hosts a \mathbb{Z}_2 vortex excitation and therefore refer to the mutual eigenspaces as *vortex sectors*.

We note that the restriction to a vortex sector is consistent with the *time-reversal symmetry* (TRS) of the system,

$$\Sigma_y H^* \Sigma_y^{-1} = H, \quad \text{where} \quad \Sigma_y = \prod_j (i\sigma_j^y), \quad (2.3)$$

since every loop on the honeycomb lattice, and in particular around a plaquette, has even length.² Despite this symmetry and the extensive number of conserved operators, solving for the spectrum in a specific vortex sector remains challenging, as the dimension of a vortex sector for a lattice of $2N$ spins is 2^N and thereby grows exponentially [118]. In fact, the conservation of all Wilson loops is a property of the model for any spin length S , while an exact solution is only known for $S = 1/2$ [17]. To find this solution, we therefore have to refine our description of specific vortex sectors further.

²We note that this is no longer the case if we define the Kitaev model on a tricoordinated but non-bipartite lattice. While the model remains (for the most part) exactly solvable on any tricoordinated lattice, the presence of loops with odd length, e.g. along a triangle, can trigger spontaneous breaking of TRS resulting in a *chiral spin liquid* [112, 236].

2.1.1 Majorana fermion representation

As discussed in Chapter 1, a characteristic feature of QSLs is the fractionalization of the spin degrees of freedom. The theoretical description of this phenomenon is typically set about by an appropriate representation of the spin in terms of operators that are associated with the creation or annihilation of fractional excitations. In many cases, however, these transformations do not diagonalize the Hamiltonian but require potentially uncontrolled approximations such as a mean-field decoupling of quartic interactions [187, 118], see my Publication P2. The representation of the spin σ_j on site j put forward by Kitaev is given by³

$$\sigma_j^x = i c_j^x c_j, \quad \sigma_j^y = i c_j^y c_j, \quad \sigma_j^z = i c_j^z c_j, \quad (2.4)$$

where c_j^α for $\alpha \in \{x, y, z\}$ and c_j are Hermitian *Majorana (fermion) operators* defined by the anticommutation relations

$$\{c_j, c_k\} = 2\delta_{jk}, \quad \{c_j^\alpha, c_k^\beta\} = 2\delta_{jk}\delta_{\alpha\beta}, \quad \{c_j, c_k^\alpha\} = 0. \quad (2.5)$$

Using Eq. (2.5), it is straightforward to show that the representation (2.4) correctly reproduces the algebra of Pauli matrices, i.e., $\{\sigma_j^\alpha, \sigma_j^\beta\} = 2\delta_{\alpha\beta}$ and $[\sigma_j^\alpha, \sigma_k^\beta] = 0$ for $j \neq k$. The representation, however, is overcomplete as it enlarges the Hilbert space. This becomes evident when we consider the operator $-i\sigma^x\sigma^y\sigma^z$. While this product simply equals the identity within our original *physical* Hilbert space \mathcal{L} , its representation in the enlarged Hilbert space $\bar{\mathcal{L}}$ is given by

$$D_j = c_j^x c_j^y c_j^z c_j \quad (2.6)$$

and, in particular, has eigenvalues $+1$ and -1 . To ensure that our states $|\Psi\rangle$ are part of the physical subspace, i.e., $|\Psi\rangle \in \mathcal{L}$, we therefore impose the local constraint

$$D_j |\Psi\rangle = |\Psi\rangle \quad (2.7)$$

for all sites j . Notably, the redundancy of the representation (2.4) is related to the invariance under the \mathbb{Z}_2 *gauge transformation*

$$c_j \rightarrow -c_j, \quad c_j^\alpha \rightarrow -c_j^\alpha \quad \forall \alpha \in \{x, y, z\}, \quad (2.8)$$

which is enforced by applying the *gauge operator* D_j .

To better understand the enlarged space $\bar{\mathcal{L}}$ and the physical relevance of Majorana operators, let us construct more familiar fermionic creation and annihilation operators. One possible way to do so is given by

$$f_j = \frac{1}{2}(c_{2j} + i c_{2j+1}), \quad f_j^\dagger = \frac{1}{2}(c_{2j} - i c_{2j+1}), \quad (2.9)$$

respectively, as it yields the correct anticommutation relations $\{f_j, f_k^\dagger\} = \delta_{jk}$ and $\{f_j, f_k\} = 0$.⁴ Based on this expression, we might think of Majoranas as the real and imaginary parts of standard *complex fermions*. The representation (2.4) of a single spin in terms of four Majoranas is therefore associated with a Fock space of two complex fermions, i.e., with a dimension of 4. As the spin degree of freedom acts on a space of dimension 2, we deduce that the physical subspace \mathcal{L} for a lattice of $2N$ spins is of size 2^{2N} , while the enlarged space $\bar{\mathcal{L}}$ is of dimension 4^{2N} and thus necessitates the local constraints (2.7).⁵

³An alternative and equivalent solution of the Kitaev model involves a Jordan-Wigner transformation [60, 44].

⁴Majorana operators are based on the work of Ettore Majorana, who proposed a real-valued modification of the Dirac equation to describe chargeless fermions which are their own antiparticle [57].

⁵We note that Eq. (2.7) is of different nature than the local constraints encountered in Chapter 1 in that violations of a constraint (2.7) do not constitute energy excitations but are merely unphysical.

Emergent \mathbb{Z}_2 gauge field

Given a well-defined representation of the spin, we can re-express the Kitaev model (2.1) in terms of Majorana operators. To this end, it is convenient to define the so-called *bond variables*

$$U_{jk} = i c_j^\alpha c_k^\alpha \quad (2.10)$$

for every bond $\langle jk \rangle_\alpha$. Inserting the representation (2.4) and this definition into Eq. (2.1) yields

$$H = i \sum_{\langle jk \rangle_\alpha} K_\alpha U_{jk} c_j c_k. \quad (2.11)$$

While this Hamiltonian is generally quartic in terms of Majorana operators, it is exactly solvable. This stems from the beautiful fact that every bond variable U_{jk} commutes with the Hamiltonian and all other bond variables. Similarly to above, we can therefore restrict our considerations to a mutual eigenspace, and replace all bond variables U_{jk} by their eigenvalues $u_{jk} = \pm 1$ to thereby arrive at a quadratic solvable Hamiltonian. Based on our discussion of QSLs in Chapter 1, we might link these formal arguments to physical meaning and say that the bond variables U_{jk} manifest an *emergent static \mathbb{Z}_2 gauge field*.⁶ In a given mutual eigenspace, that is, for a given *gauge configuration* $\{u_{jk} = \pm 1\}$, the Kitaev model thus describes Majorana fermions hopping in front of a static gauge background. As illustrated in Fig. 2.1(b), this constitutes the fractionalization of the microscopic spin degree of freedom σ_j in terms of emergent gauge and *matter* degrees of freedom, U_{jk} and c_j , respectively. Let us discuss what fractional excitations are described by these two emergent degrees of freedom, starting with the former.

To this end, let us first clarify how the gauge configurations relate to the aforementioned vortex sectors. The Majorana representation of the plaquette operators (2.2) is given by

$$W_p = U_{21} U_{23} U_{43} U_{45} U_{65} U_{61}, \quad (2.12)$$

where the sites are labeled according to Fig. 2.1(a). The plaquette operators resemble the flux of the \mathbb{Z}_2 gauge field. A plaquette is penetrated by a finite flux in a given gauge configuration if it is adjacent to an odd number of negative bond variables. It is evident that this is realized by multiple gauge configurations, and that, in particular, plaquette operators are invariant under gauge transformations (2.8). To understand this formally, let us assume the knowledge of an eigenstate $\bar{\Psi}_{\{u_{jk}\}} \in \bar{\mathcal{L}}$ of the Hamiltonian (2.11) for a given gauge configuration $\{u_{jk}\}$. We then obtain a physical state $\Psi_{\{w_p\}} \in \mathcal{L}$ in a vortex sector $\{w_p\}$ in terms of the projection $\Psi_{\{w_p\}} = \mathcal{P} \bar{\Psi}_{\{u_{jk}\}}$, where the projector

$$\mathcal{P} = \prod_j \left(\frac{1 + D_j}{2} \right) \quad (2.13)$$

eliminates all states which violate a local constraint (2.7). It is convenient to write $\mathcal{P} = \mathcal{S} \mathcal{P}_0$, where

$$\mathcal{P}_0 = \frac{1}{2} \left(1 + \prod_j D_j \right) \quad (2.14)$$

is a projector that eliminates all unphysical states for a specified gauge configuration as discussed below [168, 257]. The explicit expression for the operator \mathcal{S} can be found in Ref. [168].

⁶This is consistent with the fact that the bond variables u_{jk} are not invariant under (2.8) but transform according to $u_{jk} \rightarrow -u_{jk}$ (or $u_{kj} \rightarrow -u_{kj}$). We do not refer to the bond variables as conserved quantities as they are not observable in the physical subspace of the spin model.

Here, we just note that the action of \mathcal{S} symmetrizes over all gauge configurations, which are related to each other by a sequence of local gauge transformations of the form (2.8). A physical state in a vortex sector is therefore given by an equal-weight superposition of states for *equivalent* gauge configurations.⁷ Notably, this is somewhat reminiscent of the resonating valence bond (RVB) liquid state discussed in Chapter 1. Moreover, similarly to the RVB liquid, the ground state of the Kitaev model is in the flux-free vortex sector [130, 112], while plaquettes p with $W_p = -1$ host static gapped \mathbb{Z}_2 vortex excitations.⁸

Fermionic matter excitations

The other species of fractional excitations are *matter fermions* which exist in every vortex sector. To describe these fermions, we have to diagonalize the Hamiltonian (2.11) for a given gauge configuration $\{u_{jk}\}$. In the following, we sketch this calculation and refer to my Publication P3 for technical details. To this end, let us label the sites of the m th unit cell by $j = 2m \in \mathcal{A}$ and $j = 2m+1 \in \mathcal{B}$ according to Fig. 2.1(a). Based on Eq. (2.9), we then may introduce one complex fermion per unit cell using (for $m \in \mathbb{Z}$)

$$c_{2m} = f_m + f_m^\dagger, \quad c_{2m+1} = \frac{1}{i} (f_m - f_m^\dagger). \quad (2.15)$$

Inserting into the Hamiltonian (2.11) for a specified gauge configuration yields an expression of the form

$$H_{\{u_{jk}\}} = \sum_{m,n} t_{mn} (f_m^\dagger f_n - f_m^\dagger f_n^\dagger + \text{H.c.}), \quad (2.16)$$

where the hopping elements t_{mn} have an implicit gauge dependency and are given by

$$t_{mn} = K_\alpha u_{2m, 2n+1}, \quad (2.17)$$

if $j = 2m$ and $k = 2n+1$ are nearest neighbors connected by a bond $\langle jk \rangle_\alpha$ and zero otherwise. The Hamiltonian $H_{\{u_{jk}\}}$ describes free fermions without conserved particle number. Such models are familiar in condensed matter physics and treated within the *Bogoliubov-de Gennes formalism*. On a finite lattice of N unit cells, this formalism involves a Bogoliubov transformation to a set of N fermionic quasiparticle operators a_λ and a_λ^\dagger given by [27]

$$\begin{pmatrix} f \\ f^\dagger \end{pmatrix} = V \begin{pmatrix} a \\ a^\dagger \end{pmatrix}, \quad \text{where} \quad f = \begin{pmatrix} f_1 \\ \vdots \\ f_N \end{pmatrix}, \quad a = \begin{pmatrix} a_1 \\ \vdots \\ a_N \end{pmatrix} \quad (2.18)$$

and V is a unitary $2N \times 2N$ matrix. An appropriate choice of V then diagonalizes the free fermion problem (2.16) and yields

$$H_{\{u_{jk}\}} = \sum_{\lambda=1}^N \varepsilon_\lambda \left(a_\lambda^\dagger a_\lambda - \frac{1}{2} \right), \quad (2.19)$$

⁷The Kitaev model hosts topologically ordered phases. Depending on the geometry of the system, a vortex sector might therefore include multiple topological sectors [112], see Chapter 1.

⁸Notably, the fact that \mathbb{Z}_2 vortices are static is a property of the exactly solvable point but not of an extended Kitaev spin liquid. Below we introduce realistic perturbations to the Kitaev model and thereby render \mathbb{Z}_2 vortices dispersive.

where $\varepsilon_\lambda \geq 0$ are the single-particle energies of the fermionic excitations. Notably, within the physical subspace, fermionic many-body states have to satisfy a parity constraint. This is because one can show for periodic boundary conditions that the projector (2.14) is given by

$$\mathcal{P}_0 = \frac{1}{2} \left[1 + (-1)^\theta (-1)^{N_a} \det(V) \prod_{\langle jk \rangle_\alpha} u_{jk} \right], \quad (2.20)$$

where θ is an integer that depends on the linear size of the system and $N_a = \sum_\lambda a_\lambda^\dagger a_\lambda$ is the total number of fermionic excitations [168, 257]. The projector therefore annihilates all many-body states with a specific parity determined by the gauge configuration and geometric details. In particular, it is possible that the overall ground state on a torus includes a single fermionic excitation. As we discuss in my Publication **P3**, the parity constraint also introduces technical subtleties to the calculation of the dynamical spin correlations.

It is another remarkable property of the Kitaev model that spin correlations are *ultra local* and can be computed exactly [16, 119]. As a preparation for my Publication **P3**, let us briefly sketch the calculation of the static spin correlations $\langle \sigma_j^\alpha \sigma_k^\beta \rangle$ at zero temperature. To this end, we assume without loss of generality that site k is on sublattice \mathcal{B} and let $l \in \mathcal{A}$ be the site that is connected to k by the bond $\langle lk \rangle_\beta$. The physical ground state $|\Phi_0\rangle \in \mathcal{L}$ is associated with a state $|\Phi_g\rangle \in \bar{\mathcal{L}}$ for a flux-free gauge configuration $g = \{u_{mn}\}$ and with physical fermionic parity. Since $|\Phi_g\rangle$ lives in a mutual eigenspace of the bond variables and since $u_{lk}^2 = 1$, we can write

$$\langle \Phi_0 | \sigma_j^\alpha \sigma_k^\beta | \Phi_0 \rangle = u_{lk} \langle \Phi_g | \sigma_j^\alpha \sigma_k^\beta U_{lk} | \Phi_g \rangle. \quad (2.21)$$

Inserting the Majorana representation (2.4) and Eq. (2.10) shows that $\sigma_j^\alpha \sigma_k^\beta$ and U_{lk} commute if $j = l$ and $\alpha = \beta$ but anticommute otherwise. As U_{lk} is Hermitian, it follows that the above correlation function is only nonzero if j and k are nearest neighbors and $\alpha = \beta$ corresponds to the bond type connecting these two sites. These ultra local spin correlations reflect that the state at zero temperature is disordered and, therefore, a QSL [16]. To compute the numerical value of the correlation function for two nearest neighbors $j = 2m \in \mathcal{A}$ and $k = 2n + 1 \in \mathcal{B}$, we revert to complex fermions and write

$$\langle \Phi_0 | \sigma_j^\alpha \sigma_k^\alpha | \Phi_0 \rangle = -u_{jk} \langle \Phi_g | c_j c_k | \Phi_g \rangle = i u_{2m, 2n+1} \langle \Phi_g | f_m^\dagger f_n - f_m^\dagger f_n^\dagger + \text{H.c.} | \Phi_g \rangle \quad (2.22)$$

We reduced the problem to the computation of quadratic correlation functions of free fermions. This is straightforward in terms of the Bogoliubov transformation (2.18) since the fermionic vacuum for a given gauge configuration is annihilated by the quasiparticle operators a_λ appearing in the diagonalized Hamiltonian (2.19) [27]. We again refer to my Publication **P3** for technical details and results.

For now, we conclude that with the outlined analytical method, it is possible to compute the full energy spectrum and all two-point correlation functions of the Kitaev model. More generally speaking, the introduced analytical machinery applies to any Hamiltonian defined on any tricoordinated graph, which commutes with all bond variables in the enlarged Hilbert space of the Majorana representation (2.4). This allows the exact study of disorder [257, 103, 220, 221], different lattice geometries [236, 138, 163, 81, 206], external magnetic fields [112] and more exotic phenomena [176, 125]. For a refined discussion of the physical properties of the original unperturbed Kitaev model (2.1), let us now turn to the low-energy regime.

2.1.2 Flux-free ground state and Majorana zero modes

A fundamental theorem by Lieb for itinerant fermions on bipartite lattices [130] implies that the ground state of the Kitaev model is in the flux-free vortex sector [112]. It is convenient to describe the flux-free sector in terms of the homogeneous gauge configuration with $u_{jk} = 1$ for all bonds $\langle jk \rangle_\alpha$, since this endows the fermionic Hamiltonian $H_{\{u_{jk}\}}$ in Eq. (2.16) with translational invariance. The theoretical description is then facilitated by a Fourier transformation of the complex fermions (assuming periodic boundary conditions)

$$f_m = \frac{1}{\sqrt{N}} \sum_{\mathbf{k} \in \text{BZ}} e^{i\mathbf{k} \cdot \mathbf{r}_m} f_{\mathbf{k}}, \quad f_m^\dagger = \frac{1}{\sqrt{N}} \sum_{\mathbf{k} \in \text{BZ}} e^{-i\mathbf{k} \cdot \mathbf{r}_m} f_{\mathbf{k}}^\dagger, \quad (2.23)$$

where summation runs over the whole Brillouin zone (BZ) and \mathbf{r}_m is the location of the m th unit cell on the lattice spanned by the lattice vectors (assuming unit lattice constant)

$$\hat{\mathbf{e}}_1 = \frac{1}{2} (1, \sqrt{3})^T, \quad \hat{\mathbf{e}}_2 = \frac{1}{2} (-1, \sqrt{3})^T. \quad (2.24)$$

The standard representation of the Hamiltonian $H_0 = H_{\{u_{jk}=1\}}$ within the Bogoliubov-de-Gennes formalism is then given by [118, 147]

$$H_0 = \sum_{\mathbf{k} \in \frac{1}{2}\text{BZ}} (f_{\mathbf{k}}^\dagger, f_{-\mathbf{k}}) \begin{pmatrix} \xi_{\mathbf{k}} & i\Delta_{\mathbf{k}} \\ -i\Delta_{\mathbf{k}} & -\xi_{\mathbf{k}} \end{pmatrix} \begin{pmatrix} f_{\mathbf{k}} \\ f_{-\mathbf{k}}^\dagger \end{pmatrix}, \quad (2.25)$$

where summation runs over half of the BZ and $\xi_{\mathbf{k}} = \text{Re}(J(\mathbf{k}))$ and $\Delta_{\mathbf{k}} = \text{Im}(J(\mathbf{k}))$ are real and imaginary parts of the function

$$J(\mathbf{k}) = K_x e^{i\mathbf{k} \cdot \hat{\mathbf{e}}_1} + K_y e^{i\mathbf{k} \cdot \hat{\mathbf{e}}_2} + K_z, \quad (2.26)$$

respectively. The Hamiltonian is then diagonalized by the Bogoliubov transformation

$$\begin{pmatrix} f_{\mathbf{k}} \\ f_{-\mathbf{k}}^\dagger \end{pmatrix} = \begin{pmatrix} \cos \theta_{\mathbf{k}} & i \sin \theta_{\mathbf{k}} \\ i \sin \theta_{\mathbf{k}} & \cos \theta_{\mathbf{k}} \end{pmatrix} \begin{pmatrix} a_{\mathbf{k}} \\ a_{-\mathbf{k}}^\dagger \end{pmatrix}, \quad (2.27)$$

where $\tan(2\theta_{\mathbf{k}}) = -\Delta_{\mathbf{k}}/\xi_{\mathbf{k}}$. We arrive at

$$H_0 = \sum_{\mathbf{k} \in \text{BZ}} \varepsilon(\mathbf{k}) \left(a_{\mathbf{k}}^\dagger a_{\mathbf{k}} - \frac{1}{2} \right), \quad (2.28)$$

where $\varepsilon(\mathbf{k}) = |J(\mathbf{k})|$ is the single-particle dispersion.

Phase diagram of Kitaev model

For a discussion of the ground state properties, we are particularly interested in whether the spectrum is gapped or gapless.⁹ As one can show, the equation $J(\mathbf{k}) = 0$ has a solution $\mathbf{k} \in \text{BZ}$ if and only if the energy constants K_α satisfy the three triangle inequalities

$$|K_x| \leq |K_y| + |K_z|, \quad |K_y| \leq |K_z| + |K_x|, \quad |K_z| \leq |K_x| + |K_y|. \quad (2.29)$$

⁹ \mathbb{Z}_2 vortices are always gapped excitations in the ideal homogeneous Kitaev model. This can change in the presence of disorder [103, 220] or lattice distortion, see my Publication P2.

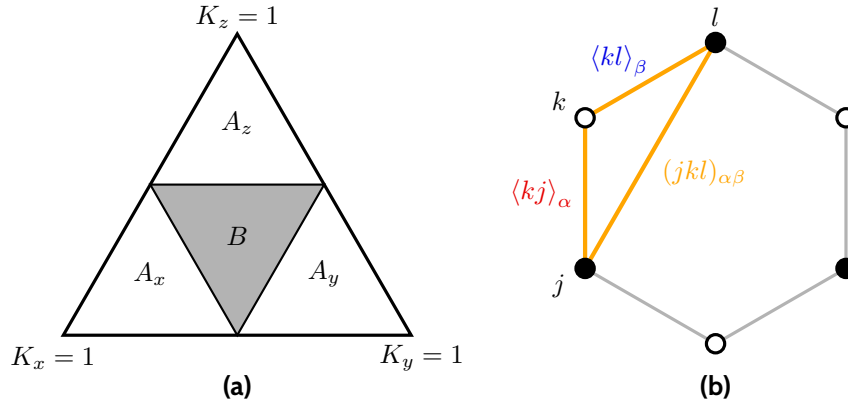


FIG. 2.2: (a) Quantum phase diagram of the Kitaev model (2.1) in the plane defined by $K_x + K_y + K_z = 1$ with $K_x, K_y, K_z > 0$. A_x , A_y and A_z label gapped Abelian phases. B is a gapless phase but gives rise to a gapped non-Abelian phase in an external magnetic field. Adapted from Ref. [112]. (b) The triangle $(jkl)_{\alpha\beta}$ (orange) for $k \in \mathcal{A}$ involved in the summation in Eq. (2.31).

The ground state of the Kitaev model is a gapless QSL if the three exchange strengths are comparable and a gapped QSL for strong exchange anisotropy. Notably, the triangle inequalities are independent of the sign of the couplings K_α .¹⁰ Focusing on ferromagnetic exchange, i.e., $K_\alpha \geq 0$, in what follows, we then arrive at the triangular quantum phase diagram in Fig. 2.2(a) with one gapless phase and three gapped phases.

Let us briefly discuss the latter. These three phases are algebraically distinct but related to each other by rotations [112]. It is therefore sufficient to focus on a single phase and assume, say, $K_z > K_x + K_y$. The qualitative description of these phases is particularly simple in the anisotropic limit $K_z \gg K_x = K_y$, where the spins tend to form dimers along the z bonds. In this limit, the energy cost associated with the creation of two \mathbb{Z}_2 vortices is smaller than the fermionic gap [118]. Moreover, a fourth-order perturbation theory in K_x/K_z allows to map the Hamiltonian to the toric code model [112, 114], see Chapter 1. We infer that the gapped phases belong to the same universality class as the toric code model and the RVB liquid and, in particular, host \mathbb{Z}_2 topological order with Abelian anyons. Since we discussed the phenomenology of the RVB liquid and its anyonic excitations in Chapter 1, we may move on to the gapless phase in what follows. Moreover, the gapless phase includes the isotropic point $K_x = K_y = K_z$ which is most relevant for material realizations, see below.

In the gapless phase, the fermionic single-particle energy $\varepsilon(\mathbf{k})$ vanishes at two points \mathbf{k}_0 and $-\mathbf{k}_0$ in the Brillouin zone and gives rise to a conic dispersion in their vicinity. As a consequence, the concept of topological order does not apply and particle exchange does not have well-defined statistics but generally depends on the details of the exchange [112]. Notably, these gapless points are protected against small perturbations which keep time-reversal symmetry (2.3) of the Hamiltonian intact. Thus, to open the gap and induce a topologically ordered state, we might break TRS using a perturbation. The physically natural choice for such perturbation is a Zeeman coupling to an external magnetic field \mathbf{h} ,

$$H_{\text{ZM}} = \sum_j \mathbf{h} \cdot \boldsymbol{\sigma}_j. \quad (2.30)$$

This term, however, does not commute with the bond variables U_{jk} and, therefore, spoils the exact solution of the Kitaev model. As a result, for finite $|\mathbf{h}|$ within the QSL phase, \mathbb{Z}_2 vortices

¹⁰In the presence of perturbations, the sign of the spin exchange has drastic physical implications [95, 206].

gain a finite dispersion [98]. For analytical results, let us thus consider a perturbation which breaks TRS but keeps the resulting Hamiltonian solvable. The most simple choice is of the form

$$H_\kappa = \kappa \sum_{(jkl)_{\alpha\beta}} \sigma_j^\alpha \sigma_k^\gamma \sigma_l^\beta, \quad (2.31)$$

where (α, β, γ) is a cyclic permutation of (x, y, z) and $(jkl)_{\alpha\beta}$ denotes the triangle with vertices at k and its two nearest neighbors j and l connected to k by bonds of type α and β , respectively, see Fig. 2.2(b). Within the physical subspace, the Majorana representation of this term is given by (taking our convention for the bonds into account)

$$H_\kappa = -i\kappa \sum_{\langle jk \rangle_\alpha \langle lk \rangle_\beta} U_{jk} U_{lk} c_j c_l - i\kappa \sum_{\langle kj \rangle_\alpha \langle kl \rangle_\beta} U_{kj} U_{kl} c_j c_l, \quad (2.32)$$

where U_{jk} are the gauge variables (2.10). Notably, this term can be derived from the Zeeman coupling (2.30) for $\kappa \propto h_x h_y h_z / K$ using a rough third-order perturbation theory assuming a small magnetic field [112].¹¹ In my Publication P2, we numerically confirm this result using a mean-field decoupling consistent with previous results in the literature [95].

In any case, it is straightforward to check that H_κ commutes with all bond variables and that we can obtain the full spectrum of the perturbed Hamiltonian using the analytical methods described above. In the case of the flux-free sector, a modification of the above arguments shows that, as anticipated, a finite κ induces a finite energy gap $\varepsilon(\mathbf{k}_0) \propto \kappa$ of the fermionic spectrum. The resulting gapped QSL phase hosts non-Abelian excitations which are subject of my Publications P2 and P3. Moreover, it belongs to the same universality class as other non-Abelian states of matter such as the fractional quantum Hall state at filling factor $\nu = 5/2$ [153] or specific topological superconductors [113, 66], which were intensively studied due to possible applications in quantum computation [92, 158].

Non-Abelian phase in an external magnetic field

Based on our discussion of topologically nontrivial systems without TRS in Chapter 1, one might first characterize this phase in terms of the *Chern number* $\nu \in \mathbb{Z}$. To this end, one can adapt Eq. (1.2) and show that the Chern number is given by [112]

$$\nu = \text{sign}(\kappa) = \text{sign}(h_x h_y h_z), \quad (2.33)$$

where we inserted the result for a perturbative magnetic field in the second equality for later reference. This result indicates that the state does not belong to the universality class of the gapped phases in Fig. 2.2(a). Moreover, on a qualitative level, we can expect universal quantized transport signatures that are associated with edge states at the system's boundary. To confirm this expectation, let us first discuss the bulk excitations.

It is a remarkable property of the phase that \mathbb{Z}_2 vortices obstruct the binding of Majorana modes to matter fermions and attach *Majorana zero modes* (MZMs). More precisely, a vortex sector with two isolated vortices hosts a delocalized complex fermion that is composed of two MZMs localized near the two \mathbb{Z}_2 vortices and that has zero energy with respect to the respective vortex sector. As long as the distance between \mathbb{Z}_2 vortices is large compared to an effective correlation length, the state associated with this fermion is effectively inaccessible to

¹¹Here, $K = K_x = K_y = K_z$ denotes isotropic coupling. We note that the second order of the perturbation theory results in a small anisotropy of the exchange coupling [112], see my Publication P2.

measurements and perturbations [112]. Only upon moving the \mathbb{Z}_2 vortices close to each other can the MZMs hybridize and form a fermion bound state at a finite energy within the bulk gap. MZMs are theoretically predicted in other condensed matter systems such as topological superconductors and one-dimensional states [66, 113, 57], and attracted massive attention in the last two decades due to their potential application in topological quantum computation [158]. This theoretically predicted implementation of robust quantum information processing employs the non-Abelian exchange statistics of fractional excitations, as briefly outlined below. In the context of our gapped QSL phase, the statistics of \mathbb{Z}_2 vortices are modified with respect to the time-reversal gapped phases due to the attachment of an MZM. The composite particle of an MZM and a \mathbb{Z}_2 vortex is called *Ising anyon* and its non-Abelian statistics are discussed below.

My Publications **P2** and **P3** are concerned with the detection of Ising anyons. While the observation of exchange statistics is rather elusive, boundary modes of the non-Abelian phase are predicted to give rise to a characteristic experimental signature. For a qualitative explanation of this, let us model an armchair or zigzag edge of the honeycomb lattice [4] by tuning the exchange couplings K_α of bonds that cross a virtual edge to zero. It follows that in the limit of zero exchange coupling, the energy cost associated with the insertion of two \mathbb{Z}_2 vortices by flipping the sign of the corresponding bond variables vanishes [59]. The attached MZMs of the \mathbb{Z}_2 vortices then constitute gapless edge modes in the ground state sector reflecting the aforementioned *bulk-boundary correspondence*. In particular, these gapless edge modes are chiral, i.e., free to propagate in only one direction [112] and the difference of left and right-moving modes at a horizontal edge is exactly given by the Chern number ν in Eq. (2.33) [79]. In the gapped non-Abelian QSL phase, we therefore expect a chiral mode winding around the system and carrying a net energy current. A schematic calculation for energy current J_E for a right-moving Majorana edge mode with energy $\varepsilon(k) = -\varepsilon(-k)$ and velocity $v(k) = d\varepsilon/dk$ yields [100, 112].

$$J_E = \int_0^\infty \frac{dk}{2\pi} \frac{\varepsilon(k)v(k)}{1 + e^{\varepsilon(k)/T}} = \frac{1}{2\pi} \int_0^\infty d\varepsilon \frac{\varepsilon}{1 + e^{\varepsilon/T}} = \frac{\pi}{24} T^2, \quad (2.34)$$

where T is the temperature.¹² Due to the analogy to the electric quantum Hall effect, we then infer a quantized thermal Hall conductivity (introducing \hbar and the Boltzmann constant k_B for clarity)

$$\kappa_{xy} = \frac{\partial J_E}{\partial T} = \frac{\nu}{2} \frac{\pi}{6} \frac{k_B^2}{\hbar} T. \quad (2.35)$$

Notably, this result differs from the thermal Hall conductivity generated by complex fermionic edge modes of quantum Hall states by a factor of $1/2$ [100]. This reflects the chiral central charge of the Majorana particle or, more loosely speaking, the fact that a Majorana is “half an electron” [112, 66, 57]. Based on our discussion of the quantum Hall effect in Chapter 1, we might expect this universally quantized signature to be a smoking gun signature of the non-Abelian phase. And, indeed, measurements of κ_{xy} in the material candidate α -RuCl₃ constitute arguably the most prominent claim of the *Kitaev spin liquid* [104, 239]. However, as we detail below, these experiments are controversial and considered insufficient due to a variety of complications that obscure their unambiguous interpretation. In my Publications **P2** and **P3**, we, therefore, design alternative detection schemes that locally probe the bulk excitations of the QSL, namely

¹²The difference to the calculation of the energy current of a complex fermionic edge mode is the range of the integration. Roughly speaking, this is because a mode created by the Fourier transform $c_{\mathbf{k}}$ of the Majorana operators c_j is annihilated by $c_{-\mathbf{k}}$. For details, see Ref. [112].

Ising anyons. In the long term, such techniques could enable the manipulation of anyons and, thereby, constitute an important step towards applications in quantum information processing.

2.1.3 Ising anyons for topological quantum computation

The non-Abelian statistics of its excitations make the Kitaev spin liquid phase appealing beyond the perspective of fundamental physics. This is due to the long-standing proposal of topological quantum computation by Kitaev and Freedman [65, 114]. The proposed idea is to, roughly speaking, encode quantum information in the non-local internal degrees of freedom of topologically nontrivial and degenerate states, and manipulate this information in terms of the matrix structure associated with the braiding of non-Abelian excitations [92, 158, 147]. The great advantage that is expected from such an implementation of quantum information memory and processing is the intrinsic fault-tolerance with respect to local noise and decoherence. Notably, the susceptibility to errors is currently the largest problem of existing platforms for quantum computation and the massive overhead necessary for quantum error correction makes the application of conventional quantum computers for practical problems (beyond the simulation of quantum systems) in the near future seem unlikely [158, 147]. It is thus unsurprising that the proposal of topological quantum computation sparked excitement and initiated extensive experimental research of putative non-Abelian excitations in topological superconductors [66] and fractional quantum Hall states [153]. However, by now it is clear that the realization of the necessary constituents in these solid-state systems faces immense experimental challenges and, so far, has not been successful or universally accepted [147]. At the time of writing, topological quantum computation is, therefore, a largely academic endeavor.

Despite this pessimistic account, let us briefly extend our discussion of anyonic exchange statistics in Chapter 1. As previously mentioned there, the possibility of anyons essentially stems from the fact that there are two topologically distinct ways of exchanging the positions of two particles if we restrict ourselves to two spatial dimensions. In the graphical representation 2.3 of the world lines of two particles, we thus distinguish between a clockwise and an anticlockwise rotation in terms of an overtake and undertake, respectively. Notably, to justify such an illustration we assume that the considered particles are sufficiently distanced from other particles and each other during the whole indicated evolution, and that the considered many-body states are degenerate [112, 147]. Anyonic statistics then become manifest if we compare an operation that involves two clockwise rotations of anyons with an operation that involves one clockwise and one anticlockwise rotation, as illustrated in Fig. 2.3(a). While the latter process should return the system to its original state, this is not necessarily true for the first process. Instead, in the Abelian case, the state accumulates a phase 2θ , where θ is the exchange angle in Eq. (1.3) and, roughly speaking, the one-dimensional irreducible representation of the associated element of the braid group [147]. The situation becomes more subtle, if we consider an ensemble of three particles. The other operations illustrated in Fig. 2.3(b) are the same for Abelian anyons but can differ for non-Abelian excitations as the generators of the braid group generally do not commute [158]. The irreducible representations of these operations are, therefore, higher dimensional and intended as the elemental unitary transformations of a topological quantum computer. In principle, such operations could be performed by moving around a number of Ising anyons in the non-Abelian phase of the Kitaev model as the MZMs attached to vortices would form a degenerate subspace that could encode quantum information [147].¹³ However,

¹³And indeed, the non-Abelian QSL of the Kitaev model is subject of a recent proposal for quantum computation applications [117].

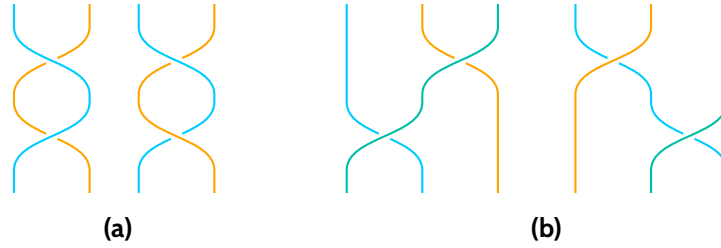


FIG. 2.3: Braiding of world lines. The vertical direction represents time while the horizontal axis represents spatial coordinates. A clockwise rotation is represented by an overtake of a world line from the left to the right. **(a)** The two operations can be inequivalent for anyons. **(b)** The two operations are equivalent for Abelian but generally inequivalent for non-Abelian anyons. Adapted from Ref. [147].

instead of further elaborating, let us move on to real materials.

2.2 Jackeli-Khaliullin mechanism

The Kitaev model was initially intended as a theoretical benchmark for the study of topologically ordered states of matter as pointed out in the previous section 2.1. Due to its seemingly artificial exchange anisotropy, one might expect that the model eludes the realization in solid-state systems. However, as first envisioned in seminal works by Jackeli and Khaliullin [107, 93], an intricate interplay of spin, orbital and electronic degrees of freedom can potentially generate the characteristic spin interaction of the Kitaev model in specific transition metal compounds [206]. These Mott insulating candidate materials are termed *Kitaev materials* and have been the subject of extensive theoretical and experimental investigation for the last 15 years. While much has been learned about Kitaev materials through this research and intriguing evidence of unconventional magnetic states has been collected, the quest for an unambiguous experimental observation of a quantum spin liquid (QSL) phase is still on-going. The design of novel probes to achieve this goal is the subject of my Publications **P2** and **P3**. Since these studies are based on the microscopic description of Kitaev materials, we may discuss the mechanism proposed by Jackeli and Khaliullin in the following.

2.2.1 Low-energy description of Mott insulators

As a first step, let us briefly review the derivation of the effective low-energy description of Mott insulating systems in terms of spin Hamiltonians. We mainly do so to fix the notation and prepare the discussion in Section 2.4 on the electric detection schemes which are employed in my Publications **P2** and **P3**. Physically, this derivation reflects the fact that in the limit of strong on-site Coulomb repulsion, the electrons are effectively decoupled from the lattice as long as the electronic filling is commensurate. Here, we study the most simple instance of a Mott insulator, namely the single-orbital half-filled Hubbard model [32, 108]

$$H_H = - \sum_{j,k,\sigma} t_{jk} \psi_{j\sigma}^\dagger \psi_{k\sigma} + U \sum_j n_{j\uparrow} n_{j\downarrow}, \quad (2.36)$$

where $U > 0$ is the on-site repulsion, $n_{j\sigma} = \psi_{j\sigma}^\dagger \psi_{j\sigma}$ is the number operator and $\psi_{j\sigma}$ is the (complex) annihilation operator of an electron with spin $\sigma \in \{\uparrow, \downarrow\}$ on site j of an arbitrary lattice. For later purposes, we allow that the real hopping integrals t_{jk} are inhomogeneous and finite for arbitrary sites j and k . In fact, the only restriction we impose is the limit of strong

repulsion $U \gg |t_{jk}|$. In this limit and at half-filling, every low-energy configuration occupies every site with exactly one electron to avoid the large energetic penalty associated with double occupancies. The effective Hamiltonian that acts on the low-energy subspace spanned by these states can be obtained from a perturbative method termed *canonical transformation* [200, 136, 48].¹⁴ Formally, the canonical transformation is an expansion of a unitary transformation based on the Campbell-Baker-Hausdorff formula

$$e^{\Omega} H_H e^{-\Omega} = H_H + [\Omega, H_H] + \frac{1}{2} [\Omega, [\Omega, H_H]] + \dots \quad (2.37)$$

The idea is to choose the anti-Hermitian generator Ω of the transformation such that all terms that change the number of double occupancies are eliminated up to a desired order in $|t_{jk}|/U$. To this end, it is convenient to rewrite the Hamiltonian to $H_H = V + T_0 + T_1 + T_{-1}$, where V is the on-site term in Eq. (2.36) and

$$\begin{aligned} T_0 &= - \sum_{j,k,\sigma} t_{jk} \left[n_{j\sigma} \psi_{j\sigma}^{\dagger} \psi_{k\sigma} n_{k\sigma} + (1 - n_{j\sigma}) \psi_{j\sigma}^{\dagger} \psi_{k\sigma} (1 - n_{k\sigma}) \right] \\ T_1 &= - \sum_{j,k,\sigma} t_{jk} n_{j\sigma} \psi_{j\sigma}^{\dagger} \psi_{k\sigma} (1 - n_{k\sigma}), \quad T_{-1} = T_1^{\dagger}. \end{aligned} \quad (2.38)$$

The action of the operator T_m for $m \in \{0, 1, -1\}$ is to change the number of double occupancies V/U exactly by m , since $[V, T_m] = mUT_m$. Through the transformation (2.37), the relevant terms $T_{\pm 1}$ are, therefore, eliminated by a generator of the form [136]

$$\Omega = \frac{1}{U} (T_1 - T_{-1}). \quad (2.39)$$

Up to the lowest order $|t_{jk}|/U$, the transformed Hamiltonian is then given by¹⁵

$$e^{-\Omega} H_H e^{\Omega} \simeq V + T_0 + \frac{1}{U} [T_1, T_{-1}]. \quad (2.40)$$

The subsequent step is a projection on the low-energy subspace using the projector

$$\mathcal{P}_{\text{low}} = \prod_j (n_{j\uparrow} - n_{j\downarrow})^2, \quad (2.41)$$

which eliminates all states with at least one double occupancy. To this end, it is convenient to introduce spin operators \mathbf{S}_j using

$$S_j^{\alpha} = \frac{1}{2} \sum_{\sigma, \sigma'} \psi_{j\sigma}^{\dagger} \sigma_{\sigma\sigma'}^{\alpha} \psi_{j\sigma'}, \quad (2.42)$$

where σ^{α} are Pauli matrices for $\alpha \in \{x, y, z\}$. For energies below the charge gap, we thereby arrive at the effective Hamiltonian

$$H_{\text{low}} = \mathcal{P}_{\text{low}} e^{-\Omega} H_H e^{\Omega} \mathcal{P}_{\text{low}} \simeq \sum_{j,k} J_{jk} \left(\mathbf{S}_j \cdot \mathbf{S}_k - \frac{1}{4} \right), \quad (2.43)$$

¹⁴Alternative perturbative methods are typically equivalent up to low orders in $|t_{jk}|/U$ [48].

¹⁵More precisely, one should expand the generator according to $\Omega = \sum_{l=1}^{\infty} \Omega_l$, where Ω_l is of order $(|t_{jk}|/U)^l$. The second-order term Ω_2 should then satisfy $[\Omega_2, V] = -[\Omega_1, T_0]$ etc.

where the spin exchange is $J_{jk} = 4t_{jk}^2/U$. As expected, we obtain an effective model that can solely be expressed in terms of localized electronic moments coupled due to virtual excursions of electrons to other sites and back. If we restrict the hopping integrals t_{jk} to nearest neighbors j and k , we arrive at an antiferromagnetic isotropic Heisenberg model reflecting the $SU(2)$ symmetry of our initial Hamiltonian (2.36). Below we may discuss how to realize the characteristic anisotropic Kitaev interaction and how to derive it using an appropriately modified canonical transformation (2.37). Moreover, for the latter discussion 2.4 of electric probes, it is important to note that we can apply the above machinery to any observable O expressed in terms of the electronic degrees of freedom to arrive at an effective operator [32, 108]

$$O_{\text{low}} \simeq \mathcal{P}_{\text{low}} e^{-\Omega} O e^{\Omega} \mathcal{P}_{\text{low}} \quad (2.44)$$

expressed solely in terms of the spin degrees of freedom.

2.2.2 Spin-orbit assisted Mott insulators

As outlined above, we are interested in Mott insulating transition metal compounds. To realize the Kitaev model (2.1) as the low-energy spin exchange of these materials, we have to ensure that, first, the effective angular moments have length $1/2$ and that, second, these moments are coupled in terms of the characteristic bond-dependent interaction of the Kitaev model.

The first of these two ingredients guides us to the study of compounds with electronic $4d^5$ or $5d^5$ configurations which are subject to an *octahedral crystal field* and strong *spin-orbit coupling* (SOC) [107, 93]. While this is the case for various iridates, osmates and rhenates [206], we focus on the prominent compound $\alpha\text{-RuCl}_3$ for concrete examples below. As illustrated in Fig. 2.4(a), this material is composed of Ru^{3+} ions positioned in octahedral cages of six Cl^- anions. The crystal field stemming from the electrostatic potential of the six ligands typically lifts the five degenerate d orbitals of the free transition metal ions. Roughly speaking, this is because the axially oriented orbitals d_{z^2} and $d_{x^2-y^2}$ have larger spatial overlap with the p orbitals of the ligands and thus exhibit stronger electrostatic repulsion than the non-axial orbitals d_{xy} , d_{xz} and d_{yz} [109]. As a result, the orbitals d_{z^2} and $d_{x^2-y^2}$ form a high-energy multiplet e_g , while the remaining d orbitals form a low-energy multiplet t_{2g} , see Fig. 2.4(b). In the compounds of interest, i.e., Kitaev materials, the crystal-field splitting is typically around a few eV and represents the largest energy scale in our following consideration. We note, however, that distortion of the ideal octahedral geometry is expected in real materials and typically lifts the degeneracy of the t_{2g} orbitals further [224]. In particular, *trigonal distortion* of the crystal field yields an additional correction to the spin exchange [206], as discussed below.

Neglecting these corrections for now, we might restrict our description to the t_{2g} manifold as the ground state of $4d^5$ or $5d^5$ configurations occupies only five of its six states. The effect of SOC is then accounted for by¹⁶

$$H_{\text{SO}} = \lambda \mathbf{L} \cdot \mathbf{S}, \quad (2.45)$$

where \mathbf{L} is the angular momentum operator acting on the t_{2g} manifold and \mathbf{S} is the spin operator. Since the t_{2g} orbitals have effective angular momentum $l_{\text{eff}} = 1$ [93], we find that sufficiently strong SOC $\lambda > 0$ splits the degenerate t_{2g} manifold into a duplet with total angular momentum $j_{\text{eff}} = 1/2$ and a quartet with $j_{\text{eff}} = 3/2$, as illustrated in Fig. 2.4(b). Notably, upon switching on SOC, the low-energy hole now resides in the $j_{\text{eff}} = 1/2$ duplet. For sufficiently

¹⁶Tetragonal splitting due to octahedral cages elongated along, say, the z axis can be included in terms of the modification $H_{\text{SOC}} = \lambda \mathbf{L} \cdot \mathbf{S} + \Delta_z \mathbf{L}_z^2$ with $\Delta_z > 0$ [93].

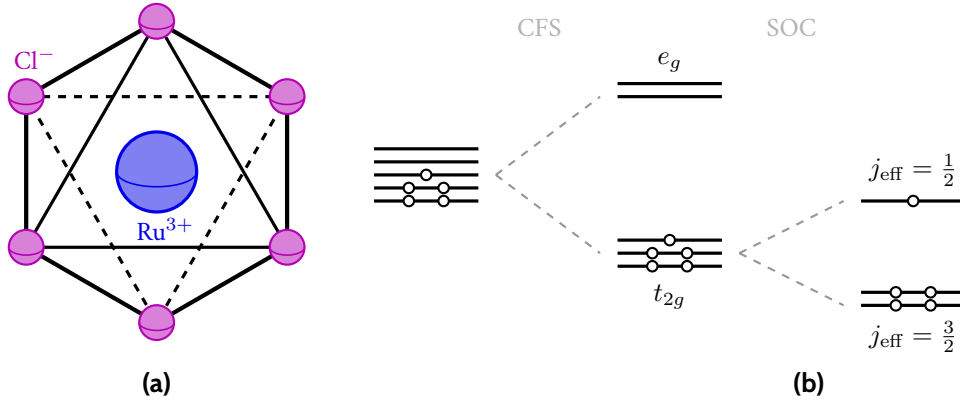


FIG. 2.4: (a) Ru^{3+} ion (blue) in octahedral cage of six Cl^- ions (pink). (b) Level scheme in the presence of crystal-field splitting (CFS) and SOC. Adapted from Ref. [224].

large λ , it is, therefore, possible to describe the low-energy physics of this compound in terms of quantum *pseudospins* with length $1/2$. In Kitaev materials, λ is typically around a few hundred meV [206] and, as we see below, thus much larger than the hopping matrix elements. In my Publications **P2** and **P3**, we do not include H_{SO} in the canonical transformation (2.37) of the microscopic Hamiltonian but account for SOC by a subsequent projection into the $j_{\text{eff}} = 1/2$ subspace spanned by the basis states

$$|+\rangle = \frac{1}{\sqrt{3}} (-|z, \uparrow\rangle - i|y, \downarrow\rangle - |x, \downarrow\rangle), \quad |-\rangle = \frac{1}{\sqrt{3}} (|z, \downarrow\rangle + i|y, \uparrow\rangle - |x, \uparrow\rangle), \quad (2.46)$$

where $|\alpha, \sigma\rangle$ denotes a state with spin $\sigma \in \{\uparrow, \downarrow\}$ and $\alpha = x, \alpha = y$ and $\alpha = z$ label the t_{2g} orbitals d_{yz} , d_{xz} and d_{xy} , respectively.

Although this approximation is well-justified, we note that the hopping strength is comparably large in these materials and, in turn, electron correlations are moderately suppressed due to the significant atomic overlap of the heavy transition metal ions [206]. It is, in fact, the large SOC in these materials that reduces the electronic bandwidth and thereby enables the formation of a Mott insulating gap. Due to this crucial role of the coupling of spin and orbital degrees of freedom, these compounds are referred to as *spin-orbit assisted Mott insulators*. The existence of a spin-orbit assisted Mott insulator with a $j_{\text{eff}} = 1/2$ pseudospin was confirmed by experiments on the perovskite iridate Sr_2IrO_4 in 2008 [110, 111, 206]. In this compound, however, the pseudospins are coupled by a conventional isotropic Heisenberg exchange despite the presence of strong SOC [206]. Let us therefore study what determines the dominant pseudospin exchange and, in particular, how one can realize the characteristic interaction of the Kitaev model.

2.2.3 Bond-directional superexchange

The entire research of the potential QSL phase of Kitaev materials is built on the remarkable insight of Jackeli and Khaliullin [107, 93] that the relative orientation of the octahedral cages enclosing the transition metal ions has crucial consequences on the dominant electronic hopping path and the resulting pseudospin exchange. As illustrated in Fig. 2.5(a), in some compounds including the aforementioned iridate Sr_2IrO_4 , the octahedral cages share a corner. The dominant hopping path that couples the electrons on neighboring ions then involves a single ligand. As one can show in terms of a modified canonical transformation (2.37), the resulting pseu-

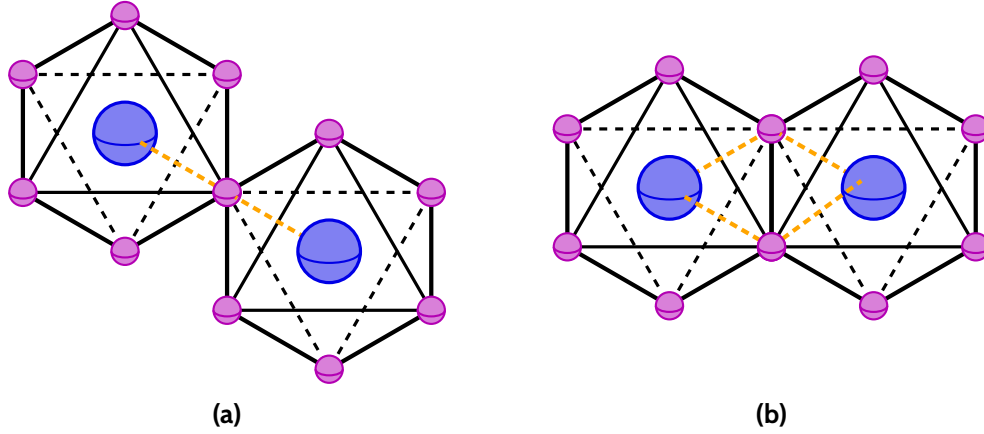


FIG. 2.5: Dominant exchange paths (orange) between two transition metal ions (blue) for **(a)** corner-sharing octahedral cages or **(b)** edge-sharing octahedral cages. Adapted from Ref. [206].

dospin interaction is then dominated by a *superexchange* in the form of an isotropic Heisenberg coupling [93, 109]. Quantum spin liquid physics is, therefore, not expected in these compounds.

The situation, however, changes dramatically for edge-sharing octahedral cages as in the case of α - RuCl_3 . For this bonding geometry, there are two alternative hopping paths mediated by two different ligands, which, most remarkably, give rise to a destructive interference of the symmetric Heisenberg interaction obtained from superexchange [93, 206], see Fig. 2.5(b). The dominating spin exchange instead arises due to a hopping path coupling a pair of different t_{2g} orbitals, which is determined by the spatial direction of the bond. It is this bond-directional hopping that ultimately gives rise to a large Kitaev interaction for edge-sharing octahedral cages and constitutes the Jackeli-Khaliullin mechanism. Notably, this interaction arises due to virtual processes involving the $j_{\text{eff}} = 3/2$ quartet and is therefore scaled by *Hund's coupling* of the orbital momentum and spin.

For a more formal and comprehensible description, let us introduce the microscopic model, which is also employed in my Publications **P2** and **P3**. The generalization of the single-orbital Hubbard model (2.36) to a system with multiple orbitals is given by the *Hubbard-Kanamori model* [99, 197]. Since we are interested in the configuration with a single hole per t_{2g} multiplet, it is convenient to express the Hamiltonian in terms of holes instead of electrons. To this end, let $h_{j\alpha\sigma}$ be the annihilation operator of a hole at site j with spin $\sigma \in \{\uparrow, \downarrow\}$ and t_{2g} orbital $\alpha = x, \alpha = y$ or $\alpha = z$ labeling d_{yz}, d_{xz} and d_{xy} , respectively. With the exception of the SOC (2.45), the on-site interactions are then described by [178, 222]

$$V = \sum_j \left[\frac{U - 3J_{\text{H}}}{2} (\bar{N}_j - 1)^2 - 2J_{\text{H}} \mathbf{S}_j^2 - \frac{J_{\text{H}}}{2} \mathbf{L}_j^2 \right], \quad (2.47)$$

where the $U > 0$ is the Coulomb repulsion, $J_{\text{H}} \in (0, U/3)$ is Hund's coupling and \bar{N}_j, \mathbf{S}_j and \mathbf{L}_j are the total number operator, spin operator and orbital momentum operator of the holes at site j , respectively. In terms of the spinor $h_j^\dagger = (h_{jx\uparrow}^\dagger, h_{jy\uparrow}^\dagger, h_{jz\uparrow}^\dagger, h_{jx\downarrow}^\dagger, h_{jy\downarrow}^\dagger, h_{jz\downarrow}^\dagger)$, these operators are given by

$$\bar{N}_j = h_j^\dagger h_j, \quad \mathbf{S}_j = \frac{1}{2} h_j^\dagger (\boldsymbol{\sigma} \otimes \mathbb{1}_3) h_j, \quad \mathbf{L}_j = h_j^\dagger (\mathbb{1}_2 \otimes \mathbf{l}) h_j, \quad (2.48)$$

where $\boldsymbol{\sigma}$ comprises the Pauli matrices acting in spin space and \mathbf{l} involves 3×3 matrices representing the effective angular momentum for $l_{\text{eff}} = 1$. Given the on-site interaction, the full

Hubbard-Kanamori model is then given by [178, 197]

$$H_{\text{HK}} = V + \bar{H}_{\text{SO}} + T, \quad (2.49)$$

where $\bar{H}_{\text{SO}} = \lambda \sum_{j,\alpha} h_j^\dagger (\sigma^\alpha \otimes l^\alpha) h_j$ is the spin-orbit coupling of holes and

$$T = - \sum_{\langle jk \rangle_\alpha} h_j^\dagger (\mathbb{1}_2 \otimes T_\alpha) h_k \quad (2.50)$$

describes the nearest-neighbor hopping on the honeycomb lattice resulting for edge-sharing octahedra enclosing the transition metal ions.¹⁷ As indicated above, the hopping matrix elements T_α have an explicit dependency on the orbitals as well as the bond type $\alpha \in \{x, y, z\}$. The numerical values of the elements are obtained by computing the Slater-Koster parameters for the overlaps of either two transition metal ions or one transition metal ion and one ligand [178]. By following this approach, we include not only the dominant paths but also subdominant hopping. In the case of a z bond, the hopping matrix is of the form [178, 222]

$$T_z = \begin{pmatrix} t_1 & t_2 & t_4 \\ t_2 & t_1 & t_4 \\ t_4 & t_4 & t_3 \end{pmatrix} \quad (2.51)$$

where the off-diagonal parameter t_2 corresponds to the paths indicated in Fig. 2.5(b) and originally considered by Jackeli and Khaliullin [93], while the off-diagonal entry t_4 arises from trigonal distortion of the octahedral environment and is neglected in the following. The matrices T_x and T_y are obtained from appropriate cyclic permutations [178].

In any case, given a hopping term T , it is possible to perform a canonical transformation (2.37) of the Hamiltonian $V + T$ at commensurate filling to obtain an effective description at low energies, as described above. Subsequently, one can project into the $j_{\text{eff}} = 1/2$ duplet spanned by the states (2.46) for every site on the lattice. This implies a restriction to the regime

$$U > J_H \gg \lambda \gg |t_1|, |t_2|, |t_3|.$$

We refer to Ref. [178] and my Publication **P2** for technical details, but note that the essential modification with respect to calculation for the single-orbital model (2.36) is the partition of the state manifold into channels with different angular momenta. As expected, one arrives at an isotropic ferromagnetic Kitaev interaction with exchange strength

$$K = -\frac{8J_H}{18} \frac{(t_1 - t_3)^2 - 3t_2^2}{(U - 3J_H)(U - J_H)}. \quad (2.52)$$

However, subdominant hopping paths for finite t_1 and t_3 give rise to additional spin exchange terms allowed by the honeycomb symmetry. The general model describing the pseudospins of typical Kitaev materials (assuming an ideal octahedral geometry) is then given by [178, 206]

$$H_{JK\Gamma} = \sum_{\langle jk \rangle_\alpha}^I \left[J \boldsymbol{\sigma}_j \cdot \boldsymbol{\sigma}_k + K \sigma_j^\alpha \sigma_k^\alpha + \Gamma \left(\sigma_j^\beta \sigma_k^\gamma + \sigma_j^\gamma \sigma_k^\beta \right) \right], \quad (2.53)$$

¹⁷Typical Kitaev materials are layered compounds with negligible interlayer coupling [206]. This justifies the use of two-dimensional models. Moreover, we note that in my Publication **P2**, we also include hopping to next-nearest neighbors as well as inhomogeneities in the hopping due to an external electrostatic potential.

where the operators σ_j^α act on the effective $j_{\text{eff}} = 1/2$ duplets and the prime over the sum indicates that (α, β, γ) are cyclic permutation of (x, y, z) . The corrections to the Kitaev interaction are thus given by an isotropic Heisenberg coupling J as well as a specific off-diagonal exchange Γ .¹⁸ This resulting model is called extended Kitaev model or sometimes simply *JK Γ model*. The perturbations J and Γ spoil the exact solution of the Kitaev model presented in Section 2.1 and, as we discuss below, can have drastic consequences on the ground state of the model. In any case, however, we demonstrated how an intricate balance of crystal fields, spin-orbit coupling and superexchange can generate strong spin exchange anisotropy and, in particular, the highly frustrated interaction of the Kitaev model [206].

2.2.4 Kitaev materials

Let us briefly outline the material family which involves all the necessary ingredients of the Jackeli-Khaliullin mechanism. This endeavor is somewhat hindered by the fact that the foundational works by Jackeli and Khaliullin [107, 93] launched massive experimental efforts and what is, at the time of writing, still a quickly developing field of research. We may therefore focus on the material platforms which are most relevant to the theory presented in my Publications P2 and P3. Moreover, for now, we are interested in the confirmation of the Jackeli-Khaliullin mechanism and detail the experimental status of the QSL phase in Kitaev materials in Section 2.3

The initial proposals for the realization of the Kitaev model comprised compounds of the form $X_2\text{IrO}_3$, where X is an alkali metal [107, 40]. At that time, the variant for $X=\text{Na}$ was already synthesized [191] and can thus be considered the first Kitaev material [206]. Angle-resolved photoemission spectroscopy and optical experiments confirmed that Na_2IrO_3 is indeed a Mott insulator with a gap of roughly $\Delta \simeq 340$ meV [50]. Due to a comparably large SOC of roughly $\lambda \simeq 400$ meV we can then identify this compound as a spin-orbit assisted Mott insulator despite an observed trigonal distortion of the octahedral field [206, 73, 74]. This is consistent with both fits of the magnetic susceptibility and X-ray absorption spectroscopy, which indicate that the magnetic moments of Na_2IrO_3 are close to ideal $j_{\text{eff}} = 1/2$ pseudospins due to weak mixing with the $j_{\text{eff}} = 3/2$ quartet [191, 192, 194]. Collecting these results shows that all necessary ingredients of the Jackeli-Khaliullin mechanism are present [93, 40]. And indeed, diffuse magnetic X-ray scattering experiments provided striking evidence for a strong bond-directional spin exchange and, moreover, a dominant Kitaev interaction [89].

Despite this remarkable confirmation of the presented theory, Na_2IrO_3 is not expected to host a QSL phase [132, 49, 237, 206]. As we further discuss below, this is because the corrections to the Kitaev exchange in Eq. (2.53) are too large to stabilize a QSL or a related state. Parts of the research, therefore, shifted their focus to other iridates such as $\alpha\text{-Li}_2\text{IrO}_3$ [206, 192] and the aforementioned compound $\alpha\text{-RuCl}_3$.¹⁹ The latter is arguably the most studied and prominent Kitaev material and subject of captivating experimental claims, which we discuss in Section 2.3. Using the same or similar techniques as applied to Na_2IrO_3 , it was verified that RuCl_3 is a Mott insulator with a charge gap of $\Delta \simeq 1.2$ eV and almost perfect octahedral crystal field [173, 172, 256, 186, 206]. Despite its experimental success, we note that the SOC $\lambda \simeq 100$ meV

¹⁸Consistent with the qualitative discussion above, the Heisenberg coupling does not arise due to the superexchange mediated by ligands but due to direct hopping between t_{2g} orbitals [224]. In many Kitaev materials, J is therefore expected to be much smaller in magnitude than K .

¹⁹ RuCl_3 has two polymorphs termed $\alpha\text{-RuCl}_3$ and $\beta\text{-RuCl}_3$ [206]. The latter is not relevant to our considerations and we drop the label α in the following.

in RuCl_3 is considerably smaller than in the iridates and thereby allows for enhanced mixing with the $j_{\text{eff}} = 3/2$ quartet and larger magnetic moments [186, 13, 120, 63, 122, 193, 206]. This is related to the fact that estimations of the Kitaev coupling in three dimensional samples either from numerical simulations or experimental analysis vary in the range of 5 and 10.6 meV [222, 85, 223, 198, 235], see also my Publication P3. Notably, these estimations can further change in two-dimensional samples, as discussed in Section 2.4.

Before discussing the experiments that probe the ground state of RuCl_3 , let us comment on other Kitaev materials for the sake of completeness. New Kitaev candidates can be obtained by modifying the iridates X_2IrO_3 in terms of soft-chemical exchange [206]. More notably, the material family also contains candidate materials with other tricoordinated lattices, including triangular and three dimensional variants. As mentioned in Section 1.1, the exact solution of the Kitaev model can be adapted for such lattice geometries and gives rise to rich phenomenology in three dimensions [236, 138, 163, 81, 206].²⁰ The first studied three-dimensional Kitaev materials are the polymorphs $\beta\text{-Li}_2\text{IrO}_3$ [201] and $\gamma\text{-Li}_2\text{IrO}_3$ [146] of the well-studied iridate candidate $\alpha\text{-Li}_2\text{IrO}_3$ [93, 192] and are, therefore, also believed to realize the Jackeli-Khaliullin mechanism. Recent theoretical proposals, however, also go beyond this established paradigm and predict Kitaev physics for systems with partially filled d^7 , d^8 or even f shells such as in rare-earth compounds [128, 206, 94]. Moreover, as we detail in Section 2.4, recent numerical and experimental efforts have been devoted to heterostructures of Kitaev materials and substrates [234, 222, 55, 26, 254, 248, 255, 121, 252]. Such systems enable novel experimental probes which could potentially advance our understanding of the QSL phase in Kitaev materials.

2.3 Experimental status of RuCl_3

The realization of a dominant Kitaev interaction through the Jackeli-Khaliullin mechanism in spin-orbit Mott insulators [107, 93] initiated a plethora of experiments in search of the predicted quantum spin liquid (QSL) phase and sparked heated discussions in the community. Instead of attempting to list all reported experiments, let us summarize key aspects of the current understanding of their results with a strong focus on the compound RuCl_3 .

2.3.1 Proximate spin liquid

As outlined in Chapter 1, *inelastic neutron scattering (INS)* represents an established technique to probe the magnetic ground state of solid-state systems in terms of the spin structure factor [118]. In the case of Kitaev materials, INS and other scattering experiments clearly demonstrated that three dimensional (3D) samples of the studied material candidates do not host a QSL but exhibit long-range magnetic order at sufficiently low temperatures [132, 49, 237, 13, 15, 206]. In RuCl_3 , the magnetically ordered state is an antiferromagnetic *zigzag phase* and is observed at temperatures below $T_c \simeq 7$ K [13].²¹ The appearance and physics of this phase can be understood in terms of the $JK\Gamma$ model (2.53), which includes subdominant contributions that perturb the pure Kitaev model (2.1). Notably, these perturbations spoil the exact solution of the model and, in particular, obstruct the conservation of the plaquette operators (2.2).

²⁰We note that Lieb's theorem [130] discussed in section 2.1 does not necessarily apply for different lattice geometries. In these cases, the flux sector of the ground state has to be verified numerically [236].

²¹Estimations of the Curie-Weiss temperature vary drastically [206] but the frustration ratio of RuCl_3 is at least $f \simeq 4$. Based on our discussion in Chapter 1, we infer that the material is considerably frustrated.

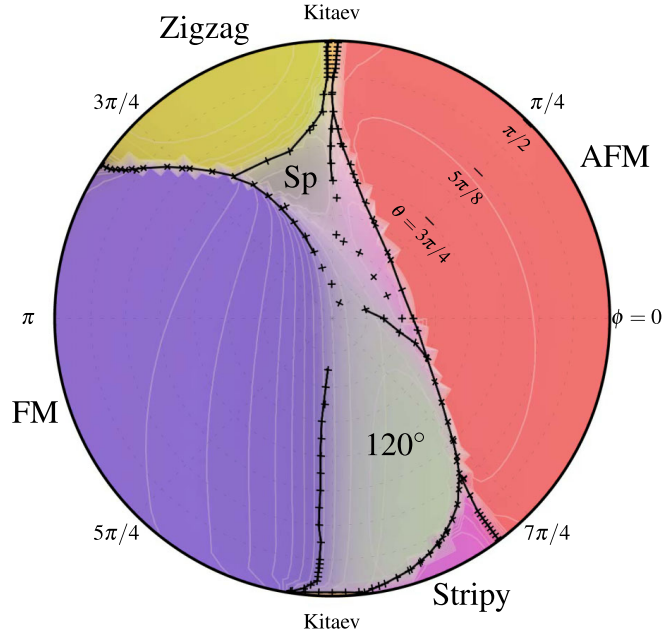


FIG. 2.6: Quantum phase diagram of $JK\Gamma$ model (2.53) for $\Gamma < 0$ using parametrization (2.54). The yellow, red, magenta, green and gray phases are magnetically ordered. The small pockets near the exactly solvable points with the label “Kitaev” are QSLs. Adapted from Ref. [178].

The $JK\Gamma$ model (2.53) has been subject of extensive numerical studies [178, 224, 223, 38, 71, 214, 249]. Although it is not fully understood, these works revealed an intricate and rich quantum phase diagram. Fig. 2.6 shows a section of this phase diagram for the spherical parametrization

$$J = -\sin \phi \sin \theta, \quad K = -\cos \phi \sin \theta, \quad \Gamma = -\cos \theta. \quad (2.54)$$

There, we identify a variety of magnetically ordered phases and small pockets of QSLs near the exactly solvable points $(\phi, \theta) = (\pi/2, \pi/2)$ and $(\phi, \theta) = (3\pi/2, \pi/2)$. Within this QSL phase, \mathbb{Z}_2 vortex excitations are generally not static but dispersive. Perturbative calculations, however, indicate a low vortex mobility [98] and thereby justify the mean-field decoupling of the Majorana representation of Eq. (2.53) that we employ in my Publication P2.

Anyhow, the estimations for J , K and Γ for RuCl_3 depend significantly on the method and modeling but typically yield parameters in the regime $K > J > 0$ and $\Gamma < 0$ [224]. For example, density functional theory estimates [233, 224]

$$J_{\text{DFT}} \simeq 0.7 \text{ meV}, \quad K_{\text{DFT}} \simeq 5.1 \text{ meV}, \quad \Gamma_{\text{DFT}} \simeq -1.8 \text{ meV},$$

and, therefore, locates RuCl_3 in the zigzag phase as observed by experiments [13, 15].

While this disappointing result makes it seem that the desired QSL state cannot be stabilized in RuCl_3 , various experiments nonetheless claim the observation of the intriguing physics of the adjacent QSL phase. These claims may be attributed to two different strategies for how to destabilize the zigzag ordered ground state, namely, by increasing the temperature or by applying an external magnetic field. The consideration of the former strategy brings us to the loosely defined concept of a *proximate spin liquid* [13, 15, 206]. A proximate spin liquid describes a point of a magnetically ordered phase in the zero-temperature quantum phase diagram, which is in the close vicinity to the QSL. While perturbations to the Kitaev model such as J and Γ in the $JK\Gamma$ model might stabilize a magnetic order below the critical temperature T_c at this point, the paramagnet above T_c could potentially show thermal signatures of the QSL phase [205], if a

smooth path in the finite-temperature phase diagram connects the two states without traversing a crossover or a phase transition [206]. As the Kitaev model at intermediate temperatures describes itinerant fermions in front of a disordered flux background [206, 180], these thermal signatures could indicate fractionalization or unconventional spin correlation [13, 205].

This somewhat speculative picture was proposed to explain a series of scattering experiments on RuCl_3 which reported intriguing similarity to the corresponding predictions in the Kitaev spin liquid phase [185, 186, 13, 15]. Namely, the temperature dependency of the Raman susceptibility observed by Raman scattering is consistent with the distribution of fermionic excitations as expected in the thermal QSL [185, 186]. Moreover, INS measurements reported a characteristic broad continuum at higher energies and more intricate features [13, 15], which roughly agree with the expected dynamical response of the Kitaev QSL [69].²² All these results suggest that RuCl_3 is a proximate spin liquid and are, therefore, symptomatic of the desired QSL phase. We note that additional evidence for this intriguing claim is provided by reported measurements of a non-quantized thermal Hall conductivity above the magnetic ordering temperature [105], which is seemingly consistent with the prediction (2.35) for the non-Abelian phase of the Kitaev model. We detail the thermal transport in RuCl_3 in our following discussion of experimental probes of a genuine QSL state at low temperatures. During this analysis, it also becomes clear that the interpretation of the results reported in Ref. [105] should be approached with care.

2.3.2 Quantum thermal Hall effect of the field-induced state

An alternative way to obstruct the magnetically ordered zigzag phase of RuCl_3 is provided by the presence of a homogeneous magnetic field. This is evident as we expect that upon increasing the external field strength B , the spins in a magnetic insulator eventually align with the field direction and form a polarized state. Notably, in the case of the pure Kitaev model (2.1), since the fully polarized state is not an eigenstate of the Hamiltonian, the magnetization does not saturate for arbitrarily large B [206]. We, therefore, refer to the large-field state of Kitaev materials as the *partially polarized phase*. Measurements of the specific heat indicate that an in-plane field of $B_c \simeq 8$ T destroys the zigzag order and gives rise to a phase transition to a field induced state [137, 124, 10, 188, 228, 9, 8].²³ This result was confirmed by various other experiments such as INS [14] and Raman spectroscopy [182, 229]. While the latter technique also demonstrated the trivial partially polarized phase for $B \geq 15$ T, the ground state at intermediate field strength is currently subject of an intense debate. This is because widely recognized experiments claim the observation of a *field-induced* quantum spin liquid phase for $B \sim 7$ -10 T [104, 239].

Before discussing these experiments in detail, we note that based on our above discussion of proximate spin liquids this claim might seem unsurprising. This is due to the fact that a partially polarized state and finite-temperature paramagnet are physically very similar, in that they are both gapped, partially magnetized and exhibit no spontaneous symmetry breaking and, therefore, no thermal phase transition upon increasing the temperature [206]. We might thus expect remnants of the adjacent QSL phase in experimental signatures in the partially polarized state. And, indeed, INS measurements at $B \geq 7$ T show a broad continuum with remarkable similarity [14] to the aforementioned experiments above the magnetic ordering temperature (for

²²We note, however, that the INS measurements have to be approached with care as magnon excitations might also form a broad energy continuum [223, 206].

²³The obstruction of the ordered phase in terms of a field perpendicular to the plane requires enormous field strength of $B > 60$ T [96, 145].

$B = 0$) [13, 15]. While this result validates the concept of proximate spin liquids, we emphasize that the experiments which we discuss in the following go beyond this picture, as they claim the observation of the *non-Abelian* QSL phase of the Kitaev magnets. Since this phase is topologically nontrivial, see Section 2.1, it should be separated from both the magnetically ordered and partially polarized phase in terms of two phase transitions. Notably, the appearance of a second field-induced phase transition was not observed in the measurements of the specific heat [137, 124, 10, 188, 228] nor the majority of other experimental techniques [14, 206].²⁴

In any case, however, the claim of the field-induced QSL phase attracted massive attention, since it is based on what can be considered a universal smoking-gun signature of the QSL phase, that is, the *quantized thermal Hall effect*. These spectacular measurements were performed by the group of Matsuda in 2018 [104] and subsequent years [239] and constitute arguably the most prominent experiments on Kitaev materials. As we discussed in Section 2.1, chiral Majorana edge modes propagating along the boundary of the non-Abelian QSL state carry an energy current and give rise to a quantized thermal conductivity (2.35)

$$\kappa_{xy}^{2D} = \pm \frac{1}{2} \frac{\pi}{6} \frac{k_B^2}{\hbar} T,$$

which differs to a thermal conductivity in the conventional quantum Hall state by a factor of $1/2$ [112]. The sign of κ_{xy}^{2D} is given by the Chern number (2.33) of the non-Abelian phase and has an explicit dependence on the field direction. Similarly to the electronic quantum Hall effect, this quantized value is expected to be robust against disorder as well as phononic effects [238, 212] and dispersive \mathbb{Z}_2 vortices [98]. To access κ_{xy}^{2D} , the group of Matsuda measured the transverse thermal conductivity κ_{xy} of a RuCl_3 Hall bar in an out-of-plane magnetic field and divided the result by the number of honeycomb layers [104]. The measured values are plotted in Fig. 2.7 and indicate a quantized plateau for magnetic fields in the range of $B \sim 7\text{-}10\text{ T}$ and temperatures in the range of $T \sim 4\text{-}6\text{ K}$.²⁵ Moreover, subsequent measurements using in-plane magnetic fields report a half-quantized plateau with a sign structure that is consistent with the Chern number (2.33) of the Kitaev model [239] and which, notably, has no analog in the electric quantum Hall physics. Collecting these spectacular results amounts to intriguing evidence for a field-induced Kitaev spin liquid and, in particular, Majorana edge modes.

However, as already suggested, these experiments are controversially debated in the community and should be approached with care. One reason for restraint is the fact that, at the time of writing, no other experimental group was able to independently reproduce these results. Instead, the group of Ong reported unconventional oscillations of κ_{xy} reminiscent of quantum oscillations in metals [53] and exotic bosonic excitations [52], which currently lack theoretical understanding. The pending validation by an independent group is most likely related to the significant sample dependency and the intricate role of defects [206]. Another complication of the thermal Hall experiments, which we may highlight in the following, is the fact that *topological magnon* excitations of the partially polarized phase also generate a finite albeit non-quantized thermal Hall conductivity with a similar sign structure with respect to the field direction [51, 47, 246]. These excitations could thus mimic the quantized effect of Majorana edge modes. Recent experimental efforts, therefore, attempted to differentiate thermal Hall signals of bosonic and fermionic excitations [90, 247]. On the other hand, the inconclusive experimental status of the field-induced QSL phase in RuCl_3 calls for new experimental

²⁴There is actually another field-induced first-order phase transition within the zigzag phase. However, this transition keeps the system magnetically ordered and is not of interest here [12].

²⁵The used thermometers in experiments were not expected to be reliable at lower temperatures [104, 206].

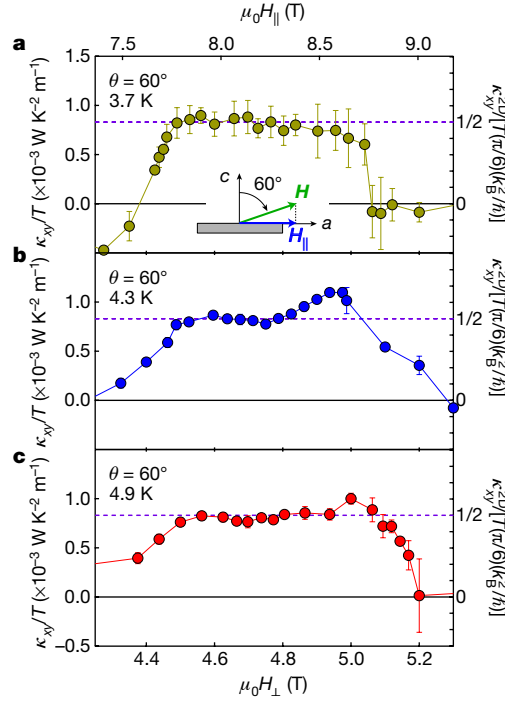


FIG. 2.7: Thermal Hall conductivity in RuCl_3 as a function of magnetic field strength at different temperatures. The dashed line indicates the half-integer value predicted for the non-Abelian QSL phase. Adapted from Ref. [104].

techniques, which are able to clarify the existence of this exotic state of matter. As we motivate in Section 2.4, the design of such experimental schemes is the objective of my Publications P2 and P3.

2.3.3 Topological magnons in the partially polarized phase

Let us discuss the magnonic excitations of the partially polarized phase in Kitaev materials in more detail [141, 51, 47, 246, 249, 46]. As said, these excitations generate a finite thermal Hall conductivity and thereby obscure the unambiguous interpretation of the quantized thermal Hall effect of the Kitaev spin liquid phase. We, therefore, compare our predictions for the QSL with magnonic effects in my Publication P3 and unravel the underlying mechanism for generic polarized two-dimensional magnets in my Publication P4. An intriguing property of spin wave excitations of the partially polarized $JK\Gamma$ model (2.53) is potentially nontrivial *band topology* [141, 51, 46]. Topological magnons have gathered considerable attention in the last view years and exhibit a similar phenomenology as electronic systems with nontrivial band topology [139, 97, 142], which was partly confirmed in experiments on the prominent ferromagnet CrI_3 using INS [45]. Another signature of topological magnons is the non-quantized thermal Hall effect which stems from to the bulk-boundary correspondence [139, 140].

Let us verify the nontrivial band topology of the $JK\Gamma$ model (2.53) on the level of *linear spin-wave theory* [171]. Although Kitaev materials are partially polarized by magnetic fields with finite in-plane components, we consider a perpendicular field \mathbf{h} along the $[111]$ direction for the purpose of a simple introduction. We may then rewrite the $JK\Gamma$ model (2.53) for spins \mathbf{S}_j of arbitrary length S and in the presence of a Zeeman coupling to [141]

$$H_{JK\Gamma} = - \sum_{\langle jk \rangle_\alpha} \mathbf{S}_j^\dagger H_\alpha \mathbf{S}_k - \sum_j \mathbf{h} \cdot \mathbf{S}_j, \quad (2.55)$$

where $\mathbf{h} = h(1, 1, 1)^T/\sqrt{3}$ is the magnetic field and the bond-dependent nearest-neighbor coupling is encoded in the matrices

$$H_x = \begin{pmatrix} J+K & 0 & 0 \\ 0 & J & \Gamma \\ 0 & \Gamma & J \end{pmatrix}, \quad H_y = \begin{pmatrix} J & 0 & \Gamma \\ 0 & J+K & 0 \\ \Gamma & 0 & J \end{pmatrix}, \quad H_z = \begin{pmatrix} J & \Gamma & 0 \\ \Gamma & J & 0 \\ 0 & 0 & J+K \end{pmatrix}. \quad (2.56)$$

Within spin-wave theory, magnon excitations represent the quantum fluctuations about classical low-energy configuration. In the partially polarized phase, the classical problem is minimized by aligning all spins with the magnetic field. Given this configuration, it is convenient to align the classical spins with the z axis in terms of the rotation $\mathbf{S}_j = R\bar{\mathbf{S}}_j$, where

$$R = \frac{1}{\sqrt{6}} \begin{pmatrix} 1 & -\sqrt{3} & \sqrt{2} \\ 1 & \sqrt{3} & \sqrt{2} \\ -2 & 0 & \sqrt{2} \end{pmatrix}. \quad (2.57)$$

Quantum fluctuations are then accounted for by the established Holstein-Primakoff transformation [171]

$$\bar{S}_j^z = S - n_j, \quad \bar{S}_j^+ = \sqrt{2S - n_j} b_j \approx \sqrt{2S} b_j, \quad \bar{S}_j^- = b_j^\dagger \sqrt{2S - n_j} \approx \sqrt{2S} b_j^\dagger, \quad (2.58)$$

where $n_j = b_j^\dagger b_j$ is the number operator and b_j and b_j^\dagger are annihilation and creation operators of a Holstein-Primakoff boson on site j , respectively. Anticipating a description on the level of linear spin wave theory, we expanded the ladder operators S_j^+ and S_j^- up to lowest order in n_j/S . Inserting the transformation and expanding the Hamiltonian (2.55) up to lowest non-trivial order in $1/S$ yields

$$H_{JK\Gamma} = E_{\text{cl}} + H_{\text{sw}} + \mathcal{O}(S^{1/2}), \quad (2.59)$$

where E_{cl} is the classical ground state energy. In the case of a system of $2N$ spins, we find

$$E_{\text{cl}} = -S^2 N (2h/S + 3J + K + 2\Gamma). \quad (2.60)$$

The next order in the $1/S$ expansion is the quadratic spin-wave Hamiltonian

$$H_{\text{sw}} = S \sum_{\langle jk \rangle_\alpha} (t_\alpha b_j^\dagger b_k + \Delta_\alpha b_j b_k + \text{H.c.}) + S \sum_j h_{\text{eff}} b_j^\dagger b_j, \quad (2.61)$$

where the effective magnetic field $h_{\text{eff}} = h/S + 3J + K + 2\Gamma$ involves both the external field and the *Weiss field* while the hopping amplitudes are given by

$$t_\alpha = -J - \frac{1}{3}(K - \Gamma), \quad \Delta_\alpha = -\frac{1}{3}e^{i2\pi\alpha/3}(K + 2\Gamma). \quad (2.62)$$

Here, $\alpha = 1, 2$ and $\alpha = 3$ label x, y and z bonds, respectively. Formally truncating the expansion at linear order S is only justified in the limit $S \rightarrow \infty$. However, for low magnon densities n_j , linear spin-wave theory for small spins S typically yields reasonable results and an appropriate starting point for more elaborate methods [141, 171]. We also note that for finite $|\Delta_\alpha|$, particle number is not conserved. We therefore obtain the spectrum of the quadratic Hamiltonian H_{sw} within the bosonic variant of Bogoliubov-de-Gennes formalism. Since we

are, for now, interested in homogeneous systems, this calculation is facilitated by a Fourier transformation. Given a site $j \in \lambda$ on sublattice $\lambda \in \{\mathcal{A}, \mathcal{B}\}$ at position \mathbf{r}_j , we write

$$b_j = \frac{1}{\sqrt{2N}} \sum_{\mathbf{k} \in \text{BZ}} e^{i\mathbf{k} \cdot \mathbf{r}_j} b_\lambda(\mathbf{k}), \quad b_j^\dagger = \frac{1}{\sqrt{2N}} \sum_{\mathbf{k} \in \text{BZ}} e^{-i\mathbf{k} \cdot \mathbf{r}_j} b_\lambda^\dagger(\mathbf{k}). \quad (2.63)$$

We skip some technical steps and refer to my Publications **P3** and **P4** for technical details. The solution involves a Bogoliubov transformation of the form [27]

$$\begin{pmatrix} b_{\mathbf{k}} \\ b_{-\mathbf{k}}^\dagger \end{pmatrix} = W_{\mathbf{k}} \begin{pmatrix} d_{\mathbf{k}} \\ d_{-\mathbf{k}}^\dagger \end{pmatrix}, \quad b_{\mathbf{k}} = \begin{pmatrix} b_{\mathcal{A}}(\mathbf{k}) \\ b_{\mathcal{B}}(\mathbf{k}) \end{pmatrix}, \quad d_{\mathbf{k}} = \begin{pmatrix} d_1(\mathbf{k}) \\ d_2(\mathbf{k}) \end{pmatrix}, \quad (2.64)$$

where $W_{\mathbf{k}}$ is 4×4 matrix with the property

$$W_{\mathbf{k}}^{-1} = \Sigma_z W_{\mathbf{k}} \Sigma_z \quad \text{for} \quad \Sigma_z = \text{diag}(1, 1, -1, -1). \quad (2.65)$$

An appropriate choice of $W_{\mathbf{k}}$ diagonalizes the spin-wave Hamiltonian (2.61) in momentum space. Up to a constant, we arrive at

$$H_{\text{sw}} = S \sum_{\mathbf{k} \in \text{BZ}} \left[\omega_1(\mathbf{k}) d_1^\dagger(\mathbf{k}) d_1(\mathbf{k}) + \omega_2(\mathbf{k}) d_2^\dagger(\mathbf{k}) d_2(\mathbf{k}) \right] + \text{const.} \quad (2.66)$$

This expression describes the dispersion of magnon modes annihilated by $d_1(\mathbf{k})$ and $d_2(\mathbf{k})$. The full analytical expression of the two magnon bands $\omega_1(\mathbf{k})$ and $\omega_2(\mathbf{k})$ is tedious and not detailed here [141]. For our purposes it is sufficient to know that for small off-diagonal exchange $|\Gamma|$, both bands are gapped according to

$$\omega_1(\mathbf{0}) = h/S + 3\Gamma \leq \omega_1 \leq \sqrt{(h/S + 3J)(h/S + 3J + 2K + 4\Gamma)} \quad (2.67)$$

and

$$h/S + 6J + 2K - \Gamma \leq \omega_2 \leq h/S + 3J + K + 2\Gamma. \quad (2.68)$$

For a strong polarizing magnetic field, the excitation gap $\omega_1(\mathbf{k} = \mathbf{0})$ is essentially given by field strength $h > 0$. In my Publication **P4**, we expand near the band minimum at $\mathbf{k} = \mathbf{0}$ to derive our continuum theory.

Anyhow, based on our general discussion in Chapter 1, we may now use our full solution of the non-interacting system to probe its band topology by means of the Chern number (1.7). To this end, we can express the (out-of-plane component of the) *Berry curvature* Ω_n of the n th band by means of the Bogoliubov transformation (2.64) using [140, 47]

$$\Omega_n(\mathbf{k}) = i \left(\Sigma_z \frac{\partial W_{\mathbf{k}}^\dagger}{\partial k_x} \Sigma_z \frac{\partial W_{\mathbf{k}}}{\partial k_y} - \Sigma_z \frac{\partial W_{\mathbf{k}}^\dagger}{\partial k_y} \Sigma_z \frac{\partial W_{\mathbf{k}}}{\partial k_x} \right)_{nn}, \quad (2.69)$$

where the indices of the brackets indicate the n th entry on the diagonal. As detailed in Eq. (1.7), the Chern number $\nu_n \in \mathbb{Z}$ of n th band is then given by²⁶

$$\nu_n = \frac{1}{2\pi} \int_{\text{BZ}} dk_x dk_y \Omega_n(\mathbf{k}). \quad (2.70)$$

²⁶We note that in Refs. [141, 46], a canonical transformation (2.37) in the large field limit was employed to simplify the Hamiltonian and the subsequent calculation of the Chern number.

As the total Chern number needs to vanish, we have $\nu_1 = -\nu_2$. Notably, in the case of the $JK\Gamma$ model (2.55) and for arbitrary field directions, the Chern number indicates a rich and intricate topological phase diagram [141, 46]. For a comprehensible discussion, let us focus on the limit of dominant Kitaev interaction, i.e., $K \gg |J|, |\Gamma|$, and a perpendicular magnetic fields as specified. In this particular regime, one finds $|\nu_1| = 1$ and, therefore, a topological band structure of magnon excitations [141]. As discussed in Chapter 1, the celebrated bulk-boundary correspondence then implies the existence of chiral edge states, which exist for energies between the two bands ω_1 and ω_2 and which give rise to a finite thermal Hall effect. According to a general formula derived by Matsumoto and Murakami [139], the thermal Hall conductivity is of the form

$$\kappa_{xy} = -T \sum_{n=1}^2 \int_{\text{BZ}} dk_x dk_y F\left(\frac{\omega_n(\mathbf{k})}{T}\right) \Omega_n(\mathbf{k}), \quad (2.71)$$

where $F(\varepsilon)$ is an intricate weight function which we do not further detail here [139, 140]. However, since this function is not constant, we infer that this weighted integral of the Berry curvature is not ensured to exact discrete values $2\pi\nu_n$. As a result, κ_{xy} is not quantized in terms of universal values but dependent on details such as the energy scales J , K and Γ . This is an important difference to the electronic quantum Hall effect. Nonetheless, κ_{xy} is generally finite and has, as one can show, a sign structure with respect to the field direction which is similar to the thermal Hall effect of the putative QSL phase [47, 246]. The observation of a robust quantization is, therefore, a crucial requirement for the unambiguous confirmation of QSL state [206].

In the context of my Publications **P3** and **P4**, it is important to clarify the implications of band topology on the effect of defects and impurities. By including disorder in our linear spin-wave theory, one finds that vacancies in the lattice trap magnon bound states at energies between the bands ω_1 and ω_2 , if the system is topologically nontrivial [144], see also my Publication **P3**. To comprehend this on a qualitative level, one can think of vacancies as boundaries of atomic size and of the trapped bound states as precursors of the topological edge states. However, these topological bound states are not particularly relevant to the local experimental probe studied in my Publication **P3**, since they exist at energies above excitation gap $\omega_1(\mathbf{0}) \sim h/S$ of the magnonic continuum while our Proposal **P3** is concerned with the low-energy excitations below the continuum gap of the QSL phase. Instead, we find that in the latter regime, topologically trivial magnon bound states can emerge in the presence of *magnetic impurities*. As detailed in my Publications **P3** and **P4**, these low-energy excitations are associated with a *spin flip transition* and have a characteristic dependency on the field strength. Using the experimental set-up, which we motivate in the following and detail in my publications, it should thus be possible to identify magnetic impurities and distinguish Majorana zero modes in the QSL phase from magnonic low-energy excitations of the partially polarized phase.

2.4 Electrical probes for magnetic insulators

Due to the inconclusive experimental status of the quantum spin liquid (QSL) phase in three dimensional (3D) samples of Kitaev materials, recent focus shifted to the genuine two dimensional (2D) limit. Monolayer films of the Kitaev material RuCl_3 can be fabricated on graphite using exfoliation [55, 254, 255] or pulsed laser deposition [121]. *Ab initio* calculations indicate that Coulomb screening in such heterostructures enhances the Kitaev interaction by more than 50% with respect to the bulk samples [26]. The improved proximity to the QSL phase was

confirmed by Raman scattering experiments [55] and similar considerations also apply to the original Kitaev material candidate Na_2IrO_3 [234, 222]. These results initiated an on-going first-principle based exploration of the rich interplay of Kitaev materials and potential substrates [252, 248] and the fabrication of the resulting heterostructures is pursued by multiple experimental groups at the time of writing. Notably, the fabrication of 2D films on substrates enables new experimental techniques and, in particular, local electric probes. This is the subject of my Publications P2 and P3. To set the stage, let us motivate the appearance of electric signatures in magnetic insulators by using a minimal model for Mott insulators - the single-orbital Hubbard model (2.36).

2.4.1 Electric polarization of Mott insulators

The mechanism underpinning my Publication P2 is based on works by Khomskii and collaborators [32, 108], which rationalized the appearance of circular currents and electric polarization in Mott insulators with inhomogeneous spin texture. Roughly speaking, these effects arise due to virtual hopping processes within a charge state and, therefore, manifest on the level of the effective description in terms of local spins.

For a formal description, we revert to the single-orbital Hubbard model (2.36) at half filling and in the limit of strong Coulomb repulsion $U \gg |t_{jk}|$. As outlined in Section 2.2, the effective low-energy Hamiltonian (2.43) can then be obtained by means of a canonical transformation (2.37) and a subsequent projection on the low-energy subspace using the projector \mathcal{P}_{low} in Eq. (2.41). Based on Eq. (2.44), the same transformation scheme can be applied to any observable of interest. In the case of the electric polarization, this observable is the local charge imbalance [32, 169]

$$\delta n_j = \sum_{\sigma} \psi_{j\sigma}^{\dagger} \psi_{j\sigma} - 1, \quad (2.72)$$

which measures the deviation from a single occupancy on site j . The effective description (2.43) at energies below the charge gap stems from processes, which do not change the number of occupancies. Since the Hubbard model in Eq. (2.36) implicitly assumed bond parity $t_{jk} = t_{kj}$, virtual second-order process involving hopping of an electron to a neighboring site and back to its original position cannot contribute to the effective charge imbalance at low energies. Instead, the lowest-order contribution is of third order and involves hopping along a triangle. Notably, on a honeycomb lattice, such processes involves next-nearest-neighbor hopping. Formally, these considerations manifest in the fact that the first and second order of the canonical transformation of δn_j within the low-energy subspace vanish identically. One then finds the effective charge imbalance operator [32, 108]

$$\delta \bar{n}_j = \mathcal{P}_{\text{low}} e^{-\Omega} \delta n_j e^{\Omega} \mathcal{P}_{\text{low}} \simeq 8 \sum_{(kl) \in \Delta_j} \frac{t_{jk} t_{kl} t_{lj}}{U^3} (\mathbf{S}_j \cdot \mathbf{S}_k + \mathbf{S}_j \cdot \mathbf{S}_l - 2\mathbf{S}_k \cdot \mathbf{S}_l), \quad (2.73)$$

where the summation runs over the set Δ_j of all possible triangles containing site j and coupled sites. Moreover, we introduced the spin operators (2.42). Notably, while overall charge neutrality is ensured by $\sum_j \delta \bar{n}_j = 0$, an inhomogeneous spin structure can give rise to non-zero charge densities $\langle \delta \bar{n}_j \rangle \neq 0$, which encode the static spin correlations of the system [32, 169]. The resulting electrostatic field can be potentially measured using a local probe such as a *scanning tunneling microscopy (STM)* tip.

This is the underlying idea of my Publication P2. There, we adapt the derivation of the effective charge imbalance for the three-orbital Hubbard-Kanamori model (2.49) including subdominant and next-nearest hopping and compute the static spin correlations for the full $JK\Gamma$

model (2.53) within a Majorana mean-field theory. Based on a preceding work of my collaborators [169], we find that \mathbb{Z}_2 vortices in the QSL phase generate a finite charge imbalance and, in turn, can be trapped or even created by a local electric potential. The search for a more thorough characterization of \mathbb{Z}_2 vortices and, in particular, Ising anyons, guides us to the proposal of my Publication P3.

2.4.2 Scanning tunneling spectroscopy of local magnetic moments

While my Publication P2 studies the response of the QSL to an electrostatic potential, my Publication P3 is concerned with the response to tunneling currents. This proposal is based on a technique which enables the detection of single localized magnetic moments on a conducting substrate using an STM tip [64, 62, 11]. While standard *scanning tunneling spectroscopy* probes the density of states in a conducting material, one can access the dynamical spin correlations of a magnetic insulating layer through the resolution of inelastic tunneling processes in the differential conductance.

For a formal description, let us consider the set-up, which involves a Mott insulating layer on a conducting substrate B below an STM tip A . In the most simple scenario, the latter two are described by a spin-degenerate diagonal Hamiltonian

$$H_{AB} = \sum_{\nu, \tau} \varepsilon_{\nu} f_{\nu\tau}^{\dagger} f_{\nu\tau}, \quad (2.74)$$

where ε_{ν} is the single-particle energy and $f_{\nu\tau}$ is the annihilation operator of an electron with spin $\tau \in \{\uparrow, \downarrow\}$ and additional quantum numbers ν . In the case of a metallic tip and substrate, these additional quantum numbers should include a subsystem label as well as the electronic momentum. Anyhow, we may couple these electrons to the fermions in the Mott insulator by means of the tunneling term

$$H_{\text{tun}} = \sum_{j, \nu, \sigma} t_{j\nu} \left(f_{\nu\sigma}^{\dagger} \psi_{j\sigma} + \psi_{j\sigma}^{\dagger} f_{\nu\sigma} \right), \quad (2.75)$$

where we assumed conservation of the spin. In the context of STM, the real tunneling matrix elements $t_{j\nu}$ have an additional dependence on the position of the STM tip [64, 62]. Notably, this term changes the particle number in the Mott insulator and it is, therefore, necessary to work with the general Hubbard model

$$H_{\text{H}} = - \sum_{j, k, \sigma} t_{jk} \psi_{j\sigma}^{\dagger} \psi_{k\sigma} + \frac{U}{2} \sum_j (n_{j\uparrow} + n_{j\downarrow} - 1)^2 \quad (2.76)$$

to energetically penalize deviations from half filling in the limit of strong Coulomb repulsion. Assuming that the tunneling strength is also much smaller than the Coulomb repulsion, i.e., $U \gg |t_{j\nu}|$, we can perform a canonical transformation (2.37) of the total Hamiltonian

$$H_{\text{tot}} = H_{\text{H}} + H_{AB} + H_{\text{tun}}. \quad (2.77)$$

The generator of this expansion has to be chosen such that up to a desired order in $(t_{jk}, t_{j\nu})/U$, all terms that change the number of double occupancies and total particle number are canceled. Within the low-energy subspace spanned by states with half filling, tunneling and hopping does not mix at second order and it is sufficient to consider both processes separately. Due to the

SU(2) symmetry of the total Hamiltonian (2.77), the effective description of the tunneling processes is of the form

$$H_{\text{cot}} = \sum_{j, \nu_1, \nu_2} f_{\nu_1}^\dagger \left(T_{j\nu_1\nu_2}^{\text{el}} + T_{j\nu_1\nu_2}^{\text{in}} \boldsymbol{\tau} \cdot \mathbf{S}_j \right) f_{\nu_2} + \text{H.c.}, \quad (2.78)$$

where $f_\nu^\dagger = (f_{\nu\uparrow}^\dagger, f_{\nu\downarrow}^\dagger)$ is a spinor, $\boldsymbol{\tau}$ comprises Pauli matrices which act on the resulting spin space of the tunneling electrons and the coefficients $T_{j\nu_1\nu_2}^{\text{el}}$ and $T_{j\nu_1\nu_2}^{\text{in}}$ are of order $(t_{j\nu}/U)^2$. This term describes *cotunneling* between the tip and the substrate through the magnetic layer [64, 62, 11]. While the first term in the brackets corresponds to elastic processes, we find that the second term couples to the local moment \mathbf{S}_j in the magnetic layer. When neglecting effects on the metallic system H_{AB} , these moments are still described by the low-energy Hamiltonian (2.43). Given the cotunneling term H_{cot} , one might use then Fermi's golden rule to compute the current from the tip to the substrate at a given bias voltage [64, 62]. As we derive in my Publication P3, the inelastic contribution to the resulting differential conductance encodes the dynamical spin correlations in the frequency domain [64, 62, 59]

$$C_{jk}^{\alpha\beta}(\omega) = \int dt e^{i\omega t} \langle S_j^\alpha(t) S_k^\beta(0) \rangle, \quad (2.79)$$

which reveals important information of the excitation spectrum of the magnetic system.

This is the experimental technique studied in my Publications P3 and P4. In the former, we adapt the outlined derivation of the cotunneling term (2.78) to the three-orbital Hubbard-Kanamori model (2.49) and revert to the exactly solvable Kitaev model (2.1) to compute the dynamical spin correlations $C_{jk}^{\alpha\beta}(\omega)$ [113, 119]. Focusing on a dilute gas of isolated \mathbb{Z}_2 vortices [166], we then identify a characteristic conductance profile of Majorana zero modes. In my Publication P4, we compare this prediction to the magnon bound states trapped by magnetic impurities in the partially polarized phase. There, we compute the dynamical spin correlations $C_{jk}^{\alpha\beta}(\omega)$ within linear spin-wave theory and discuss how to characterize magnetic impurities by varying the strength of the external magnetic field. By combining these results, we are confident that scanning tunneling spectroscopy enables the unambiguous detection of the long-sought quantum spin liquid phase in Kitaev materials.

Chapter 3

Scientific publications

This chapter reproduces articles that I co-authored, and which have been published in peer-reviewed scientific journals. Each article is prefaced with a statement detailing the authors' contributions and a copyright notice. References cited within the articles are listed in their respective sections.

P1 Quantum description of Fermi arcs in Weyl semimetals in a magnetic field

The following text is reproduced from the publication

T. Bauer, F. Buccheri, A. D. Martino, and R. Egger
Quantum description of Fermi arcs in Weyl semimetals in a magnetic field
Physical Review Research, vol. 6, no. 4, p. 043201 (2024).

Digital Object Identifier (DOI): [10.1103/PhysRevResearch.6.043201](https://doi.org/10.1103/PhysRevResearch.6.043201)

Statement of contribution

The idea for this work was developed during multiple discussions among all authors. I performed all initial analytical calculations except for the derivation of the Goos-Hänchen shift, which FB carried out. FB also refined the semiclassical estimations using a more accurate expansion of the Fermi arc dispersion. I conducted all numerical computations and prepared all figures. Throughout the project, I received continuous advice from FB, ADM, and RE. I drafted the initial version of the manuscript, which all authors subsequently finalized. FB and RE supervised the project.

Copyright and license notice

The American Physical Society published this article under the terms of the [Creative Commons Attribution 4.0 International](https://creativecommons.org/licenses/by/4.0/) license. Distribution of this work is permitted, provided that attribution to the authors, the article's title, journal citation, and DOI are maintained. The authors retain copyright.

Quantum description of Fermi arcs in Weyl semimetals in a magnetic field

Tim Bauer¹, Francesco Buccheri^{2,3}, Alessandro De Martino⁴, and Reinhold Egger¹¹*Institut für Theoretische Physik, Heinrich-Heine-Universität, D-40225 Düsseldorf, Germany*²*Dipartimento Scienza Applicata e Tecnologia, Politecnico di Torino, Corso Duca degli Abruzzi 24, 10129 Torino, Italy*³*Istituto Nazionale di Fisica Nucleare, Sezione di Torino, Via Pietro Giuria 1, 10125 Torino, Italy*⁴*Department of Mathematics, City Saint George's, University of London, Northampton Square, EC1V 0HB London, England, United Kingdom*

(Received 24 July 2024; accepted 8 November 2024; published 25 November 2024)

For a Weyl semimetal (WSM) in a magnetic field, a semiclassical description of the Fermi-arc surface state dynamics is usually employed for explaining various unconventional magnetotransport phenomena, e.g., Weyl orbits, the three-dimensional quantum Hall effect, and the high transmission through twisted WSM interfaces. For a half-space geometry, we determine the low-energy quantum eigenstates for a four-band model of a WSM in a magnetic field perpendicular to the surface. The eigenstates correspond to in- and out-going chiral Landau level (LL) states, propagating (anti)parallel to the field direction near different Weyl nodes, which are coupled by evanescent surface-state contributions generated by all other LLs. These replace the Fermi arc in a magnetic field. Computing the phase shift accumulated between in- and out-going chiral LL states, we compare our quantum-mechanical results to semiclassical predictions. We find quantitative agreement between both approaches.

DOI: [10.1103/PhysRevResearch.6.043201](https://doi.org/10.1103/PhysRevResearch.6.043201)

I. INTRODUCTION

Two hallmark features of topological electronic systems are their anomalous magnetotransport properties and the existence of robust boundary states. In the rich material class of Weyl semimetals (WSMs) [1–4], these distinct features manifest themselves in the chiral anomaly and in Fermi-arc surface states, respectively. WSMs are three-dimensional (3D) semimetals characterized by touching points of nondegenerate bands near the Fermi energy which are separated in the Brillouin zone. These so-called Weyl nodes are effectively described by massless relativistic Weyl fermions with conserved chirality. In the presence of electromagnetic fields, Weyl fermions exhibit the chiral anomaly which, on the level of the electronic band structure, implies the formation of a chiral zeroth Landau level (LL). This chiral LL state has a gapless linear dispersion along a direction determined by the chirality which is parallel or antiparallel to the magnetic field [5–8]. On the other hand, Weyl nodes act as sources or sinks of Berry curvature and give rise to nontrivial band topology [3,9]. Correspondingly, topological surface states emerge near the boundary of a WSM. Since the Nielsen-Ninomiya theorem requires Weyl nodes to come in pairs of opposite chirality [10], the energy contour of these surface states must terminate at the projection of the bulk cones of two Weyl nodes on the surface Brillouin zone and form an open disjoint curve—the Fermi arc.

Given the experimental observation of signatures for both the chiral anomaly and Fermi arcs [11–14], it is natural to ask how both phenomena conspire near the boundary of a semi-infinite WSM in a homogeneous magnetic field oriented perpendicular to the surface. In a semiclassical picture, the presence of the Lorentz force implies that fermions slide along the Fermi arc connecting two Weyl node projections. Due to the open nature of the Fermi-arc energy contour, no closed cyclotron orbit can form on the surface. Accordingly, fermions have to tunnel into the bulk upon reaching the chiral termination point of the Fermi arc [15] (see Fig. 1 for a schematic illustration in a half-space geometry). Since the only available bulk states at low energies are provided by the chiral LL states, semiclassics predicts that fermions will then move through the bulk and thereby escape from the surface. Consequently, Fermi-arc states acquire a finite lifetime in a perpendicular magnetic field B , and thus ultimately become unstable. Indeed, as we show in detail for the model studied below, for $B \neq 0$, no stable surface states exist anymore. The true eigenstates for $B \neq 0$ have a component representing the zeroth-order chiral Landau levels in the bulk of the system. For $B \neq 0$, Fermi-arc electrons thus escape from the surface into the bulk via chiral Landau states, and therefore acquire a finite lifetime.

Furthermore, in a WSM slab geometry (or in similar confined nanostructures), fermions in a chiral LL state move through the bulk and eventually tunnel into the opposite surface. There, they will traverse the corresponding opposite Fermi arc (in the semiclassical picture). In the simplest scenario, the fermion subsequently occupies the chiral LL state with opposite chirality and travels back to the initial Fermi arc state. This closed trajectory resembles an exotic cyclotron orbit, commonly referred to as “Weyl orbit.” Such orbits are

Published by the American Physical Society under the terms of the Creative Commons Attribution 4.0 International license. Further distribution of this work must maintain attribution to the author(s) and the published article's title, journal citation, and DOI.

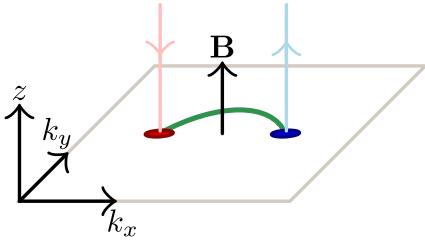


FIG. 1. Schematic sketch of the half-space WSM geometry (defined by $z \geq 0$) in a homogeneous magnetic field $\mathbf{B} = B\hat{\mathbf{e}}_z$ perpendicular to the surface. The 3D WSM has two bulk Weyl nodes at momenta $\mathbf{k} = (\pm k_0, 0, 0)^T$, corresponding to the red and blue circles for their surface projections. For $B = 0$, the surface projections are connected by a Fermi-arc surface state (green curve). For $B \neq 0$, the low-energy bulk physics is dominated by the $n = 0$ chiral LLs which have opposite chirality near different Weyl nodes (pink and light blue arrows show the respective propagation direction). Fermions incoming from a bulk chiral LL enter the arc at the surface. After sliding along the arc to the opposite Weyl node surface projection (in a semiclassical picture), they tunnel into the outgoing chiral LL [15].

predicted to cause unconventional quantum oscillations in the magnetoconductivity, with a strong dependence on the sample thickness [15,16]. The initial prediction of Weyl orbits sparked excitement in the WSM community and led to a variety of subsequent theoretical proposals [17], including nonlocal transport experiments [18–20], the detection of chiral separation [21], and the chiral magnetic effect [22]. Weyl orbits are also important ingredients for an unconventional so-called 3D quantum Hall effect (QHE) [23,24]. Both Shubnikov–de Haas oscillations due to Weyl orbits and the 3D QHE were thoroughly investigated in transport experiments for the Dirac semimetal (DSM) Cd_3As_2 [25–31] (see also the review [17]).

In a DSM, Weyl nodes of opposite chirality share the same position in momentum space but are stabilized by space group symmetries of the crystal [3]. While the band structure is topologically trivial, pairs of Dirac cones can be connected by Fermi-arc surface states nevertheless. The semiclassical argument for the surface-bulk hybridization of Weyl orbits can be adapted to DSMs despite the formally closed energy contour of surface states [15]. While clear experimental evidence for the predicted signatures has been collected for Cd_3As_2 [25–30], their interpretation in terms of Weyl orbits remains debated [17]. In particular, thin films of Cd_3As_2 show an intricate dependence of the QHE on sample thickness [29,32]. Moreover, energy quantization due to Weyl orbits is difficult to distinguish from the trivial size quantization of confined bulk states [33]. Similar arguments might also apply to the Weyl orbits reported in the noncentrosymmetric WSMs NbAs [34], TaAs [35], and WTe_2 [36]. So far, no Weyl orbits have been observed in magnetic WSMs with broken time-reversal symmetry [17]. However, recent experimental work on magnetic WSMs [37] and progress in quasiparticle interference experiments [38] render near-future advances in Weyl-orbit physics for this class of materials likely. These developments also motivated us to perform the study reported in the present paper.

A related exciting topic concerns twisted WSM interfaces [39–42] and tunnel junctions [43]. Upon twisting interfaces with respect to each other, theory predicts a Fermi-arc reconstruction, implying the existence of “homochiral” Fermi arcs connecting Weyl nodes of equal chirality [40,41]. In a magnetic field perpendicular to the interface, incoming electrons in a chiral LL may traverse the homochiral Fermi arc and tunnel back into bulk states on the other side of the junction, thereby achieving (almost) perfect transmission. Numerical transport simulations show good agreement with this semiclassical picture [43–45].

Adopting the half-space geometry, we here study the fate of Fermi-arc surface states in WSMs in a magnetic field. We construct a full quantum solution, going beyond semiclassics. To this end, we study a four-band low-energy continuum model for a magnetic WSM. While we find analytical solutions of the eigenproblem for the DSM limit of two degenerate Weyl nodes, we develop a numerical approach (with a controlled cutoff procedure) to obtain the eigenstates for the WSM scenario. We find that the eigenstates with lowest energy are composed of in- and out-going chiral zeroth-order LLs which are coupled by evanescent states localized near the surface. These are generated by all remaining higher-order LLs and cause a phase shift between in- and outgoing chiral LLs. In a slab geometry, this phase shift is experimentally observable through magnetoconductivity oscillations [15]. We compare our numerical results for the phase shift to semiclassical predictions by varying the energy ε and a boundary parameter α encoding the arc curvature in the surface momentum plane. In addition, the energy derivative of the phase shift determines the Fermi-arc lifetime which is finite for $B \neq 0$. We show how the lifetime depends on key parameters such as α , ε , and B , and compare it to the semiclassical traversal time across the Fermi arc.

The remainder of this paper is structured as follows. In Sec. II we discuss the continuum WSM model employed here, derive boundary conditions for the half-space geometry, and present the surface state spectrum at zero magnetic field. We include the magnetic field in Sec. III and construct the eigenstates in the half-space geometry. In addition, we consider the limit of a DSM and obtain analytical solutions in several limiting cases. Subsequently, we derive the corresponding semiclassical predictions in Sec. IV and compare them with our quantum-mechanical results for the phase shift and for the Fermi-arc lifetime. The paper closes with concluding remarks in Sec. V. Details of our calculations can be found in the Appendixes. A derivation of $B = 0$ Fermi-arc surface states is given in Appendix A. Their spin and current structure are discussed in Appendix B. We validate our numerical approach for finite magnetic fields in Appendix C, and discuss the Goos-Hänchen effect for the present setup in Appendix D. Throughout this paper, we use units with Fermi velocity $v_F = 1$ and put $\hbar = 1$.

II. WSM IN HALF SPACE

In this section, we discuss the four-band WSM model employed in our paper. The 3D model (in the absence of a magnetic field) is introduced in Sec. II A. We then discuss the half-space geometry in terms of boundary conditions in

Sec. II B. The Fermi-arc surface states for $B = 0$ are specified in Sec. II C (see also Appendixes A and B for further details).

A. Model

We study a four-band continuum WSM model which in 3D space, with conserved momentum $\mathbf{k} = (k_x, k_y, k_z)^T$, is defined by the Hamiltonian [3]

$$H(\mathbf{k}) = \mathbf{k} \cdot \boldsymbol{\sigma} \tau^z + k_0 \sigma^x \tau^0, \quad (1)$$

where $k_0 \geq 0$ is the only free parameter. This parameter determines the distance between the Weyl nodes in momentum space. In Eq. (1), σ^μ and τ^μ are Pauli matrices acting on effective spin and orbital degrees of freedoms, respectively, where $\mu = 0$ refers to the identity and $\mu = x, y, z$ otherwise. We use $\boldsymbol{\sigma} = (\sigma^x, \sigma^y, \sigma^z)$. While the limit $k_0 = 0$ describes a degenerate Dirac cone centered at $\mathbf{k} = \mathbf{0}$, i.e., a Dirac semimetal, the model exhibits two separated Weyl nodes at momenta $\mathbf{k} = \pm k_0 \hat{\mathbf{e}}_x$ for $k_0 > 0$. Due to the block diagonal structure of H , these Weyl nodes are decoupled. Their conserved chirality χ is associated with the orbital degree of freedom, namely the eigenvalues $\chi = \pm 1$ of τ^z .

We note that adding a mass term $H' = m \sigma^0 \tau^x$ in Eq. (1) couples the Weyl nodes. However, for $m < k_0$, the Weyl nodes are thereby only shifted in momentum space and the low-energy description is not changed in an essential manner [3]. We thus put $m = 0$ throughout this paper. The two Weyl nodes are then fully decoupled *in the bulk*. This key simplification allows us to obtain explicit results in a finite magnetic field. Importantly, in our approach, the boundary conditions will couple both Weyl nodes. Furthermore, while Eq. (1) formally describes a type-I WSM with broken time-reversal symmetry and the minimum number of two Weyl nodes, we expect our arguments to apply to any WSM involving a pair of two isolated type-I Weyl nodes.

Below, we use the standard representation of Pauli matrices. States are written in the eigenbasis of σ^z and τ^z , i.e., $|\chi\rangle_\tau$ for chirality $\chi = \pm 1$ and $|\sigma\rangle_\sigma$ for spin $\sigma \in \{\uparrow, \downarrow\}$, with the spinor representations

$$\begin{aligned} |+\rangle_\tau &= \begin{pmatrix} 1 \\ 0 \end{pmatrix}_\tau, & |-\rangle_\tau &= \begin{pmatrix} 0 \\ 1 \end{pmatrix}_\tau, \\ |\uparrow\rangle_\sigma &= \begin{pmatrix} 1 \\ 0 \end{pmatrix}_\sigma, & |\downarrow\rangle_\sigma &= \begin{pmatrix} 0 \\ 1 \end{pmatrix}_\sigma. \end{aligned} \quad (2)$$

B. Half-space geometry and boundary conditions

We next proceed to the half-space geometry defined by $z \geq 0$, where we have a planar boundary at $z = 0$ as illustrated in Fig. 1. Since the surface projections of the two Weyl nodes are separated, topological Fermi-arc surface states with an open energy contour connecting the projected nodes arise [3]. Before solving for the Fermi arcs, we first derive the general boundary condition from the constraint of Hermiticity of the Hamiltonian. For relativistic continuum models, such an approach typically allows for a few free parameters with physical implications on the surface state dispersion [46–49]. We note that a more realistic modeling of the boundary might include band bending near the surface which can drastically change the dispersion [50,51].

For a derivation that is also valid in the presence of a finite magnetic field, we switch to real space by using the substitution $\mathbf{k} \rightarrow -i\nabla_{\mathbf{r}}$ in Eq. (1). Following standard arguments [46–48], we impose $\langle \Psi_1 | H | \Psi_2 \rangle - \langle H | \Psi_1 | \Psi_2 \rangle = 0$ for arbitrary states Ψ_1 and Ψ_2 in the half-space geometry to infer a *sufficient* boundary condition:

$$\Psi_1^\dagger(\mathbf{r}_\perp, z=0) j^z \Psi_2(\mathbf{r}_\perp, z=0) = 0. \quad (3)$$

Here, $\mathbf{r}_\perp = (x, y)^T$ is the in-plane position and $j^z = \sigma^z \tau^z$ is the z component of the relativistic fermion particle current operator, $\mathbf{j} = \boldsymbol{\sigma} \tau^z$. Physically, Eq. (3) thus prohibits any local current flowing through the surface. This condition is ensured for states that satisfy boundary conditions of the form

$$M \Psi(\mathbf{r}_\perp, z=0) = \Psi(\mathbf{r}_\perp, z=0), \quad (4)$$

where M is an operator with the properties

$$j^z M = -M^\dagger j^z, \quad M^2 = \mathbb{1}, \quad (5)$$

where $\mathbb{1} = \sigma^0 \tau^0$ is the identity. In Eq. (4), we assumed a local boundary condition where the matrix M does not depend on the in-plane position \mathbf{r}_\perp . To parametrize all possible choices of M , we define the operators

$$M_\gamma^\tau = \tau^x \cos \gamma + \tau^y \sin \gamma, \quad M_\delta^\sigma = \sigma^x \cos \delta + \sigma^y \sin \delta, \quad (6)$$

in orbital and spin space, respectively. The most general Hermitian parametrization then involves four real parameters $(\alpha, \beta, \gamma, \delta)$ [52]:

$$\begin{aligned} M_{\alpha\beta\gamma\delta} &= \cos \alpha (\sigma^z M_\gamma^\tau \cos \beta + \sigma^0 M_{\gamma-\pi/2}^\tau \sin \beta) \\ &+ \sin \alpha (\tau^0 M_\delta^\sigma \cos \beta + \tau^z M_{\delta-\pi/2}^\sigma \sin \beta). \end{aligned} \quad (7)$$

An equivalent parametrization was found in Refs. [53,54] in the context of graphene monolayers. On general grounds, the number of free parameters in the boundary condition increases with the number of higher-energy bands in the model Hamiltonian [55,56]. Consequently, the low-energy spectrum is not expected to change significantly when varying parameters within certain submanifolds of the full parameter space. Below, we do not exploit the complete parameter freedom in Eq. (7) but instead focus on a simple one-parameter boundary matrix M allowing us to describe curved Fermi arcs.

C. Boundary spectrum at zero magnetic field

Given the boundary condition (4) with the general parametrization (7), we next construct physical Fermi arc solutions for $B = 0$, which are labeled by the conserved in-plane momentum $\mathbf{k}_\perp = (k_x, k_y)^T$. The simplest approach is to choose a block diagonal matrix M , e.g., the parametrization $M_{\frac{\pi}{2}, 0, 0, \delta}$ in Eq. (7), which allows one to solve the problem for both Weyl nodes separately. The Fermi arc of a single Weyl node, which after a shift of k_x is effectively described by $H_\chi = \chi \mathbf{k} \cdot \boldsymbol{\sigma}$, then becomes a semi-infinite line which terminates at the Weyl cone projection at an angle determined by the parameter δ [46–48]. The resulting surface-state spectrum of the four-band WSM model thus yields two semi-infinite arcs, in contrast to physical Fermi arcs which are open curves connecting both Weyl cone projections. Here, we will use boundary conditions which couple different Weyl nodes. This approach is especially convenient for $B \neq 0$.

To this end, we consider off-diagonal boundary matrices M satisfying $[M, \sigma^0 \tau^z] \neq 0$. The resulting boundary conditions couple the Weyl nodes *at the surface* [52]. This picture is analogous to the one in Ref. [54], where armchair edges in graphene monolayers are modeled by boundary conditions that are nondiagonal in the valley degree of freedom. Below, we assume the boundary condition (4) with

$$M_\alpha = M_{\alpha,0,0,0} = \sigma^z \tau^x \cos \alpha + \sigma^x \tau^0 \sin \alpha. \quad (8)$$

The parametrization (8) is a simple choice that allows us to construct physical Fermi arcs with a curvature in the surface momentum plane controlled by the single parameter α . A curved arc is then symmetric under midpoint reflection, and a straight arc is found for $\alpha = 0 \pmod{\pi}$. As discussed in Appendix A, the particular choice of M_α in Eq. (8) is motivated by the observation that a straight arc requires $[M, j^y] = 0$, where $j^y = \sigma^y \tau^z$ is the in-plane current operator along $\hat{\mathbf{e}}_y$. For a microscopic analysis of a specific material, one may instead employ boundary matrices M containing more parameters (while still coupling both Weyl nodes), possibly guided by numerical calculations for lattice models. For simplicity, however, we focus on the one-parameter family of matrices in Eq. (8). In Appendix A, we derive the corresponding $B = 0$ surface-state spectrum presented next.

We find that a physical Fermi-arc contour at energy ε is given by $k_y = q_\alpha(\varepsilon, k_x)$, where

$$q_\alpha(\varepsilon, k_x) = \frac{(\varepsilon \sin \alpha - k_0)(\varepsilon - k_0 \sin \alpha) - k_x^2 \sin \alpha}{\cos \alpha \sqrt{(\varepsilon \sin \alpha - k_0)^2 - k_x^2 \sin^2 \alpha}}. \quad (9)$$

At zero energy, the contour terminates at both Weyl node surface projections ($k_x = \pm k_0$, $k_y = 0$). The termination points $k_x = \pm k_{\varepsilon\alpha}$ for $\varepsilon \neq 0$ are implicitly given by

$$\varepsilon^2 = (|k_x| - k_0)^2 + [q_\alpha(\varepsilon, k_x)]^2. \quad (10)$$

Assuming $|\varepsilon| \ll k_0$ and expanding Eq. (9) to lowest order in ε/k_0 , we estimate

$$k_{\varepsilon\alpha} = k_0 - \frac{4\varepsilon \sin \alpha}{3 - \cos(2\alpha)}. \quad (11)$$

Moreover, we find the low-energy dispersion relation

$$\begin{aligned} \varepsilon(\mathbf{k}_\perp) &\simeq \frac{k_0^2 - k_x^2 \sin^2 \alpha}{k_0^2 - k_x^2 \sin^4 \alpha} \\ &\times \left(\frac{k_0^2 - k_x^2}{k_0} \sin \alpha - \sqrt{k_0^2 - k_x^2 \sin^2 \alpha} \frac{k_y}{k_0} \cos \alpha \right). \end{aligned} \quad (12)$$

For $\alpha = 0$, the above expressions are exact and describe a straight arc with $\varepsilon(\mathbf{k}_\perp) = -k_y$. For $\alpha \neq 0$, the arc is curved in the surface momentum plane as illustrated in Fig. 2(a). We note that the Fermi arc for $\alpha \rightarrow \pi - \alpha$ with the same energy ε follows by reflection with respect to the k_x axis. In effect, this transformation yields the Fermi arc for the same boundary condition but in the opposite half space $z \leq 0$ (see Appendix A). We briefly discuss the in-plane spin and current densities associated with Fermi-arc states in Appendix B.

Next, we turn to the limit $k_0 \rightarrow 0$ describing the low-energy theory of a DSM with a single degenerate cone. While

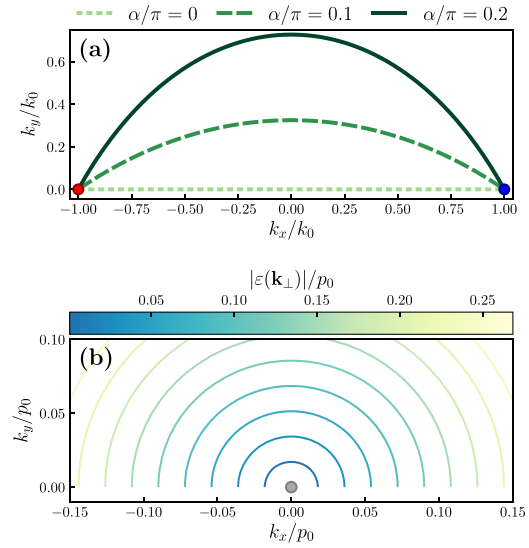


FIG. 2. Surface-state spectrum of the four-band model (1) in a half space for $B = 0$. (a) Zero-energy Fermi-arc contours in the k_x - k_y plane as described by Eq. (9) for different boundary parameters α (see also Fig. 1). (b) Surface-state contour plot in the k_x - k_y plane for a DSM ($k_0 \rightarrow 0$) with $\alpha/\pi = 0.1$ for different energies $\varepsilon(\mathbf{k}_\perp)$ as indicated by the color bar, using a fixed scale p_0 as reference. The surface-state termination points result from the condition in Eq. (14).

the band structure is now topologically trivial, surface states may nonetheless exist. Such states become important for $B \neq 0$ (see Sec. IV). Deferring technical details to Appendix A, we find topologically trivial surface states with the dispersion relation

$$\varepsilon_\pm(\mathbf{k}_\perp) = \pm \sqrt{k_x^2 + k_y^2 \cos^2 \alpha}, \quad (13)$$

which only exist if the condition

$$k_y \sin \alpha > 0 \quad (14)$$

is satisfied. In particular, there are no surface state solutions for either $\alpha = 0 \pmod{\pi}$, corresponding to a straight arc for finite k_0 , or $\varepsilon = 0$. Below, we focus on those two cases for analytical results. For finite α or ε , however, surface states emerge which form open energy contours. These contours shrink with decreasing energy [see Fig. 2(b)].

III. HALF SPACE IN A MAGNETIC FIELD

In this section, we include the magnetic field $\mathbf{B} = B\hat{\mathbf{e}}_z$ with $B > 0$ and study the WSM model in Sec. II for the half-space geometry using the boundary condition (4) defined by the matrix M_α in Eq. (8). The parameter α determines the curvature of the $B = 0$ Fermi arc solutions. In Sec. III A, we briefly review the eigenstates for the infinite 3D problem. In Sec. III B, we then turn to the half-space problem and construct the low-energy quantum-mechanical eigenstates.

A. Landau quantization

We start with the free-space WSM model and we incorporate the homogeneous magnetic field \mathbf{B} by minimal coupling, $\mathbf{k} \rightarrow -i\nabla_{\mathbf{r}} + \frac{e}{c}\mathbf{A}$, where $e > 0$ is the (absolute value of the) electron charge and c is the speed of light. For convenience, we choose the Landau gauge, $\mathbf{A} = -By\hat{\mathbf{e}}_x$, where Eq. (1) gives

$$H = -i\nabla_{\mathbf{r}} \cdot \boldsymbol{\sigma} \tau^z - \frac{y}{\ell_B^2} \sigma^x \tau^z + k_0 \sigma^x \tau^0 = \begin{pmatrix} H_+ & 0 \\ 0 & H_- \end{pmatrix}_{\tau} \quad (15)$$

with the magnetic length $\ell_B = \sqrt{c/eB}$. Note that the chosen gauge retains translation invariance along $\hat{\mathbf{e}}_x$. The momentum component k_x therefore remains a good quantum number. Below, we consider the orbital magnetic field only and neglect the Zeeman effect by following standard arguments [5–8]. Including a Zeeman term, say, of the form $H_Z \propto \sigma^z \tau^0$ shifts the position of the Weyl nodes in the xz plane. While such an effect can be readily taken into account, we assume here for simplicity that its contribution is insignificant compared to the second term in Eq. (1).

When solving for LL solutions, it is convenient to consider the Weyl nodes separately. A single Weyl node with chirality $\chi = \pm 1$ and momentum $\mathbf{k} = -\chi k_0 \hat{\mathbf{e}}_x$ is described by the Hamiltonian H_{χ} in spin space using the block diagonal form in Eq. (15). For given χ and k_x , we define the bosonic ladder operator

$$a_{\chi}^{\dagger} = \frac{\ell_B}{\sqrt{2}} \left(\frac{y}{\ell_B^2} - k_x - \chi k_0 - \partial_y \right), \quad (16)$$

with the commutator $[a_{\chi}, a_{\chi}^{\dagger}] = 1$. The transverse part of $H_{\chi} = -i\chi \partial_z \sigma^z + H_{\chi}^{\perp}$ is thereby written as

$$H_{\chi}^{\perp} = -\frac{\chi}{\sqrt{2}\ell_B} [(a_{\chi} + a_{\chi}^{\dagger})\sigma^x + i(a_{\chi} - a_{\chi}^{\dagger})\sigma^y]. \quad (17)$$

In the infinite 3D system (without boundary), the momentum component k_z is also conserved. It is then straightforward to obtain the well-known relativistic LLs $\varepsilon_{n,k_z}^{\chi}$ labeled by non-negative integer $n \in \mathbb{N}_0$ [3]:

$$\varepsilon_{0,k_z}^{\chi} = -\chi k_z, \quad \varepsilon_{\pm,n>0,k_z}^{\chi} = \pm \chi \sqrt{\frac{2n}{\ell_B^2} + k_z^2}. \quad (18)$$

Here, $\varepsilon_{0,k_z}^{\chi}$ is the dispersion of the gapless chiral LL, while $n > 0$ correspond to higher-order gapped LL states. Eigenstates are expressed in terms of harmonic oscillator eigenfunctions:

$$\varphi_n(y) = \frac{H_n(y/\ell_B)}{\sqrt{2^n n! \sqrt{\pi} \ell_B}} e^{-\frac{1}{2}(y/\ell_B)^2}, \quad (19)$$

where H_n is the n th-order Hermite polynomial. Writing $a_{\chi}^{\dagger} a_{\chi} \varphi_n^{\chi} = n \varphi_n^{\chi}$, the wave functions

$$\varphi_n^{\chi}(y) = \varphi_n(y - \ell_B^2 k_x - \chi \ell_B^2 k_0) \quad (20)$$

incorporate a shift with respect to the Weyl node position. In anticipation of the half-space geometry, we label the solutions $|\psi_{n\varepsilon}^{\chi}\rangle$ of $H_{\chi}|\psi_{n\varepsilon}^{\chi}\rangle = \varepsilon|\psi_{n\varepsilon}^{\chi}\rangle$ in terms of energy ε instead of k_z . The chiral LL with $n = 0$ is then described by

$$\psi_{0,\varepsilon}^{\chi}(y, z) = \frac{e^{-i\chi \varepsilon z}}{\sqrt{2\pi}} \begin{pmatrix} 0 \\ \varphi_0^{\chi}(y) \end{pmatrix}_{\sigma}. \quad (21)$$

Since k_x is conserved, we keep plane-wave factors $e^{ik_x x}$ and the k_x dependence of observables implicit below. Similar expressions as Eq. (21) hold for the wave functions of $n > 0$ bulk LLs [5].

In the following, we focus on the *ultraquantum regime*, $|\varepsilon| < \sqrt{2}/\ell_B$. While $n > 0$ bulk LLs do not exist in this regime, it is possible to construct *evanescent* solutions in the half-space geometry by solving the eigenproblem for imaginary momentum $k_z = i\kappa$ with $\kappa = \kappa_{n\varepsilon} > 0$. The evanescent solution for $n > 0$ is given by

$$\psi_{n\varepsilon}^{\chi}(y, z) = \sqrt{\kappa_{n\varepsilon}} e^{-\kappa_{n\varepsilon} z} \begin{pmatrix} \chi e^{i\chi \gamma_{n\varepsilon}} \varphi_{n-1}^{\chi}(y) \\ \varphi_n^{\chi}(y) \end{pmatrix}_{\sigma}, \quad (22)$$

with the inverse penetration length

$$\kappa_{n\varepsilon} = \sqrt{2n/\ell_B^2 - \varepsilon^2} \quad (23)$$

and the phase $\gamma_{n\varepsilon}$ defined by

$$e^{i\gamma_{n\varepsilon}} = -\frac{\ell_B}{\sqrt{2n}} (\varepsilon + i\kappa_{n\varepsilon}). \quad (24)$$

One can rationalize the appearance of this complex phase factor by noticing that evanescent solutions do not carry any current along $\hat{\mathbf{e}}_z$, i.e., $\langle \psi_{n\varepsilon}^{\chi} | \sigma^z | \psi_{n\varepsilon}^{\chi} \rangle = 0$ for $n > 0$.

B. Half-space geometry

1. Coupling of Weyl nodes at the boundary

We now proceed to the half-space geometry $z \geq 0$ sketched in Fig. 1 (see Sec. II for the $B = 0$ case). We first rewrite the boundary condition (4) with the matrix M_{α} in Eq. (8) as

$$\mathbb{V}_{\alpha}(z)\Psi(\mathbf{r}) = 0, \quad \mathbb{V}_{\alpha}(z) = \delta(z)(\mathbb{1} - M_{\alpha}). \quad (25)$$

Our ansatz for solving Eq. (25) is a superposition of all eigenstates of H in Eq. (15) with given ε and k_x . We focus on the ultraquantum regime $|\varepsilon| < \sqrt{2}/\ell_B$, where $n > 0$ LL states only contribute through evanescent-state solutions in Eq. (22). Combining the results of Eqs. (21) and (22) gives

$$|\Psi_{\varepsilon}\rangle = \sum_{\chi=\pm} \sum_{n \geq 0} c_{n\varepsilon}^{\chi} |\psi_{n\varepsilon}^{\chi}\rangle_{\sigma} |\chi\rangle_{\tau}, \quad (26)$$

where the $c_{n\varepsilon}^{\chi}$ are complex coefficients which have to be determined. Equation (25) states that $|\Psi_{\varepsilon}\rangle$ is an element of the kernel of \mathbb{V}_{α} . Matrix elements of this operator, restricted to the subspace with fixed energy ε , are of the form

$$[V_{\alpha}(\varepsilon)]_{n,n'}^{\chi,\chi'} = {}_{\tau} \langle \chi | {}_{\sigma} \langle \psi_{n\varepsilon}^{\chi} | \mathbb{V}_{\alpha}(z) | \psi_{n'\varepsilon}^{\chi'} \rangle_{\sigma} | \chi' \rangle_{\tau}. \quad (27)$$

For convenience, we rescale them as

$$[\hat{V}_{\alpha}(\varepsilon)]_{n,n'}^{\chi,\chi'} = (\kappa_{n\varepsilon} \kappa_{n'\varepsilon})^{-\frac{1}{2}} [V_{\alpha}(\varepsilon)]_{n,n'}^{\chi,\chi'} \quad (28)$$

with $\kappa_{0,\varepsilon} = 1/2\pi$. Matrix elements between a chiral $n = 0$ LL and $n \geq 0$ LLs with equal chirality χ are given by

$$[\hat{V}_{\alpha}(\varepsilon)]_{0,n}^{\chi,\chi} = \delta_{n,0} - \chi e^{i\chi \gamma_{n\varepsilon}} \delta_{n,1} \sin \alpha, \quad (29)$$

while for $n, n' > 0$, we find

$$[\hat{V}_{\alpha}(\varepsilon)]_{n,n'}^{\chi,\chi} = 2\delta_{n,n'} - \chi e^{i\chi \gamma_{n+1,\varepsilon}} \delta_{n,n'-1} \sin \alpha - \chi e^{-i\chi \gamma_{n\varepsilon}} \delta_{n,n'+1} \sin \alpha. \quad (30)$$

Matrix elements for opposite chiralities resemble the coupling of Weyl nodes in terms of the boundary condition. For $n \geq 0$, we obtain

$$[\hat{V}_\alpha(\varepsilon)]_{0,n}^{\chi,-\chi} = \langle \varphi_0^\chi | \varphi_n^{-\chi} \rangle \cos \alpha. \quad (31)$$

Finally, for $n, n' > 0$, we find

$$[\hat{V}_\alpha(\varepsilon)]_{nn'}^{\chi,-\chi} = \cos \alpha \left(e^{-i\chi(\gamma_{nn} + \gamma_{n'n})} \langle \varphi_{n-1}^\chi | \varphi_{n'-1}^{-\chi} \rangle + \langle \varphi_n^\chi | \varphi_{n'}^{-\chi} \rangle \right). \quad (32)$$

The overlap $\langle \varphi_n^\chi | \varphi_m^{-\chi} \rangle$ involves shifted harmonic oscillator eigenfunctions associated with different Weyl nodes. Performing the integration for $n \geq m$ yields [57]

$$\begin{aligned} \langle \varphi_n^- | \varphi_m^+ \rangle &= \int dy \varphi_n(y - l_B^2 k_0) \varphi_m(y + l_B^2 k_0) \\ &= \sqrt{2^{n-m} \frac{m!}{n!}} \lambda_B^{n-m} L_m^{n-m}(2\lambda_B^2) e^{-\lambda_B^2}, \end{aligned} \quad (33)$$

with the dimensionless quantity

$$\lambda_B = k_0 \ell_B, \quad (34)$$

which measures the decoupling of the Weyl nodes by the magnetic field. In Eq. (33), L_n^m is a generalized n th-order Laguerre polynomial. In Appendix C, we describe a recursion relation allowing for the numerically efficient computation of the overlaps in Eq. (33). The remaining terms follow from the relation $\langle \varphi_n^+ | \varphi_m^- \rangle = (-1)^{n-m} \langle \varphi_n^- | \varphi_m^+ \rangle$. We note that the overlaps allow for a perturbative treatment in the large-field limit $\lambda_B \ll 1$. Let us also mention in passing that similar expressions appear when computing matrix elements of the bulk mass term $m\sigma^0 \tau^x$. In that case, the coupling opens a gap in the dispersion of the chiral LLs of the order of $\langle \varphi_0^+ | \varphi_0^- \rangle = e^{-\lambda_B^2}$. This result is consistent with the WKB approximation for a two-band WSM model with two Weyl nodes [58,59].

In any case, convergence of the overlaps $\lim_{n \rightarrow \infty} \langle \varphi_n^+ | \varphi_m^- \rangle = 0$ is ensured for arbitrary λ_B . This fact justifies the introduction of a cutoff N for the LL index, $n < N$, reducing the numerical solution of the boundary problem to a linear algebra problem:

$$V_\alpha(\varepsilon) \mathbf{c}_\varepsilon = \mathbf{0}, \quad (35)$$

where $V_\alpha(\varepsilon)$ is a $2N \times 2N$ matrix formed by the matrix elements (27) of the lowest N LLs and \mathbf{c}_ε is a vector containing the corresponding coefficients $c_{n\varepsilon}^\chi$. The numerical solution of Eq. (35) then determines the eigenstates of the WSM in the half-space geometry for $B \neq 0$. In Appendix C, we carefully verify the controlled nature of the above cutoff procedure and the accuracy of the boundary condition.

Due to current conservation, coefficients with the same (n, ε, k_x) but different chiralities have the same absolute value, $|c_{n\varepsilon}^+| = |c_{n\varepsilon}^-|$. In particular, we are interested in the phase shift $\theta_\alpha(\varepsilon)$ between in- and out-going chiral $n = 0$ Landau states:

$$c_{0,\varepsilon}^- = e^{i\theta_\alpha(\varepsilon)} c_{0,\varepsilon}^+. \quad (36)$$

We note that all phases below are defined only modulo 2π . The phase shift $\theta_\alpha(\varepsilon)$ depends on the global phase choices for the basis states in Eq. (26). While for a fixed phase choice, $\theta_\alpha(\varepsilon)$ is formally gauge invariant, observable quantities must also be independent of the phase choice. Full gauge invariance

is ensured below by only considering phase-shift differences, $\Phi = \theta_{\alpha'}(\varepsilon') - \theta_\alpha(\varepsilon)$. When combined with the corresponding phase shift on the opposite surface in a slab geometry, one can infer the magnetoconductivity oscillation period of the corresponding Weyl orbit from Eq. (36) [15]. We compare our quantum-mechanical results for Φ to semiclassical estimates in Sec. IV.

We note that for a straight arc at zero energy, $\alpha = 0 \pmod{2\pi}$ and $\varepsilon = 0$, with the basis choice in Eq. (26), one finds

$$\theta_{\alpha=0}(\varepsilon = 0) = \pi. \quad (37)$$

We verify Eq. (37) by evaluating the boundary condition at $y = \ell_B^2 k_x$, where $\varphi_n^+(\ell_B^2 k_x) = (-1)^n \varphi_n^-(\ell_B^2 k_x)$. By virtue of $|c_{n\varepsilon}^+| = |c_{n\varepsilon}^-|$ and the boundary condition, we then arrive at $c_{n,0}^+ = (-1)^{n+1} c_{n,0}^-$, and thus at Eq. (37).

Since eigenstates in the half-space geometry can be written in the form (26), a nontrivial y dependence arises since the separation between Weyl nodes in momentum space appears in the argument of Eq. (20). As shown in Appendix D, this observation implies that an electron incident on the surface undergoes a shift (assuming $\varepsilon > 0$)

$$\delta y = -2\ell_B^2 k_0 \quad (38)$$

in the y direction. This effect can be interpreted semiclassically in terms of chiral transport associated to Fermi arcs (see Appendix B).

2. Dirac semimetal

In order to identify contributions to the phase shift (36) picked up by fermions traversing the Fermi arc in Sec. IV, let us briefly consider the analogous problem in the DSM limit $k_0 \rightarrow 0$. The corresponding linear system follows from Eq. (35) by inserting diagonal overlaps $\langle \varphi_n^- | \varphi_m^+ \rangle = \delta_{nm}$ in Eqs. (31) and (32). For analytical results, we focus on cases without topologically trivial surface states for $B = 0$, i.e., we consider either $\alpha = 0 \pmod{\pi}$ or $\varepsilon = 0$.

First, for $\alpha = 0 \pmod{2\pi}$, it is straightforward to show that the boundary condition (4) with $M_0 = \sigma^z \tau^x$ is satisfied by antisymmetric superpositions of chiral LLs:

$$|\Psi_\varepsilon\rangle = \frac{1}{\sqrt{2}} (|\psi_{0,\varepsilon}^+\rangle_\sigma |+\rangle_\tau - |\psi_{0,\varepsilon}^-\rangle_\sigma |-\rangle_\tau). \quad (39)$$

With the above basis choice, we then obtain the phase shift $\theta_{\alpha=0}(\varepsilon) = \theta_{\alpha=0}^{\text{DSM}}(\varepsilon) = \pi$ for arbitrary ε . Similarly, one finds $\theta_\pi^{\text{DSM}}(\varepsilon) = 0$.

Second, for $\varepsilon = 0$ but arbitrary α , by using $\gamma_{n,\varepsilon=0} = -\pi/2$, the linear system (35), expressed in terms of the rescaled coefficients $\hat{c}_n^\chi = \sqrt{k_{n,\varepsilon=0}} c_{n,\varepsilon=0}^\chi$, simplifies to

$$\begin{aligned} 0 &= \hat{c}_0^\chi + \cos \alpha \hat{c}_0^{-\chi} + i \sin \alpha \hat{c}_1^\chi, \\ 0 &= 2\hat{c}_n^\chi - i \sin \alpha (\hat{c}_{n+1}^\chi - \hat{c}_{n-1}^\chi). \end{aligned} \quad (40)$$

The physical solution of the recursion relation is (we here assume $\cos \alpha > 0$)

$$\hat{c}_0^+ = -\hat{c}_0^-, \quad \hat{c}_n^\chi = \left(i \tan \frac{\alpha}{2} \right)^n \hat{c}_0^\chi. \quad (41)$$

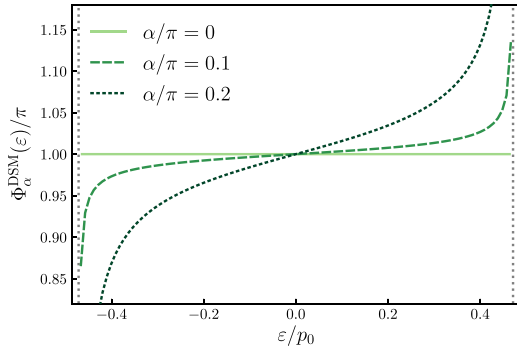


FIG. 3. Gauge invariant phase shift $\Phi_\alpha^{\text{DSM}}(\varepsilon)$ vs energy ε for chiral LLs in a DSM ($k_0 \rightarrow 0$) for several values of α [see Eq. (43)]. The shown results were obtained by a numerical solution of the quantum-mechanical problem. We use $p_0 \ell_B = 3$ with a reference scale p_0 , where ε is shown in units of p_0 (with $v_F = 1$). The ultraquantum regime $|\varepsilon| < \sqrt{2}/\ell_B$ is indicated by vertical dotted lines.

Without need for a cutoff N and up to normalization, we thereby arrive at the exact solution:

$$|\Psi_{\varepsilon=0}\rangle \propto \sum_{\chi=\pm} \chi \sum_{n \geq 0} \frac{1}{\sqrt{\kappa_{n,0}}} \left(i \tan \frac{\alpha}{2} \right)^n |\psi_{n,0}^\chi\rangle_\sigma |\chi\rangle_\tau. \quad (42)$$

Clearly, the phase shift is again given by $\theta_\alpha^{\text{DSM}}(\varepsilon = 0) = \pi$. Remarkably, the superposition state (42) involves evanescent contributions even though no surface state exists for $\varepsilon = 0$ with $B = 0$ and $k_0 = 0$ [see Eqs. (13) and (14)]. An analogous calculation leads to $\theta_{\pi-\alpha}^{\text{DSM}}(0) = 0$.

For finite α and finite ε , we solve the problem numerically as described above. As shown in Fig. 3, we then find a finite gauge invariant phase shift, which we define as

$$\Phi_\alpha^{\text{DSM}}(\varepsilon) = \theta_\alpha^{\text{DSM}}(\varepsilon) - \theta_\pi^{\text{DSM}}(\varepsilon). \quad (43)$$

(The reason for subtracting the phase for $\alpha = \pi$ is explained in Sec. IV.) For small α and ε , this phase shift turns out to be small compared to the corresponding phase shifts in WSMs (see Sec. IV). Since the main focus of this paper is on the WSM case, we leave a detailed (semiclassical) discussion of phase shifts in DSMs to future studies.

IV. RESULTS AND COMPARISON TO SEMICLASSICS

The semiclassical theory for Fermi arcs in WSMs in a magnetic field is well established [15,16]. According to this standard picture, fermions in the chiral LL tunnel into a Fermi-arc state upon reaching the surface. The Lorentz force then drives the fermion along the arc to the other Weyl cone projection of opposite chirality, where it can tunnel back into the bulk and thereby escape from the surface. In a slab geometry, this process is repeated on the opposite surface, and the semiclassical trajectory forms a closed Weyl orbit which can be described using semiclassical quantization [15,16].

In the half-space geometry, the semiclassical trajectory is open and no quantization is expected. This enables us to disentangle bulk and surface contributions. The latter are

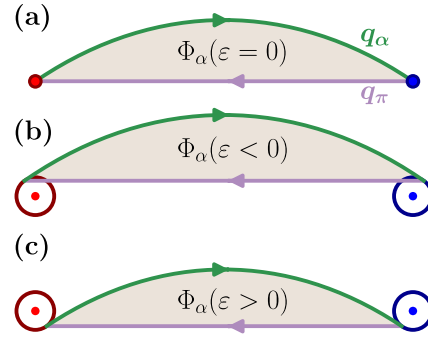


FIG. 4. Schematic illustration of closed trajectories in the surface momentum plane used for the semiclassical calculation of the gauge invariant phase $\Phi_\alpha(\varepsilon)$ in Eq. (47). A curved Fermi arc (green) with $0 < \cos \alpha < 1$ is joined with a straight Fermi arc (purple) for $\alpha = \pi$. Arrows indicate the direction of \mathbf{k} as described by Eq. (44). We show the corresponding closed trajectories (a) for zero energy ($\varepsilon = 0$), (b) for $\varepsilon < 0$, and (c) for $\varepsilon > 0$. For $\varepsilon \neq 0$, the curved arc termination points, $(k_x, k_y) = (\pm k_{\varepsilon\alpha}, q_\alpha(\varepsilon, k_{\varepsilon\alpha}))$, differ from the Weyl node projections $(\pm k_0, 0)$ corresponding to the circle centers in panels (b) and (c). To match the arc termination points of the curved arc and the straight reference arc, we employ a rescaling $k_0 \rightarrow k_{\varepsilon\alpha}$ for the straight arc case. For details, see main text.

determined by the semiclassical equations of motion for an electron moving along the Fermi arc (with $\mathbf{k} = \mathbf{k}_\perp$) [15,60]:

$$\dot{\mathbf{k}} = -\frac{1}{\ell_B^2} \mathbf{v}_\mathbf{k} \times \hat{\mathbf{e}}_z, \quad \dot{\mathbf{r}} = \mathbf{v}_\mathbf{k} = \nabla_{\mathbf{k}} \varepsilon(\mathbf{k}), \quad (44)$$

where $\mathbf{v}_\mathbf{k}$ is the group velocity in the x - y plane and $\varepsilon = \varepsilon(\mathbf{k})$ is the arc dispersion relation. Here, we neglect the anomalous velocity contribution due to the Berry curvature of generic Fermi-arc states [60,61]. This approximation can be justified by noting that the Berry curvature vanishes for a straight arc and we consider the small- α case below. As a consequence, \mathbf{k} is tangential to the energy contour.

A. Phase shifts accumulated along Fermi-arc curves

We first consider the phase shift $\theta_\alpha(\varepsilon)$ between the chiral LLs in Eq. (36) for a curved Fermi arc with $0 < \cos \alpha < 1$. In a semiclassical picture, this phase shift can be estimated by a phase-space integral of the schematic form

$$\theta_\alpha(\varepsilon) = \int d\mathbf{r} \cdot \left(\mathbf{k} - \frac{e}{c} \mathbf{A} \right). \quad (45)$$

For gauge invariant phases, we need closed trajectories in real space. This issue is closely related to the fact that the quantum-mechanical phase shift $\theta_\alpha(\varepsilon)$ discussed in Sec. III B becomes gauge invariant only after switching to a phase-shift difference. For the semiclassical counterpart, we resolve this issue by introducing a straight reference arc which reconnects the termination points of the curved Fermi arc. We thereby obtain a closed trajectory in the surface momentum plane (see Fig. 4), where the phase $\Phi_\alpha(\varepsilon)$ accumulated along the trajectory is gauge invariant. To ensure that also the corresponding

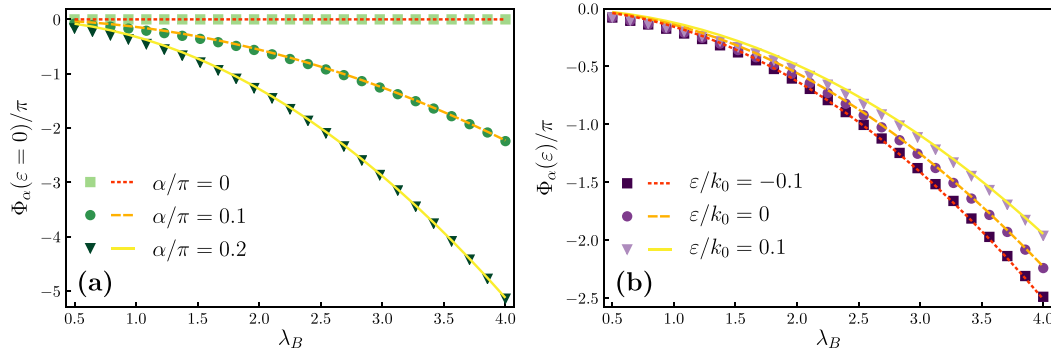


FIG. 5. Comparison of quantum-mechanical results and semiclassical estimates for the gauge invariant Fermi-arc surface-state phase shift $\Phi_\alpha(\varepsilon)$ [see Eqs. (46) and (48), respectively]. The phase $\Phi_\alpha(\varepsilon)$ is shown as a function of the parameter $\lambda_B = k_0 \ell_B$ and gives the phase accumulated along the closed trajectories in surface-momentum space illustrated in Fig. 4. Symbols show the numerical solution of the quantum problem, and curves show the corresponding semiclassical predictions. Integer multiples of 2π have been added to obtain smooth curves. (a) Zero-energy case ($\varepsilon = 0$) for different α . (b) Case $\alpha/\pi = 0.1$ for different energies ε .

real-space trajectory is closed, we recall that the transformation $\alpha \rightarrow \alpha + \pi$ inverts the sign of the group velocity component v_y , and thus of k_x [see Eq. (44)]. In effect, this allows for a closed motion in the surface momentum plane, where the straight reference arc is chosen to have $\alpha = \pi$.

The above procedure is straightforwardly implemented at zero energy ($\varepsilon = 0$), where the arc termination points are at $(k_x, k_y) = (\pm k_0, 0)$ for all values of α [see Fig. 4(a)]. On the quantum level, we then consider the phase-shift difference $\Phi_\alpha(\varepsilon = 0) = \theta_\alpha(0) - \theta_\pi(0)$, where $\theta_\pi(0) = \pi$ [see Eq. (37)].

The situation becomes more intricate for $\varepsilon \neq 0$ since now the curved arc termination points, $(k_x, k_y) = (\pm k_{\varepsilon\alpha}, q_\alpha(\varepsilon, k_{\varepsilon\alpha}))$, differ from the corresponding Weyl node projections at $(\pm k_0, 0)$. [We recall that $k_{\varepsilon\alpha}$ follows by solving Eq. (10); see also the estimate in Eq. (12). Moreover, the function $q_\alpha(\varepsilon, k_x)$ parametrizing the Fermi-arc contour at energy ε has been defined in Eq. (9).] For the straight reference arc, we therefore consider a system with rescaled Weyl node separation, $k_0 \rightarrow k_{\varepsilon\alpha}$, at energy $\varepsilon \rightarrow \bar{\varepsilon} = q_\alpha(\varepsilon, k_{\varepsilon\alpha})$. The arc termination points for the straight reference arc are then located at $(\pm k_{\varepsilon\alpha}, \bar{\varepsilon})$ and match the termination points of the curved arc [see Figs. 4(b) and 4(c)]. We note that the energy of the reference arc differs from the energy of the curved Fermi arc. We can ensure only in this manner that both arc contours connect at their termination points and enclose a finite area in momentum space. No need for such a construction would arise for Weyl orbits in a slab geometry, where tunneling processes via bulk states take care of the corresponding momentum shifts between arc termination points on opposite surfaces. The advantage of our approach is that bulk states do not appear explicitly in the semiclassical calculation.

On the quantum level, we then define the gauge invariant phase-shift difference as

$$\Phi_\alpha(\varepsilon) = \theta_\alpha(\varepsilon) - \bar{\theta}_\pi[-q_\alpha(\varepsilon, k_{\varepsilon\alpha})] - \Phi_\alpha^{\text{DSM}}(\varepsilon), \quad (46)$$

where $\bar{\theta}_\pi$ follows by solving the linear system (35) with the rescaled parameter $\lambda_B \rightarrow \bar{\lambda}_B = \ell_B^2 k_{\varepsilon\alpha}$. For a comparison to

semiclassical results, in Eq. (46), we also subtract the phase-shift difference $\Phi_\alpha^{\text{DSM}}(\varepsilon)$ [see Eq. (43)] for the corresponding DSM case as shown in Fig. 3.

On the semiclassical level, the above gauge invariant phase shift takes the form

$$\begin{aligned} \Phi_\alpha(\varepsilon) &= \oint d\mathbf{r} \cdot \left(\mathbf{k} - \frac{e}{c} \mathbf{A} \right) \\ &= -\ell_B^2 \int_{-k_{\varepsilon\alpha}}^{k_{\varepsilon\alpha}} dk_x [q_\alpha(\varepsilon, k_x) - q_\alpha(\varepsilon, k_{\varepsilon\alpha})]. \end{aligned} \quad (47)$$

As illustrated in Fig. 4, the phase $\Phi_\alpha(\varepsilon)$ in Eq. (47) corresponds to the momentum-space area enclosed by the curved Fermi arc and the straight reference arc. Assuming $|\varepsilon| \ll k_0$, we find

$$\begin{aligned} \Phi_\alpha(\varepsilon) &\simeq \ell_B^2 k_0^2 \frac{2\alpha \cot(2\alpha) - 1}{\sin \alpha} \\ &\quad + 2\ell_B^2 \varepsilon k_0 \left(1 + \alpha \tan \alpha - \frac{2 \cos^2 \alpha}{3 - \cos(2\alpha)} \right). \end{aligned} \quad (48)$$

In Fig. 5, for small energies ε , we compare quantum-mechanical results for $\Phi_\alpha(\varepsilon)$ obtained numerically from Eq. (46) to the corresponding semiclassical predictions in Eq. (48). We find quantitative agreement both for different arc curvatures [see Fig. 5(a)] and for different energies [see Fig. 5(b)]. It is worth noting that the semiclassical description remains accurate even for large magnetic fields with $\lambda_B < 1$.

B. Fermi-arc lifetime and semiclassical traversal time

As discussed in Sec. I, one expects that Fermi-arc surface states acquire a finite *lifetime* $\tau_\alpha(\varepsilon)$ in a finite magnetic field $B \neq 0$. The lifetime describes the time scale for escaping into the bulk via the chiral LLs and follows from the general relation [62,63]

$$\tau_\alpha(\varepsilon) = \frac{d\theta_\alpha(\varepsilon)}{d\varepsilon}. \quad (49)$$

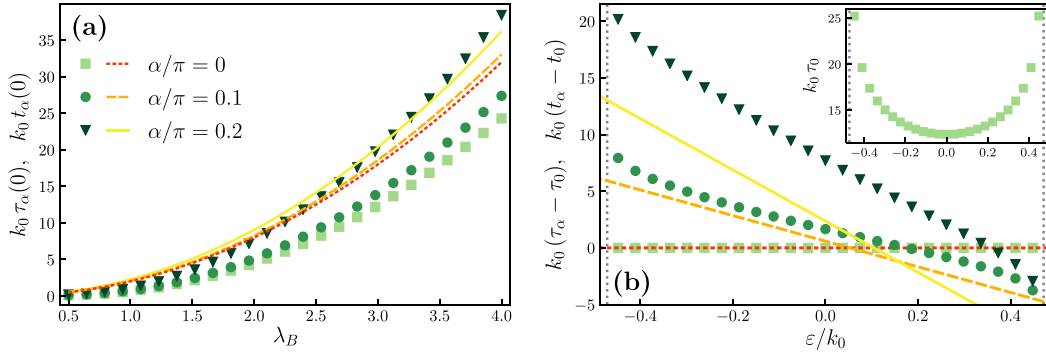


FIG. 6. Quantum-mechanical results for the Fermi-arc lifetime $\tau_\alpha(\varepsilon)$ (symbols) and for the semiclassical arc traversal time $t_\alpha(\varepsilon)$ (curves) [see Eqs. (49) and (51), respectively], for several values of α and given in units of k_0^{-1} . (a) Dependence of τ_α and t_α on λ_B for $\varepsilon = 0$. (b) $\tau_\alpha - \tau_0$ vs ε in the ultraquantum regime (delimited by vertical dotted lines) for $\lambda_B = 3$. Different symbols are for different α as in panel (a). We also show the corresponding semiclassical traversal time differences $t_\alpha - t_0$. The inset shows the straight-arc lifetime $\tau_{\alpha=0}$ vs ε , again for $\lambda_B = 3$.

Indeed, as first shown in a seminal work by Wigner [62], the energy derivative of the phase shift $\theta_\alpha(\varepsilon)$ encodes the time delay of a scattered particle which in turn is directly linked to its lifetime. We note that the phase shift (49) includes DSM contributions. Being a physical observable, Eq. (49) is gauge invariant. We compute Eq. (49) numerically using the quantum-mechanical approach detailed in Sec. III.

On the semiclassical level, we define another time scale, namely the *traversal time* $t_\alpha(\varepsilon)$. This is the time required to traverse the Fermi arc from one termination point to the other. Since the lifetime is due to the escape of Fermi-arc electrons into the bulk at the arc termination points, one expects that $t_\alpha(\varepsilon)$ is of the same order as $\tau_\alpha(\varepsilon)$. Even though these two time scales are not related to each other in a strict mathematical sense, one expects on physical grounds that they should exhibit similar behavior. We therefore compare them in some detail below. The semiclassical traversal time follows with Eq. (9) in the gauge invariant form

$$t_\alpha(\varepsilon) = \ell_B^2 \int_{-k_{\alpha}}^{k_{\alpha}} dk_x \sqrt{1 + \left(\frac{\partial q_\alpha(\varepsilon, k_x)}{\partial k_x} \right)^2} |\mathbf{v}_k|^{-1}. \quad (50)$$

Simple analytical expressions [see Eqs. (9) and (12)] follow for $|\alpha| \ll 1$ by expanding in α up to second order. We then obtain the semiclassical estimate:

$$t_\alpha(\varepsilon) \simeq 2\ell_B^2 \left[k_0 \left(1 + \frac{\alpha^2}{3} \right) - 2\varepsilon\alpha \right]. \quad (51)$$

We note that for a straight arc ($\alpha = 0$), the energy-independent traversal time $t_0 = 2\ell_B^2 k_0$ results.

In Fig. 6, we compare the semiclassical traversal time $t_\alpha(\varepsilon)$ to the quantum-mechanical lifetime $\tau_\alpha(\varepsilon)$. As shown in Fig. 6(a), the zero-energy lifetime diverges with increasing λ_B (i.e., with decreasing magnetic field), where the stable $B = 0$ Fermi arcs are approached. The semiclassical traversal time qualitatively captures this behavior, but no quantitative agreement between $t_\alpha(\varepsilon)$ and $\tau_\alpha(\varepsilon)$ is found. As shown in the inset of Fig. 6(b), the lifetime of the straight arc ($\alpha = 0$) increases with $|\varepsilon|$ and diverges upon reaching the $n = 1$ bulk LL. (We

recall that our construction in Sec. III B is limited to the ultraquantum regime. For energies above the bulk gap of the $n = 1$ LL, the $n = 1$ LL contributes in terms of propagating states.) Since the semiclassical estimate for t_0 is independent of energy, the energy dependence of $\tau_\alpha(\varepsilon)$ shown in the inset of Fig. 6(b) hints at quantum effects beyond semiclassics.

To compare the two time scales $\tau_\alpha(\varepsilon)$ and $t_\alpha(\varepsilon)$ for curved arcs, we have subtracted the respective $\alpha = 0$ contributions, and consider $\tau_\alpha - \tau_0$ and $t_\alpha - t_0$ in the main panel of Fig. 6(b). We find that both quantities are approximately linear functions of energy (at low energies). The lifetime differences $\tau_\alpha(\varepsilon) - \tau_0(\varepsilon)$ are again qualitatively captured by the corresponding traversal-time differences $t_\alpha(\varepsilon) - t_0$ (up to a constant offset).

We conclude that while the Fermi-arc lifetime $\tau_\alpha(\varepsilon)$ includes quantum contributions beyond semiclassics, essential low-energy features are captured by the semiclassical traversal time, at least in a qualitative fashion.

V. DISCUSSION

In this paper, we have studied the eigenstates of a four-band continuum model for a WSM in a half-space geometry, with a magnetic field perpendicular to the surface. At low energies in the ultraquantum regime dominated by the zeroth LL in the bulk, eigenstates are superpositions of in- and out-going chiral $n = 0$ LL states coupled by evanescent surface states originating from $n \neq 0$ LL states. The latter states replace the $B = 0$ Fermi-arc surface state, which acquires a finite lifetime for $B \neq 0$ and hence is not a stable solution.

We have compared our quantum-mechanical results with the corresponding semiclassical estimates by calculating the phase shift between in- and out-going $n = 0$ chiral LL states with the corresponding semiclassical results. These results depend on the energy ε and on a boundary parameter α determining the Fermi-arc curvature for $B = 0$. According to Refs. [15,16], the coupling between the chiral LLs is established by a semiclassical motion of fermions along the arc due to the Lorentz force. For the phase shifts, we find quantitative agreement between the quantum description and

semiclassical estimates. Moreover, from the energy derivative of the phase shift, one can define the lifetime of the Fermi-arc state. By comparing the lifetime to the semiclassical arc traversal time, we have argued that quantum contributions beyond semiclassics are important for the lifetime. Our results indicate that quantum corrections remain significant upon lowering the magnetic field strength or when increasing the Fermi energy. Understanding the lifetime of Fermi-arc surface states in an electromagnetic environment is a prerequisite for surface-sensitive tests such as quasiparticle interference experiments [38]. In the future, the theoretical modeling of such experiments could also profit from our explicit numerical construction of the eigenstates.

Our results are, at least qualitatively, consistent with numerical work on thin WSM films employing lattice models [16,64], hybrid models [65], and wave packet simulations [66]. The continuum approach used here employs a boundary condition which allows one to disentangle bulk and surface contributions to semiclassical trajectories. Our analysis shows that a semiclassical phase-space integral along the Fermi arc provides accurate estimates for phase shifts. When extending our arguments to a slab geometry or to thin films, one can describe the phase shift associated with Weyl orbits. This phase shift is observable in quantum magnetoconductance oscillation experiments (see Refs. [34–36] for recent reports). Similar phase shifts are also expected to appear in transport experiments on WSM junctions with heterochiral Fermi arcs at the interface [43]. Our results justify semiclassical explanations of these experiments and provide analytical estimates for a minimal model that incorporates the Fermi-arc curvature. Importantly, the observability of quantum oscillations from Weyl orbits crucially depends on the comparison between the time needed to traverse the Fermi surface and the scattering time [67]. Our estimates improve the evaluation of the former.

A more direct measurement of the traversal time can be devised along the lines of Ref. [19]. In the regime considered in our paper, one can indeed consider a setup with two gates generating an electric field on one surface and measure the current on the opposite surface. As a consequence of the described hybridization of bulk and surface states, a pulsed electric field generates a current response on the opposite surface, within a duration given by the traversal time.

We have been able to make substantial progress, and in some cases even obtained exact analytical solutions, since the studied four-band WSM model has decoupled Weyl nodes in the bulk. Omitting bulk Weyl-node coupling terms, e.g., a mass term $m\sigma^0\tau^x$, is typically justified for materials with well-separated Weyl nodes. Indeed, assuming a Weyl node separation $2k_0 \simeq 2 \text{ \AA}^{-1}$, Eq. (34) gives $\lambda_B \simeq 2.57$ for $B \simeq 1 \text{ T}$. The hybridization of LLs corresponding to different Weyl nodes is then exponentially suppressed by a factor $e^{-\lambda_B^2} \simeq 0.0014$. We conclude that only for much smaller k_0 and/or stronger B , effects of bulk Weyl-node coupling are expected to become relevant. For such cases, one expects a bulk gap for the hybridized $n = 0$ LLs. As a consequence, the chiral anomaly will eventually break down, and a nonmonotonic magnetoconductance should appear [58,59]. While such phenomena are not present in our paper, they are unavoidable in lattice models. In fact, we believe that they

obscure a semiclassical interpretation of previous numerical studies of WSM thin films [16,64–66]. Studying the effects of chiral mixing, e.g., by including the mass term $m\sigma^0\tau^x$ in our approach, is an interesting direction for future work. Notably, numerical works in the Hofstadter regime suggest that depending on the exact nature of the Weyl node annihilation associated with the opening of the gap, the resulting insulating system can be either trivial or topological [64,68]. In the latter case, localized topological surface states might emerge in the gap of the hybridized $n = 0$ LLs. Such states seem to be outside the reach of the established semiclassical picture.

The above-mentioned subtleties are absent if the magnetic field is oriented parallel to the axis along the Weyl node separation ($\hat{\mathbf{e}}_x$ in our case). This scenario was studied for a thin-film geometry [65], where a much smaller surface-bulk hybridization was reported, consistent with the semiclassical point of view. Magnetic fields oriented in the surface plane generally result in qualitatively different physics [69,70] than reported here.

Our paper has also covered the limiting DSM case. The considered Dirac Hamiltonian is an appropriate effective model as long as crystal symmetries protect the Dirac node degeneracy. It would be interesting in a future study to apply our approach and compare numerical and analytical solutions at $B \neq 0$ to the semiclassical description of topologically trivial surface states at $B = 0$.

In view of the recent experimental progress on magnetic WSMs [37], such as Co_2MnGa [71] and $\text{Co}_3\text{Sn}_2\text{S}_2$ [38,72], we are optimistic that Weyl orbit physics will soon be clearly established also beyond DSMs and noncentrosymmetric crystals. The underlying physics of such compounds should be captured by our results.

The data used for preparing the figures is available at the zenodo website [73].

ACKNOWLEDGMENTS

We thank M. Breitzkreiz, P. Brouwer, A. Chaou, and V. Dwivedi for discussions. We acknowledge funding by the Deutsche Forschungsgemeinschaft under TRR 183 Grant No. 277101999 (Project No. A02) and under Germany's Excellence Strategy—Cluster of Excellence Matter and Light for Quantum Computing (ML4Q) EXC 2004/1 Grant No. 390534769. F.B. acknowledges financial support from the TOPMASQ Project, CUP Grant No. E13C24001560001, Spoke 5 of the National Quantum Science and Technology Institute, Grant No. PE0000023 of the Piano Nazionale di Ripresa e Resilienza, financed by the European Union—NextGenerationEU.

APPENDIX A: SURFACE STATE SOLUTIONS

Here we provide detailed derivations for the $B = 0$ surface states given in Sec. II C. We begin with the topologically trivial surface states for the *Dirac semimetal* case, $k_0 = 0$, described by $H = \mathbf{k} \cdot \boldsymbol{\sigma} \tau^z$. After the unitary transformation $U_\alpha = \exp(\frac{i}{2}\alpha\sigma^y\tau^x)$, we obtain

$$\begin{aligned} \tilde{H}_\alpha = U_\alpha H U_\alpha^\dagger &= (k_x \sigma^x + k_y \sigma^y \cos \alpha - i \partial_z \sigma^z) \tau^z \\ &\quad + k_y \sigma^0 \tau^y \sin \alpha. \end{aligned} \quad (\text{A1})$$

This transformation is convenient since it eliminates the boundary parameter α from the boundary condition, $U_\alpha M_\alpha U_\alpha^\dagger = M_0 = \sigma^z \tau^x$ [see Eq. (8)]. Note that the unitary transformation leaves the current operator j^z invariant. Therefore, eigenstates $|\Psi\rangle$ with $\hat{H}|\Psi\rangle = \varepsilon|\Psi\rangle$ must satisfy the boundary condition $M_0 \hat{\Psi}(z=0) = \hat{\Psi}(z=0)$. We next make a (normalized) ansatz for a surface state confined to the half-space region $z \geq 0$:

$$|\Psi\rangle = \sqrt{\frac{\kappa}{2}} \begin{pmatrix} \tilde{\psi}^+ \\ \tilde{\psi}^- \end{pmatrix}_\tau, \quad \tilde{\psi}^X(z) = e^{-\kappa z} \begin{pmatrix} 1 \\ \chi e^{i\delta} \end{pmatrix}_\sigma, \quad (\text{A2})$$

where δ and κ are a phase and an inverse penetration length, respectively. These quantities have yet to be determined, where Eq. (A2) satisfies the boundary condition for arbitrary δ . To construct energy eigenstates, we first note that the chiral components satisfy $M_\delta^\sigma |\tilde{\psi}^X\rangle_\sigma = \chi |\tilde{\psi}^X\rangle_\sigma$ for M_δ^σ in Eq. (6). Eigenstates of \hat{H} thus obey

$$(k_x \sigma^x + k_y \sigma^y \cos \alpha) |\Psi\rangle = \varepsilon M_\delta^\sigma |\Psi\rangle. \quad (\text{A3})$$

For given in-plane momentum \mathbf{k}_\perp , the phase $\delta = \delta_\pm(\mathbf{k}_\perp)$ then follows from

$$\cos \delta_\pm(\mathbf{k}_\perp) = \frac{k_x}{\varepsilon_\pm(\mathbf{k}_\perp)}, \quad \sin \delta_\pm(\mathbf{k}_\perp) = \frac{k_y \cos \alpha}{\varepsilon_\pm(\mathbf{k}_\perp)}, \quad (\text{A4})$$

with $\varepsilon_\pm(\mathbf{k}_\perp)$ in Eq. (13). Inserting the corresponding ansatz into the eigenproblem of \hat{H} confirms that $\varepsilon_\pm(\mathbf{k}_\perp)$ is the energy dispersion of the surface state and yields the inverse decay length κ in the form

$$\kappa = k_y \sin \alpha. \quad (\text{A5})$$

The normalization condition $\kappa > 0$ implies Eq. (14) for physical solutions.

Next, we construct the solution for a *straight Fermi arc*, corresponding to the choice $\alpha = 0$. For the purpose of generality, we here allow for a free parameter in the parametrization (7). The trivial dependence of our results on this parameter (see below) helps to develop physical insight. We consider the boundary condition (4) with the matrix

$$M'_\gamma = M_{0,0,\gamma,0} = \sigma^z (\tau^x \cos \gamma + \tau^y \sin \gamma). \quad (\text{A6})$$

The following results for $\gamma = 0$ describe the $\alpha = 0$ results in Sec. II C since $M'_{\gamma=0} = M_{\alpha=0}$ with M_α in Eq. (8). [Note that δ in Eq. (7) is redundant for $\alpha = 0$.] We choose the normalized ansatz

$$|\Psi\rangle = \sqrt{\frac{\kappa_+ \kappa_-}{\kappa_+ + \kappa_-}} \begin{pmatrix} \psi^+ \\ e^{i\gamma} \psi^- \end{pmatrix}_\tau, \quad (\text{A7})$$

with the chiral spinor components

$$\psi^X(z) = e^{-\kappa_X z} \begin{pmatrix} 1 \\ -i\chi \end{pmatrix}_\sigma. \quad (\text{A8})$$

This ansatz satisfies the boundary condition. From $H|\Psi\rangle = \varepsilon|\Psi\rangle$, we find

$$\varepsilon(k_y) = -k_y, \quad \kappa_\chi(k_x) = k_0 + \chi k_x. \quad (\text{A9})$$

The normalization conditions $\kappa_+ > 0$ and $\kappa_- > 0$ for surface-state solutions restrict the in-plane momentum k_x to the open interval $-k_0 < k_x < k_0$. We thus obtain a physical Fermi arc

for a model with two decoupled Weyl nodes in the bulk. Here it turns out that the energy dispersion $\varepsilon(k_y)$ and the inverse penetration length scales κ_χ are independent of γ . This is expected since the parametric freedom in the boundary condition increases with the number of higher-energy bands. However, in this instance, we can extend the relation between the arc curvature and the corresponding boundary matrix parametrization further. To this end, we note that a straight arc is characterized by a chiral dispersion along $\hat{\mathbf{e}}_y$, and consequently a maximal current flows along this direction. Accordingly, the found solutions are eigenstates of the in-plane current $j^y = \sigma^y \tau^z$, which is only possible since M'_γ commutes with j^y . We can therefore infer the necessary condition that a straight arc corresponds to a parametrization of M with $[M, j^y] = 0$. Note that for the parametrization M_α in Eq. (8), this condition is only met for $\alpha = 0 \bmod \pi$.

In fact, we find *curved Fermi arcs* for all other values of α . For solving the surface-state problem, we here use a different approach which applies to a large family of parametrizations. We first consider the eigenproblem $H_\chi |\psi^X\rangle_\sigma = \varepsilon |\psi^X\rangle_\sigma$ for a single Weyl node with chirality $\chi = \pm 1$, described by $H_\chi = \chi \mathbf{k} \cdot \boldsymbol{\sigma} + k_0 \sigma^x$. The most general evanescent and normalized solution at given energy ε and in-plane momentum \mathbf{k}_\perp is

$$\psi_{\varepsilon \mathbf{k}_\perp}^X(z) = \sqrt{\frac{\kappa_\chi}{\varepsilon^2 + \kappa_\chi^2}} e^{-\kappa_\chi z} \begin{pmatrix} \chi \varepsilon + i \kappa_\chi \\ k_x + \chi k_0 + i k_y \end{pmatrix}_\sigma, \quad (\text{A10})$$

where $\kappa_\chi(\varepsilon, \mathbf{k}_\perp) = \sqrt{(k_x + \chi k_0)^2 + k_y^2 - \varepsilon^2}$ is the inverse length scale describing the decay of the surface state into the bulk. The requirement that κ is real restricts the energy of physical solutions to

$$\varepsilon^2 < (|k_x| - k_0)^2 + k_y^2. \quad (\text{A11})$$

The solution with energy ε in this interval is given by

$$|\Psi_{\varepsilon \mathbf{k}_\perp}\rangle = \begin{pmatrix} c_+ \psi_{\varepsilon \mathbf{k}_\perp}^+ \\ c_- \psi_{\varepsilon \mathbf{k}_\perp}^- \end{pmatrix}_\tau, \quad (\text{A12})$$

where c_\pm are complex coefficients. We now consider the boundary condition (4) with a general Hermitian parametrization:

$$M = \begin{pmatrix} X & Y \\ Y^\dagger & Z \end{pmatrix}, \quad X = X^\dagger, \quad Z = Z^\dagger. \quad (\text{A13})$$

Here, we assume that Y is invertible, which implies the condition $[M, \sigma^0 \tau^z] \neq 0$ for a physical Fermi arc (see Sec. II B). Together with $M^2 = \mathbb{1}$, we obtain the identities $Z = -Y^{-1}XY$ and $Y^{-1}X^2 = Y^{-1} - Y^\dagger$. It is then sufficient to consider the upper two spinor components in the boundary condition $(\mathbb{1} - M)\Psi_{\varepsilon \mathbf{k}_\perp}(z=0) = 0$, since the lower two components are implied. One can express the upper two components as a linear system of equations, $\mathbb{B}\mathbf{c} = \mathbf{0}$, where

$$\mathbb{B}(\varepsilon, \mathbf{k}_\perp) = [(\sigma^0 - X)\psi_{\varepsilon \mathbf{k}_\perp}^+(0) - Y\psi_{\varepsilon \mathbf{k}_\perp}^-(0)] \quad (\text{A14})$$

is a 2×2 matrix and $\mathbf{c} = (c_+, c_-)^T$ contains the coefficients in Eq. (A12). For M_α in Eq. (8), we have $X_\alpha = \sigma^x \sin \alpha$ and $Y_\alpha = \sigma^z \cos \alpha$. Solutions of the boundary condition thus satisfy $\det(\mathbb{B}) = 0$. We then obtain a secular equation that gives analytical solutions for $k_y = q_\alpha(\varepsilon, k_x)$, where Eq. (9) is the only solution satisfying Eq. (A11).

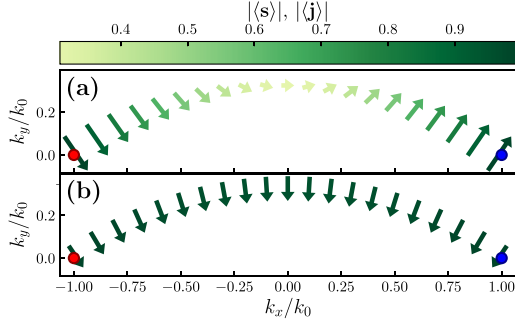


FIG. 7. In-plane spin polarization and particle current corresponding to the Fermi surface state for $B = 0$, $\alpha/\pi = 0.1$, and $\varepsilon = 0$, shown as color-scale plots in the k_x - k_y plane (see Appendix B). Red and blue dots indicate the surface projections of the Weyl nodes; arrows show the in-plane components of the spin polarization (\mathbf{s}) (a) and of the particle current (\mathbf{j}) (b).

We note that surface-state solutions for the opposite half space ($z \leq 0$) with the same boundary condition (4) follow from the transformation $\alpha \rightarrow \pi - \alpha$. This is because the transformation $\kappa_\chi \rightarrow -\kappa_\chi < 0$, necessary for constructing physical states in this geometry, amounts to $\psi_{\varepsilon, k_x, k_y}^\chi(0) \rightarrow [\psi_{\varepsilon, k_x, -k_y}^\chi(0)]^*$. The corresponding secular equation $\det[\mathbb{B}^*(\varepsilon, k_x, -k_y)] = 0$ then yields $k_y = -q_\alpha = q_{\pi-\alpha}$.

APPENDIX B: SURFACE SPIN POLARIZATION AND CURRENT

In this Appendix, we discuss the spin texture related to $s^\mu = \sigma^\mu \tau^0$ (with $\mu = x, y, z$) along a Fermi arc for the $B = 0$ case. Getting access to this type of quantity is an advantage of the four-band model with respect to two-band models [49,55,56]. Furthermore, we compute the in-plane current $j^\mu = \sigma^\mu \tau^z$ generated by the Fermi arc. Given a normalized Fermi-arc solution $|\Psi\rangle$, we need to evaluate expectation values of the form $\langle \sigma^\nu \tau^\mu \rangle = \int_0^\infty dz \Psi^\dagger(z) \sigma^\nu \tau^\mu \Psi(z)$.

For a straight arc ($\alpha = 0$), the corresponding solutions in Eq. (A8) satisfy $\sigma^y |\psi^\chi\rangle_\sigma = -\chi |\psi^\chi\rangle_\sigma$, implying $\langle \mathbf{s} \rangle = k_x \hat{\mathbf{e}}_y/k_0$ and $\langle \mathbf{j} \rangle = -\hat{\mathbf{e}}_y$.

For curved arcs with $\alpha > 0$, we use the general solution (A10) and perform the integration. The spin polarization follows from

$$\langle s^\mu \rangle = \sum_{\chi=\pm} \frac{|c_\chi|^2}{2\kappa_\chi} \psi^{\chi\dagger}(0) \sigma^\mu \psi^\chi(0), \quad (\text{B1})$$

where the expression for the in-plane current only differs by a relative sign in the sum:

$$\langle j^\mu \rangle = \sum_{\chi=\pm} \chi \frac{|c_\chi|^2}{2\kappa_\chi} \psi^{\chi\dagger}(0) \sigma^\mu \psi^\chi(0). \quad (\text{B2})$$

Above, we have suppressed the momentum dependence of c_χ and of $|\psi^\chi\rangle_\sigma$.

Results obtained from the above expressions are shown in Fig. 7. Our model correctly reproduces the main features

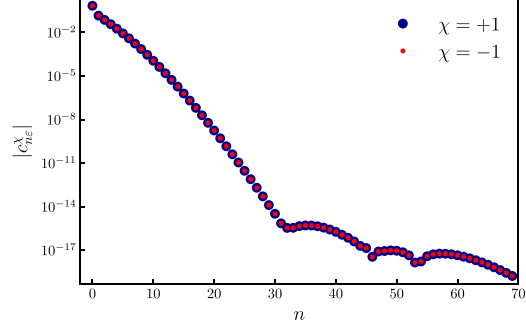


FIG. 8. Absolute value of the coefficients c_{ne}^χ appearing in the superposition (26) vs order n . Note the logarithmic scale for the coefficients. The shown results were obtained by numerically solving Eq. (35) for $\varepsilon/k_0 = 0.1$, $\alpha/\pi = 0.1$, $\lambda_B = 1$, with a cutoff value of $N = 70$.

of Fermi arcs as experimentally detected. First and foremost, the chiral transport is shown by the current in Fig. 7(b). In addition, the spin polarization rotates along the arc as dictated by the fact that the spin orientation at the two termination points corresponds to the chirality of the Weyl nodes. This behavior is manifest in Fig. 7(a) and in accordance with the spin texture observed experimentally by spin-filtered angle-resolved photoemission spectroscopy [74,75].

APPENDIX C: NUMERICAL IMPLEMENTATION OF BOUNDARY CONDITIONS

In this Appendix, we discuss the numerical approach introduced in Sec. III. Figure 8 shows representative results for the coefficients c_ε in Eq. (26), which are obtained by numerically solving Eq. (35) for a Landau level cutoff $N = 70$. These results already indicate that the numerical scheme is well controlled and convergent. A nontrivial benchmark that is passed accurately by our numerical scheme is provided by the analytical solutions (39) and (42) for a DSM with $\alpha = 0$ or $\varepsilon = 0$, respectively.

Let us next give additional details about our numerical approach. To avoid numerical overflow (or underflow) when computing the matrix elements (27) for a large cutoff N , it is convenient to compute the overlaps (33) using the recursion relation ($n \geq m > 1$)

$$\begin{aligned} \langle \varphi_n^- | \varphi_m^+ \rangle &= \frac{1}{\sqrt{nm}} (n+m-1-2\lambda_B^2) \langle \varphi_{n-1}^- | \varphi_{m-1}^+ \rangle \\ &\quad - \sqrt{\frac{(n-1)(m-1)}{nm}} \langle \varphi_{n-2}^- | \varphi_{m-2}^+ \rangle, \end{aligned} \quad (\text{C1})$$

with

$$\langle \varphi_{n-m+1}^- | \varphi_1^+ \rangle = \frac{n-m+1-2\lambda_B^2}{\sqrt{n-m+1}} \langle \varphi_{n-m}^- | \varphi_0^+ \rangle \quad (\text{C2})$$

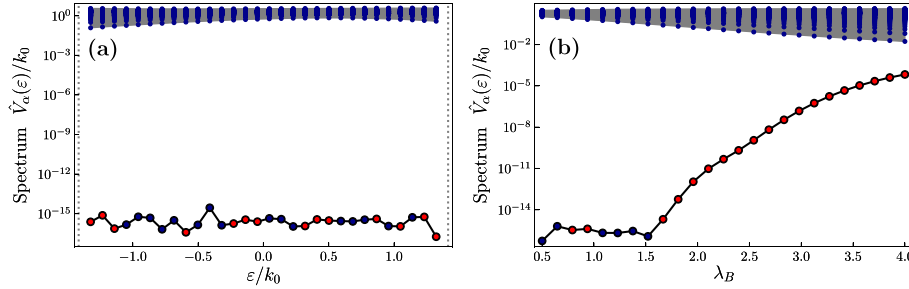


FIG. 9. Spectrum of \hat{V}_α as obtained from Eq. (28) for $\alpha/\pi = 0.1$, with the cutoff value $N = 100$. Note the semilogarithmic scales. Blue (red) dots correspond to positive (negative) eigenvalues. Since \mathbb{V}_α is positive semidefinite, negative eigenvalues indicate numerical errors. (a) Spectrum vs energy ε (in units of k_0) in the ultraquantum regime $|\varepsilon| < \sqrt{2}/\ell_B$ delimited by the vertical gray line, for $\lambda_B = 1$. (b) Spectrum vs λ_B for $\varepsilon/k_0 = 0.1$.

and

$$\langle \varphi_{n-m}^- | \varphi_0^+ \rangle = \sqrt{\frac{2^{n-m}}{(n-m)!}} \lambda_B^{n-m} e^{-\lambda_B^2}. \quad (\text{C3})$$

With these relations, we can easily employ a LL number cutoff of order $N = 250$ or even larger. For all results shown in this paper, we have carefully checked that results do not change when further increasing the cutoff.

Numerical solutions are then found from the kernel of $V_\alpha(\varepsilon)$, i.e., from the matrix representation of \mathbb{V}_α in the subspace with fixed ε and k_x . Note that we physically expect a single solution in this subspace in the ultraquantum regime. Consequently, the spectrum of $V_\alpha(\varepsilon)$ should have a single zero eigenvalue which is well separated from all other eigenvalues. Figure 9 shows representative results for the spectrum of the rescaled matrix \hat{V}_α obtained from Eq. (28). We find a non-degenerate, well-separated, and vanishing eigenvalue for all ε in the ultraquantum regime. However, for $\lambda_B \gtrsim 1.5$ (weak magnetic fields), numerical errors become slightly larger. Nonetheless, our numerical solutions still satisfy the boundary condition as demonstrated for $\lambda_B = 3$ in Fig. 10, where we show the four components of the real and imaginary parts of $\Psi(y, z = 0)$ and $M_\alpha \Psi(y, z = 0)$, respectively. The boundary

condition $\Psi(y, z = 0) = M_\alpha \Psi(y, z = 0)$ is indeed satisfied to high precision for all values of y .

APPENDIX D: SHIFT OF THE REFLECTED ELECTRON

The electronic Goos-Hänchen effect is a quantum phenomenon, best described as a lateral shift of a wave packet after reflection from a surface [76]. We can see an analog of this effect in the system at hand at the level of the expectation value of the position operator. In particular, we can read Eq. (26) in the ultraquantum regime $0 < \varepsilon < \sqrt{2}/\ell_B$ as the superposition of an incoming wave in the chiral LL with $\chi = +1$, an outgoing wave in the chiral LL with $\chi = -1$, and a series of bound states [see Eq. (21)]. Considering first a single momentum component k_x , the expectation value of the y coordinate for an incoming electron arriving on the surface ($z = 0$) is computed from the fundamental eigenmode of the harmonic oscillator in Eq. (19) as $\langle y \rangle_{\text{in}} = \ell_B^2(k_x + k_0)$. The momentum k_x is conserved in the reflection process, and one readily sees that the electron leaving the surface has the expectation value $\langle y \rangle_{\text{out}} = \ell_B^2(k_x - k_0)$. We note that the shift $\langle y \rangle_{\text{out}} - \langle y \rangle_{\text{in}}$ is gauge invariant.

Following Ref. [76], we now generalize this argument and write an electronic wave packet formed by a superposition of plane waves with various momenta k_x and, for simplicity,

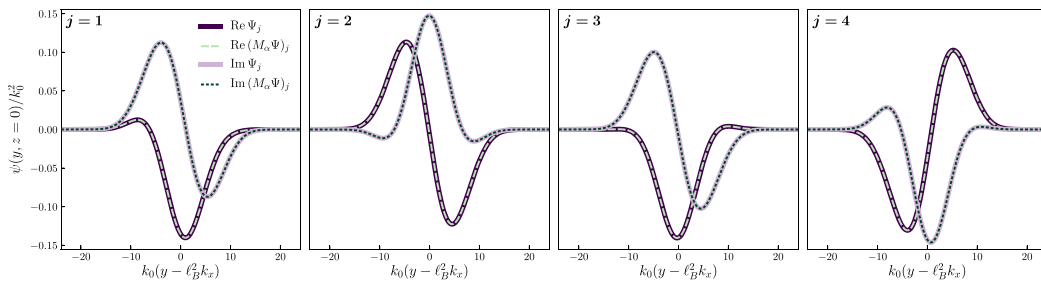


FIG. 10. Spinor components $\Psi_{j=1,2,3,4}$ of the eigenstate solution at the surface, $\Psi(y, z = 0) = (\Psi_1(y), \Psi_2(y), \Psi_3(y), \Psi_4(y))^T$, compared with the corresponding components of $M_\alpha \Psi(y, z = 0)$. Parameters are given by $\varepsilon/k_0 = 0.1$, $\alpha/\pi = 0.1$, and $\lambda_B = 3$. We separately show the real and imaginary parts, which verify that the boundary condition $M_\alpha \Psi(y, z = 0) = \Psi(y, z = 0)$ is numerically satisfied to high accuracy.

a Gaussian envelope function centered around momentum p with spread Δk . Such a wave packet, in the $\chi = +1$ block, has the form

$$\Psi_{\varepsilon,\text{in}}(\mathbf{r}) = \frac{1}{\sqrt{2\pi}} \int dk_x F(k_x - p) e^{ik_x x} \psi_{0,\varepsilon}^+(y, z), \quad (\text{D1})$$

with $F(k_x) = (\sqrt{\pi} \Delta k)^{-\frac{1}{2}} e^{-\frac{1}{2}(k_x/\Delta k)^2}$. The expectation value of the y coordinate for the wave packet arriving on the surface then follows as

$$\langle y \rangle_{\text{in}} = \ell_B^2(p + k_0). \quad (\text{D2})$$

Repeating the calculation for the outgoing wave packet in the $\chi = -1$ block,

$$\Psi_{\varepsilon,\text{out}}(\mathbf{r}) = \frac{1}{\sqrt{2\pi}} \int dk_x F(k_x - p) e^{ik_x x} \psi_{0,\varepsilon}^-(y, z), \quad (\text{D3})$$

one finds $\langle y \rangle_{\text{out}} = \ell_B^2(p - k_0)$. We conclude that the electronic Goos-Hänchen shift is given by Eq. (38). As this result is separately valid for each k_x , we expect it to hold for every choice of the envelope function.

-
- [1] A. Burkov, Topological semimetals, *Nat. Mater.* **15**, 1145 (2016).
- [2] B. Yan and C. Felser, Topological materials: Weyl semimetals, *Annu. Rev. Condens. Matter Phys.* **8**, 337 (2017).
- [3] N. P. Armitage, E. J. Mele, and A. Vishwanath, Weyl and Dirac semimetals in three-dimensional solids, *Rev. Mod. Phys.* **90**, 015001 (2018).
- [4] A. Burkov, Weyl metals, *Annu. Rev. Condens. Matter Phys.* **9**, 359 (2018).
- [5] H. B. Nielsen and M. Ninomiya, The Adler-Bell-Jackiw anomaly and Weyl fermions in a crystal, *Phys. Lett. B* **130**, 389 (1983).
- [6] P. Hosur and X. Qi, Recent developments in transport phenomena in Weyl semimetals, *C. R. Phys.* **14**, 857 (2013).
- [7] A. Burkov, Chiral anomaly and transport in Weyl metals, *J. Phys.: Condens. Matter* **27**, 113201 (2015).
- [8] E. Gorbar, V. Miransky, I. Shovkovy, and P. Sukhachov, Anomalous transport properties of Dirac and Weyl semimetals, *Low Temp. Phys.* **44**, 487 (2018).
- [9] G. Volovik, Zeros in the fermion spectrum in superfluid systems as diabolical points, *JETP Lett.* **46**, 98 (1987).
- [10] H. B. Nielsen and M. Ninomiya, Absence of neutrinos on a lattice: (I). Proof by homotopy theory, *Nucl. Phys. B* **185**, 20 (1981).
- [11] S.-Y. Xu *et al.*, Discovery of a Weyl fermion semimetal and topological Fermi arcs, *Science* **349**, 613 (2015).
- [12] C.-L. Zhang *et al.*, Signatures of the Adler-Bell-Jackiw chiral anomaly in a Weyl fermion semimetal, *Nat. Commun.* **7**, 10735 (2016).
- [13] M. Z. Hasan, S.-Y. Xu, I. Belopolski, and S.-M. Huang, Discovery of Weyl fermion semimetals and topological Fermi arc states, *Annu. Rev. Condens. Matter Phys.* **8**, 289 (2017).
- [14] N. Ong and S. Liang, Experimental signatures of the chiral anomaly in Dirac-Weyl semimetals, *Nat. Rev. Phys.* **3**, 394 (2021).
- [15] A. C. Potter, I. Kimchi, and A. Vishwanath, Quantum oscillations from surface Fermi arcs in Weyl and Dirac semimetals, *Nat. Commun.* **5**, 5161 (2014).
- [16] Y. Zhang, D. Bulmash, P. Hosur, A. C. Potter, and A. Vishwanath, Quantum oscillations from generic surface Fermi arcs and bulk chiral modes in Weyl semimetals, *Sci. Rep.* **6**, 23741 (2016).
- [17] C. Zhang, Y. Zhang, H.-Z. Lu, X. Xie, and F. Xiu, Cycling Fermi arc electrons with Weyl orbits, *Nat. Rev. Phys.* **3**, 660 (2021).
- [18] S. A. Parameswaran, T. Grover, D. A. Abanin, D. A. Pesin, and A. Vishwanath, Probing the chiral anomaly with nonlocal transport in three-dimensional topological semimetals, *Phys. Rev. X* **4**, 031035 (2014).
- [19] Y. Baum, E. Berg, S. A. Parameswaran, and A. Stern, Current at a distance and resonant transparency in Weyl semimetals, *Phys. Rev. X* **5**, 041046 (2015).
- [20] Z. Hou and Q.-F. Sun, Nonlocal correlation mediated by Weyl orbits, *Phys. Rev. Res.* **2**, 023236 (2020).
- [21] E. V. Gorbar, V. A. Miransky, I. A. Shovkovy, and P. O. Sukhachov, Quantum oscillations as a probe of interaction effects in Weyl semimetals in a magnetic field, *Phys. Rev. B* **90**, 115131 (2014).
- [22] M. A. Zubkov, Weyl orbits as probe of chiral separation effect in magnetic Weyl semimetals, *J. Phys.: Condens. Matter* **36**, 415501 (2024).
- [23] C. M. Wang, H.-P. Sun, H.-Z. Lu, and X. C. Xie, 3D quantum Hall effect of Fermi arcs in topological semimetals, *Phys. Rev. Lett.* **119**, 136806 (2017).
- [24] H. Li, H. Liu, H. Jiang, and X. C. Xie, 3D quantum Hall effect and a global picture of edge states in Weyl semimetals, *Phys. Rev. Lett.* **125**, 036602 (2020).
- [25] P. J. Moll, N. L. Nair, T. Helm, A. C. Potter, I. Kimchi, A. Vishwanath, and J. G. Analytis, Transport evidence for Fermi-arc-mediated chirality transfer in the Dirac semimetal Cd_3As_2 , *Nature (London)* **535**, 266 (2016).
- [26] C. Zhang *et al.*, Evolution of Weyl orbit and quantum Hall effect in Dirac semimetal Cd_3As_2 , *Nat. Commun.* **8**, 1272 (2017).
- [27] G. Zheng *et al.*, Recognition of Fermi-arc states through the magnetoresistance quantum oscillations in Dirac semimetal Cd_3As_2 nanoplates, *Phys. Rev. B* **96**, 121407(R) (2017).
- [28] C. Zhang *et al.*, Quantum Hall effect based on Weyl orbits in Cd_3As_2 , *Nature (London)* **565**, 331 (2019).
- [29] S. Nishihaya, M. Uchida, Y. Nakazawa, R. Kurihara, K. Akiba, M. Kriener, A. Miyake, Y. Taguchi, M. Tokunaga, and M. Kawasaki, Quantized surface transport in topological Dirac semimetal films, *Nat. Commun.* **10**, 2564 (2019).
- [30] S. Nishihaya, M. Uchida, Y. Nakazawa, M. Kriener, Y. Taguchi, and M. Kawasaki, Intrinsic coupling between spatially-separated surface Fermi-arcs in Weyl orbit quantum Hall states, *Nat. Commun.* **12**, 2572 (2021).
- [31] R. Chen, T. Liu, C. M. Wang, H.-Z. Lu, and X. C. Xie, Field-tunable one-sided higher-order topological hinge states in Dirac semimetals, *Phys. Rev. Lett.* **127**, 066801 (2021).

- [32] M. Chang, H. Geng, L. Sheng, and D. Y. Xing, Three-dimensional quantum Hall effect in Weyl semimetals, *Phys. Rev. B* **103**, 245434 (2021).
- [33] D.-H.-M. Nguyen, K. Kobayashi, J.-E. R. Wichmann, and K. Nomura, Quantum Hall effect induced by chiral Landau levels in topological type-II Weyl semimetal films, *Phys. Rev. B* **104**, 045302 (2021).
- [34] C. Zhang *et al.*, Ultrahigh conductivity in Weyl semimetal NbAs nanobelts, *Nat. Mater.* **18**, 482 (2019).
- [35] N. L. Nair *et al.*, Signatures of possible surface states in TaAs, *Phys. Rev. B* **102**, 075402 (2020).
- [36] P. Li, Y. Wen, X. He, Q. Zhang, C. Xia, Z.-M. Yu, S. A. Yang, Z. Zhu, H. N. Alshareef, and X.-X. Zhang, Evidence for topological type-II Weyl semimetal WTe₂, *Nat. Commun.* **8**, 2150 (2017).
- [37] B. A. Bernevig, C. Felser, and H. Beidenkopf, Progress and prospects in magnetic topological materials, *Nature (London)* **603**, 41 (2022).
- [38] N. Morali, R. Batabyal, P. K. Nag, E. Liu, Q. Xu, Y. Sun, B. Yan, C. Felser, N. Avraham, and H. Beidenkopf, Fermi-arc diversity on surface terminations of the magnetic Weyl semimetal Co₃Sn₂S₂, *Science* **365**, 1286 (2019).
- [39] V. Dwivedi, Fermi arc reconstruction at junctions between Weyl semimetals, *Phys. Rev. B* **97**, 064201 (2018).
- [40] F. Abdulla, S. Rao, and G. Murthy, Fermi arc reconstruction at the interface of twisted Weyl semimetals, *Phys. Rev. B* **103**, 235308 (2021).
- [41] F. Bucccheri, R. Egger, and A. De Martino, Transport, refraction, and interface arcs in junctions of Weyl semimetals, *Phys. Rev. B* **106**, 045413 (2022).
- [42] S. Kaushik, I. Robredo, N. Mathur, L. M. Schoop, S. Jin, M. G. Vergniory, and J. Cano, Transport signatures of Fermi arcs at twin boundaries in Weyl materials, *arXiv:2207.14109*.
- [43] A. Y. Chaou, V. Dwivedi, and M. Breitzkreiz, Magnetic breakdown and chiral magnetic effect at Weyl-semimetal tunnel junctions, *Phys. Rev. B* **107**, L241109 (2023).
- [44] A. Y. Chaou, V. Dwivedi, and M. Breitzkreiz, Quantum oscillation signatures of interface Fermi arcs, *Phys. Rev. B* **110**, 035116 (2024).
- [45] M. Breitzkreiz and P. W. Brouwer, Fermi-arc metals, *Phys. Rev. Lett.* **130**, 196602 (2023).
- [46] E. Witten, Three lectures on topological phases of matter, *La Riv. del Nuovo Cimento* **39**, 313 (2016).
- [47] K. Hashimoto, T. Kimura, and X. Wu, Boundary conditions of Weyl semimetals, *Prog. Theor. Exp. Phys.* **2017**, 053101 (2017).
- [48] G. C. Thiang, On spectral flow and Fermi arcs, *Commun. Math. Phys.* **385**, 465 (2021).
- [49] F. Bucccheri, A. De Martino, R. G. Pereira, P. W. Brouwer, and R. Egger, Phonon-limited transport and Fermi arc lifetime in Weyl semimetals, *Phys. Rev. B* **105**, 085410 (2022).
- [50] F. Bucccheri, R. Egger, and A. De Martino, Dispersive drumhead states in nodal-line semimetal junctions, *Phys. Rev. Res.* **6**, 013193 (2024).
- [51] S. Li and A. Andreev, Spiraling Fermi arcs in Weyl materials, *Phys. Rev. B* **92**, 201107(R) (2015).
- [52] Z. Faraei, T. Farajollahpour, and S. A. Jafari, Green's function of semi-infinite Weyl semimetals, *Phys. Rev. B* **98**, 195402 (2018).
- [53] A. R. Akhmerov and C. W. J. Beenakker, Detection of valley polarization in graphene by a superconducting contact, *Phys. Rev. Lett.* **98**, 157003 (2007).
- [54] A. R. Akhmerov and C. W. J. Beenakker, Boundary conditions for Dirac fermions on a terminated honeycomb lattice, *Phys. Rev. B* **77**, 085423 (2008).
- [55] N. Bovenzi, M. Breitzkreiz, T. O'Brien, J. Tworzydło, and C. Beenakker, Twisted Fermi surface of a thin-film Weyl semimetal, *New J. Phys.* **20**, 023023 (2018).
- [56] M. Burrello, E. Guadagnini, L. Lepori, and M. Mintchev, Field theory approach to the quantum transport in Weyl semimetals, *Phys. Rev. B* **100**, 155131 (2019).
- [57] I. S. Gradshteyn and I. M. Ryzhik, *Table of Integrals, Series, and Products* (Academic Press, New York, 2014).
- [58] D. R. Saykin, K. S. Tikhonov, and Y. I. Rodionov, Landau levels with magnetic tunneling in a Weyl semimetal and magnetoconductance of a ballistic *p-n* junction, *Phys. Rev. B* **97**, 041202(R) (2018).
- [59] C.-K. Chan and P. A. Lee, Emergence of gapped bulk and metallic side walls in the zeroth Landau level in Dirac and Weyl semimetals, *Phys. Rev. B* **96**, 195143 (2017).
- [60] G. Sundaram and Q. Niu, Wave-packet dynamics in slowly perturbed crystals: Gradient corrections and Berry-phase effects, *Phys. Rev. B* **59**, 14915 (1999).
- [61] D. Wawrzik, J.-S. You, J. I. Facio, J. van den Brink, and I. Sodemann, Infinite Berry curvature of Weyl Fermi arcs, *Phys. Rev. Lett.* **127**, 056601 (2021).
- [62] E. P. Wigner, Lower limit for the energy derivative of the scattering phase shift, *Phys. Rev.* **98**, 145 (1955).
- [63] F. T. Smith, Lifetime matrix in collision theory, *Phys. Rev.* **118**, 349 (1960).
- [64] F. Abdulla, A. Das, S. Rao, and G. Murthy, Time-reversal-broken Weyl semimetal in the Hofstadter regime, *SciPost Physics Core* **5**, 014 (2022).
- [65] E. Benito-Matías, R. A. Molina, and J. González, Surface and bulk Landau levels in thin films of Weyl semimetals, *Phys. Rev. B* **101**, 085420 (2020).
- [66] H. Yao, M. Zhu, L. Jiang, and Y. Zheng, Simulation on the electronic wave packet cyclotron motion in a Weyl semimetal slab, *J. Phys.: Condens. Matter* **29**, 155502 (2017).
- [67] D. Bulmash and X.-L. Qi, Quantum oscillations in Weyl and Dirac semimetal ultrathin films, *Phys. Rev. B* **93**, 081103(R) (2016).
- [68] F. Abdulla, Pairwise annihilation of Weyl nodes induced by magnetic fields in the Hofstadter regime, *Phys. Rev. B* **109**, 155142 (2024).
- [69] S. Tchoumakov, M. Civelli, and M. O. Goerbig, Magnetic description of the Fermi arc in type-I and type-II Weyl semimetals, *Phys. Rev. B* **95**, 125306 (2017).
- [70] J. Behrends, S. Roy, M. H. Kolodrubetz, J. H. Bardarson, and A. G. Grushin, Landau levels, Bardeen polynomials, and Fermi arcs in Weyl semimetals: Lattice-based approach to the chiral anomaly, *Phys. Rev. B* **99**, 140201(R) (2019).
- [71] I. Belopolski *et al.*, Discovery of topological Weyl fermion lines and drumhead surface states in a room temperature magnet, *Science* **365**, 1278 (2019).
- [72] D. Liu *et al.*, Magnetic Weyl semimetal phase in a Kagomé crystal, *Science* **365**, 1282 (2019).
- [73] <https://zenodo.org/records/14062003>.

BAUER, BUCCHERI, DE MARTINO, AND EGGER

PHYSICAL REVIEW RESEARCH 6, 043201 (2024)

- [74] B. Q. Lv, S. Muff, T. Qian, Z. D. Song, S. M. Nie, N. Xu, P. Richard, C. E. Matt, N. C. Plumb, L. X. Zhao, G. F. Chen, Z. Fang, X. Dai, J. H. Dil, J. Mesot, M. Shi, H. M. Weng, and H. Ding, Observation of Fermi-arc spin texture in TaAs, [Phys. Rev. Lett. **115**, 217601 \(2015\)](#).
- [75] S.-Y. Xu *et al.*, Spin polarization and texture of the Fermi arcs in the Weyl fermion semimetal TaAs, [Phys. Rev. Lett. **116**, 096801 \(2016\)](#).
- [76] X. Chen, X.-J. Lu, Y. Ban, and C.-F. Li, Electronic analogy of the Goos-Hänchen effect: A review, [J. Opt. **15**, 033001 \(2013\)](#).

P2 Electric polarization near vortices in the extended Kitaev model

The following text is reproduced from the publication

L. R. D. Freitas, **T. Bauer**, R. Egger, and R. G. Pereira
Electric polarization near vortices in the extended Kitaev model
npj Quantum Materials, vol. 9, no. 1, p. 33 (2024).

The supplementary material provided with this publication is attached to the text.

Digital Object Identifier (DOI): [10.1038/s41535-024-00643-5](https://doi.org/10.1038/s41535-024-00643-5)

Statement of contribution

RE and RGP conceived and supervised this work. LRDF developed and carried out the mean-field calculations with my help. The results were interpreted and discussed by all authors. LRDF also prepared the figures for the manuscript, which RE and RGP drafted and all authors subsequently finalized.

Copyright and license notice

Nature Springer Limited published this article under the terms of the [Creative Commons Attribution 4.0 International](#) license. Distribution of this work is permitted, provided that attribution to the authors, the article's title, journal citation, and DOI are maintained. The authors retain copyright.

<https://doi.org/10.1038/s41535-024-00643-5>

Electric polarization near vortices in the extended Kitaev model

Lucas R. D. Freitas¹, Tim Bauer², Reinhold Egger²✉ & Rodrigo G. Pereira¹

We formulate a Majorana mean-field theory for the extended JKT Kitaev model in a magnetic Zeeman field of arbitrary direction, and apply it for studying spatially inhomogeneous states harboring vortices. This mean-field theory is exact in the pure Kitaev limit and captures the essential physics throughout the Kitaev spin liquid phase. We determine the charge profile around vortices and the corresponding quadrupole tensor. The quadrupole-quadrupole interaction between distant vortices is shown to be either repulsive or attractive, depending on parameters. We predict that electrically biased scanning probe tips enable the creation of vortices at preselected positions. Our results paves the way for the electric manipulation of Ising anyons in Kitaev spin liquids.

A hallmark of Kitaev spin liquids is the fractionalization of spin-1/2 local moments into Majorana fermions and a \mathbb{Z}_2 gauge field^{1–9}. When time reversal symmetry is broken by an external magnetic field, both types of excitations become gapped, and vortices of the \mathbb{Z}_2 gauge field bind Majorana zero modes that behave as non-Abelian anyons. These properties can be demonstrated in the exactly solvable Kitaev honeycomb model¹. Since the observation that the bond-directional exchange interactions of the pure Kitaev model are realized in quasi-two-dimensional Mott insulators with strong spin-orbit coupling¹⁰, identifying signatures of fractional excitations in Kitaev materials has become a major goal of condensed matter physics^{11–14}. Most notably, there is evidence for a half-quantized thermal Hall conductance in the candidate material α -RuCl₃ at intermediate temperatures and magnetic fields, but its interpretation in terms of chiral Majorana edge modes remains controversial^{15–18}. This ambiguity calls for alternative experimental probes that may help distinguish a Kitaev spin liquid from a more conventional partially polarized phase with topological magnons^{19,20}.

A promising route to detect and manipulate the fractional excitations of Kitaev spin liquids is to exploit their nontrivial responses to electrical probes. Theoretical proposals in this direction include electric dipole contributions to the subgap optical conductivity^{21,22}, scanning tunneling spectroscopy^{23–27}, interferometry in electrical conductance^{28,29}, and electric polarization and orbital currents associated with localized excitations^{30,31}. In fact, the charge polarization in Mott insulators can be captured by an effective density operator written in terms of spin correlations in the low-energy sector^{32,33}. The effective density operator for Kitaev materials was derived in ref. 30 starting from the multi-orbital Hubbard–Kanamori model in the ideal limit where the dominant exchange path only generates the pure Kitaev interaction¹⁰. The electric field effects then work both ways. On the

one hand, the inhomogeneous spin correlations around a \mathbb{Z}_2 vortex imply that vortices produce an intrinsic electric charge distribution. On the other hand, vortices are attracted by electrostatic potentials that locally modify exchange couplings, and this effect can be used to trap and move anyons adiabatically^{30,34}.

In this work we generalize the theory of the electric charge response in ref. 30 to consider the generic spin model for Kitaev materials^{35,36}. Our starting point is the three-orbital Hubbard–Kanamori model which takes into account sub-dominant hopping processes that, in addition to Kitaev (K) interactions, also generate Heisenberg (J) and off-diagonal (Γ) exchange interactions. Using perturbation theory to leading order in the hopping parameters, we derive an expression for the effective charge density operator in the Mott insulating phase that contains all two-spin terms allowed by symmetry. Since the additional interactions spoil the integrability of the pure Kitaev model, we compute spin correlations using a Majorana mean-field theory. This type of approximation has been applied to map out the ground state phase diagram and to compute response functions of the extended Kitaev model^{37–46}. Here we generalize the mean-field approach to treat position-dependent order parameters in the case where translation symmetry is broken by the presence of vortices in the \mathbb{Z}_2 flux configuration. Including a Zeeman coupling, we show that the spatial anisotropy of the charge distribution around a vortex varies with the direction of the magnetic field and can be quantified by the components of the electric quadrupole moment. We also discuss how a local electrostatic potential renormalizes the couplings in the extended Kitaev model and gives rise to an effective attractive potential for vortices. Remarkably, the effect is stronger in the presence of non-Kitaev interactions, and we find that it is possible to close the vortex gap by means of electric modulation of the local spin interactions.

¹International Institute of Physics and Departamento de Física Teórica e Experimental, Universidade Federal do Rio Grande do Norte, Natal, RN 59078-970, Brazil.

²Institut für Theoretische Physik, Heinrich-Heine-Universität, D-40225 Düsseldorf, Germany. ✉ e-mail: egger@hhu.de

<https://doi.org/10.1038/s41535-024-00643-5>

Article

Results

Mean-field theory for the extended Kitaev model

The local degrees of freedom of Kitaev materials are transition metal ions with $4d^6$ or $5d^6$ electronic configuration and strong spin-orbit coupling^{4,5}. In the presence of the crystal field of an octahedral ligand cage, this configuration is equivalent to a single hole in a t_{2g} orbital. Starting from a three-orbital Hubbard–Kanamori Hamiltonian on the honeycomb lattice, in the presence of a Zeeman coupling to an external magnetic field \mathbf{h} , we find from a projection scheme that the low-energy effective spin Hamiltonian is given by the extended Kitaev (aka JKT) model³⁵:

$$H = \frac{1}{2} \sum_{ij} \sum_{\alpha\beta} \sigma_i^\alpha \mathbf{J}_{ij}^{\alpha\beta} \sigma_j^\beta - \sum_i \mathbf{h} \cdot \boldsymbol{\sigma}_i, \quad (1)$$

where σ_i denotes the vector of the pseudospin-1/2 Pauli operators at site i . Moreover, i and j are nearest neighbors, \mathbf{J}_{ij} is the bond-dependent exchange matrix, and the indices $\alpha, \beta, \gamma \in \{x, y, z\} = \{1, 2, 3\}$ label both spin components and bonds on the honeycomb lattice. We denote by $\langle ij \rangle_\gamma$ a nearest-neighbor bond of type γ with site i belonging to sublattice A and j to

sublattice B. For bond $\langle ij \rangle_\gamma$ we have $\mathbf{J}_{ij} = \begin{pmatrix} J & \Gamma & 0 \\ \Gamma & J & 0 \\ 0 & 0 & J+K \end{pmatrix}$. The

exchange matrices for x and y bonds follow by cyclic permutation of the spin and bond indices. The ideal Kitaev case with $J = \Gamma = 0$ corresponds to a single hopping path mediated by ligands on edge-sharing octahedra with ideal 90° bonds¹⁰. Numerical studies show that the Kitaev spin liquid phase is stable in the regime $|\Gamma|, |J| \ll |K|$ ^{35,47–49}. For estimates of the hopping and exchange parameters for α -RuCl₃, see for instance refs. 5, 50. In this material, one finds a ferromagnetic Kitaev coupling ($K < 0$) and the leading perturbation to the idealized Kitaev model is given by $0 < \Gamma < |K|$.

We employ a mean-field approximation for calculating spin correlations in the extended Kitaev model and to verify the stability of the spin liquid phase against integrability-breaking perturbations. For $J = \Gamma = h = 0$, the model can be solved exactly¹ using the Kitaev representation $\sigma_i^\gamma = i c_i^\mu c_i^\nu$ in terms of four Majorana fermions which obey $(c_i^\mu)^\dagger = c_i^\mu$ and $\{c_i^\mu, c_j^\nu\} = 2\delta_{ij}\delta_{\mu\nu}$. Throughout, we use indices $\mu, \nu, \rho \in \{0, 1, 2, 3\}$ to denote all four fermion flavors, in contrast with $\alpha, \beta, \gamma \in \{1, 2, 3\}$. Physical states must respect the local constraint $D_i = c_i^0 c_i^1 c_i^2 c_i^3 = +1$. The algebra of the spin operators can be satisfied using different representations⁵¹. It is convenient to write the Kitaev representation in terms of the vector $c_i = (c_i^0, c_i^1, c_i^2, c_i^3)^T$ and the anti-symmetric matrices N^γ defined by:

$$\sigma_i^\gamma = \frac{i}{2} c_i^T N^\gamma c_i \equiv \frac{i}{2} (c_i^0 c_i^\gamma - c_i^\gamma c_i^0). \quad (2)$$

Instead of imposing $D_i = +1$, we use the equivalent constraint⁵²:

$$c_i^T G^\gamma c_i \equiv c_i^0 c_i^\gamma - c_i^\gamma c_i^0 + \sum_{\alpha\beta} \epsilon^{\alpha\beta\gamma} c_i^\alpha c_i^\beta = 0. \quad (3)$$

Note that the constraints $c_i^T G^\gamma c_i = 0$ for $\gamma = x, y, z$ are redundant. If the constraint is implemented exactly, it suffices to impose it for a single value of γ . However, when treating the constraints (3) numerically through the corresponding Lagrange multipliers $\lambda_i^{42,44}$, it is advantageous to enforce them in a symmetric manner for all three values of γ . We thereby rewrite the spin Hamiltonian as:

$$H = \frac{1}{8} \sum_{ij} \sum_{\alpha\beta} i c_i^T N^\alpha c_i \mathbf{J}_{ij}^{\alpha\beta} i c_j^T N^\beta c_j - \frac{1}{4} \sum_{i\gamma} (2h^\gamma i c_i^T N^\gamma c_i - \lambda_i^\gamma i c_i^T G^\gamma c_i). \quad (4)$$

We decouple the quartic terms using two types of real-valued mean-field parameters:

$$U_{ij}^{\mu\nu} = \langle i c_i^\mu c_j^\nu \rangle, \quad V_i^{\mu\nu} = \langle i c_i^\mu c_i^\nu \rangle, \quad (5)$$

which obey $U_{ij}^{\mu\nu} = -U_{ji}^{\nu\mu}$ and $V_i^{\mu\nu} = 2i\delta^{\mu\nu} - V_i^{\nu\mu}$. For the exactly solvable Kitaev model, one finds that $U_{ij}^{\mu\nu}$ is diagonal in the indices μ, ν . In particular, the components $U_{ij}^{\gamma\gamma}$ are related to the static \mathbb{Z}_2 gauge field and take values $U_{ij}^{\gamma\gamma} = \pm 1$ when i, j form a nearest-neighbor γ bond, and $U_{ij}^{\gamma\gamma} = 0$ otherwise. Thus, $U_{ij}^{\gamma\gamma}$ can be viewed as an “order parameter” for the Kitaev spin liquid phase. For comparison with the exact solution, we also define $W_p = \prod_{\langle ij \rangle \in p} U_{ij}^{\gamma\gamma}$, where p is a hexagonal plaquette. In the pure Kitaev model, W_p is identified with the gauge-invariant \mathbb{Z}_2 flux, and the ground state lies in the sector with $W_p = +1$ for all plaquettes. States with $W_p = -1$ at isolated plaquettes are associated with vortex excitations¹. Besides the link variables $U_{ij}^{\mu\nu}$, in the mean-field approach we also consider the on-site fermion bilinears $V_i^{\mu\nu}$. It follows from the Kitaev representation that $V_i^{\gamma\gamma} = \langle \sigma_i^\gamma \rangle$. Moreover, the constraint in Eq. (3) implies $V_i^{\alpha\beta} = -V_i^{\beta\alpha}$ for $(\alpha\beta\gamma)$ a cyclic permutation of (xyz) . Thus, there are only three independent components of $V_i^{\mu\nu}$ at each site, and they are related to the local magnetization induced by the external magnetic field. In the limit $|h| \gg |K|, |J|, |\Gamma|$, we expect to encounter a partially polarized phase characterized by $V_i^{\mu\nu} \neq 0$ while $U_{ij}^{\mu\nu} = 0$ for all bonds. For further detail, see the “Methods” section.

Homogeneous case

We first describe the mean-field solution for the homogeneous case, i.e., in the absence of vortices. If the ground state does not break spin rotation or lattice symmetries, as in the Kitaev spin liquid phase, the matrices $U_{ij}^{\mu\nu}$ depend only on the bond type γ , and we set $U_{ij}^{\mu\nu} = U_\gamma^{\mu\nu}$ for bonds $\langle ij \rangle_\gamma$. Moreover, $V_i^{\mu\nu} = V^{\mu\nu}$ becomes a constant matrix. More generally, we can allow these parameters to vary with the sublattice within larger unit cells to describe magnetically ordered phases. We then solve the mean field self-consistency equations using a Fourier transform of the Majorana modes in the thermodynamic limit. As a first step, we have verified that our mean-field approach recovers the exact results for the Kitaev model¹ when we set $\Gamma = J = h = 0$. The resulting dispersion relation of Majorana fermions is depicted by dashed lines in Fig. 1. In this case, the only dispersive band is associated with the fermion c^0 . This band is gapless with a Dirac spectrum near the K point in the Brillouin zone (BZ). In addition, there are three degenerate flat bands associated with the fermions c^γ , which are related to the static gauge variables $U_\gamma^{\gamma\gamma}$ (whose value is independent of y).

Moving away from the exactly solvable point, we find that all bands become dispersive. For $h = 0$ and $K, J, \Gamma \neq 0$, our results are in quantitative agreement with a previous mean-field calculation³⁷. Our approach also allows us to take into account the magnetic field nonperturbatively. Figure 1 shows the dispersion for a magnetic field pointing along the crystallographic c direction (perpendicular to the honeycomb plane), with unit vector $\hat{c} = \frac{1}{\sqrt{3}}(1, 1, 1)$. Here the coordinates are specified in terms of the crystallographic axes \hat{x}, \hat{y} and \hat{z} of the ligand octahedra. For later reference, the in-plane unit vectors are $\hat{a} = \frac{1}{\sqrt{6}}(1, 1, -2)$ and $\hat{b} = \frac{1}{\sqrt{2}}(-1, 1, 0)$. As shown in Fig. 2, the magnetic field opens up a gap in the fermion spectrum, as expected for the non-Abelian Kitaev spin liquid phase. As we increase the magnetic field, the gap at the K point increases, but the gap at the Γ point decreases. The fermion gap Δ_f is given by the minimum between the energies at the K and Γ points in the BZ. If these energies cross, Δ_f exhibits a kink at the corresponding value of h (e.g., for $\Gamma = 0$ in Fig. 2). As we increase the magnetic field, we encounter a critical value h_c at which the gap either changes discontinuously, as in a first-order transition (e.g., for $\Gamma = -0.1|K|$ in Fig. 2), or it vanishes and varies continuously across the phase transition (e.g., for $\Gamma = 0.1|K|$ in Fig. 2). For $\mathbf{h} = h\hat{c}$ and $h \ll h_c$, the fermion gap increases with the magnetic field as $\Delta_f \propto h^2$, as expected from perturbation theory¹; see the inset in Fig. 2. For general field directions, the fermion gap behaves as $\Delta_f \propto h_x h_y h_z$, closing when one component of \mathbf{h} vanishes.

<https://doi.org/10.1038/s41535-024-00643-5>

Article

Fig. 1 | Majorana fermion dispersion. The dispersion relation of Majorana fermions calculated within the mean-field approach for the homogeneous system with $K = -1$, $J = 0$, $\Gamma = 0.2$, and $h = 0.4\hat{c}$, along the indicated BZ path. For comparison, the dashed lines show the dispersion in the pure Kitaev limit ($\Gamma = J = h = 0$).

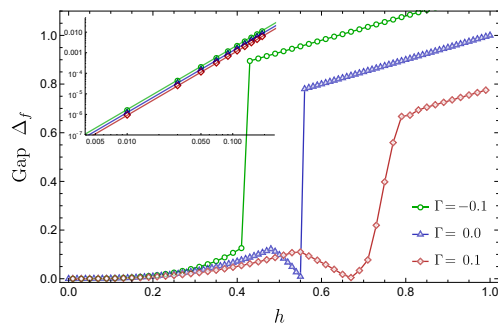
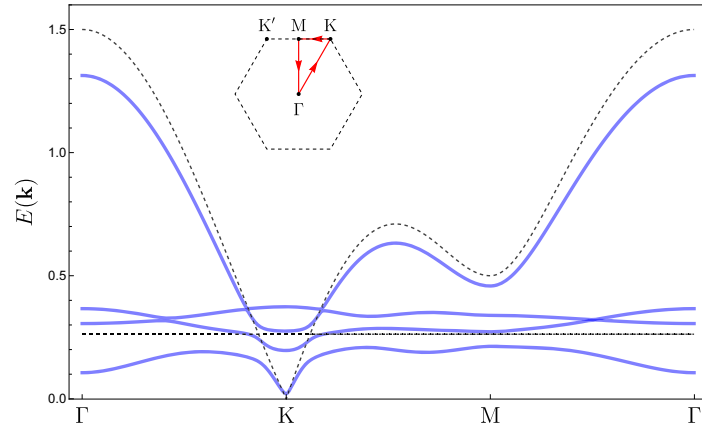


Fig. 2 | Field dependence of fermion gap. Fermion gap as a function of magnetic field for $h = h\hat{c}$ along the \hat{c} axis, with $K = -1$, $J = 0$, and for three values of Γ : $\Gamma = -0.1$ (green circles), $\Gamma = 0$ (blue triangles) and $\Gamma = 0.1$ (red diamonds). The inset shows that for weak fields the fermion gap agrees with the perturbative result to leading order in h , $\Delta_f \propto h^2$.

We further assess the stability of the Kitaev spin liquid phase by evaluating the \mathbb{Z}_2 flux parameter. In a homogeneous ground state, we have $W_p = (U_\gamma^\gamma)^6$. The result for the extended Kitaev model with $J = 0$ and $\Gamma, h \neq 0$ is shown in Fig. 3 for a magnetic field along the \hat{c} direction and for an in-plane field along the \hat{a} direction (perpendicular to the z bonds). As expected, U_γ^γ decreases as we increase h or Γ . The dots in this figure mark the transition where the gap Δ_f vanishes continuously. Note that U_γ^γ varies smoothly across the continuous transition for $h \parallel \hat{c}$ and $\Gamma > 0$.

The results in Figs. 2 and 3 allow us to determine the parameter regime where both U_γ^γ and Δ_f vary smoothly and take values comparable to those at the exactly solvable point. In this regime, we expect the mean-field approach to yield qualitatively correct results for the charge response of the Kitaev spin liquid phase. By contrast, the regime of strong magnetic fields should be identified with the partially polarized phase, whereas the regime of large $|\Gamma|$ or $|J|$ harbors magnetically ordered phases^{35,44,48,53}. Here we do not explore the various phases of the extended Kitaev model, whose nature is not completely settled³⁶. Nevertheless, our mean-field results reproduce qualitative features of phase diagrams reported in the literature. For instance, we find that adding $\Gamma > 0$ increases the critical magnetic field along the \hat{c} direction, but the Kitaev spin liquid phase shrinks as we tilt the field toward the plane, in agreement with exact diagonalization results⁴⁸. However, in general the mean-field approach overestimates the value of the critical

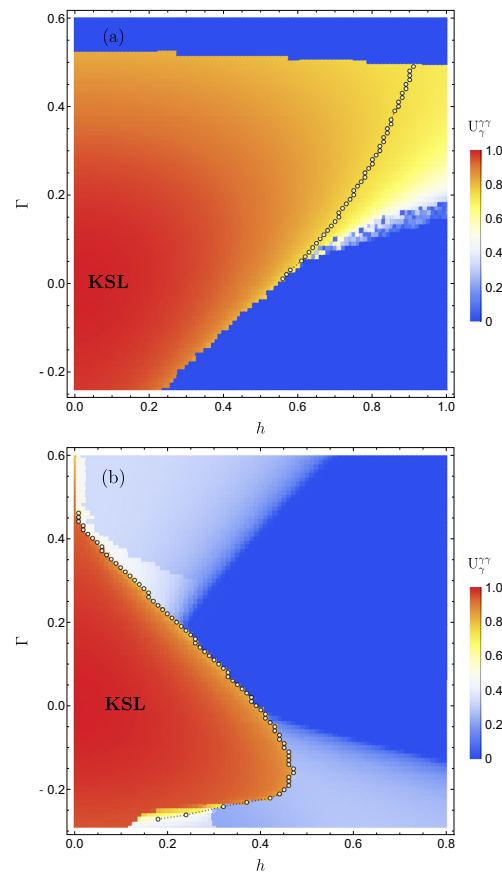


Fig. 3 | Mean-field parameter for Kitaev spin liquid phase. Mean-field parameter U_γ^γ for fixed $K = -1$ and $J = 0$ as a function of the Γ interaction and the strength of the magnetic field along two directions: **a** $h \parallel \hat{c}$, perpendicular to the honeycomb plane; **b** an in-plane field $h \parallel \hat{a}$. White circles represent critical points where the fermion gap closes at the Γ point in the BZ. The region labeled as KSL is identified with the Kitaev spin liquid phase.

<https://doi.org/10.1038/s41535-024-00643-5>

Article

magnetic field for a ferromagnetic Kitaev coupling in comparison with more accurate numerical methods^{48,54–56}.

Vortex charge density profile

Inhomogeneous spin correlations can bring on a charge redistribution in Mott insulators^{32,33}. We here discuss the charge density profile induced by the presence of \mathbb{Z}_2 vortices in a Kitaev spin liquid. In the “Methods” section, we derive the effective charge imbalance operator in terms of two-spin operators and show how to compute its expectation value $\langle \delta n_l \rangle$ at lattice site l using the Majorana mean-field approach.

We consider an inhomogeneous state in which translation symmetry is broken by the presence of vortices. In this case, we analyze the mean-field Hamiltonian on a finite system with linear size L along the directions of the primitive lattice vectors $\hat{\mathbf{e}}_1 = \frac{1}{2}\hat{\mathbf{a}} + \frac{\sqrt{3}}{2}\hat{\mathbf{b}}$ and $\hat{\mathbf{e}}_2 = -\frac{1}{2}\hat{\mathbf{a}} + \frac{\sqrt{3}}{2}\hat{\mathbf{b}}$, imposing periodic boundary conditions. To create vortices, we initialize the mean-field parameters in a configuration where we flip the sign of $U_{ij}^{\mu\nu}$ on bonds crossed by open strings. In the pure Kitaev model, this procedure generates exact eigenstates with two localized vortices at the ends of the string. In the extended Kitaev model, vortices become mobile excitations with effective bandwidths governed by the integrability-breaking perturbations^{57,58}. In fact, for sufficiently large values of these perturbations, near the border of the Kitaev spin liquid phase in Fig. 3, we observe that the vortex positions vary as we iterate the self-consistency equations. When this happens, the string length decreases and the vortices move closer to each other until they annihilate, and the mean-field solution converges to the vortex-free ground-state configuration. However, for $|\Gamma|, |J|, |h| \ll |K|$ and well separated vortices, we find a self-consistent solution with (metastable) localized vortices which corresponds to a local energy minimum in this sector of the Hilbert space. These results seem consistent with the real-time dynamics described by time-dependent mean-field theory, which show that only when the perturbations are strong enough do vortices become mobile as signaled by the time decay of the fermion Green’s function⁴⁶. In reality, the lifetime of a vortex is limited by processes in which two vortices meet and annihilate⁵⁸, and can become arbitrarily long at low temperatures due to the low vortex density; see Supplementary Note 1. Focusing on the regime of small perturbations, we can then compute static spin correlations near vortices using position-dependent mean-field parameters $U_{ij}^{\mu\nu}$ and $V_i^{\mu\nu}$. We consider a configuration with four equally spaced vortices, see inset of Fig. 5b, which preserves rotational symmetries and minimizes finite-size effects as compared to a two-vortex configuration. Unless stated otherwise, we use $L = 40$, so the distance between vortices is 20 unit cells. The charge imbalance near a vortex is then effectively the property of a single vortex and finite-size effects only appear in long-distance tails (see Supplementary Note 2).

In ref. 30, the charge imbalance profile in the vicinity of a vortex was investigated within the exactly solvable Kitaev model¹:

$$H_K = \sum_{\langle ij \rangle_\gamma} K_\gamma \sigma_i^\gamma \sigma_j^\gamma - \sum_{\langle ij \rangle_\alpha \langle jk \rangle_\beta} \kappa \sigma_i^\alpha \sigma_j^\gamma \sigma_k^\beta, \quad (6)$$

setting $K_\gamma = K$ for isotropic Kitaev interactions. The three-spin interaction breaks time-reversal symmetry while preserving integrability. The coupling constant derived from perturbation theory in the magnetic field is¹:

$$\kappa = 0.338 \frac{h_x h_y h_z}{\Delta_{2v}^2}, \quad (7)$$

where $\Delta_{2v} \approx 0.263|K|^{3/2}$ is the energy gap for creating two adjacent vortices at zero magnetic field. The prefactor in Eq. (7) was obtained by fitting the fermion gap $\Delta_v = 6\sqrt{3}\kappa$ at low fields; see the inset of Fig. 2. Our mean-field results for the extended Kitaev model confirm the qualitative behavior obtained for the exactly solvable model; see Fig. 4. The charge imbalance oscillates between positive and negative values as we vary the distance from the center of the vortex, identified with the plaquette where $W_p < 0$. Moreover, as shown in Fig. 5, the magnitude of $\langle \delta n_l \rangle$ decays exponentially with the distance from the vortex. The comparison with the result for $\Gamma = 0$

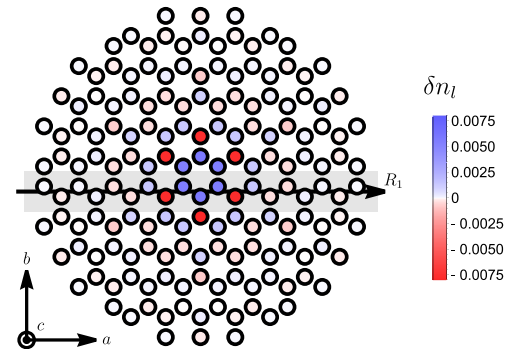


Fig. 4 | Charge imbalance around a vortex. Charge imbalance $\langle \delta n_l \rangle$ in a state with a vortex located in the central hexagon. As parameters of the Hubbard–Kanamori model, we use $t_1 = 13$ meV, $t_2 = 160$ meV, $t_3 = -33$ meV, $t'_2 = -60$ meV, $U = 2.6$ eV, and $J_H = 300$ meV. The values of δn_l are in units of $|t_2^2 t_3^2 / U^3| \approx 8.739 \times 10^{-5}$. The ratio between the exchange couplings calculated using Eq. (22) are $\Gamma/|K| = 0.20$ and $J/|K| = -0.02$. We set the magnetic field $h/|K| = 0.2\hat{\mathbf{c}}$. The solid line marks the zigzag path considered in Fig. 5.

(dashed lines in Fig. 5) reveals that weak Γ and/or J interactions have an only minor effect on the ideal charge imbalance profile found in the pure Kitaev limit³⁰. However, changing the magnetic field direction away from the $\hat{\mathbf{c}}$ direction can induce more pronounced charge oscillations, cf. Fig. 5b, and thus has a more substantial effect. The value of $|\delta n_l|$ on sites around the vortex is of the order of 10^{-6} , producing local electric fields near the detection limit of state-of-the-art atomic force microscopy^{60,62}. Importantly, here we use estimates for the hopping and interaction parameters for bulk α -RuCl₃, but the charge fluctuations can be greatly enhanced if the on-site repulsion U is screened in a monolayer by the interaction with a substrate.

Since the mean-field approach allows us to treat the Zeeman term nonperturbatively, we can go beyond the results of ref. 30 and analyze the dependence of the charge redistribution on the field direction. For a field along the $\hat{\mathbf{c}}$ direction, the charge imbalance profile is isotropic around the position of the vortex, up to small variations due to the finite distance between vortices in the finite-size system. As we tilt the magnetic field on the ac plane (perpendicular to the z bonds), a small anisotropy develops in a way that the charge imbalance is enhanced in the direction perpendicular to the field. This effect can be seen in Fig. 5b as the difference between $\langle \delta n_l \rangle$ for the sites that belong to the hexagon that contains the vortex (three blue dots in the center, cf. Fig. 4).

We next quantify the anisotropy in the charge distribution by computing the electric multipole moments. We note that the electric quadrupole moment has also been studied in the context of the spin nematic transition in the vortex-free ground state of a perturbed Kitaev model⁶³. In the limit of very large distance between vortices, the electric dipole moment vanishes because the system is invariant under spatial inversion about the vortex center. The first nontrivial multipole moment is the traceless quadrupole tensor, with components:

$$Q_{\alpha\beta} = \sum_l \langle \delta n_l \rangle (3R_{l\alpha}R_{l\beta} - |\mathbf{R}_l|^2 \delta_{\alpha\beta}). \quad (8)$$

Here $\alpha, \beta \in \{1, 2, 3\}$ and $\mathbf{R}_l = R_{l1}\hat{\mathbf{a}} + R_{l2}\hat{\mathbf{b}}$ (with $R_{l3} = 0$) is the position of site l , setting the lattice spacing to unity. Due to the finite system size, we calculate the quadrupole moment by summing over all sites within a finite radius around the vortex. This radius is taken to be slightly smaller than half the distance between vortices, but due to the exponential decay of $\langle \delta n_l \rangle$ with the distance from the vortex center, changing this radius causes only exponentially small changes in the quadrupole tensor. For a magnetic field

<https://doi.org/10.1038/s41535-024-00643-5>

Article

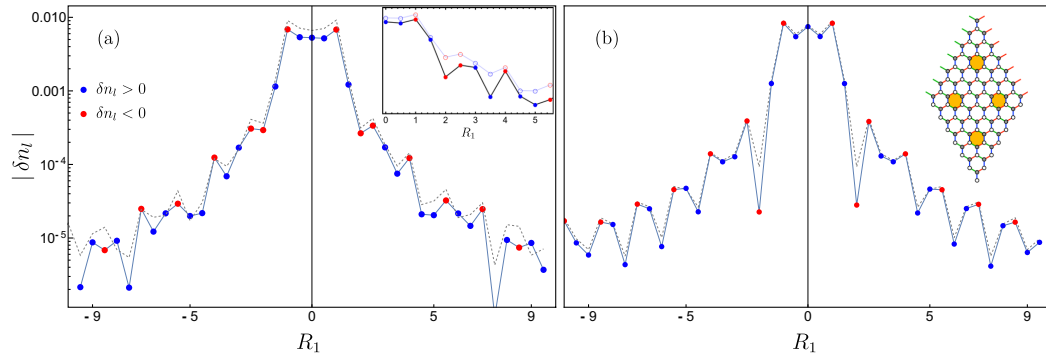


Fig. 5 | Spatial and magnetic field dependence of the charge imbalance profile. Magnitude of the charge imbalance as a function of the position R_1 along the zigzag path represented by the black line in Fig. 4. The dots (connected by solid lines to guide the eye) correspond to the extended Kitaev model with exchange couplings $\Gamma/|K| = 0.2$ and $J/|K| = -0.02$. Blue and red represent positive and negative charges, respectively. We set $|\mathbf{h}| = 0.3|K|$ and consider two field directions: $\mathbf{a} \parallel \hat{\mathbf{h}}$ and

$\mathbf{b} \parallel \hat{\mathbf{z}}$. For comparison, dashed lines represent the corresponding mean-field results for $\Gamma = 0$ and otherwise identical parameters. The inset in (a) shows the corresponding case with $\Gamma/|K| = 0.35$ and $J/|K| = -0.05$ for $\mathbf{h} \parallel \hat{\mathbf{c}}$ (filled circles), comparing with the results for $\Gamma/|K| = 0.2$ and $J/|K| = -0.02$ in the main plot (empty circles). The values of δn_l are in units of $|t_2^2 t_2'/U^3|$. The inset in (b) shows the geometry with four equally spaced vortices on the torus with a smaller system size.

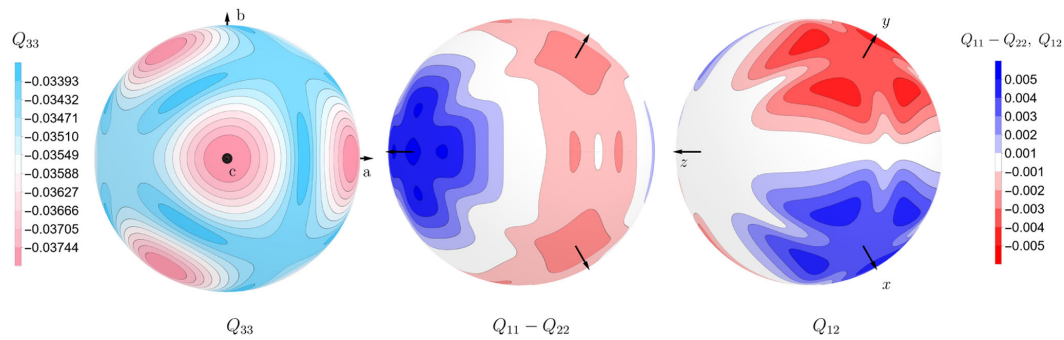


Fig. 6 | Quadrupole moment for different field directions. Quadrupole components as a function of magnetic field direction, calculated using the exactly solvable Hamiltonian in Eq. (6), i.e., for $J = \Gamma = 0$. The coupling constants K_y and κ were

calculated using Eqs. (7) and (9) with $|\mathbf{h}| = 0.2|K|$ and $\Delta_{2v} = 0.263|K|$. The scale is in units of $t_2^2 t_2'/U^3$ and we set the lattice spacing to unity. Here we use $L = 42$.

along the $\hat{\mathbf{c}}$ direction, the rotational symmetry implies that the quadrupole tensor is diagonal and $Q_{11} = Q_{22} = -Q_{33}/2$. As we vary the field direction, the anisotropy is manifested in the difference between Q_{11} and Q_{22} and in the off-diagonal element Q_{12} . Note that Q_{13} vanishes identically because $R_{13} = 0$.

In a first approximation, let us discuss the dependence of the quadrupole tensor on the magnetic field direction by treating the field perturbatively in the pure Kitaev model. For magnetic field directions not perpendicular to the lattice plane, the (often discarded) contribution from second-order perturbation theory generates an anisotropic renormalization of the Kitaev couplings. This effect is captured by the Hamiltonian in Eq. (6) with:

$$K_y = K - \frac{(h_y)^2}{\Delta_{2v}}. \quad (9)$$

In Fig. 6, we show the angular dependence of the quadrupole components Q_{33} , $Q_{11} - Q_{22}$ and Q_{12} calculated from the spin correlations for the model in Eq. (6). The component Q_{33} does not change sign, but varies slightly around an average value with an angular dependence qualitatively similar to $|h_x h_y h_z|$. In particular, Q_{33} is maximum for a field along the $\hat{\mathbf{c}}$ direction,

which may be interesting to maximize the intrinsic electric field produced at positions right above the vortex. On the other hand, the difference $Q_{11} - Q_{22}$ vanishes for $\mathbf{h} \parallel \hat{\mathbf{c}}$, but is maximum when the field points along the $\hat{\mathbf{z}}$ axis; this is the direction in which the anisotropy in the effective Kitaev couplings is maximized, with $K_z < K_x = K_y$. Finally, Q_{12} vanishes if we tilt the field along the high-symmetry ac plane, but becomes nonzero for more general field directions.

The spin correlations calculated within the mean-field approach for the extended Kitaev model lead to the same qualitative dependence on the field direction as in Fig. 6. To maximize the anisotropy in the quadrupole tensor, we focus on the direction $\mathbf{h} = h\hat{\mathbf{z}}$, in which case all off-diagonal components vanish, and analyze how the diagonal components vary with the strength of the magnetic field. Here it is convenient to introduce the dimensionless anisotropy parameter $\Delta Q = (Q_{11} - Q_{22})/|Q_{33}|$. As shown in Fig. 7, ΔQ increases with h , and the effect is more pronounced in the presence of the Γ interaction. We have also studied the case $\Gamma < 0$ and find qualitatively similar results (see Supplementary Note 3).

The spatial anisotropy of the charge density profile affects the electric quadrupole interaction between vortices. Suppose the first vortex is located at the origin and the second one at $\mathbf{r} = x_1 \hat{\mathbf{a}} + x_2 \hat{\mathbf{b}}$, with $r = |\mathbf{r}|$ much larger than the length scale in the decay of δn_l . The interaction is given by the

<https://doi.org/10.1038/s41535-024-00643-5>

Article

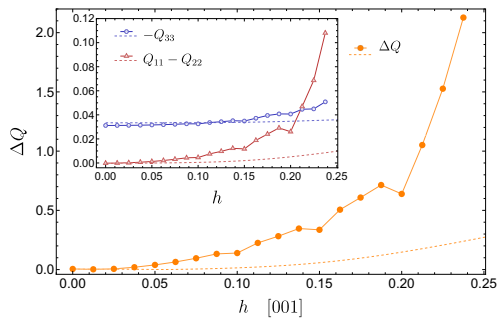


Fig. 7 | Dependence of the quadrupole anisotropy on the magnetic field strength. Symbols represent the mean-field results for $\Delta Q = (Q_{11} - Q_{22})/|Q_{33}|$ in the extended Kitaev model with $\Gamma/K = 0.3$, $J = 0$, and $\mathbf{h} = h\hat{z}$. Dashed lines follow from the solvable Hamiltonian in Eq. (6) with $K = -1$. Inset: quadrupole components Q_{33} and $Q_{11} - Q_{22}$ (in units of $t_2^2 t_2 / U^2$) and setting the lattice spacing to unity).

energy \mathcal{E} of the quadrupole tensor $Q^{(2)}$ of the second vortex in the electrostatic potential $V^{(1)}$ generated by the first vortex:

$$\mathcal{E} = \frac{1}{6} \sum_{\alpha\beta} Q_{\alpha\beta}^{(2)} \partial_\alpha \partial_\beta V^{(1)}(\mathbf{r}), \quad (10)$$

where $V^{(1)}(\mathbf{r}) = \frac{1}{2\pi\epsilon} \sum_{\alpha\beta} x_\alpha x_\beta Q_{\alpha\beta}^{(1)}$. Since well-separated vortices generate the same charge distribution, we now assume $Q^{(1)} = Q^{(2)} = Q$. As a result, the quadrupolar interaction can be written as:

$$\mathcal{E} = \frac{1}{12} \left[\frac{35}{r^9} (\mathbf{r} \cdot \mathbf{Q} \cdot \mathbf{r})^2 - \frac{20}{r^7} (\mathbf{r} \cdot \mathbf{Q}^2 \cdot \mathbf{r}) + \frac{2}{r^5} \text{tr}(Q^2) \right]. \quad (11)$$

When the magnetic field varies along the ac plane, the quadrupole tensor is diagonal and we obtain $\mathcal{E} = \frac{Q_{33}}{r^5} F(\Delta Q, \theta)$. Here θ is the angle between \mathbf{r} and $\hat{\mathbf{a}}$, and we use:

$$F(\Delta Q, \theta) = \frac{9}{8} + \frac{5}{4} \cos(2\theta) \Delta Q + \left[\frac{35}{24} \cos^2(2\theta) - \frac{2}{3} \right] \Delta Q^2, \quad (12)$$

with the property $F(-\Delta Q, \theta) = F(\Delta Q, \pi/2 - \theta)$. In particular, $\Delta Q = 0$ for a magnetic field along the \hat{c} direction; in this case, the quadrupolar interaction becomes strictly repulsive and independent of θ . However, as illustrated in Fig. 8, the interaction can change sign for some particular directions of \mathbf{r} if the anisotropy is strong enough. The attractive regime appears for $|\Delta Q| > \sqrt{9/7} \approx 1.13$. According to the result in Fig. 7, this regime becomes accessible for sufficiently large h and Γ with \mathbf{h} along the \hat{z} direction. We note that already in the pure Kitaev model, vortices have an effective interaction that depends on the vortex separation⁶⁴. The charge redistribution discussed here provides a mechanism to make this interaction spatially anisotropic. In the extended Kitaev model, where vortices acquire a small mobility³⁸, the charge density profile must be carried along with the slow vortex motion, and the anisotropic interaction may cause some nontrivial dynamics in a system of dilute vortices. Importantly, the quadrupole interaction decays algebraically with the distance between vortices; thus, at large distances it dominates over other sources of vortex-vortex interactions that are expected to decay exponentially⁶⁴.

Electrical manipulation of vortices

We now consider the effect of a local electrostatic potential on vortices. Going back to the Hubbard–Kanamori model, we couple the hole density to a potential V_0 on the six sites surrounding a hexagonal plaquette p where a vortex is located. This local potential can be generated by the electric field of a scanning tunneling microscope (STM) tip. Redoing the derivation of the

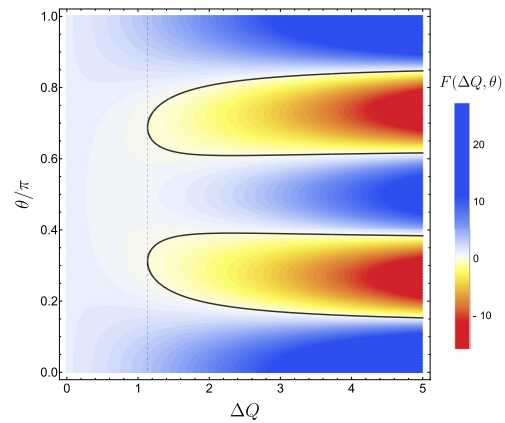


Fig. 8 | Quadrupolar interaction. Function $F(\Delta Q, \theta)$ that governs the sign of the quadrupolar interaction for $\Delta Q > 0$. For $\Delta Q < 0$, see the relation below Eq. (12). The dashed line marks the critical value $|\Delta Q| = \sqrt{9/7}$, below which the interaction is always repulsive. The black solid line corresponds to $F(\Delta Q, \theta) = 0$.

effective spin Hamiltonian by second-order perturbation theory, we find that the local potential modifies the couplings on bonds between sites in p and their nearest neighbors outside p ; see Eq. (23). In addition, the local electric potential breaks inversion symmetry and generates a Dzyaloshinskii–Moriya (DM) interaction³⁴. Microscopically, the DM interaction stems from crystal field splittings in the atomic Hamiltonian and asymmetries in the hopping matrix due to lattice distortions⁵. We investigate this effect phenomenologically by adding to the effective spin Hamiltonian (1) the term:

$$H_{\text{DM}} = \sum_{\gamma} \sum_{\langle ij \rangle_{\gamma}} D_{ij} \left(\sigma_i^{\alpha} \sigma_j^{\beta} - \sigma_i^{\beta} \sigma_j^{\alpha} \right), \quad (13)$$

where $(\alpha\beta\gamma)$ is a cyclic permutation of (xyz) . The coupling $D_{ij} = D(V_0)$ is taken to be independent of the bond type γ but restricted to the bonds exterior to the plaquette with the local potential. For the DM coupling, we assume (see Supplementary Note 4):

$$D(V_0) = \xi_1 D_1 |K(0)|, \quad \xi_1 = \frac{eV_0}{U - 3J_{\text{H}}}, \quad (14)$$

such that $D(V_0) \propto V_0$ with a dimensionless free parameter D_1 . In fact, for $V_0 = 0$, the DM coupling is absent since it will be generated by the tip potential.

In the solvable Kitaev model, the local electric potential lowers the energy of an isolated vortex with respect to the vortex-free configuration, but never closes the vortex gap in the absence of the DM interaction³⁰. In that case, this effect can be used to attract and bind vortices that have been created by some other mechanism, such as thermal fluctuations, but it does not induce vortices in the ground state of the system. Using the mean-field approach, we can now analyze how the vortex gap varies with the electric potential in the extended Kitaev model. We consider again the configuration with four equally spaced vortices, see the inset in Fig. 5b, and apply the electric potential on the four corresponding plaquettes. The difference between the energy E_{4v} of this four-vortex configuration and the energy E_{0v} of the vortex-free state is equal to four times the vison gap. As shown in Fig. 9, the vison gap monotonically decreases with the applied electric potential, and it is further reduced for nonzero Γ and finite DM coupling D_1 . When the gap becomes too small, we encounter difficulties in the convergence of the mean-field equations. However, the extrapolation of the

<https://doi.org/10.1038/s41535-024-00643-5>

Article

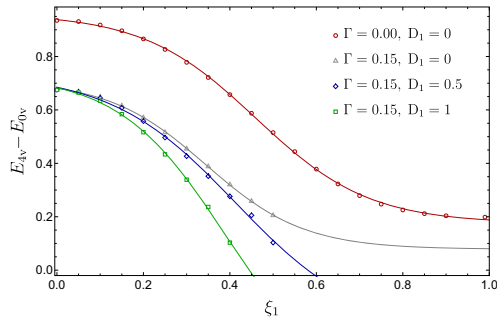


Fig. 9 | Energy of four-vortex state. Energy of the four-vortex state vs. applied electrostatic potential V_0 , with the dimensionless quantity $\xi_1 = eV_0/(U - 3J_H)$, for different values of Γ and of the DM coupling D_1 ; see Eq. (14). Symbols represent mean-field results for the extended Kitaev model with $K = -1$, $J = 0$ and the magnetic field $\mathbf{h} = 0.2\hat{z}$. The linear system size is $L = 28$, and solid lines are a guide to the eye only. They were obtained by a fit to the function $a + b \tanh[c(\xi_1 - d)]$.

results indicates that the gap vanishes for sufficiently large V_0 . As a consequence, we predict that it is possible to create (or remove) vortices by modulating the local interactions, in agreement with the results of ref. 34. We emphasize that this remarkable functionality arises due to the interplay between Γ interactions and the local DM terms induced by an STM tip. From Fig. 9, we observe that $\xi_1 \sim 0.5$ is sufficient to create vortices. Using the parameters listed in Fig. 4, we find that this corresponds to realistic tip voltages of the order of $V_0 < 1$ V.

Discussion

We have studied how vortices in Kitaev spin liquids generate and respond to nonuniform electric fields. While Kitaev materials are Mott insulators, charge fluctuations can be generated at low energies by inhomogeneous spin correlations that carry signatures of localized excitations. To describe this effect, we started from the three-orbital Hubbard–Kanamori model for Kitaev materials. Using a canonical transformation, we obtain effective operators in the low-energy sector in terms of spin operators that act on the pseudospin-1/2 states. The effective spin Hamiltonian is the extended Kitaev model in a magnetic field, in which the exact solvability is broken by the Heisenberg and Γ interactions as well as by a Zeeman coupling to a magnetic field. We generalized the effective density operator beyond the results of ref. 30 to include off-diagonal terms that are absent in the pure Kitaev model.

We have developed and applied a Majorana mean-field approach which allows us to consider inhomogeneous parameters. While this approach is exact for the pure Kitaev model, we have demonstrated that it captures qualitative features of the Kitaev spin liquid phase in the extended JKT model, where additional spin interactions are present. This model is believed to describe the candidate material α -RuCl₃. The electric charge distribution follows by computing the spin correlations around vortices in the mean-field approach. Importantly, vortices remain localized on sufficiently long time scales even in the presence of small perturbations around the Kitaev limit, as long as the system remains deep in the Kitaev spin liquid phase. We find that the charge profile decays with the distance from the vortex in an oscillatory fashion.

Our results allow us to calculate the intrinsic electric quadrupole tensor of a vortex which is far away from all other vortices. The anisotropy of the quadrupole tensor can here be controlled by the magnetic field, and depending on the parameter regime, the interaction between different vortices is either repulsive or attractive. The interaction is generally enhanced by the Γ interaction.

Finally, in the presence of local STM tips near vortices, we find that one can close the vortex gap by applying a local electric potential to the tips. We

thus predict that one can create vortices in a Kitaev spin liquid by means of STM tips in a controlled way. Given the recent advances in STM technology^{60–62}, our work paves the way for the electrical detection and manipulation in Kitaev materials. In particular, the successful control of Ising anyons in such materials would constitute a key step toward implementing a platform for topological quantum computation.

Methods

Extended Kitaev model

The JKT model in Eq. (1) follows by projecting the three-orbital Hubbard–Kanamori Hamiltonian on the honeycomb lattice, $H_{HK} = V + H_{so} + T$, to the low-energy sector spanned by a single hole per site. On-site interactions are encoded by:

$$V = \sum_i \left[\frac{U - 3J_H}{2} (\bar{N}_i - 1)^2 - 2J_H S_i^2 - \frac{J_H}{2} \mathbf{L}_i^2 \right], \quad (15)$$

where U is the repulsive interaction strength, J_H is Hund's coupling, and the operators \bar{N}_i , S_i and \mathbf{L}_i are the total number, spin and orbital angular momentum of holes at site i . The operator $h_{i\alpha\sigma}^\dagger$ creates a hole at site i with spin $\sigma \in \{\uparrow, \downarrow\}$ and orbital $\alpha \in \{x, y, z\}$ for yz, xz , and xy orbitals, respectively. Defining the spinor $h_i^\dagger = (h_{ix\uparrow}^\dagger, h_{iy\uparrow}^\dagger, h_{iz\uparrow}^\dagger, h_{ix\downarrow}^\dagger, h_{iy\downarrow}^\dagger, h_{iz\downarrow}^\dagger)$, we write:

$$\bar{N}_i = h_i^\dagger h_i, \quad S_i = \frac{1}{2} h_i^\dagger (\boldsymbol{\sigma} \otimes \mathbb{1}_3) h_i, \quad \mathbf{L}_i = h_i^\dagger (\mathbb{1}_2 \otimes \mathbf{L}) h_i, \quad (16)$$

where $\boldsymbol{\sigma}$ is the vector of Pauli matrices acting in spin space and $\mathbf{L} = (L_x, L_y, L_z)$ is a vector of 3×3 matrices that represent the effective $l = 1$ angular momentum of the t_{2g} states³⁰. The spin-orbit coupling term $H_{so} = \lambda \sum_{i\alpha} h_i^\dagger (\boldsymbol{\sigma}^\alpha \otimes \mathbf{I}^\alpha) h_i$ splits the degeneracy of the t_{2g} manifold. At each site, the low-energy subspace is spanned by the states:

$$\begin{aligned} |+\rangle &= \frac{1}{\sqrt{3}} (|z, \uparrow\rangle - i|y, \downarrow\rangle - |x, \downarrow\rangle), \\ |-\rangle &= \frac{1}{\sqrt{3}} (|z, \downarrow\rangle + i|y, \uparrow\rangle - |x, \uparrow\rangle), \end{aligned} \quad (17)$$

which are associated with total angular momentum $j_{\text{eff}} = \frac{1}{2}$. Finally, the hopping term in H_K has the form $T = -\sum_{ij} h_i^\dagger (\mathbb{1}_2 \otimes \mathbf{T}_{ij}) h_j$. The hopping matrix \mathbf{T}_{ij} in orbital space depends on the orientation of the bond between sites i and j . We label the bonds on the honeycomb lattice by $\gamma \in \{x, y, z\}$ $\equiv \{1, 2, 3\}$ corresponding to nearest-neighbor vectors $\boldsymbol{\delta}_x = \frac{1}{2}\hat{\mathbf{a}} + \frac{1}{2\sqrt{3}}\hat{\mathbf{b}}$, $\boldsymbol{\delta}_y = -\frac{1}{2}\hat{\mathbf{a}} + \frac{1}{2\sqrt{3}}\hat{\mathbf{b}}$, and $\boldsymbol{\delta}_z = -\frac{1}{\sqrt{3}}\hat{\mathbf{b}}$, respectively. We parametrize the hopping matrix for a nearest-neighbor z bond as³⁵

$$\mathbf{T}_{(ij)_z} = \begin{pmatrix} t_1 & t_2 & t_4 \\ t_2 & t_1 & t_4 \\ t_4 & t_4 & t_3 \end{pmatrix}. \text{ The hopping matrix for } x \text{ and } y \text{ bonds follows}$$

by cyclic permutation of the orbital indices. Microscopically, the hopping parameters are associated with direct hopping between d orbitals or hoppings mediated by the ligand ions. Neglecting trigonal distortions for simplicity, we set $t_4 = 0$ ³⁵.

The effective spin Hamiltonian for the Mott insulating phase can now be derived by applying perturbation theory in the regime $U, J_H \gg \lambda \gg t_1, t_2, t_3$. We use the canonical transformation:

$$\begin{aligned} \tilde{H}_{HK} &= e^S H_{HK} e^{-S} \\ &= H_{HK} + [S, H_{HK}] + \frac{1}{2} [S, [S, H_{HK}]] + \dots \end{aligned} \quad (18)$$

The anti-Hermitian operator $S = \sum_{k=1}^\infty S_k$ is chosen so that S_k eliminates the terms that change the hole occupation numbers \bar{N}_i at k -th order in the hopping parameters. We can write $S_k = S_k^+ - S_k^-$, where S_k^+ creates excitations with $\bar{N}_i \neq 1$ and $S_k^- = (S_k^+)^\dagger$. For the calculation of the effective spin Hamiltonian, it suffices to consider the first-order term $S_1 = S_1^+ - S_1^-$,

<https://doi.org/10.1038/s41535-024-00643-5>

Article

with:

$$S_1^+ = \sum_{ij} \sum_{\ell=0}^2 \frac{1}{\Delta E_\ell} \mathcal{P}_{i,\ell}^{(2)} h_i^\dagger (1 \otimes \mathbf{T}_{ij}) h_j \mathcal{P}_j^{(1)}. \quad (19)$$

Here $\mathcal{P}_j^{(1)}$ is a projector onto the subspace of a single hole at site j and $\mathcal{P}_{j,\ell}^{(2)}$ projects onto the subspace of two holes with total angular momentum $\ell \in \{0, 1, 2\}$. The excited states have energies ΔE_ℓ given by:

$$\Delta E_0 = U + 2J_H, \quad \Delta E_1 = U - 3J_H, \quad \Delta E_2 = U - J_H, \quad (20)$$

with $J_H < U/3$ in the Mott insulating phase. We then take $H = P_{\text{low}} \tilde{H}_{\text{HK}} P_{\text{low}}$, where $P_{\text{low}} = \prod_i (|+i\rangle\langle +i| + |-i\rangle\langle -i|)$ is the projector onto the low-energy subspace restricted to $j_{\text{eff}} = \frac{1}{2}$ states at every site. We thereby arrive at the JKT model³⁵:

$$H = \sum_{\langle ij \rangle} \left[J \sigma_i \cdot \sigma_j + K \sigma_i^y \sigma_j^y + \Gamma \left(\sigma_i^\alpha \sigma_j^\beta + \sigma_i^\beta \sigma_j^\alpha \right) \right], \quad (21)$$

with an implicit sum over bond type γ , and α, β chosen so that $(\alpha\beta\gamma)$ is a cyclic permutation of (xyz) . The couplings are:

$$\begin{aligned} J &= \frac{1}{27} \left[\frac{(2t_1 + t_2)^2}{\Delta E_0} + \frac{6t_1(t_1 + 2t_2)}{\Delta E_1} + \frac{2(t_1 - t_2)^2}{\Delta E_2} \right], \\ K &= \frac{2J_H}{9} \frac{(t_1 - t_2)^2 - 3t_2^2}{\Delta E_1 \Delta E_2}, \quad \Gamma = \frac{4J_H}{9} \frac{t_2(t_1 - t_2)}{\Delta E_1 \Delta E_2}. \end{aligned} \quad (22)$$

In the limit $t_1, t_2 \rightarrow 0$ and $t_2 \neq 0$, Eq. (21) reduces to the exactly solvable Kitaev model¹ with a ferromagnetic Kitaev interaction ($K < 0$). Finally, in the presence of a potential V_0 , the respective couplings are renormalized according to:

$$\begin{aligned} J(V_0) &= \frac{1}{27} \left[\frac{(2t_1 + t_2)^2}{(1 - \xi_0^2) \Delta E_0} + \frac{6t_1(t_1 + 2t_2)}{(1 - \xi_1^2) \Delta E_1} + \frac{2(t_1 - t_2)^2}{(1 - \xi_2^2) \Delta E_2} \right], \\ \frac{K(V_0)}{K(0)} &= \frac{\Gamma(V_0)}{\Gamma(0)} = \frac{1 + \xi_1 \xi_2}{(1 - \xi_1^2)(1 - \xi_2^2)}, \end{aligned} \quad (23)$$

where $\xi_\ell = eV_0/\Delta E_\ell$.

Mean-field Hamiltonian

Using the mean-field parameters in Eq. (5), the Majorana mean-field Hamiltonian for Eq. (4) is given by:

$$H_{\text{MF}} = \sum_{ij} \frac{i}{4} c_i^\dagger A_{ij} c_j + \sum_i \frac{i}{4} c_i^\dagger B_i c_i - C. \quad (24)$$

The first term on the right-hand side couples Majorana fermions on nearest-neighbor bonds $\langle ij \rangle$ via the 4×4 bond-dependent matrix:

$$A_{ij} = 2 \sum_{\alpha\beta} J_{ij}^{\alpha\beta} \mathbf{N}^\alpha U_{ij} \mathbf{N}^\beta. \quad (25)$$

The on-site term involves the matrix:

$$B_i = \sum_{j \in \mathcal{V}_i} \sum_{\alpha\beta} J_{ij}^{\alpha\beta} \mathbf{N}^\alpha \text{tr}(\mathbf{V}_j^\dagger \mathbf{N}^\beta) + \sum_\gamma (\lambda_i^\gamma G^\gamma - 2h^\gamma \mathbf{N}^\gamma), \quad (26)$$

where \mathcal{V}_i denotes the set of nearest neighbors of site i . Finally, the constant term is:

$$C = \frac{1}{8} \sum_{ij} \sum_{\alpha\beta} J_{ij}^{\alpha\beta} \left[\text{tr}(\mathbf{V}_i^\dagger \mathbf{N}^\alpha) \text{tr}(\mathbf{V}_j^\dagger \mathbf{N}^\beta) + 2 \text{tr}(\mathbf{U}_{ij}^\dagger \mathbf{N}^\alpha \mathbf{U}_{ij} \mathbf{N}^\beta) \right]. \quad (27)$$

We diagonalize Eq. (24) for N unit cells of the honeycomb lattice with periodic boundary conditions by using:

$$c = \sqrt{2} \mathbb{U} \begin{pmatrix} d \\ d^\dagger \end{pmatrix}, \quad \mathbb{U} = \begin{pmatrix} \mathbb{U}_< & \mathbb{U}_> \end{pmatrix}, \quad (28)$$

where c is a vector defined from $8N$ Majorana fermions, \mathbb{U} is a unitary transformation, and d is a $4N$ -component vector of annihilation operators of complex fermions. The columns of $\mathbb{U}_{<(>)}$ correspond to the eigenvectors of the mean-field Hamiltonian with negative (positive) energy. The mean-field ground state is the state annihilated by all d operators, from which we obtain the self-consistency conditions:

$$\langle ic_1 c_1 \rangle = i(\mathbb{U}_< \mathbb{U}_<^\dagger)_{11}, \quad (29)$$

where $I = (i, \mu)$ and $J = (j, \nu)$ combine site and fermion flavor indices. We obtain the mean-field parameters in Eq. (5) by setting i and j to be either nearest neighbors or the same site. Together with the mean-field Hamiltonian, Eq. (29) defines a set of self-consistent equations which we then solve numerically.

In our approach, we require that the constraint in Eq. (3) is satisfied by the mean-field solution as accurately as possible. Since $ic_i^\dagger G^\gamma c_i$ are linear combinations of operators with eigenvalues ± 1 , we define the quantities $\mathcal{G}_i^\gamma \equiv \frac{1}{4} |\langle c_i^\dagger G^\gamma c_i \rangle|$ for the mean-field ground state average, with $0 \leq \mathcal{G}_i^\gamma \leq 1$. For zero magnetic field and in the absence of magnetic order, the constraints are automatically satisfied, $\mathcal{G}_i^\gamma = 0$, since $\mathbf{V}_i^{0\gamma} = \mathbf{V}_i^{\alpha\beta} = 0$. To describe the Kitaev spin liquid phase at finite magnetic field, we tune the Lagrange multipliers λ_i^γ contained in B_i in order to minimize the violation of the constraint measured by \mathcal{G}_i^γ . For all results shown below, we guarantee $\mathcal{G}_i^\gamma < 0.05$ for all values of (γ, i) . In the homogeneous case (cf. Figs. 1–3), the largest violations occur in the vicinity of phase transitions. Away from transitions, we instead find $\mathcal{G}_i^\gamma < 10^{-3}$. Similarly, in the presence of vortices, the largest violations occur near a vortex but they are always bounded as specified.

Charge density coefficients

Consider the hole density operator \tilde{N}_l at site l in the Hubbard–Kanamori model. Using the canonical transformation in Eq. (18), we can write the effective charge imbalance operator in the low-energy sector as:

$$\delta n_l = \mathcal{P}_{\text{low}} e^S (\tilde{N}_l - 1) e^{-S} \mathcal{P}_{\text{low}}. \quad (30)$$

We calculate δn_l using perturbation theory to leading order in the hopping matrix \mathbf{T}_{ij} . In systems with bond-inversion symmetry like the Hubbard–Kanamori model, the first non-vanishing contribution appears at third order and is associated with virtual processes in which an electron or hole moves around a triangle^{30,32,33}. To obtain this leading contribution, we generalize the hopping matrix to include hopping between next-nearest-neighbor sites on the honeycomb lattice. We denote by $\langle\langle ij \rangle\rangle_\gamma$ a second-neighbor bond perpendicular to nearest-neighbor γ bonds, see Fig. 10a. Sizeable second- and third-neighbor hopping parameters have been calculated for Kitaev materials using ab initio methods⁵⁰. For simplicity, we consider only the dominant second-neighbor hopping, which on z bonds

is described by the matrix $\mathbf{T}_{\langle\langle ij \rangle\rangle_z} = \begin{pmatrix} 0 & t'_2 & 0 \\ t'_2 & 0 & 0 \\ 0 & 0 & 0 \end{pmatrix}$. The corresponding

matrices for x and y bonds follow by cyclic permutation of the indices. Assuming $|t'_2| \ll |t_1|, |t_2|, |t_3|$, we calculate the charge density response to first order in t'_2 . In this approximation, we neglect the second-neighbor exchange interaction generated by perturbation theory at order $(t'_2)^2$, keeping only the nearest-neighbor exchange couplings as in Eq. (21).

Following ref. 30, we write the effective charge imbalance operator as $\delta n_l = \sum_{\langle jk \rangle} \delta n_{l(jk)}$, where the sum over (jk) runs over pairs of sites such that jkl

<https://doi.org/10.1038/s41535-024-00643-5>

Article

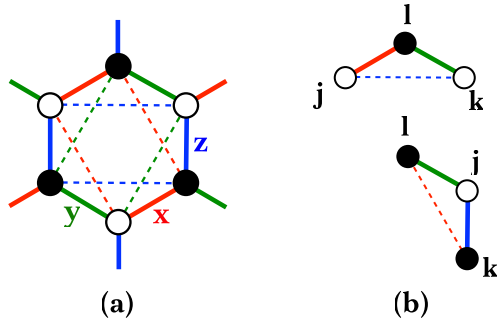


Fig. 10 | Honeycomb lattice with nearest- and next-nearest-neighbor hopping. a Red, green and blue lines correspond to $\gamma = x, y, z$ bonds, respectively. The hopping matrix on nearest-neighbor bonds (solid lines) is written in terms of hopping parameters t_1, t_2, t_3 , and t_4 . On second-neighbor bonds (dashed lines), we consider a single hopping parameter t'_2 . b Examples of triangles that contribute to the effective charge density operator at site l .

forms a triangle, and each triangle is counted once. These triangles contain two nearest-neighbor bonds and one next-nearest-neighbor bond, see the examples in Fig. 10b. The calculation of δn_l requires the generator of the canonical transformation up to second order in the hopping matrices, $S \approx S_1 + S_2$. After the projection onto the $j_{\text{eff}} = \frac{1}{2}$ subspace, we write the end result in the form:

$$\delta n_{l(jk)} = \sum_{\alpha\beta} \left(C_{jkl}^{\alpha\alpha\beta} \sigma_j^\alpha \sigma_l^\beta + C_{jkl}^{\alpha\alpha\beta} \sigma_k^\alpha \sigma_l^\beta + C_{jkl}^{\alpha\beta\alpha} \sigma_j^\alpha \sigma_k^\beta \right). \quad (31)$$

Note that the effective density operator involves only two-spin operators because it must be invariant under time reversal. The coefficients $C_{jkl}^{\alpha\alpha\beta}$ can be calculated as explained below. We find closed-form but lengthy expressions for general values of the hopping parameters. For $t_1 = t_3 = 0$ and $t_2, t'_2 \neq 0$, we recover the result of ref. 30, in which the nonzero coefficients are diagonal in spin indices, e.g., $C_{jkl}^{\alpha\alpha\beta} \sim \delta_{\alpha\beta} t'_2 t_2 / U^3$. Similarly to the derivation of the effective Hamiltonian, the addition of the subleading hopping parameters t_1 and t_3 generates off-diagonal terms in $\delta n_{l(jk)}$ which are reminiscent of the Γ interaction. Equation (31) implies that the charge density profile of a given state is determined by its spin correlations. Charge neutrality of the Mott insulator, $\sum_l \langle \delta n_l \rangle = 0$, implies that there is no charge polarization in a homogeneous state where $\langle \delta n_l \rangle$ is uniform. This condition is indeed satisfied when we impose that the spin correlations on different bonds respect translation and rotation symmetries, which provides a nontrivial check for the coefficients $C_{jkl}^{\alpha\alpha\beta}$.

Let us outline some steps in the calculation of the coefficients $C_{jkl}^{\alpha\alpha\beta}$ in Eq. (31). At third order in the hopping term, the canonical transformation in Eq. (30) gives $\delta n_l^{(3)} = -S_2 [N_l, S_l^\dagger] + \text{h.c.}$, where we organize the contributions in terms of triangles with site l at one vertex. In this notation, the contribution from each triangle with two other sites $(jk) \equiv (kj)$ contains two terms, $\delta n_{l(jk)}^{(3)} = \delta n_{l,jk}^{(3)} + \delta n_{l,kj}^{(3)}$. Explicit expressions for the matrix elements of $\delta n_{l(jk)}^{(3)}$ can be found in ref. 30. The last step is to project these matrices onto the low-energy subspace spanned by the states in Eq. (17). The coefficients in Eq. (31) are given by:

$$C_{jkl}^{\alpha\alpha\beta} = \frac{1}{8} \text{Tr} \left(\mathcal{P}_{\text{low}} \delta n_{l(jk)}^{(3)} \mathcal{P}_{\text{low}} \sigma_j^\alpha \sigma_k^\beta \sigma_l^\alpha \right), \quad (32)$$

where $\sigma^0 = 1$. Since the charge density operator is even under time reversal, terms that act nontrivially on an odd number of spins vanish identically:

$$C_{jkl}^{\alpha\beta\gamma} = C_{jkl}^{\alpha\alpha 0} = C_{jkl}^{\alpha 0 \alpha} = C_{jkl}^{\alpha 0 0} = 0, \quad (33)$$

with $\alpha, \beta, \gamma \in \{1, 2, 3\}$. The nonzero terms can be written as in Eq. (31) and depend on the specific triangle. The simplest coefficients are the ones that are already present in the solvable Kitaev model³⁰. For instance, for the top triangle in Fig. 10b, we obtain:

$$C_{jkl}^{110} = C_{jkl}^{220} = \frac{t'_2 t_2}{U^3} \frac{\eta^2 (1 - 2\eta)}{9(1 - \eta)^3 (1 - 3\eta)^3}, \quad (34)$$

where $\eta = J_H/U < 1/3$. Note that this term is sensitive to the sign of the second-neighbor hopping t'_2 . In ref. 30, the charge imbalance was calculated assuming a positive value of t'_2 , but in this work we use $t'_2 < 0$ as obtained in ref. 50 for $\alpha\text{-RuCl}_3$. As an example for a coefficient associated with off-diagonal terms in δn_b which are generated by the hoppings t_1 and t_3 , we have:

$$C_{jkl}^{230} = -\frac{t'_2 \eta (t_1 - t_3)}{U^3} \frac{[(276\eta^4 - 94\eta^2 - 6\eta + 22)t_1 + (26\eta^4 - 20\eta^3 - 7\eta^2 - 4\eta + 5)t_3]}{54(1 - \eta)^3 (1 + 2\eta)^2 (1 - 3\eta)^2}. \quad (35)$$

Data availability

All data supporting the findings of this paper are shown in the paper. Raw data and code used for preparing the figures are accessible on Zenodo under <https://doi.org/10.5281/zenodo.10616443>.

Received: 27 November 2023; Accepted: 14 March 2024;

Published online: 29 March 2024

References

- Kitaev, A. Anyons in an exactly solved model and beyond. *Ann. Phys.* **321**, 2–111 (2006).
- Savary, L. & Balents, L. Quantum spin liquids: a review. *Rep. Prog. Phys.* **80**, 016502 (2016).
- Zhou, Y., Kanoda, K. & Ng, T.-K. Quantum spin liquid states. *Rev. Mod. Phys.* **89**, 025003 (2017).
- Trebst, S. & Hickey, C. Kitaev materials. *Phys. Rep.* **950**, 1–37 (2022).
- Winter, S. M. et al. Models and materials for generalized Kitaev magnetism. *J. Phys. Condens. Matter* **29**, 493002 (2017).
- Takagi, H., Takayama, T., Jackeli, G., Khaliullin, G. & Nagler, S. E. Concept and realization of Kitaev quantum spin liquids. *Nat. Rev. Phys.* **1**, 264–280 (2019).
- Hermanns, M., Kimchi, I. & Knolle, J. Physics of the Kitaev model: fractionalization, dynamic correlations, and material connections. *Annu. Rev. Condens. Matter Phys.* **9**, 17–33 (2018).
- Knolle, J. & Moessner, R. A field guide to spin liquids. *Annu. Rev. Condens. Matter Phys.* **10**, 451–472 (2019).
- Motome, Y. & Nasu, J. Hunting Majorana fermions in Kitaev magnets. *J. Phys. Soc. Jpn.* **89**, 012002 (2020).
- Jackeli, G. & Khaliullin, G. Mott insulators in the strong spin-orbit coupling limit: from Heisenberg to a quantum compass and Kitaev models. *Phys. Rev. Lett.* **102**, 017205 (2009).
- Plumb, K. W. et al. $\alpha\text{-RuCl}_3$: a spin-orbit assisted Mott insulator on a honeycomb lattice. *Phys. Rev. B* **90**, 041112 (2014).
- Sandilands, L. J., Tian, Y., Plumb, K. W., Kim, Y.-J. & Burch, K. S. Scattering continuum and possible fractionalized excitations in $\alpha\text{-RuCl}_3$. *Phys. Rev. Lett.* **114**, 147201 (2015).
- Banerjee, A. et al. Proximate Kitaev quantum spin liquid behaviour in a honeycomb magnet. *Nat. Mater.* **15**, 733–740 (2016).
- Baek, S.-H. et al. Evidence for a field-induced quantum spin liquid in $\alpha\text{-RuCl}_3$. *Phys. Rev. Lett.* **119**, 037201 (2017).
- Kasahara, Y. et al. Majorana quantization and half-integer thermal quantum Hall effect in a Kitaev spin liquid. *Nature* **559**, 227–231 (2018).
- Yokoi, T. et al. Half-integer quantized anomalous thermal Hall effect in the Kitaev material candidate $\alpha\text{-RuCl}_3$. *Science* **373**, 568–572 (2021).

<https://doi.org/10.1038/s41535-024-00643-5>

Article

17. Czajka, P. et al. Planar thermal Hall effect of topological bosons in the Kitaev magnet α -RuCl₃. *Nat. Mater.* **22**, 36–41 (2022).
18. Bruin, J. A. N. et al. Robustness of the thermal Hall effect close to half-quantization in α -RuCl₃. *Nat. Phys.* **18**, 401–405 (2022).
19. Cookmeyer, T. & Moore, J. E. Spin-wave analysis of the low-temperature thermal Hall effect in the candidate Kitaev spin liquid α -RuCl₃. *Phys. Rev. B* **98**, 060412 (2018).
20. Chern, L. E., Zhang, E. Z. & Kim, Y. B. Sign structure of thermal Hall conductivity and topological magnons for in-plane field polarized Kitaev magnets. *Phys. Rev. Lett.* **126**, 147201 (2021).
21. Bolens, A. Theory of electronic magnetoelectric coupling in d^5 mott insulators. *Phys. Rev. B* **98**, 125135 (2018).
22. Bolens, A., Katsura, H., Ogata, M. & Miyashita, S. Mechanism for subgap optical conductivity in honeycomb Kitaev materials. *Phys. Rev. B* **97**, 161108 (2018).
23. Feldmeier, J., Natori, W., Knap, M. & Knolle, J. Local probes for charge-neutral edge states in two-dimensional quantum magnets. *Phys. Rev. B* **102**, 134423 (2020).
24. König, E. J., Randeria, M. T. & Jäck, B. Tunneling spectroscopy of quantum spin liquids. *Phys. Rev. Lett.* **125**, 267206 (2020).
25. Carrega, M., Vera-Marun, I. J. & Principi, A. Tunneling spectroscopy as a probe of fractionalization in two-dimensional magnetic heterostructures. *Phys. Rev. B* **102**, 085412 (2020).
26. Udagawa, M., Takayoshi, S. & Oka, T. Scanning tunneling microscopy as a single Majorana detector of Kitaev's chiral spin liquid. *Phys. Rev. Lett.* **126**, 127201 (2021).
27. Bauer, T., Freitas, L. R. D., Pereira, R. G. & Egger, R. Scanning tunneling spectroscopy of Majorana zero modes in a Kitaev spin liquid. *Phys. Rev. B* **107**, 054432 (2023).
28. Aasen, D., Mong, R. S., Hunt, B. M., Mandrus, D. & Alicea, J. Electrical probes of the non-Abelian spin liquid in Kitaev materials. *Phys. Rev. X* **10**, 031014 (2020).
29. Halász, G. B. Gate-controlled anyon generation and detection in Kitaev spin liquids. Preprint at <https://arxiv.org/abs/2308.05154> (2023).
30. Pereira, R. G. & Egger, R. Electrical access to Ising anyons in Kitaev spin liquids. *Phys. Rev. Lett.* **125**, 227202 (2020).
31. Banerjee, S. & Lin, S.-Z. Emergent orbital magnetization in Kitaev quantum magnets. *SciPost Phys.* **14**, 127 (2023).
32. Bulaevskii, L. N., Batista, C. D., Mostovoy, M. V. & Khomskii, D. I. Electronic orbital currents and polarization in Mott insulators. *Phys. Rev. B* **78**, 024402 (2008).
33. Khomskii, D. I. Spin chirality and nontrivial charge dynamics in frustrated Mott insulators: spontaneous currents and charge redistribution. *J. Phys. Condens. Matter* **22**, 164209 (2010).
34. Jang, S.-H., Kato, Y. & Motome, Y. Vortex creation and control in the Kitaev spin liquid by local bond modulations. *Phys. Rev. B* **104**, 085142 (2021).
35. Rau, J. G., Lee, E. K.-H. & Kee, H.-Y. Generic spin model for the honeycomb iridates beyond the Kitaev limit. *Phys. Rev. Lett.* **112**, 077204 (2014).
36. Rouschatzakis, I., Perkins, N. B., Luo, Q. & Kee, H.-Y. Beyond Kitaev physics in strong spin-orbit coupled magnets. Preprint at <https://arxiv.org/abs/2308.01943> (2023).
37. Knolle, J., Bhattacharjee, S. & Moessner, R. Dynamics of a quantum spin liquid beyond integrability: the Kitaev-Heisenberg- Γ model in an augmented parton mean-field theory. *Phys. Rev. B* **97**, 134432 (2018).
38. Liang, S., Jiang, M.-H., Chen, W., Li, J.-X. & Wang, Q.-H. Intermediate gapless phase and topological phase transition of the Kitaev model in a uniform magnetic field. *Phys. Rev. B* **98**, 054433 (2018).
39. Nasu, J., Kato, Y., Kamiya, Y. & Motome, Y. Successive Majorana topological transitions driven by a magnetic field in the Kitaev model. *Phys. Rev. B* **98**, 060416 (2018).
40. Gohlke, M., Wachtel, G., Yamaji, Y., Pollmann, F. & Kim, Y. B. Quantum spin liquid signatures in Kitaev-like frustrated magnets. *Phys. Rev. B* **97**, 075126 (2018).
41. Go, A., Jung, J. & Moon, E.-G. Vestiges of topological phase transitions in Kitaev quantum spin liquids. *Phys. Rev. Lett.* **122**, 147203 (2019).
42. Ralko, A. & Merino, J. Novel chiral quantum spin liquids in Kitaev magnets. *Phys. Rev. Lett.* **124**, 217203 (2020).
43. Li, H., Kim, Y. B. & Kee, H.-Y. Magnetic field induced topological transitions and thermal conductivity in a generalized Kitaev model. *Phys. Rev. B* **105**, 245142 (2022).
44. Yilmaz, F., Kampf, A. P. & Yip, S. K. Phase diagrams of Kitaev models for arbitrary magnetic field orientations. *Phys. Rev. Res.* **4**, 043024 (2022).
45. Merino, J. & Ralko, A. Majorana chiral spin liquid in a model for Mott insulating cuprates. *Phys. Rev. Res.* **4**, 023122 (2022).
46. Cookmeyer, T. & Moore, J. E. Dynamics of fractionalized mean-field theories: consequences for Kitaev materials. *Phys. Rev. B* **107**, 224428 (2023).
47. Catuneanu, A., Yamaji, Y., Wachtel, G., Kim, Y. B. & Kee, H.-Y. Path to stable quantum spin liquids in spin-orbit coupled correlated materials. *npj Quantum Mater.* **3**, 23 (2018).
48. Gordon, J. S., Catuneanu, A., Sørensen, E. S. & Kee, H.-Y. Theory of the field-revealed Kitaev spin liquid. *Nat. Commun.* **10**, 2470 (2019).
49. Wang, J., Normand, B. & Liu, Z.-X. One proximate Kitaev spin liquid in the K - J - Γ model on the honeycomb lattice. *Phys. Rev. Lett.* **123**, 197201 (2019).
50. Winter, S. M., Li, Y., Jeschke, H. O. & Valentí, R. Challenges in design of Kitaev materials: magnetic interactions from competing energy scales. *Phys. Rev. B* **93**, 214431 (2016).
51. Fu, J., Knolle, J. & Perkins, N. B. Three types of representation of spin in terms of Majorana fermions and an alternative solution of the Kitaev honeycomb model. *Phys. Rev. B* **97**, 115142 (2018).
52. Seifert, U. F. P., Meng, T. & Vojta, M. Fractionalized fermi liquids and exotic superconductivity in the Kitaev-Kondo lattice. *Phys. Rev. B* **97**, 085118 (2018).
53. Yadav, R. et al. Kitaev exchange and field-induced quantum spin-liquid states in honeycomb α -RuCl₃. *Sci. Rep.* **6**, 37925 (2016).
54. Zhu, Z., Kimchi, I., Sheng, D. N. & Fu, L. Robust non-Abelian spin liquid and a possible intermediate phase in the antiferromagnetic Kitaev model with magnetic field. *Phys. Rev. B* **97**, 241110 (2018).
55. Hickey, C. & Trebst, S. Emergence of a field-driven U(1) spin liquid in the Kitaev honeycomb model. *Nat. Commun.* **10**, 530 (2019).
56. Kim, B. H., Sota, S., Shirakawa, T., Yunoki, S. & Son, Y.-W. Proximate Kitaev system for an intermediate magnetic phase in in-plane magnetic fields. *Phys. Rev. B* **102**, 140402 (2020).
57. Zhang, S.-S., Halász, G. B., Zhu, W. & Batista, C. D. Variational study of the Kitaev-Heisenberg-Gamma model. *Phys. Rev. B* **104**, 014411 (2021).
58. Joy, A. P. & Rosch, A. Dynamics of visons and thermal Hall effect in perturbed Kitaev models. *Phys. Rev. X* **12**, 041004 (2022).
59. Panigrahi, A., Coleman, P. & Tsvelik, A. Analytic calculation of the vison gap in the Kitaev spin liquid. *Phys. Rev. B* **108**, 045151 (2023).
60. Wagner, C. et al. Quantitative imaging of electric surface potentials with single-atom sensitivity. *Nat. Mater.* **18**, 853–859 (2019).
61. Bian, K. et al. Scanning probe microscopy. *Nat. Rev. Methods Primers* **1**, 36 (2021).
62. Yin, J.-X., Pan, S. H. & Hasan, M. Z. Probing topological quantum matter with scanning tunneling microscopy. *Nat. Rev. Phys.* **3**, 249 (2021).
63. Yamada, M. G. & Fujimoto, S. Electric probe for the toric code phase in Kitaev materials through the hyperfine interaction. *Phys. Rev. Lett.* **127**, 047201 (2021).

<https://doi.org/10.1038/s41535-024-00643-5>

Article

64. Lahtinen, V., Ludwig, A. W. W., Pachos, J. K. & Trebst, S. Topological liquid nucleation induced by vortex-vortex interactions in Kitaev's honeycomb model. *Phys. Rev. B* **86**, 075115 (2012).

Acknowledgements

We acknowledge funding by Brazilian agencies Conselho Nacional de Desenvolvimento Científico e Tecnológico (CNPq) and Coordenação de Aperfeiçoamento de Pessoal de Nível Superior—Brasil (CAPES), by the Deutsche Forschungsgemeinschaft (DFG, German Research Foundation), Projektnummer 277101999—TRR 183 (project B04), and under Germany's Excellence Strategy—Cluster of Excellence Matter and Light for Quantum Computing (ML4Q) EXC 2004/1—390534769. This work was supported by a grant from the Simons Foundation (1023171, R.G.P.). Research at IIP-UFRN is supported by Brazilian ministries MEC and MCTI.

Author contributions

R.E. and R.G.P. conceived and managed the project. The mean-field calculations were developed and carried out by L.R.D.F. with help from T.B., and the results were interpreted and discussed by all authors. The paper was written by R.E. and R.G.P., with input from all authors.

Funding

Open Access funding enabled and organized by Projekt DEAL.

Competing interests

The authors declare no competing interests.

Additional information

Supplementary information The online version contains supplementary material available at <https://doi.org/10.1038/s41535-024-00643-5>.

Correspondence and requests for materials should be addressed to Reinhold Egger.

Reprints and permissions information is available at <http://www.nature.com/reprints>

Publisher's note Springer Nature remains neutral with regard to jurisdictional claims in published maps and institutional affiliations.

Open Access This article is licensed under a Creative Commons Attribution 4.0 International License, which permits use, sharing, adaptation, distribution and reproduction in any medium or format, as long as you give appropriate credit to the original author(s) and the source, provide a link to the Creative Commons licence, and indicate if changes were made. The images or other third party material in this article are included in the article's Creative Commons licence, unless indicated otherwise in a credit line to the material. If material is not included in the article's Creative Commons licence and your intended use is not permitted by statutory regulation or exceeds the permitted use, you will need to obtain permission directly from the copyright holder. To view a copy of this licence, visit <http://creativecommons.org/licenses/by/4.0/>.

© The Author(s) 2024

Supplementary Information for “Electric polarization near vortices in the extended Kitaev model”

Lucas R. D. Freitas,^{1,2} Tim Bauer,^{2,1} Reinhold Egger,² and Rodrigo G. Pereira¹

¹*International Institute of Physics and Departamento de Física Teórica e Experimental,
Universidade Federal do Rio Grande do Norte, Natal, RN, 59078-970, Brazil*

²*Institut für Theoretische Physik, Heinrich-Heine-Universität, D-40225 Düsseldorf, Germany*

SUPPLEMENTARY NOTE 1: ON THE VORTEX LIFETIME

In our setup, vortices could be created by different mechanisms. Once they have been trapped by a local potential, they can decay if they meet another vortex that has been created far away in the bulk but then has propagated to the position of our designated vortex. As shown in Ref. [1], the time scale for two vortices to meet is given by $\tau_{VV} \sim 1/(Dn_V)$. Here D is the diffusion constant, which is related to the vortex mobility μ by the Einstein relation, $D = \mu T$, and n_V is the density of vortices (we set the Boltzmann constant $k_B = 1$). At temperatures $T \ll \Delta_{2v}$, where Δ_{2v} is the vison gap for creating a pair of vortices [1, 2], the diffusion constant becomes independent of the vison dispersion and is given by $D \approx 6v_m^2/T$, where v_m is the characteristic velocity of Majorana fermion excitations. Since in this regime the diffusion constant does not depend explicitly on the effective hopping parameter of the visons, there is no strong dependence on the magnetic field, of arbitrary direction. On the other hand, the vortex density becomes small at temperatures far below the vison gap, $T \ll \Delta_{2v}$. For this reason, we expect the trapped vortex to have a very long lifetime at low temperatures. In the main text, we therefore assume that vortices are effectively stable and spatially localized entities.

SUPPLEMENTARY NOTE 2: FINITE-SIZE EFFECTS

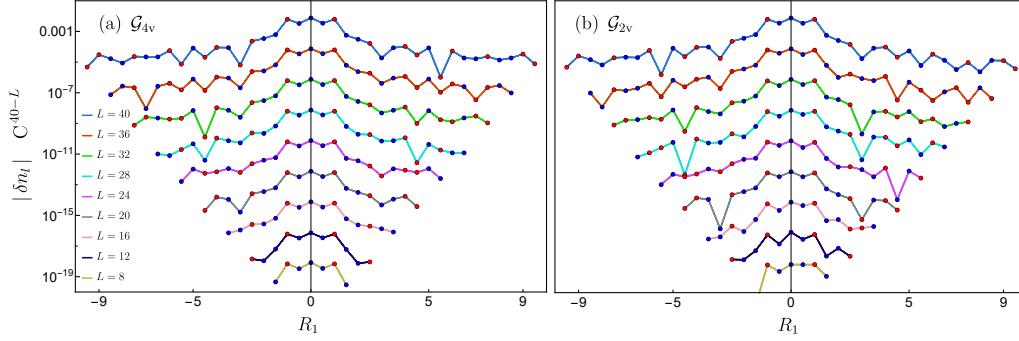
In Supplementary Figure 1 we show how finite-size effects impact the charge distribution around vortices in the extended Kitaev model. The coordinate R_1 corresponds to the zigzag path represented in Fig. 4 of the main text. In the thermodynamic limit and for infinitely separated vortices, the charge imbalance δn_i must be symmetric with respect to the vortex center, i.e., with respect to $R_1 \mapsto -R_1$. However, in a finite-size $L \times L$ geometry (periodic boundary conditions) with vortices located at maximal distance from each other, we see deviations from the symmetric distribution when the distance $|R_1|$ becomes comparable to the separation between two vortices. The asymmetry in the charge distribution is substantially smaller for a configuration with four equally spaced vortices than for two vortices. To see this, compare the data for smaller values of L in Supplementary Figure 1(a) and Supplementary Figure 1(b). This fact can be rationalized by noting that for periodic boundary conditions, the four-vortex configuration preserves a C_3 lattice rotation symmetry about the center of a given vortex, which helps to minimize finite-size effects. As we increase L , the results for both four-vortex and two-vortex configurations converge to the same values, especially close to the vortex, where the charge imbalance is larger. We have verified that all results reported in the main text for the components of the quadrupole tensor, in particular the anisotropy parameter ΔQ , are fully converged for $L \geq 40$.

SUPPLEMENTARY NOTE 3: VORTEX QUADRUPOLE MOMENT FOR NEGATIVE VALUES OF Γ

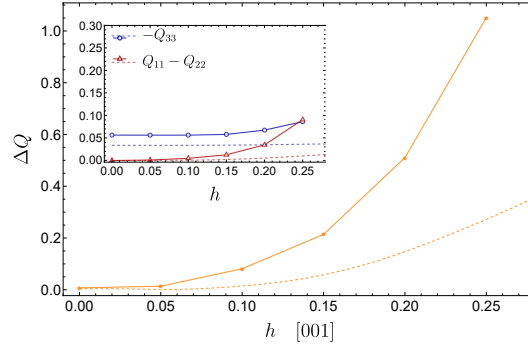
When discussing the vortex charge density profile in the main text, we have focused on the parameter regime $\Gamma > 0$, which is relevant for α -RuCl₃. In Supplementary Figure 2, we show the anisotropy parameter ΔQ and other components of the quadrupole tensor for a negative value of Γ . Comparing with Fig. 7 of the main text, we observe that the result is qualitatively similar to that for $\Gamma > 0$.

SUPPLEMENTARY NOTE 4: DISCUSSION OF EQ. (14) IN THE MAIN TEXT

Unlike the other spin interactions included in our model, the DM interaction requires breaking bond inversion symmetries. Starting from the Hubbard-Kanamori model, the DM interaction can be generated, for instance, by generalizing the hopping matrix to be asymmetric, which introduces three new hopping parameters; see e.g. the derivation in Ref. [3]. In addition, the locally applied potential V_0 induces lattice distortions and introduces an anisotropic crystal field term of the form $\delta_{CF}(\mathbf{L}_i \cdot \mathbf{n})^2$, where \mathbf{n} is a unit vector in the direction of the local electric field



Supplementary Figure 1: **Charge profile near a vortex.** Charge distribution near a vortex for different system sizes for gauge configurations with (a) four, and (b) two maximally spaced vortices, along the path variable R_1 shown in Fig. 4 of the main text. Here we fix the parameters of the Hubbard-Kanamori model so that $\Gamma/|K| = 0.3$, $J/|K| = -0.04$, and the magnetic field is $\mathbf{h} = 0.2|K|\hat{\mathbf{z}}$. The curve for $L = 40$ is shown using the same scale as in Fig. 5 of the main text. To aid visualization, the curves for other values of L have been shifted down by rescaling the data by a factor C^{40-L} with $C = 1/\sqrt{10}$.



Supplementary Figure 2: **Quadrupole anisotropy for $\Gamma < 0$.** Same as Fig. 7 of the main text but for $\Gamma = -0.3|K|$, i.e., opposite sign of Γ .

and $\delta_{\text{CF}} \sim V_0$ is the energy scale associated with the crystal field splitting. This term enters in the atomic Hamiltonian and modifies the expressions for the low-energy states in Eq. (17) of the main text, which would now depend on the ratio between δ_{CF} and the spin-orbit coupling λ . Instead of introducing a large number of new parameters in our model, we here prefer to follow a more phenomenological approach and include a single DM term which is allowed by symmetry, with a coupling constant that increases linearly with the local potential V_0 . This dependence is plausible because the DM vector for nearest-neighbor bonds vanishes in the absence of the electric potential. We also fixed the dependence on the Hubbard interaction and Hund's coupling to be in terms of $\Delta E_1 = U - 3J_H$ because this is the lowest among the three energy scales in Eq. (20) of the main text, and it sets an upper bound for the electric potential that can be applied before the perturbative expressions break down. We note that this dependence on ΔE_1 does show up in some of the several interaction terms generated by an asymmetric hopping matrix (see Ref. [3]).

In summary, we propose Eq. (14) in the main text as the simplest expression that captures the main properties of the DM interaction and allows one to probe its effects on the vortex gap. A more detailed study, including all possible

DM-type terms, should be guided by material-specific parameters as determined by *ab initio* calculations.

-
- [1] Joy, A. P. & Rosch, A. Dynamics of visons and thermal Hall effect in perturbed Kitaev models. *Phys. Rev. X* **12**, 041004 (2022).
 - [2] Savary, L. & Balents, L. Quantum spin liquids: a review. *Rep. Prog. Phys.* **80**, 016502 (2016).
 - [3] Winter, S. M. *et al.* Models and materials for generalized Kitaev magnetism. *J. Phys.: Condens. Matter* **29**, 493002 (2017).

P3 Scanning tunneling spectroscopy of Majorana zero modes in a Kitaev spin liquid

The following text is reproduced from the publication

T. Bauer, L. R. D. Freitas, R. G. Pereira, and R. Egger

Scanning tunneling spectroscopy of Majorana zero modes in a Kitaev spin liquid

Physical Review B, vol. 107, no. 5, p. 054432 (2023).

Digital Object Identifier (DOI): [10.1103/PhysRevB.107.054432](https://doi.org/10.1103/PhysRevB.107.054432)

Statement of contribution

RE and RGP conceived and supervised this work. I derived the expressions for the cotunneling theory from the microscopic Hubbard-Kanamori model and the differential conductance. RGP designed the orbital dependency of the tunneling couplings. I developed and carried out the numerical calculation of the dynamical spin correlations. To this end, I resolved complications arising from the breakdown of Thouless' theorem and verified that Eq. (3.14) holds for a finite perturbative magnetic field. With the help of continuous advice from RE, RGP and LRDF, I interpreted the results and computed the differential conductance. RGP conceived the appearance of magnon bound states and calculated the spectrum within linear spin-wave theory. RGP and I prepared the figures for the manuscript, which was drafted by RE and finalized with input from all authors.

Copyright and license notice

The copyright for this article is held by the American Physical Society (APS). APS grants authors the right to use their articles or portions of their articles in a dissertation without requesting permission from APS, provided the bibliographic citation and the APS copyright credit line are given on the appropriate pages.

Scanning tunneling spectroscopy of Majorana zero modes in a Kitaev spin liquid

Tim Bauer^{1,2}, Lucas R. D. Freitas^{2,1}, Rodrigo G. Pereira², and Reinhold Egger¹¹*Institut für Theoretische Physik, Heinrich-Heine-Universität, D-40225 Düsseldorf, Germany*²*International Institute of Physics and Departamento de Física Teórica e Experimental, Universidade Federal do Rio Grande do Norte, Natal, Rio Grande do Norte 59078-970, Brazil*

(Received 25 September 2022; accepted 8 February 2023; published 22 February 2023)

We describe scanning tunneling spectroscopic signatures of Majorana zero modes (MZMs) in Kitaev spin liquids. The tunnel conductance is determined by the dynamical spin correlations of the spin liquid, which we compute exactly, and by spin-anisotropic cotunneling form factors. Near a \mathbb{Z}_2 vortex, the tunnel conductance has a staircase voltage dependence, where conductance steps arise from MZMs and (at higher voltages) from additional vortex configurations. By scanning the probe tip position, one can detect the vortex locations. Our analysis suggests that topological magnon bound states near defects or magnetic impurities generate spectroscopic signatures that are qualitatively different from those of MZMs.

DOI: [10.1103/PhysRevB.107.054432](https://doi.org/10.1103/PhysRevB.107.054432)

I. INTRODUCTION

Presently a major goal in condensed matter physics is to realize, detect, and manipulate topologically ordered phases of frustrated quantum magnets, commonly referred to as quantum spin liquids (QSLs). A famous exactly solvable paradigm is given by Kitaev's two-dimensional (2D) honeycomb lattice spin model with bond-dependent anisotropic exchange which, in a magnetic field, describes a gapped non-Abelian chiral QSL [1]. Emergent excitations of the Kitaev spin liquid include Majorana zero modes (MZMs) bound to \mathbb{Z}_2 vortices ("visons"), which are Ising anyons of interest for quantum information processing, as well as gapped bulk fermions and a chiral Majorana edge mode at the boundary. Being excitations of an insulating magnet, they are electrically neutral. Sizable Kitaev couplings are expected [2] and have been reported in various material platforms for Mott insulators with strong spin-orbit coupling, e.g., in iridate compounds or in α -RuCl₃, where the smallness of interlayer couplings justifies the use of 2D models. For recent reviews, see Refs. [3–12]. Despite the impressive experimental progress achieved over the past decade, however, no consensus has emerged whether α -RuCl₃ or any other known material harbors a QSL. In particular, the half-quantized thermal Hall conductivity due to the chiral Majorana edge mode reported in Refs. [13–15] has not been found in other experiments [16,17]. In fact, some spin-liquid predictions can be mimicked by topological magnons in a polarized phase [18–20].

We here show that characteristic signatures of Ising anyons should be seen in scanning tunneling spectroscopy (STS) experiments [21] on a 2D Kitaev layer [22–25] by scanning the probe-tip position in the vicinity of an isolated \mathbb{Z}_2 vortex (located far away from all other vortices and from the sample boundary) and/or by changing the applied voltage; see Fig. 1. Below we will also compare our results to an alternative scenario with topological magnon bound states near defects or magnetic impurities, which could also cause low-energy

features in the STS tunnel conductance. Such a comparison is important as evidenced by the corresponding topological superconductor case [26], where the tunnel conductance has a zero-bias anomaly with quantized peak conductance $2e^2/h$ due to MZM-mediated resonant Andreev reflection [27–30]. STS experiments have found such zero-bias anomalies near vortex cores in various superconducting materials and attributed them to MZMs [21,31–34]. A major obstacle to this interpretation is that very similar conductance peaks can be caused by conventional disorder-induced Andreev bound states [35]. However, the magnetic QSL case is rather different and warrants a separate investigation. The absence of a Cooper pair condensate implies that the charge of an electron (tunneling in from the tip via the MZM) is much harder to accommodate. For the pure Kitaev model, the infinite charge gap implies a vanishing tunnel conductance, $G(V) = 0$.

To obtain a finite $G(V)$, we start from the Hubbard-Kanamori model for Kitaev materials [2,36–39]. Adding a tunneling Hamiltonian for the QSL couplings to tip and substrate, see Fig. 1(a), and projecting to states with energy below the charge gap, we obtain $H = H_K + H_{\text{cot}}$, where H_K describes the Kitaev model [2] and the cotunneling Hamiltonian H_{cot} encodes tip-substrate electron transfer due to virtual excursions to high-energy intermediate states [40–42]. We compute H_{cot} for arbitrary tip position and find that it is anisotropic in spin space. One then obtains $G(V)$ from the dynamical spin correlations of the QSL [43–47], which can be computed exactly [48–53]. However, in the presence of \mathbb{Z}_2 vortices, we encounter a technical challenge described and resolved below.

As a function of voltage, we predict a characteristic sequence of conductance steps linked to MZMs. By scanning the tip location at fixed voltage, one can locate MZMs in real space and obtain information about the vortex configurations contributing to the conductance. It stands to reason that experimental tests of our theory will help in identifying QSLs. (For other proposals aimed at the electric detection of QSLs,

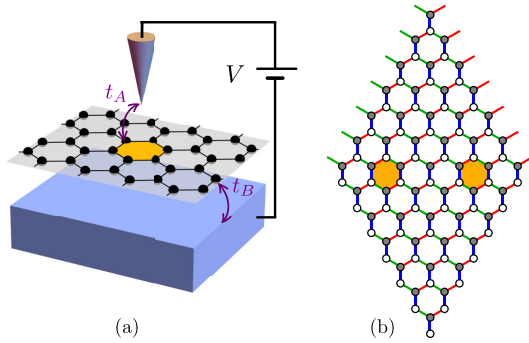


FIG. 1. (a) Schematic STS setup. Tunnel couplings t_A and t_B connect the QSL layer to the tip and the substrate, respectively. The differential conductance $G(V) = \frac{dI}{dV}$ follows by measuring the tunnel current I from tip to substrate as function of the applied voltage V . (b) Finite 2D Kitaev honeycomb lattice with $L \times L$ unit cells and periodic boundary conditions, shown for $L = 7$ and a configuration \mathcal{G} with two \mathbb{Z}_2 vortices (shaded). Full and open circles represent the two sublattices. Nearest-neighbor bonds $\langle jl \rangle_\alpha$ of type $\alpha \in \{x, y, z\}$ are distinguished by different colors.

see Refs. [39,54–57].) Our study of an alternative topological magnon scenario suggests that MZM signatures obtained by STS on a Kitaev layer are easier to distinguish from other mechanisms than in the superconducting case.

The structure of the remainder of this article is as follows. In Sec. II, we derive the low-energy theory used for calculating the differential conductance, where technical details have been relegated to the Appendix. We then show in Sec. III how to compute the conductance in terms of an exact evaluation of dynamical spin-spin correlation functions of the Kitaev layer. Our results for the conductance profile are shown in Sec. IV. In Sec. V, we then address a complementary topological magnon scenario. Finally, we offer concluding remarks in Sec. VI.

II. EFFECTIVE LOW-ENERGY THEORY

We consider the setup in Fig. 1(a), where a scanning probe tip at position $\mathbf{r} = (x, y, d)$ is tunnel-coupled to a 2D Kitaev layer at vertical distance d . The layer is also coupled to a metallic substrate. Throughout, we assume weak and spin-independent tunnel amplitudes. Due to the charge gap in the magnetic layer, electron transport at subgap voltages V , applied between the tip [with conduction electron creation operator $\Psi_{A\tau}^\dagger(\mathbf{r})$ for spin projection $\tau = \uparrow, \downarrow$] and the substrate [with $\Psi_{B\tau}^\dagger(\mathbf{R}_j)$ below lattice site \mathbf{R}_j], can only take place via cotunneling [41,43,58]. We use the Hubbard-Kanamori model for strongly correlated d^5 electrons in α -RuCl₃ or related materials [2,36,37,39], where on-site correlations are captured by a large Coulomb energy U and a Hund coupling J_H . Including a tunneling Hamiltonian for the contacts to tip and substrate, the projection to energies below the charge gap $\sim U$ can be performed by a canonical transformation [2,39]. We show this calculation in some detail in the Appendix.

TABLE I. Kitaev couplings reported from different methods for several materials.

Material	K (meV)	Method
α -RuCl ₃	5.0	experimental analysis [60]
	6.7	exact diagonalization [38]
	8.0–8.25	ab initio [61,62]
Na ₂ IrO ₃	10.6	density functional theory [63]
	16.8	exact diagonalization [38]
	16.9	quantum chemistry methods [64]
α -Li ₂ IrO ₃	29.4	perturbation theory [65]
Li ₂ RhO ₃	6.3–9.8	exact diagonalization [38]
	2.9–11.7	quantum chemistry methods [66]

The low-energy theory is described by spin-1/2 operators, $\mathbf{S}_j = \frac{1}{2}\boldsymbol{\sigma}_j$, in the QSL layer, where $H = H_K + H_{\text{cot}}$ includes the Kitaev model [1,2]

$$H_K = -K \sum_{\langle jl \rangle_\alpha} \sigma_j^\alpha \sigma_l^\alpha - \kappa \sum_{\langle jk \rangle_\alpha, \langle kl \rangle_\beta} \sigma_j^\alpha \sigma_k^\gamma \sigma_l^\beta, \quad (2.1)$$

with $\langle jl \rangle_\alpha$ denoting a nearest-neighbor bond of type $\alpha \in \{x, y, z\}$; see Fig. 1(b). The term $\propto \kappa$ describes a magnetic field [1,52], where $(\alpha\beta\gamma)$ is a cyclic permutation of (xyz) and the sum runs over triangles (jkl) with two adjacent nearest-neighbor bonds. We measure lengths in units of the lattice spacing a_0 , where $a_0 \approx 5.9\text{\AA}$ for α -RuCl₃ [59]. The projection scheme yields a ferromagnetic (positive) Kitaev coupling $K \propto J_H$ [2], where experimental analysis gives $K \approx 5$ meV for α -RuCl₃ [60]. Theoretical estimates for K in different Kitaev materials have been reported in Refs. [38,61–66]; see Table I.

Similarly, summing over all lattice sites, the cotunneling Hamiltonian follows as

$$H_{\text{cot}} = \sum_j \Psi_{A\tau}^\dagger(\mathbf{r}) [T_0(\mathbf{r} - \mathbf{R}_j) \mathbb{1}_j + \mathbf{T}(\mathbf{r} - \mathbf{R}_j) \cdot \boldsymbol{\sigma}_j] \times \Psi_{B\tau}(\mathbf{R}_j) + \text{H.c.}, \quad (2.2)$$

where $\boldsymbol{\sigma}_j$ and $\mathbb{1}_j$ act in Kitaev spin space. The 2×2 matrices T_0 and T^α , with $\mathbf{T} = (T^x, T^y, T^z)$, act in conduction electron spin space. All T -matrix elements scale $\propto t_A t_B / U$, with real-valued tunnel couplings t_A (t_B) from tip (substrate) to a given site. We assume a constant substrate coupling t_B . The tip couplings depend on the overlap between the spherically symmetric tip wave function and the respective t_{2g} orbital (labeled by $\alpha = x, y, z$) for the d^5 electrons. With an energy scale t_0 and a tunneling length $l_0 \lesssim a_0$, we write [41,43]

$$t_{A\alpha}(\mathbf{r}, \mathbf{R}_j) = t_0 e^{-|\mathbf{r} \pm \mathbf{v}_\alpha - \mathbf{R}_j|/l_0}, \quad (2.3)$$

with the overall coupling $t_A \equiv \sqrt{t_{Ax}^2 + t_{Ay}^2 + t_{Az}^2}$. The vectors \mathbf{v}_α with $|\mathbf{v}_\alpha| \approx 0.1a_0$ encode the orbital overlaps, where the \pm signs in Eq. (2.3) label the sublattice type of site \mathbf{R}_j ; see the Appendix. The exponential scaling in Eq. (2.3) implies that only a few sites near the tip location \mathbf{r} contribute. Analytical but lengthy expressions for T_0 and \mathbf{T} are given in the Appendix.

Simpler results emerge by approximating $\mathbf{v}_\alpha = 0$, which gives exact results for a tip located on top of a lattice site and

otherwise causes deviations $\sim 10\%$ in the tunnel couplings. (For the figures shown below, we have used the full expressions.) We then obtain

$$H_{\text{cot}} = \sum_j \frac{t_A(\mathbf{r} - \mathbf{R}_j)t_B}{U} \Psi_A^\dagger(\mathbf{r})[\eta_0 + \eta_1 \boldsymbol{\tau} \cdot \boldsymbol{\sigma}_j + \eta_2(\tau^x + \tau^y + \tau^z)(\sigma^x + \sigma^y + \sigma^z)] \Psi_B(\mathbf{R}_j) + \text{H.c.}, \quad (2.4)$$

with the $\frac{J_H}{U}$ -dependent numbers $\eta_j \sim O(1)$; see the Appendix. The $SU(2)$ spin rotation symmetry assumed in Refs. [43–45] is in fact lowered to a \mathbb{Z}_3 symmetry around the [111] axis.

III. DIFFERENTIAL CONDUCTANCE

At this point, it is straightforward to compute the differential conductance, $G(V) = \frac{dI}{dV}$, from Fermi's golden rule [43,44,58]. In the zero-temperature limit, we find

$$G(V) = \sum_{jl, \alpha\beta} C_{jl}^{\alpha\beta}(\mathbf{r}) \int_0^{eV} d\omega S_{jl}^{\alpha\beta}(\omega) = \frac{e^2}{\hbar} \int_0^{eV} d\omega S_G(\omega), \quad (3.1)$$

with the dynamical spin correlation function of the QSL,

$$S_{jl}^{\alpha\beta}(\omega) = \int \frac{dt}{2\pi} e^{i\omega t} \langle \Phi | \sigma_j^\alpha(t) \sigma_l^\beta(0) | \Phi \rangle. \quad (3.2)$$

The second step in Eq. (3.1) defines the averaged dynamical spin correlator $S_G(\omega)$, which follows by weighting $S_{jl}^{\alpha\beta}(\omega)$ with its form factor,

$$C_{jl}^{\alpha\beta}(\mathbf{r}) = \frac{2e^2 d_A d_B}{\hbar} \text{Tr}[T^\alpha(\mathbf{r} - \mathbf{R}_j) T^\beta(\mathbf{r} - \mathbf{R}_l)], \quad (3.3)$$

with the tip (substrate) density of states d_A (d_B) and a trace over conduction electron spin space. Note that $\frac{dG}{dV} \propto S_G(V)$. The term $\propto T_0$ in Eq. (2.2) generates a voltage-independent background (including a mixing term of T_0 and \mathbf{T}) not contained in Eq. (3.1). However, this term is insensitive to \mathbb{Z}_2 vortices and can be disentangled from Eq. (3.1).

The correlation function (3.2) can be computed exactly for H_K by means of a Majorana representation of the spin degrees of freedom [48–51]. By writing $\sigma_j^\alpha = ic_j c_j^\alpha$ in terms of Majorana fermions with a local parity constraint, $D_j = c_j c_j^\alpha c_j^\alpha = +1$, one obtains an exactly solvable noninteracting Hamiltonian for “matter” Majorana fermions, $\{c_j\}$, which move in a conserved \mathbb{Z}_2 gauge field $u_{(jl)a} = ic_j^\alpha c_l^\alpha = \pm 1$ [1],

$$H_K = iK \sum_{(jl)a} u_{(jl)a} c_j c_l - iK \sum_{(jk)a, (kl)\beta} u_{(jk)a} u_{(kl)\beta} c_j c_l. \quad (3.4)$$

All eigenstates of H_K can be written as a projected tensor product of a matter fermion state, $|\varphi(\mathcal{G})\rangle$, for given static gauge field configuration $|\mathcal{G}\rangle$,

$$|\Phi\rangle = \mathcal{P}|\mathcal{G}\rangle|\varphi(\mathcal{G})\rangle, \quad (3.5)$$

with $H_K|\Phi\rangle = E_\Phi|\Phi\rangle = E_{\varphi(\mathcal{G})}|\Phi\rangle$, where the projection $\mathcal{P} = \prod_j \frac{1+D_j}{2}$ projects onto the physical subspace. Defining gauge-

invariant plaquette operators,

$$W_p = \prod_{(jl)a \in p} u_{(jl)a} = \pm 1, \quad (3.6)$$

the ground state has $W_p = +1$ for all hexagonal plaquettes p [1]. Plaquettes with $W_p = -1$ then define \mathbb{Z}_2 vortices, which are expected near vacancies or magnetic impurities [67–69] and harbor MZMs. In order to study the case shown in Fig. 1(a), we will then consider $|\Phi\rangle$ as the matter ground state $|\varphi_0(\mathcal{G})\rangle$ for a gauge configuration \mathcal{G} with two well-separated \mathbb{Z}_2 vortices. We note that \mathcal{G} can be constructed from a zero-vortex configuration \mathcal{G}_0 (with all bond variables $u_{(jl)a} = +1$ for j in sublattice \mathcal{A} and l in sublattice \mathcal{B}) by reversing the bond variables along an arbitrary string connecting both vortices.

For explicit calculations, we consider a finite honeycomb lattice with $L \times L$ unit cells and periodic boundary conditions. The $2N = 2L^2$ matter Majoranas are written as $c_j = c_\lambda(m, n)$, where $\lambda \in (\mathcal{A}, \mathcal{B})$ labels the sublattice and $m, n = 1, \dots, L$ the unit cell at $\mathbf{R}_j = m\hat{\mathbf{e}}_1 + n\hat{\mathbf{e}}_2$, with the primitive lattice vectors $\hat{\mathbf{e}}_1 = \frac{1}{2}\hat{\mathbf{x}} + \frac{\sqrt{3}}{2}\hat{\mathbf{y}}$ and $\hat{\mathbf{e}}_2 = -\frac{1}{2}\hat{\mathbf{x}} + \frac{\sqrt{3}}{2}\hat{\mathbf{y}}$. We next define the $2N$ -dimensional Majorana vector $c = (c_{\mathcal{A}}, c_{\mathcal{B}})^T$, with the ordering convention $c_\lambda = (c_\lambda(1, 1), \dots, c_\lambda(L, 1), c_\lambda(1, 2), \dots, c_\lambda(L, L))^T$, and a complex fermion for each unit cell, $f(m, n) = \frac{1}{2}[c_{\mathcal{A}}(m, n) - ic_{\mathcal{B}}(m, n)]$. With an N -dimensional vector f formed in analogy to c_λ , the linear transformation between both representations is given by

$$c = T \begin{pmatrix} f \\ f^\dagger \end{pmatrix}, \quad T = \begin{pmatrix} \mathbb{1}_N & \mathbb{1}_N \\ i\mathbb{1}_N & -i\mathbb{1}_N \end{pmatrix}, \quad (3.7)$$

with the $N \times N$ identity $\mathbb{1}_N$ and $T^{-1} = \frac{1}{2}T^\dagger$. The projection \mathcal{P} here implies a parity constraint for the total number N_f of f fermions and the total number N_χ of bond fermions $\chi_{(jl)a} = \frac{1}{2}(c_j^\alpha - ic_l^\alpha)$ [49–51],

$$(-1)^{N_f + N_\chi} = 1, \quad (3.8)$$

where we assume a vanishing boundary condition twist parameter in Ref. [51]. We note that N_χ is uniquely determined by the bond variables $\{u_{(jl)a}\}$ defining the gauge configuration \mathcal{G} . Using the f fermions, we obtain

$$H_K = \frac{1}{2}(f^\dagger f) T^\dagger \begin{pmatrix} \mathcal{H}_{\mathcal{AA}}^\mathcal{G} & \mathcal{H}_{\mathcal{AB}}^\mathcal{G} \\ \mathcal{H}_{\mathcal{BA}}^\mathcal{G} & \mathcal{H}_{\mathcal{BB}}^\mathcal{G} \end{pmatrix} T \begin{pmatrix} f \\ f^\dagger \end{pmatrix}, \quad (3.9)$$

where the $N \times N$ matrices $\mathcal{H}_{\lambda\lambda'}^\mathcal{G}$, for given \mathcal{G} can be read off from Eq. (3.4); see Ref. [39] for explicit expressions.

We next apply a unitary Bogoliubov transformation,

$$\begin{pmatrix} f \\ f^\dagger \end{pmatrix} = U_\mathcal{G} \begin{pmatrix} a \\ a^\dagger \end{pmatrix}, \quad (3.10)$$

in order to diagonalize Eq. (3.9) in terms of new (complex) matter fermions a_μ ,

$$H_K = \frac{1}{2} \sum_{\mu=1}^N \varepsilon_\mu (2a_\mu^\dagger a_\mu - 1), \quad (3.11)$$

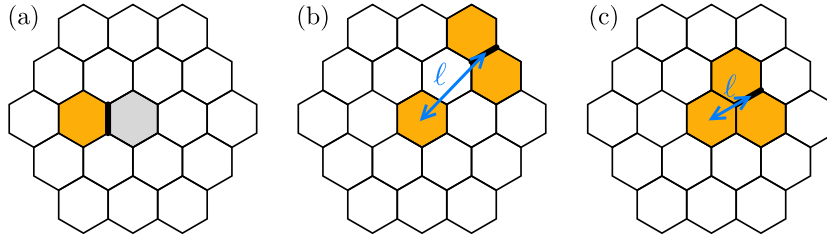


FIG. 2. Illustration of several gauge configurations \mathcal{G}_j^α contributing to the dynamical spin correlation functions determining the tunnel conductance. The central plaquette always refers to one of the two well-separated \mathbb{Z}_2 vortices (the other one is not shown) present in the reference configuration \mathcal{G} . Thick black bonds indicate a flip of the corresponding bond variable $u_{(jl)_a} \rightarrow -u_{(jl)_a}$. (a) The vortex is translated by one plaquette. (b) An additional pair of adjacent vortices at relatively large distance ℓ (blue double arrow) is created by the bond flip. (c) Same as (b) but for small distance ℓ .

where ε_μ are the non-negative eigenenergies ordered as

$$0 \leq \varepsilon_1 \leq \varepsilon_2 \leq \dots \leq \varepsilon_N. \quad (3.12)$$

We often use the additional index \mathcal{G} , i.e., $a_\mu \rightarrow a_{\mathcal{G},\mu}$ and $\varepsilon_\mu \rightarrow \varepsilon_{\mathcal{G},\mu}$, to emphasize that those operators and energies refer to the corresponding gauge configuration. The matter ground state, $|\varphi_0(\mathcal{G})\rangle$, is determined by the conditions $a_\mu |\varphi_0(\mathcal{G})\rangle = 0$ (for all μ) and has the energy

$$E_{\mathcal{G},0} = -\frac{1}{2} \sum_{\mu=1}^N \varepsilon_{\mathcal{G},\mu}. \quad (3.13)$$

However, we still have to check that this state respects the parity constraint (3.8). To that end, we first note that the parity of the a fermions, $(-1)^{N_a}$ with $N_a = \sum_\mu a_\mu^\dagger a_\mu$, satisfies the relation

$$(-1)^{N_f} = (-1)^{N_a} \det U_{\mathcal{G}}, \quad (3.14)$$

where we have verified that the proof for Eq. (3.14) given in Ref. [51] for $\kappa = 0$ can be extended to $\kappa \neq 0$. Equation (3.8) can therefore be written as

$$(-1)^{N_a} \pi_{\mathcal{G}} = 1, \quad \pi_{\mathcal{G}} = (-1)^{N_x} \det U_{\mathcal{G}}, \quad (3.15)$$

where the ground-state parity operator, $\pi_{\mathcal{G}} = \pm 1$, is gauge invariant. For configurations with $\pi_{\mathcal{G}} = -1$, the matter ground state $|\varphi_0(\mathcal{G})\rangle$ is not in the physical subspace. One then has to add a single fermion to the ε_1 level for satisfying the parity constraint (3.15). The corresponding changes,

$$|\varphi_0(\mathcal{G})\rangle \rightarrow a_{\mu=1}^\dagger |\varphi_0(\mathcal{G})\rangle, \quad E_{\mathcal{G},0} \rightarrow E_{\mathcal{G},0} + \varepsilon_1, \quad (3.16)$$

are implicitly understood below.

We now turn to the dynamical spin correlator, where a Fourier transformation gives the Lehmann representation (with j in sublattice \mathcal{A})

$$S_{jl}^{\alpha\beta}(\omega) = \sum_{\Phi'} \langle \Phi | \sigma_j^\alpha | \Phi' \rangle \langle \Phi' | \sigma_l^\beta | \Phi \rangle \delta(\omega + E_\Phi - E_{\Phi'}). \quad (3.17)$$

We consider $|\Phi\rangle$ as the matter ground state $|\varphi_0(\mathcal{G})\rangle$ for a given gauge configuration \mathcal{G} (which we will later choose to contain two vortices), with energy $E_0 = E_{\mathcal{G},0}$ in Eq. (3.13). Inserting the Majorana decomposition into Eq. (3.17), we next observe that c_j^α commutes with all terms in H_K that do not contain

$u_{(jl)_a}$, but anticommutes with all terms that do. Starting from $\mathcal{G} = \{u_{(j'l')_{a'}}\}$, we then define a new gauge configuration $\mathcal{G}_j^\alpha = \{\tilde{u}_{(j'l')_{a'}}\}$, see Fig. 2, with the bond variables

$$\tilde{u}_{(j'l')_{a'}} = \begin{cases} -u_{(j'l')_{a'}}, & \text{if } \langle j'l' \rangle_{a'} = \langle jl \rangle_a, \\ u_{(j'l')_{a'}}, & \text{otherwise.} \end{cases} \quad (3.18)$$

With this definition, Eq. (3.17) yields [49–51]

$$S_{jl}^{\alpha\beta}(\omega) = \sum_{\varphi(\mathcal{G}_j^\alpha)} \langle \varphi_0(\mathcal{G}) | c_j | \varphi(\mathcal{G}_j^\alpha) \rangle \langle \varphi(\mathcal{G}_j^\alpha) | c_l | \varphi_0(\mathcal{G}) \rangle \times \delta(\omega + E_0 - E_{\varphi(\mathcal{G}_j^\alpha)}) (\delta_{jl} - i u_{(jl)_a} \delta_{(jl)_a}) \delta_{\alpha\beta}. \quad (3.19)$$

Here $\delta_{(jl)_a} = 1$ if (jl) form a nearest-neighbor bond of type $\langle jl \rangle_a$, and zero otherwise. Hence $S_{jl}^{\alpha\beta}(\omega) \neq 0$ is possible only for equal spin indices ($\alpha = \beta$) and on-site terms or nearest-neighbor bonds. As sketched in Fig. 2, \mathcal{G} and \mathcal{G}_j^α are connected by either moving a vortex by one plaquette, or by creating two additional vortices. We note that the zero-frequency peak in $S_G(\omega)$ is connected to the configurations in Fig. 2(a). Since we expect this peak to move to a finite but very small frequency ω_0 in practice, see Sec. IV, we have taken it into account with the full weight of the delta function peak in the tunnel conductance (3.1), even though the integral in Eq. (3.1) runs over positive frequencies only.

Since matter states for two different gauge configurations are needed in Eq. (3.19), it is convenient to use the notations

$$a_\mu = a_{\mathcal{G},\mu}, \quad b_\mu = a_{\mathcal{G}_j^\alpha,\mu}, \quad (3.20)$$

$$|0_a\rangle = |\varphi_0(\mathcal{G})\rangle, \quad |0_b\rangle = |\varphi_0(\mathcal{G}_j^\alpha)\rangle,$$

with the N -component spinors $a = (a_1, \dots, a_N)^T$ and $b = (b_1, \dots, b_N)^T$. The a matter fermions with ground state $|0_a\rangle$ thus refer to the gauge configuration \mathcal{G} , while the b fermions with ground state $|0_b\rangle$ refer to \mathcal{G}_j^α . The corresponding ground-state energies are denoted by $E_{|0_a\rangle}$ and $E_{|0_b\rangle}$, respectively. From Eq. (3.10), the a and b fermions must be connected by a unitary Bogoliubov transformation [50,51,70],

$$\begin{pmatrix} b \\ b^\dagger \end{pmatrix} = \mathcal{W} \begin{pmatrix} a \\ a^\dagger \end{pmatrix}, \quad \mathcal{W} = U_{\mathcal{G}_j^\alpha}^\dagger U_{\mathcal{G}} = \begin{pmatrix} X^* & Y^* \\ Y & X \end{pmatrix}, \quad (3.21)$$

where the $N \times N$ matrices X and Y satisfy the relations

$$XX^\dagger + YY^\dagger = 1, \quad X^\dagger X + Y^T Y^* = 1, \\ XY^T + YX^T = 0, \quad X^T Y^* + Y^\dagger X = 0.$$

For $\det \mathcal{W} = +1$, we next observe that $|0_b\rangle$ can be obtained from $|0_a\rangle$ by means of the Thouless theorem [72]. As a result, one finds [51,73]

$$|0_b\rangle = [\det(X^\dagger X)]^{1/4} \exp\left(-\frac{1}{2}a^\dagger X^{*-1} Y^* a^\dagger\right) |0_a\rangle. \quad (3.22)$$

The matrix elements needed in Eq. (3.19) are of the form

$$\langle \varphi_0(\mathcal{G}) | c_j | \varphi(\mathcal{G}_j^\alpha) \rangle = \langle 0_a | c_j b_{\mu_1}^\dagger \dots b_{\mu_n}^\dagger | 0_b \rangle, \quad (3.23)$$

where $\mu_1 \leq \dots \leq \mu_n$ and n is constrained by $(-1)^n = \pi_{\mathcal{G}_j^\alpha}$. One can understand this constraint by noting that Eq. (3.23), which is a matrix element of the single fermion operator c_j , must vanish if $|\varphi_0(\mathcal{G})\rangle$ and $|\varphi(\mathcal{G}_j^\alpha)\rangle$ have the same fermion parity. We note that for $\det \mathcal{W} = 1$, exactly one of the two fermionic vacua $|0_a\rangle$ and $|0_b\rangle$ will not be in the physical subspace since the $\pi_{\mathcal{G}}$ operator will change sign when flipping a bond. As discussed above, we therefore have to add a single fermion to one of the two states. Using Eq. (3.22) and the relation $c = T U_{\mathcal{G}}(a, a^\dagger)^T$, which follows from Eqs. (3.7) and (3.10), we can finally express all matrix elements (3.23) exclusively in terms of a and a^\dagger operators, facilitating their practical computation.

For a numerical implementation, we restrict the number n of excitations in Eq. (3.23) by imposing $0 \leq n \leq n_{\max}$. Under this truncation, exactness of the computed dynamical spin correlations is ensured only for frequencies

$$\omega < \omega_{\max} = E_{|0_b\rangle} - E_{|0_a\rangle} + \sum_{\mu=1}^{n_{\max}+2} \varepsilon_{\mathcal{G}_j^\alpha, \mu}. \quad (3.24)$$

However, already for $n_{\max} = 2$, accurate results can be obtained even for $\omega > \omega_{\max}$ in the vortex-free configuration \mathcal{G}_0 [51]. For the two-vortex configuration \mathcal{G} , rapid convergence of the numerical results upon increasing n_{\max} was observed. Since the characteristic MZM features stem from the low-frequency part of $S_{ji}^{\alpha\beta}(\omega)$, in all cases shown here, a truncation with $n_{\max} = 2$ was sufficient to reach convergence for $\omega < \omega_{\max}$.

However, for selected bonds $\langle jl \rangle_a$ in the two-vortex configuration \mathcal{G} , we find that $\det \mathcal{W} = -1$. In such cases, the Thouless theorem breaks down and X in Eq. (3.21) is a singular $N \times N$ matrix. As a result, Eq. (3.22) does not apply anymore. For computing the STS tunnel conductance near a single \mathbb{Z}_2 vortex, it is essential to resolve this issue. For closely related problems, Refs. [71,72] have obtained a solution by interchanging the ground-state occupancies of a single particle and its hole partner. We follow their approach and define the matrices $X^{(\mu)}$ and $Y^{(\mu)}$, see Eq. (3.21), according to

$$X_{kl}^{(\mu)} = \begin{cases} X_{kl}, & l \neq \mu, \\ Y_{kl}, & l = \mu, \end{cases} \quad Y_{kl}^{(\mu)} = \begin{cases} Y_{kl}, & l \neq \mu, \\ X_{kl}, & l = \mu, \end{cases} \quad (3.25)$$

where μ refers to the index of the interchanged particle and hole. This interchange of columns renders $X^{(\mu)}$ nonsingular as it corresponds to a Bogoliubov transformation with positive determinant. We can then use the Thouless theorem again, such that after the operation (3.25), we can effectively use Eq. (3.22). The thereby obtained state, $|0_b'\rangle$, has the energy $E_{|0_b'\rangle} = E_{\mathcal{G}_j^\alpha, 0} + \varepsilon_{\mathcal{G}_j^\alpha, \mu}$, and the chosen index μ should minimize $\varepsilon_{\mathcal{G}_j^\alpha, \mu}$. For instance, if it corresponds to a zero mode, $\varepsilon_{\mathcal{G}_j^\alpha, \mu} = 0$, the interchange (3.25) introduces no approximation, the energy ordering in Eq. (3.12) remains unaffected,

and $|0_b'\rangle$ captures the ground state for the b fermions. For the configurations studied in this work, we can always find a low-energy fermion level that approaches a zero mode in the thermodynamic limit for $\kappa \neq 0$. These low-energy modes are well separated from the fermion continuum which has a finite gap $\propto |\kappa|$.

It is worth mentioning that two consistency checks are passed successfully by our numerical calculations. First, $\lim_{V \rightarrow \infty} \int_0^{eV} d\omega S_{ji}^{\alpha\beta}(\omega)$ recovers the static equal-time spin correlator [39]. Second, dynamical spin correlations are radially isotropic around an isolated \mathbb{Z}_2 vortex despite of the presence of a gauge string.

IV. CONDUCTANCE SIGNATURES OF MZMs

Figure 3 shows numerical results for $S_G(\omega)$ and $G(V)$ for three different tip positions near an isolated \mathbb{Z}_2 vortex. The different peaks in each $S_G(\omega)$ curve have a clear physical meaning. First, the $\omega = 0$ peak is directly connected to MZMs and stems from configurations \mathcal{G}_j^α with the vortex translated by one step. (For nonuniform Kitaev couplings, the peak can shift to a small frequency ω_0 ; see below.) The support for this peak comes only from on-site terms and nearest-neighbor bonds directly enclosing the vortex. Indeed, Fig. 3(a) shows that the peak weight decreases rapidly with the tip-vortex distance. Second, the peaks at $\omega = \Delta E_{2v}(\ell) \approx 0.1K$ in Fig. 3) correspond to the energy cost for creating a configuration \mathcal{G}_j^α with an additional pair of adjacent vortices by flipping a bond at distance ℓ from the original vortex, with the fermion bound state built from the new overlapping MZM pair unoccupied. This peak may contain several subpeaks since various configurations \mathcal{G}_j^α with different ℓ , and hence different $\Delta E_{2v}(\ell)$, may contribute to $S_G(\omega)$ in this frequency range. Third, the peak structure at $\omega = \Delta E_{2v}(\ell) + \varepsilon_f(\ell) \approx 0.25K$ includes the energy cost $\varepsilon_f(\ell)$ for occupying the fermion bound state. Finally, the onset of the gapped two-fermion continuum is marked by a (small) peak at $\omega = \Delta E_{2f} = \frac{3\sqrt{3}}{2}|\kappa| \approx 0.5K$ in Fig. 3).

The conductance $G(V)$ in Fig. 3(b) follows by integrating $S_G(\omega)$ and therefore shows steps at the voltages matching a peak in $S_G(\omega)$. One can thus measure the important energy scales ΔE_{2v} , ε_f , and ΔE_{2f} by STS. However, the respective step sizes are not universal because the peak weights in $S_G(\omega)$ depend on the tip position and on the form factors. It is instructive to compare to the vortex-free configuration \mathcal{G}_0 , see Fig. 3(b), where $G(V)$ is strongly suppressed for $eV < \Delta E_{2v}(\infty) + \varepsilon_f(\infty)$. Indeed, here the lowest-energy excitation probed by $G(V)$ corresponds to adding a vortex pair and filling the fermion bound state in order to respect the parity constraint. In this low-voltage regime, the conductance for the two-vortex configuration \mathcal{G} is instead dominated by MZMs and will be finite at small V , with a step at $eV = \Delta E_{2v}(\ell)$. We also observe from Fig. 3(b) that the “bulk” behavior of $G(V)$, found for arbitrary tip position in configuration \mathcal{G}_0 , is approached by moving the probe tip far away from the vortex center. We note that the zero-voltage step is particular to the integrable Kitaev model with uniform couplings (assumed in Fig. 3), where the eigenstates are degenerate with respect to the vortex position. In a generic nonintegrable case, vortices

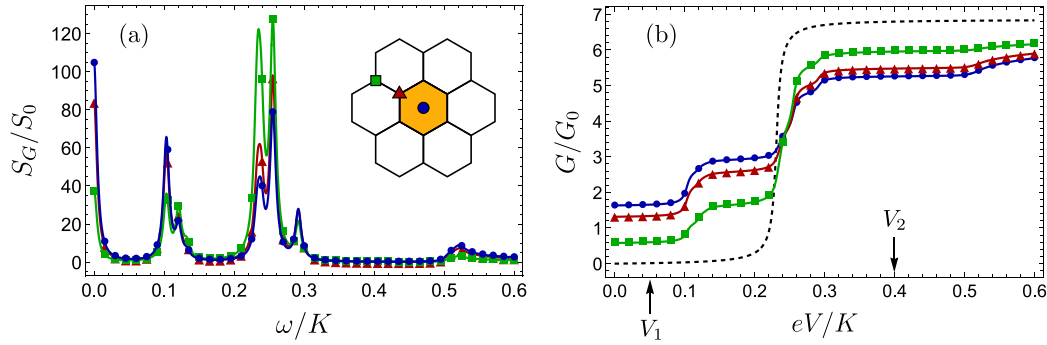


FIG. 3. STS for a Kitaev QSL in a two-vortex configuration \mathcal{G} , see Fig. 1(b), for $\kappa = 0.2K$, $L = 37$, $J_H = 0.05U$, $l_0 = 0.75a_0$, and $d = l_0$. For α -RuCl₃, one expects $K \approx 5$ meV [60]. (a) Weighted spin correlation function S_G vs ω , see Eq. (3.1), for three tip positions (inset). We plot $S_G(\omega)$ in units of $S_0 = d_A d_B (t_0 t_B / U)^2$, with delta function peaks replaced by Lorentzians of width $\Gamma_L = 0.005K$ due to higher-order tunneling processes. (b) Conductance G (in units of $G_0 = S_0 \frac{e^2}{h}$) vs V , see Eq. (3.1), for the tip positions in (a). The black dashed curve is for the vortex-free configuration \mathcal{G}_0 . The voltages $V_{1,2}$ are used in Fig. 4.

are mobile but can be trapped by bond disorder, vacancies, magnetic impurities, or by an external electrostatic potential. The $V = 0$ step may then shift to a small finite voltage $eV = \omega_0$, where ω_0 describes the difference in vortex creation energies on different plaquettes. Such shifts may be useful to distinguish MZM-induced conductance steps from the background conductance due to T_0 in Eq. (2.2).

For the voltages $V_{1,2}$ marked in Fig. 3(b), we show the tip-position dependence of the conductance in Fig. 4. For $V = V_1$, see Fig. 4(a), the physics is dominated by the zero-frequency MZM peak in $S_G(\omega)$, and the spatial profile in Fig. 4(a) encodes a convolution of the (squared) MZM wave function [53] with the form factor (3.3). However, in contrast to the standard situation in STS [21], it is not possible to map out the MZM wave function beyond the immediate vicinity of the vortex because only terms from sites or bonds encircling the vortex contribute for $eV < \Delta E_{2v}(\ell)$. The conductance profile for $V = V_2$ in Fig. 4(b) reveals a dip in the center, which arises because for a tip away from the vortex, the form factors enhance the peak contribution for $eV > \Delta E_{2v}(\ell)$. However, this voltage regime involves many vortex configurations \mathcal{G}_j^α , rendering

it difficult to extract the MZM wave function. Nonetheless, the conductance profile allows us to detect the MZM at the vortex location. Finally, the angular isotropy of the spatial profile approximately found at low voltage is reduced to a C_6 symmetry at higher voltages. While this effect is hardly visible for the tip distance $d = l_0$ in Fig. 4, it becomes more prominent for smaller d .

V. TOPOLOGICAL MAGNONS

In this section, we explore a different mechanism that could in principle generate similar tunnel conductance features to those reported above for MZMs in the spin-liquid phase. To that end, we consider topological magnons in the polarized phase of the Kitaev model in a magnetic field [18,19,43]. Such models have been proposed as an alternative scenario for explaining the observed half-quantized thermal Hall conductivity [18,19]. Below we clarify whether local defects or magnetic impurities are able to generate topological magnon bound states below the magnon gap. If present, such bound states may produce tunnel conductance steps at voltages

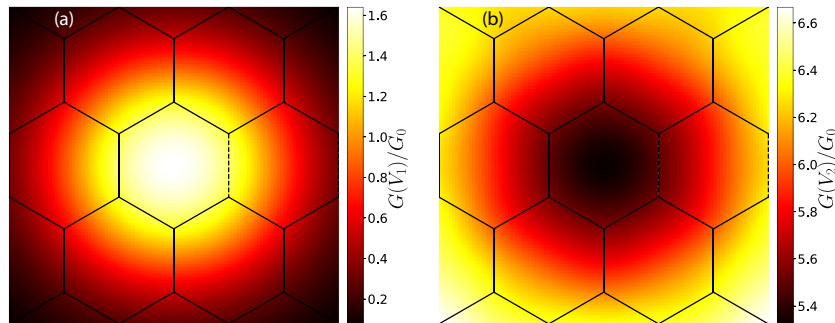


FIG. 4. Spatial conductance profile near a vortex (central plaquette) in the xy plane, for the parameters in Fig. 3 with (a) $V = V_1$ and (b) $V = V_2$; see Fig. 3(b). Note the different color scales.

matching the respective bound-state energies. In analogy to the topological superconductor case, magnon-induced conductance steps could then be difficult to distinguish from those caused by MZMs in a Kitaev spin liquid.

We consider spin- S operators S_i^γ on the 2D honeycomb lattice with Kitaev couplings. The Hamiltonian is given by

$$H_m = - \sum_{\langle ij \rangle_\gamma} K_{ij} S_i^\gamma S_j^\gamma - \sum_j \mathbf{h}_j \cdot \mathbf{S}_j, \quad (5.1)$$

where $\gamma \in \{x, y, z\} \equiv \{1, 2, 3\}$ denotes the spin components as well as the bond directions; see Sec. II. For simplicity, we assume that the local magnetic fields are oriented along the [111] direction, $\mathbf{h}_j = h_j \mathbf{c}$, with the unit vector \mathbf{c} in Eq. (A14); see the Appendix. In the homogeneous case, the Kitaev couplings and local fields are given by $K_{ij} = K$ and $\mathbf{h}_j = \mathbf{h}$, respectively. In order to model a *defect*, we study inhomogeneous Kitaev couplings K_{ij} near a single plaquette corresponding to the defect, similar to models for bond disorder and vacancies [74–76]. Recalling that a large-spin *magnetic impurity* is equivalent to a local change of the magnetic field at a single site [77], we model a magnetic impurity by a local change of the field $h_i \neq h$ at this site relative to the bulk field h . We follow Refs. [18, 19] and derive the linear spin wave theory which becomes exact in the large- S limit.

We first rotate the local basis to have the magnetization axis along the c direction. With the orthogonal matrix $R = (\mathbf{a} \mathbf{b} \mathbf{c})$, see Eq. (A14), we have the rotated spin operators $\tilde{S}_i^\alpha = R_{\alpha\beta} S_i^\beta$. Next, we employ a Holstein-Primakoff transformation to expand around the polarized state,

$$\begin{aligned} \tilde{S}_i^z &= S - b_i^\dagger b_i, & \tilde{S}_i^x &\approx \sqrt{\frac{S}{2}}(b_i + b_i^\dagger), \\ \tilde{S}_i^y &\approx -i\sqrt{\frac{S}{2}}(b_i - b_i^\dagger), \end{aligned} \quad (5.2)$$

with bosonic magnon operators b_i . Expanding H_m in Eq. (5.1) in powers of $1/S$, we obtain $H_m = E_{\text{cl}} + H_1 + H_2 + O(S^{1/2})$. The first term describes the classical ground state energy, $E_{\text{cl}} = -\frac{S^2}{3} \sum_{\langle ij \rangle} K_{ij} - S \sum_j h_j$. The second term is linear in the bosons,

$$H_1 = \frac{S^{3/2}}{3} \sum_i \left(\sum_\gamma e^{-i2\pi\gamma/3} K_{i,i+\delta_\gamma} \right) b_i + \text{H.c.}, \quad (5.3)$$

with the in-plane nearest-neighbor vectors

$$\delta_1 = \frac{1}{2}\hat{\mathbf{x}} + \frac{1}{2\sqrt{3}}\hat{\mathbf{y}}, \quad \delta_2 = -\frac{1}{2}\hat{\mathbf{x}} + \frac{1}{2\sqrt{3}}\hat{\mathbf{y}}, \quad \delta_3 = -\frac{1}{\sqrt{3}}\hat{\mathbf{y}}. \quad (5.4)$$

One finds $H_1 = 0$ for $K_{ij} = K$, but in the presence of defects, $H_1 \neq 0$ indicates that we have expanded around the wrong classical state. Due to the anisotropy of the Kitaev interactions, the spins do not align with the [111] direction anymore if the \mathbb{Z}_3 symmetry is broken by defect bonds. To correct for this problem, one has to find the correct classical state with an inhomogeneous magnetization and then apply position-dependent R matrices in order to rotate the spins to their local magnetization axis. While such refinements could

give quantitative corrections, we here focus on the quadratic term,

$$\begin{aligned} H_2 &= -\frac{S}{3} \sum_{\langle ij \rangle_\gamma} K_{ij} (b_i^\dagger b_j + b_j^\dagger b_i + e^{i2\pi\gamma/3} b_i b_j + e^{-i2\pi\gamma/3} b_j^\dagger b_i^\dagger) \\ &\quad + S \sum_i \left(h_i + \frac{1}{3} \sum_j K_{ij} \right) b_i^\dagger b_i. \end{aligned} \quad (5.5)$$

Indeed, in general terms, the linear spin wave theory resulting from Kitaev (or other) interactions on the 2D honeycomb lattice must be of the form

$$\begin{aligned} H_2 &= S \sum_{\langle ij \rangle_\gamma} (t_{ij} b_i^\dagger b_j + t_{ij}^* b_j^\dagger b_i + \Delta_{ij} b_i b_j + \Delta_{ij}^* b_j^\dagger b_i^\dagger) \\ &\quad + S \sum_i B_i b_i^\dagger b_i, \end{aligned} \quad (5.6)$$

where B_i is an effective magnetic field including the Weiss field. The misalignment of spins around defects here should give rise to an additional position dependence in the parameters t_{ij} , Δ_{ij} , and B_i in Eq. (5.6), on top of the immediate effects of K_{ij} anisotropy in Eq. (5.5). In what follows, we consider $H_m \simeq H_2$ as given by Eq. (5.5).

We first address the homogeneous case, where Fourier transformation gives $H_2 = S \sum_{\mathbf{k} \in \frac{1}{2}\text{BZ}} \Psi_{\mathbf{k}}^\dagger M_{\mathbf{k}} \Psi_{\mathbf{k}}$. Here \mathbf{k} runs over half the Brillouin zone, $\Psi_{\mathbf{k}}^\dagger = (b_{\mathbf{k},A}^\dagger \ b_{\mathbf{k},B}^\dagger \ b_{-\mathbf{k},A} \ b_{-\mathbf{k},B})$ is a four-component spinor (including the sublattice index), and

$$M_{\mathbf{k}} = \begin{pmatrix} A_{\mathbf{k}} & B_{\mathbf{k}} \\ B_{-\mathbf{k}}^* & A_{-\mathbf{k}}^T \end{pmatrix}. \quad (5.7)$$

Using the notation $\Gamma_{\mathbf{k},n} = \sum_\gamma e^{-i2\pi n\gamma/3} e^{i\mathbf{k} \cdot \delta_\gamma}$ with $n \in \{0, 1\}$, we have defined the matrices

$$\begin{aligned} A_{\mathbf{k}} &= \begin{pmatrix} h + K & -\frac{1}{3}K\Gamma_{\mathbf{k},0} \\ -\frac{1}{3}K\Gamma_{-\mathbf{k},0} & h + K \end{pmatrix}, \\ B_{\mathbf{k}} &= \begin{pmatrix} 0 & -\frac{1}{3}K\Gamma_{\mathbf{k},1} \\ -\frac{1}{3}K\Gamma_{-\mathbf{k},1} & 0 \end{pmatrix}. \end{aligned} \quad (5.8)$$

This Hamiltonian can be diagonalized by a Bogoliubov transformation. With $\Sigma = \text{diag}(1, 1, -1, -1)$, we obtain the magnon band dispersion from the positive eigenvalues of $\Sigma M_{\mathbf{k}}$. The result is illustrated in Fig. 5. We find two bands $\omega_1(\mathbf{k})$ and $\omega_2(\mathbf{k})$, where analytical but lengthy expressions are available. These topological magnon bands cover the energy range

$$h < \omega_1(\mathbf{k}) < \sqrt{h(h+2K)}, \quad h + K < \omega_2(\mathbf{k}) < h + 2K. \quad (5.9)$$

The magnon band gap is thus given by $\Delta E_m = h$. For $h \rightarrow 0$, the lower magnon band becomes a zero-energy flat band, signaling the degeneracy of the classical Kitaev model at zero field.

A. Defect from bond disorder

Next we turn to inhomogeneous Kitaev interactions, where we model a defect by modifying the bonds $K_{ij} \rightarrow \xi K$ around

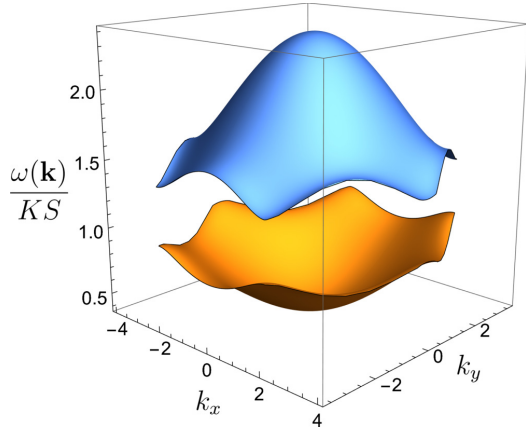


FIG. 5. Topological magnon bands for $h/K = 0.4$ (with momentum unit a_0^{-1}) from linear spin wave theory for the homogeneous model (5.1).

a given plaquette representing the defect by a positive factor $\xi \neq 1$. We have studied two different radially symmetric bond defect patterns. In the first case, we modify only the six bonds directly surrounding the defect plaquette. In the second case, we instead change only the six adjacent bonds pointing radially outward from this plaquette. The conclusions described below are identical for both cases. We have studied the spectrum of H_2 in Eq. (5.5) by numerical diagonalization on a finite $L \times L$ honeycomb lattice as described in Sec. III. We observe that making the bonds stronger ($\xi > 1$) creates a repulsive potential for magnons, which generates antibound states above the top of the upper band, $\varepsilon'_m > h + 2K$. There are also bound states in the gap between both bands. However, even if we make the bonds significantly weaker, $\xi < 1$, we never observe bound states below the lower band, $\varepsilon_m < \Delta E_m$. We conclude that bond defects are unlikely to produce magnon bound states at subgap energies. At the same time, we cannot rule out that a more complex bond defect pattern could cause subgap features that can mimic the Majorana features described in Sec. IV. Future work should investigate this issue in more detail.

B. Magnetic impurity

Another limiting case is to locally modify only the magnetic field h_i in Eq. (5.5), keeping homogeneous Kitaev couplings $K_{ij} = K$. For a radially symmetric inhomogeneous magnetic field profile, \mathbb{Z}_3 symmetry remains intact and the linear-boson term H_1 in Eq. (5.3) vanishes. If we change the field only at a single site, $h_i = h' \neq h$, with the bulk field h acting at all other sites, we can find a single subgap bound state for $h' < h$ as shown in Fig. 6. The bound-state energy $\varepsilon_m < \Delta E_m$ vanishes for $h' \approx -1.1h$ for $h = 0.4K$. For smaller h , the vanishing of ε_m occurs at lower values of $h'/h < 0$. For generic values of h'/h , we find that ε_m is positive. The dynamical spin correlation function then will have a peak at $\omega = \varepsilon_m$, and Eq. (3.1) yields a single steplike feature in $G(V)$ at $eV = \varepsilon_m$. Except for the fine-tuned case with $\varepsilon_m = 0$,

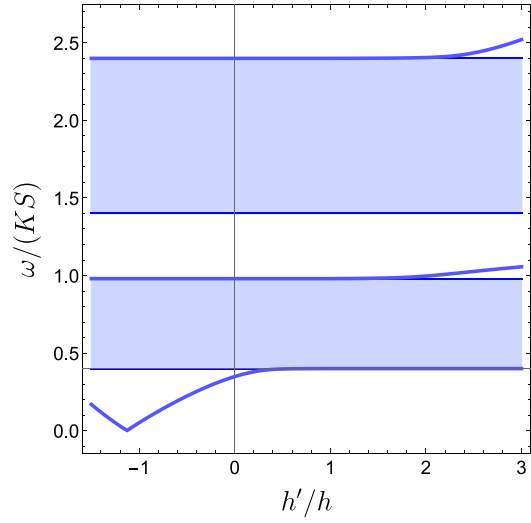


FIG. 6. Magnon spectrum ω vs h'/h for a local magnetic field $h' \neq h$ at a single site. The bulk field is $h = 0.4K$. Shaded regions describe continuum states; see Eq. (5.9). A single subgap bound state can exist for $h' < h$. A high-energy antibound state is visible for $h' > h$, and another bound state exists in the minigap between both bands.

this step does not occur at zero voltage as expected for the MZM case.

For a wider field profile, with the field change extending over several sites, we typically find several subgap bound states. This case can be realized if the impurity is coupled to several sites. In such cases, from the $G(V)$ curve alone, it can be difficult to disentangle the effects of magnon bound states from those due to MZMs. However, a collection of several nearby magnetic impurities causing such a field profile should be identifiable by concomitant STM surface topography scans.

VI. CONCLUSIONS

Based on the above analysis, we expect that the tunnel conductance features due to MZMs in a spin liquid will be quite robust. For the topological magnon scenario in Sec. V, we find that defects modeled by locally inhomogeneous Kitaev couplings do not bind subgap magnon bound states. On the other hand, a large-spin magnetic impurity can induce a single subgap bound state centered at the corresponding site. One then expects a single conductance step, where the spatial distribution of the STS tunnel conductance peaks at this site. For the MZM case, we instead predict a characteristic sequence of steps and the spatial distribution should peak at the center of the hexagon defining the vortex.

We conclude that the perspectives for STS detection of MZMs in spin liquids appear promising. In fact, tunneling experiments on monolayers of α -RuCl₃ have recently observed interesting low-energy excitations [62]. Given the rapid progress in encapsulating and probing atomically thin

materials [78], detailed experimental tests of our predictions will likely soon be available.

ACKNOWLEDGMENTS

We acknowledge funding by the Deutsche Forschungsgemeinschaft (DFG; German Research Foundation), Projektnummer 277101999–TRR 183 (Project No. B04), Normalverfahren Projektnummer EG 96-13/1, and under Germany's Excellence Strategy–Cluster of Excellence Matter and Light for Quantum Computing (ML4Q) EXC 2004/1–390534769, by the Brazilian ministries MEC and MCTI, by the Brazilian agency CNPq, and by the Coordenação de Aperfeiçoamento de Pessoal de Nível Superior–Brasil (CAPES)–Finance Code 001.

APPENDIX: DERIVATION OF LOW-ENERGY THEORY

This Appendix provides a derivation of the cotunneling Hamiltonian (2.2) with the corresponding transition matrix elements. As starting point, we take the general Hamiltonian $H_{\text{tot}} = H_M + V_{\text{at}} + H_{\text{tun}}$, where H_M describes noninteracting metallic leads representing the scanning probe tip and the substrate,

$$H_M = \sum_{v \in \{A, B\}} \sum_{\tau \in \{\uparrow, \downarrow\}} \sum_{\mathbf{k}} \varepsilon_{v\tau}(\mathbf{k}) c_{v\tau}^\dagger(\mathbf{k}) c_{v\tau}(\mathbf{k}). \quad (\text{A1})$$

The fermion annihilation operators $c_{v\tau}(\mathbf{k})$ with $v = A, B$ refer to tip and substrate electrons, respectively, where τ is the spin projection and $\varepsilon_{v\tau}(\mathbf{k})$ the energy with respect to the Fermi energy. The Pauli matrices τ used below act in the spin space of the conduction electrons.

For the 2D Kitaev layer, we start from a Hubbard-Kanamori model for the d^5 electrons in an edge-sharing octahedral environment, e.g., those of the Ru^{3+} ions in $\alpha\text{-RuCl}_3$. For lowest-order perturbation theory in the tunnel Hamiltonian H_{tun} connecting the layer to the STM tip and to the substrate, only the single-site atomic Hamiltonian V_{at} in the Hubbard-Kanamori model is needed (see, for instance, Ref. [39]),

$$V_{\text{at}} = \frac{U - 3J_H}{2} (\tilde{N} - 1)^2 - 2J_H \tilde{\mathbf{S}}^2 - \frac{J_H}{2} \tilde{\mathbf{L}}^2 + \lambda_{\text{so}} \tilde{\mathbf{L}} \cdot \tilde{\mathbf{S}}, \quad (\text{A2})$$

with the on-site Coulomb energy U , the Hund coupling J_H , and the spin-orbit coupling λ_{so} . The respective couplings can be renormalized by screening processes resulting from the presence of the tip and the substrate, but one expects $U \approx$

2 eV and $\lambda_{\text{so}} \ll J_H, U$. For definiteness, we assume $J_H \ll U$. To lowest order in H_{tun} , contributions from different lattice sites simply add up. The operators \tilde{N} , $\tilde{\mathbf{S}}$, and $\tilde{\mathbf{L}}$ in Eq. (A2) refer to hole number, spin, and angular momentum, respectively. In terms of the hole annihilation operators h_s with the combined spin-orbital index $s = (\alpha, \sigma)$, they are expressed as

$$\tilde{N} = h^\dagger h, \quad \tilde{\mathbf{S}} = \frac{1}{2} h^\dagger (\tilde{\sigma} \otimes \mathbb{1}_3) h, \quad \tilde{\mathbf{L}} = h^\dagger (\mathbb{1}_2 \otimes \tilde{\mathbf{I}}) h, \quad (\text{A3})$$

with $h^\dagger = (h_{x\uparrow}^\dagger, h_{y\uparrow}^\dagger, h_{z\uparrow}^\dagger, h_{x\downarrow}^\dagger, h_{y\downarrow}^\dagger, h_{z\downarrow}^\dagger)$. The five d electrons in a cubic crystal field occupy three t_{2g} orbitals (xy, yz, zx), denoted here by the complementary index $\alpha = (z, x, y)$. The Pauli matrices $\tilde{\sigma}$ act in the spin space of the magnetic layer site, and $\tilde{\mathbf{I}} = (\tilde{I}^x, \tilde{I}^y, \tilde{I}^z)$ represents the $l_{\text{eff}} = 1$ orbital angular momentum of the corresponding t_{2g} states, with explicit matrix representations specified in Ref. [39]. Following standard practice, the spin-orbit coupling λ_{so} will be taken into account later through a projection to the lowest-lying hole states with total angular momentum $j_{\text{eff}} = 1/2$.

Electron transfer between tip (or substrate) and the Mott insulating site is described by a tunneling Hamiltonian $H_{\text{tun}} = \mathcal{T}_1 + \mathcal{T}_{-1}$, where $\mathcal{T}_{\pm 1}$ refers to changes of the hole number by $\Delta \tilde{N} = \pm 1$, respectively. With the complex-valued tunnel amplitude $t_{v\tau s}(\mathbf{k})$ connecting a conduction electron in lead $v = A, B$ with spin τ and momentum \mathbf{k} to the spin-orbital hole state $s = (\alpha, -\sigma)$ on the magnetic site,

$$\mathcal{T}_1 = \sum_{v, \tau, s} \sum_{\mathbf{k}} t_{v\tau s}(\mathbf{k}) c_{v\tau}^\dagger(\mathbf{k}) h_s^\dagger, \quad \mathcal{T}_{-1} = \mathcal{T}_1^\dagger. \quad (\text{A4})$$

We then employ $H_0 = H_M + V_{\text{at}}$ as the unperturbed Hamiltonian. The ground-state sector has a single hole at the spin-liquid site, and the intermediate states have either $\tilde{N} = 0$ or $\tilde{N} = 2$ holes, depending on whether \mathcal{T}_{-1} or \mathcal{T}_1 is applied to a single-hole state. In the latter case, we have to distinguish between angular momentum channels with $L = 0, 1, 2$. Following Ref. [39], we use the notation $\mathcal{P}_L^{(n)}$ for the projection operators to states with angular momentum L and hole number $n = 0, 1, 2$. We omit the lower index for $n = 0, 1$ because in those cases there is only a single angular momentum channel. The projector to two-hole states is $\mathcal{P}^{(2)} = \sum_L \mathcal{P}_L^{(2)}$. For a lowest-order expansion in H_{tun} , the Hilbert space can be truncated to have at most two holes at the magnetic layer site, $\mathbb{1} \simeq \mathcal{P}^{(0)} + \mathcal{P}^{(1)} + \mathcal{P}^{(2)}$.

Next we employ a canonical transformation to perform the projection to the low-energy sector, which is equivalent to a Schrieffer-Wolff transformation. Writing $\tilde{H} = e^S H e^{-S} = H + [S, H] + \dots$, the first-order generator $S = S_1$ must then obey $[H_0, S_1] = H_{\text{tun}}$. Using the commutators

$$\begin{aligned} [H_0, \mathcal{P}_L^{(2)} \mathcal{T}_1 \mathcal{P}^{(1)}] &= \sum_{v, \tau, s} \sum_{\mathbf{k}} t_{v\tau s}(\mathbf{k}) [\Delta E_L + \varepsilon_{v\tau}(\mathbf{k})] c_{v\tau}^\dagger(\mathbf{k}) \mathcal{P}_L^{(2)} h_s^\dagger \mathcal{P}^{(1)}, \\ [H_0, \mathcal{P}^{(0)} \mathcal{T}_{-1} \mathcal{P}^{(1)}] &= \sum_{v, \tau, s} \sum_{\mathbf{k}} t_{v\tau s}^*(\mathbf{k}) [\Delta E_0 - \varepsilon_{v\tau}(\mathbf{k})] \mathcal{P}^{(0)} h_s \mathcal{P}^{(1)} c_{v\tau}(\mathbf{k}), \end{aligned} \quad (\text{A5})$$

and writing $S_1 = S_1^{(+)} - S_1^{(-)}$ with $S_1^{(-)} = S_1^{(+)\dagger}$, the part increasing the hole number at the magnetic site is

$$S_1^{(+)} = \sum_{v, \tau, s} \sum_{\mathbf{k}} c_{v\tau}^\dagger(\mathbf{k}) \left(-\frac{t_{v\tau s}(\mathbf{k})}{\Delta E_0 - \varepsilon_{v\tau}(\mathbf{k})} \mathcal{P}^{(1)} h_s^\dagger \mathcal{P}^{(0)} + \sum_L \frac{t_{v\tau s}(\mathbf{k})}{\Delta E_L + \varepsilon_{v\tau}(\mathbf{k})} \mathcal{P}_L^{(2)} h_s^\dagger \mathcal{P}^{(1)} \right). \quad (\text{A6})$$

The excitation energies ΔE_L are given by

$$\Delta E_0 = \frac{U}{2} + J_H, \quad \Delta E_1 = \frac{U}{2} - 4J_H, \quad \Delta E_2 = \frac{U}{2} - 2J_H, \quad (\text{A7})$$

where the energy for the transition to a state with zero holes is the same as for the transition to two holes with $L = 0$. The charge gap is set by the smallest of those energies, $E_g = \Delta E_1$.

The canonical transformation then results in the cotunneling Hamiltonian

$$H_{\text{cot}} = -\frac{1}{2} \mathcal{P}^{(1)} (\mathcal{T}_1 S_1^{(+)} - \mathcal{T}_1 S_1^{(-)}) \mathcal{P}^{(1)} + \text{H.c.}, \quad (\text{A8})$$

which accurately describes the low-energy subspace with energy scales below E_g . Inserting the above expressions, we find the explicit representation

$$H_{\text{cot}} = -\frac{1}{2} \sum_{\nu_1, \tau_1, s_1} \sum_{\nu_2, \tau_2, s_2} \sum_{\mathbf{k}_1, \mathbf{k}_2} \frac{t_{\nu_2 \tau_2 s_2}(\mathbf{k}_2) t_{\nu_1 \tau_1 s_1}^*(\mathbf{k}_1)}{\Delta E_0 - \varepsilon_{\nu_1 \tau_1}(\mathbf{k}_1)} \mathcal{P}^{(1)} h_{s_2}^\dagger h_{s_1} \mathcal{P}^{(1)} c_{\nu_2 \tau_2}^\dagger(\mathbf{k}_2) c_{\nu_1 \tau_1}(\mathbf{k}_1) \\ - \frac{1}{2} \sum_{\nu_1, \tau_1, s_1} \sum_{\nu_2, \tau_2, s_2} \sum_{\mathbf{k}_1, \mathbf{k}_2} \sum_L \frac{t_{\nu_2 \tau_2 s_2}^*(\mathbf{k}_2) t_{\nu_1 \tau_1 s_1}(\mathbf{k}_1)}{\Delta E_L + \varepsilon_{\nu_1 \tau_1}(\mathbf{k}_1)} \mathcal{P}^{(1)} h_{s_2} \mathcal{P}_L^{(2)} h_{s_1}^\dagger \mathcal{P}^{(1)} c_{\nu_2 \tau_2}(\mathbf{k}_2) c_{\nu_1 \tau_1}^\dagger(\mathbf{k}_1) + \text{H.c.} \quad (\text{A9})$$

We next compute the required matrix elements between spin-orbital states (where $\bar{\sigma} = -\sigma$ for $\sigma = \uparrow, \downarrow = +1, -1$),

$$\langle s' | h_{s_2}^\dagger h_{s_1} | s \rangle = \delta_{s' s_2} \delta_{s s_1}, \quad \langle s' | h_{s_2} \mathcal{P}_{L=0}^{(2)} h_{s_1}^\dagger | s \rangle = \frac{1}{3} \sigma_2 \sigma_1 \delta_{\alpha' \alpha_2} \delta_{\alpha \alpha_1} \delta_{\sigma_2 \bar{\sigma}'} \delta_{\sigma_1 \bar{\sigma}}, \\ \langle s' | h_{s_2} \mathcal{P}_{L=1}^{(2)} h_{s_1}^\dagger | s \rangle = \frac{1}{2} (\delta_{\alpha_2 \alpha_1} \delta_{\alpha' \alpha} - \delta_{\alpha_2 \alpha} \delta_{\alpha' \alpha_1}) (\delta_{\sigma_2 \sigma_1} \delta_{\sigma \sigma'} + \delta_{\sigma_2 \sigma} \delta_{\sigma_1 \sigma'}), \\ \langle s' | h_{s_2} \mathcal{P}_{L=2}^{(2)} h_{s_1}^\dagger | s \rangle = \delta_{s_2 s_1} \delta_{s s'} - \delta_{s_2 s} \delta_{s_1 s'} - \langle s' | h_{s_2} \mathcal{P}_{L=0}^{(2)} h_{s_1}^\dagger | s \rangle - \langle s' | h_{s_2} \mathcal{P}_{L=1}^{(2)} h_{s_1}^\dagger | s \rangle. \quad (\text{A10})$$

We then obtain the matrix elements of H_{cot} in spin-orbital space as

$$(H_{\text{cot}})_{s' s} = -\frac{1}{2} \sum_{\mathbf{k}_1 \nu_1 \tau_1} \sum_{\mathbf{k}_2 \nu_2 \tau_2} F_{s' s}(\mathbf{k}_2, \nu_2, \tau_2; \mathbf{k}_1, \nu_1, \tau_1) c_{\nu_2 \tau_2}^\dagger(\mathbf{k}_2) c_{\nu_1 \tau_1}(\mathbf{k}_1) \\ - \frac{1}{2} \sum_{\mathbf{k}_1 \nu_1 \tau_1} \sum_{\mathbf{k}_2 \nu_2 \tau_2} \sum_{L=0}^2 G_{s' s}^L(\mathbf{k}_2, \nu_2, \tau_2; \mathbf{k}_1, \nu_1, \tau_1) c_{\nu_2 \tau_2}(\mathbf{k}_2) c_{\nu_1 \tau_1}^\dagger(\mathbf{k}_1) + \text{H.c.}, \quad (\text{A11})$$

with the definitions

$$F_{s' s}(\mathbf{k}_2, \nu_2, \tau_2; \mathbf{k}_1, \nu_1, \tau_1) = \frac{t_{\nu_2 \tau_2 s'}(\mathbf{k}_2) t_{\nu_1 \tau_1 s}^*(\mathbf{k}_1)}{\Delta E_0 - \varepsilon_{\nu_1 \tau_1}(\mathbf{k}_1)}, \\ G_{s' s}^L(\mathbf{k}_2, \nu_2, \tau_2; \mathbf{k}_1, \nu_1, \tau_1) = \sum_{s_1, s_2} \frac{t_{\nu_2 \tau_2 s_2}^*(\mathbf{k}_2) t_{\nu_1 \tau_1 s_1}(\mathbf{k}_1)}{\Delta E_L + \varepsilon_{\nu_1 \tau_1}(\mathbf{k}_1)} \langle s' | h_{s_2} \mathcal{P}_L^{(2)} h_{s_1}^\dagger | s \rangle. \quad (\text{A12})$$

In a low-energy approach, we can now assume low energies, $|\varepsilon_{\nu \tau}(\mathbf{k})| \ll E_g$, for all conduction electron states involved in virtual processes. For simplicity, we also consider effectively \mathbf{k} -independent, spin-conserving, and spin-independent tunneling amplitudes,

$$t_{\nu \tau s}(\mathbf{k}) = t_{\nu \alpha} \delta_{\tau \sigma}, \quad (\text{A13})$$

with $s = (\alpha, -\sigma)$. Tunneling between the substrate ($\nu = B$) and the magnetic layer is modeled by a featureless isotropic coupling, $t_{B\alpha} = t_B$. However, the tunnel couplings connecting the tip ($\nu = A$) to a magnetic site depend on the t_{2g} orbital (α) as well as on the relative position between tip and site. For definiteness, we model the t_{2g} orbitals by real wave functions with the proper symmetry. For instance, for the xy orbital centered at $\mathbf{R}_j = 0$, we take $\Phi_{xy}(\mathbf{r}') \propto x'y'e^{-|\mathbf{r}'|/l_d}$, where l_d sets the size of the orbital. Here the components of \mathbf{r}' refer to the axes fixed by the octahedral environment of the magnetic ion; see Fig. 7(a). In these coordinates, the unit vectors for the

conventional crystallographic directions are given by

$$\mathbf{a} = \frac{1}{\sqrt{6}} \begin{pmatrix} 1 \\ 1 \\ -2 \end{pmatrix}, \quad \mathbf{b} = \frac{1}{\sqrt{2}} \begin{pmatrix} -1 \\ 1 \\ 0 \end{pmatrix}, \quad \mathbf{c} = \frac{1}{\sqrt{3}} \begin{pmatrix} 1 \\ 1 \\ 1 \end{pmatrix}, \quad (\text{A14})$$

where \mathbf{c} is perpendicular to the honeycomb plane. As the wave function for the tip at position \mathbf{r} , we consider

$$\Phi_s(\mathbf{r}') \propto e^{-|\mathbf{r}' - \mathbf{r}|/l_s}, \quad (\text{A15})$$

with characteristic length l_s .

In Fig. 7(b) we show the overlap between Φ_{xy} and Φ_s as a function of the tip position, keeping the tip height $\mathbf{r} \cdot \mathbf{c} > 0$ constant and varying the coordinates parallel to the honeycomb plane. The coordinates are scaled by the effective radius of the t_{2g} orbitals, $r_d = \int d^3 r' r' |\Phi_\alpha(\mathbf{r}')|^2 = 7l_d/2$. We denote by \mathbf{v}_α the in-plane vector that corresponds to the relative position of maximum overlap between the tip and the α orbital. Note that \mathbf{v}_α lies in the direction perpendicular to the α bond. This shift in the position of maximum overlap can be

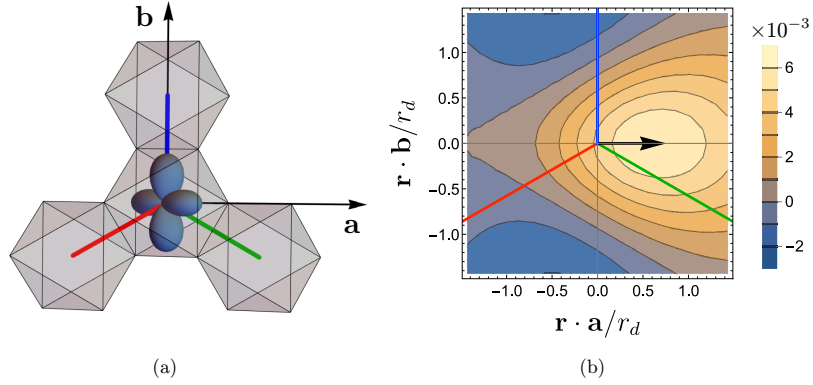


FIG. 7. Orbital and spatial dependence of tunnel couplings. (a) xy orbital in the edge-sharing octahedra geometry of α - RuCl_3 . The red, green, and blue lines represent the directions of x , y , and z bonds in the honeycomb plane, respectively. (b) Overlap between the xy orbital at $\mathbf{R}_j = 0$ and the wave function for electrons in the tip, modeled as an s orbital centered at position \mathbf{r} ; see Eq. (A15). The arrow indicates the point of maximum overlap, corresponding to the vector \mathbf{v}_z . Here we set $l_s = 4l_d$ and $\mathbf{r} \cdot \mathbf{c} = 3l_d$.

interpreted in terms of the direction in which the α orbital points above the plane; see Fig. 7(a). Comparing the ionic radius of Ru^{3+} with the lattice spacing of α - RuCl_3 , we estimate $|\mathbf{v}_\alpha| \approx 0.1a_0$. To capture the orbital and position dependence in the tunnel couplings within a simple analytical expression, we parametrize $t_{A\alpha}(\mathbf{r}, \mathbf{R}_j)$ as given in Eq. (2.3), with tunneling length $l_0 \sim l_s \lesssim a_0$.

For given \mathbf{r} and \mathbf{R}_j , it is convenient to express the tunnel couplings $t_{A\alpha}$ in terms of spherical angles $\varphi \in [0, 2\pi)$ and $\theta \in [-\pi, \pi]$,

$$\begin{pmatrix} t_{Ax} \\ t_{Ay} \\ t_{Az} \end{pmatrix} = t_A \begin{pmatrix} \cos \varphi \sin \theta \\ \sin \varphi \sin \theta \\ \cos \theta \end{pmatrix}. \quad (\text{A16})$$

Inserting the above expressions into Eq. (A12) and using Eq. (A10), we finally perform the projection to the $j_{\text{eff}} = 1/2$ subspace selected by the spin-orbit coupling. The corresponding basis states are [39]

$$\begin{aligned} |+\rangle &= \frac{1}{\sqrt{3}}(-|z, \uparrow\rangle - i|y, \downarrow\rangle - |x, \downarrow\rangle), \\ |-\rangle &= \frac{1}{\sqrt{3}}(|z, \downarrow\rangle + i|y, \uparrow\rangle - |x, \uparrow\rangle). \end{aligned} \quad (\text{A17})$$

The spin operator appearing in the Kitaev model for this site, $\mathbf{S} = \frac{1}{2}\boldsymbol{\sigma}$, acts in the space spanned by Eq. (A17). The cotunneling Hamiltonian follows as

$$H_{\text{cot}} = - \sum_{\mathbf{k}_1 \nu_1} \sum_{\mathbf{k}_2 \nu_2} \frac{t_{\nu_1} t_{\nu_2}}{2\Delta E_0} c_{\nu_2}^\dagger(\mathbf{k}_2) (f_0 \mathbb{1} + \mathbf{f} \cdot \boldsymbol{\sigma}) c_{\nu_1}(\mathbf{k}_1) - \sum_{\mathbf{k}_1 \nu_1 \tau_1} \sum_{\mathbf{k}_2 \nu_2 \tau_2} \sum_L \frac{t_{\nu_1} t_{\nu_2}}{2\Delta E_L} c_{\nu_2}(\mathbf{k}_2) (g_0^L \mathbb{1} + \mathbf{g}^L \cdot \boldsymbol{\sigma}) c_{\nu_1}^\dagger(\mathbf{k}_1) + \text{H.c.}, \quad (\text{A18})$$

with f_0 and $\mathbf{f} = (f_x, f_y, f_z)$ given by

$$f_0 = \frac{F_{\uparrow\uparrow} + F_{\downarrow\downarrow}}{2}, \quad f_x = \frac{F_{\uparrow\downarrow} + F_{\downarrow\uparrow}}{2}, \quad f_y = i \frac{F_{\uparrow\downarrow} - F_{\downarrow\uparrow}}{2}, \quad f_z = \frac{F_{\uparrow\uparrow} - F_{\downarrow\downarrow}}{2}, \quad (\text{A19})$$

and likewise for g_0^L and \mathbf{g}^L . For given (σ, σ') indices, the 2×2 matrices $F_{\sigma\sigma'}$ and $G_{\sigma\sigma'}^L$ act in conduction electron spin space. We find

$$\begin{aligned} F_{\uparrow\uparrow} &= \frac{1}{3} \begin{pmatrix} \cos \theta & (1+i)\cos \theta \\ e^{-i\varphi} \sin \theta & (1+i)e^{-i\varphi} \sin \theta \end{pmatrix}, \quad F_{\uparrow\downarrow} = \frac{1}{3} \begin{pmatrix} (1-i)\cos \theta & -\cos \theta \\ (1-i)e^{-i\varphi} \sin \theta & -e^{-i\varphi} \sin \theta \end{pmatrix}, \quad G_{\uparrow\uparrow}^0 = \frac{F_{\downarrow\downarrow}}{3}, \quad G_{\uparrow\downarrow}^0 = -\frac{F_{\uparrow\downarrow}}{3}, \\ G_{\uparrow\uparrow}^1 &= \frac{1}{6} \begin{pmatrix} (1-i)e^{i\varphi} \sin \theta + 2\cos \theta & (1+i)\cos \theta \\ e^{-i\varphi} \sin \theta & (\sin \varphi + \cos \varphi) \sin \theta \end{pmatrix}, \quad G_{\uparrow\downarrow}^1 = \frac{1}{6} \begin{pmatrix} e^{-i\varphi} \sin \theta & (\sin \varphi + \cos \varphi) \sin \theta \\ (1-i)e^{-i\varphi} \sin \theta & -(1-i)\cos \theta \end{pmatrix}, \\ G_{\uparrow\uparrow}^2 &= [(\cos \varphi + \sin \varphi) \sin \theta + \cos \theta] \mathbb{1} - F_{\uparrow\uparrow} - G_{\uparrow\uparrow}^0 - G_{\uparrow\uparrow}^1, \quad G_{\uparrow\downarrow}^2 = -F_{\uparrow\downarrow} - G_{\uparrow\downarrow}^0 - G_{\uparrow\downarrow}^1. \end{aligned} \quad (\text{A20})$$

The remaining matrices are obtained by using a time-reversal operation,

$$F_{\downarrow\downarrow} = \tau_y F_{\uparrow\uparrow}^* \tau_y, \quad F_{\downarrow\uparrow} = -\tau_y F_{\uparrow\downarrow}^* \tau_y, \quad G_{\downarrow\downarrow}^L = \tau_y (G_{\uparrow\uparrow}^L)^* \tau_y, \quad G_{\downarrow\uparrow}^L = -\tau_y (G_{\uparrow\downarrow}^L)^* \tau_y, \quad (\text{A21})$$

with Pauli matrices $\boldsymbol{\tau}$ in conduction electron spin space. In the second term of Eq. (A18), we now use

$$c_{\nu_2 \tau_2}(\mathbf{k}_2) c_{\nu_1 \tau_1}^\dagger(\mathbf{k}_1) = -c_{\nu_1 \tau_1}^\dagger(\mathbf{k}_1) c_{\nu_2 \tau_2}(\mathbf{k}_2) + \delta_{\nu_1 \nu_2} \delta_{\tau_1 \tau_2} \delta_{\mathbf{k}_1 \mathbf{k}_2}.$$

The factor $\delta_{\tau_1 \tau_2}$ in the last term implies a trace over the 2×2 matrices for conduction electrons. As a result, only the identity can contribute. We thereby obtain the cotunneling Hamiltonian (2.2), where $\Psi_A(\mathbf{r}) = \sum_{\mathbf{k}} c_A(\mathbf{k})$ is a real-space two-component spinor field describing conduction electrons on the tip at position \mathbf{r} . Likewise, $\Psi_B(\mathbf{R})$ refers to the substrate spinor field below the site with position \mathbf{R} . Cotunneling processes are then characterized by the transition matrices T_0 and T^α , with $\mathbf{T} = (T^x, T^y, T^z)$, which act in conduction electron spin space and are given by

$$\begin{aligned} T_0 &= -\frac{t_{AB}}{\Delta E_0} f_0 + \sum_{L=0}^2 \frac{t_{AB}}{\Delta E_L} g_0^L, \\ \mathbf{T} &= -\frac{t_{AB}}{\Delta E_0} \mathbf{f} + \sum_{L=0}^2 \frac{t_{AB}}{\Delta E_L} \mathbf{g}^L. \end{aligned} \quad (\text{A22})$$

All matrix elements scale $\propto t_{AB}/U$, where individual contributions carry $\frac{U}{\Delta E}$ -dependent factors. We emphasize that T_0 and \mathbf{T} depend on $\mathbf{r} - \mathbf{R}_j$, with the tip (site) position $\mathbf{r} (\mathbf{R}_j)$.

The above expressions can be simplified considerably when neglecting the orbital-dependent shifts \mathbf{v}_α in Eq. (2.3). This approximation becomes exact for a tip placed right on top

of a magnetic site, and otherwise causes quantitative ($\approx 10\%$) deviations in the tunnel couplings. We then obtain

$$\begin{aligned} f_0 &= \frac{1}{2\sqrt{3}} \mathbb{1}, & f_\alpha &= \frac{1}{3\sqrt{3}} (\tau^x + \tau^y + \tau^z) - \frac{1}{2\sqrt{3}} \tau^\alpha, \\ g_0^0 &= \frac{1}{6\sqrt{3}} \mathbb{1}, & g_\alpha^0 &= -\frac{29}{2\sqrt{3}} (\tau^x + \tau^y + \tau^z) + \frac{1}{6\sqrt{3}} \tau^\alpha, \\ g_0^1 &= \frac{1}{2\sqrt{3}} \mathbb{1}, & g_\alpha^1 &= \frac{13}{2\sqrt{3}} \tau^\alpha, \\ g_0^2 &= \frac{23}{3\sqrt{3}} \mathbb{1}, & g_\alpha^2 &= -\frac{55}{9\sqrt{3}} (\tau^x + \tau^y + \tau^z) + \frac{26}{3\sqrt{3}} \tau^\alpha, \end{aligned}$$

and H_{cot} takes the form (2.4), where we define the $\frac{U}{\Delta E}$ -dependent coefficients ($j = 0, 1, 2$)

$$\eta_j = \frac{U}{2\sqrt{3}\Delta E_0} \zeta_j + \sum_{L=0}^2 \frac{U}{2\sqrt{3}\Delta E_L} \zeta_j^L \quad (\text{A23})$$

with ΔE_L in Eq. (A7) and the numbers

$$\begin{aligned} \zeta_0 &= 1, & \zeta_0^1 &= \frac{1}{3}, & \zeta_0^2 &= 1, & \zeta_0^3 &= \frac{46}{3}, \\ \zeta_1 &= -\frac{1}{2}, & \zeta_2 &= \frac{1}{3}, & \zeta_1^0 &= \frac{1}{6}, & \zeta_2^0 &= -\frac{1}{9}, & \zeta_1^1 &= 0, \\ \zeta_2^1 &= \frac{1}{6}, & \zeta_1^2 &= \frac{1}{3}, & \zeta_2^2 &= -\frac{7}{18}. \end{aligned}$$

-
- [1] A. Kitaev, *Ann. Phys.* **321**, 2 (2006).
 - [2] G. Jackeli and G. Khaliullin, *Phys. Rev. Lett.* **102**, 017205 (2009).
 - [3] L. Savary and L. Balents, *Rep. Prog. Phys.* **80**, 016502 (2017).
 - [4] Y. Zhou, K. Kanoda, and T.-K. Ng, *Rev. Mod. Phys.* **89**, 025003 (2017).
 - [5] X. G. Wen, *Rev. Mod. Phys.* **89**, 041004 (2017).
 - [6] S. M. Winter, A. A. Tsirlin, M. Daghofer, J. van den Brink, Y. Singh, P. Gegenwart, and R. Valentí, *J. Phys.: Condens. Matter* **29**, 493002 (2017).
 - [7] M. Hermanns, I. Kimchi, and J. Knolle, *Annu. Rev. Condens. Matter Phys.* **9**, 17 (2018).
 - [8] J. Knolle and R. Moessner, *Annu. Rev. Condens. Matter Phys.* **10**, 451 (2019).
 - [9] H. Takagi, T. Takayama, G. Jackeli, G. Khaliullin, and S. E. Nagler, *Nat. Rev. Phys.* **1**, 264 (2019).
 - [10] Y. Motome and J. Nasu, *J. Phys. Soc. Jpn.* **89**, 012002 (2020).
 - [11] C. Broholm, R. J. Cava, S. A. Kivelson, D. G. Nocera, M. R. Norman, and T. Senthil, *Science* **367**, eaay0668 (2020).
 - [12] S. Trebst and C. Hickey, *Phys. Rep.* **950**, 1 (2022).
 - [13] Y. Kasahara, T. Ohnishi, Y. Mizukami, O. Tanaka, S. Ma, K. Sugii, N. Kurita, H. Tanaka, J. Nasu, Y. Motome, T. Shibauchi, and Y. Matsuda, *Nature (London)* **559**, 227 (2018).
 - [14] T. Yokoi, S. Ma, Y. Kasahara, S. Kasahara, T. Shibauchi, N. Kurita, H. Tanaka, J. Nasu, Y. Motome, C. Hickey, S. Trebst, and Y. Matsuda, *Science* **373**, 568 (2021).
 - [15] J. Bruin, R. Claus, Y. Matsumoto, N. Kurita, H. Tanaka, and H. Takagi, *Nat. Phys.* **18**, 401 (2022).
 - [16] P. Czajka, T. Gao, M. Hirschberger, P. Lampen-Kelley, A. Banerjee, J. Yan, D. G. Mandrus, S. E. Nagler, and N. Ong, *Nat. Phys.* **17**, 915 (2021).
 - [17] P. Czajka, T. Gao, M. Hirschberger, Paula Lampen-Kelley, A. Banerjee, N. Quirk, D. G. Mandrus, S. E. Nagler, and N. P. Ong, *Nat. Mater.* **22**, 36 (2023).
 - [18] L. E. Chern, E. Z. Zhang, and Y. B. Kim, *Phys. Rev. Lett.* **126**, 147201 (2021).
 - [19] E. Z. Zhang, L. E. Chern, and Y. B. Kim, *Phys. Rev. B* **103**, 174402 (2021).
 - [20] D. Wulferding, Y. Choi, S. H. Do, C. H. Lee, P. Lemmens, C. Faugeras, Y. Gallais, and K. Y. Choi, *Nat. Commun.* **11**, 1603 (2020).
 - [21] J.-X. Yin, S. H. Pan, and M. Zahid Hasan, *Nat. Rev. Phys.* **3**, 249 (2021).
 - [22] M. Ziatdinov, A. Banerjee, A. Maksov, T. Berlijn, W. Zhou, H. B. Cao, J.-Q. Yan, C. A. Bridges, D. G. Mandrus, S. E. Nagler, A. P. Baddorf, and S. V. Kalinin, *Nat. Commun.* **7**, 13774 (2016).
 - [23] D. Weber, L. M. Schoop, V. Duppel, J. M. Lippmann, J. Nuss, and B. V. Lotsch, *Nano Lett.* **16**, 3578 (2016).
 - [24] L. Du, Y. Huang, Y. Wang, Q. Wang, R. Yang, J. Tang, M. Liao, D. Shi, Y. Shi, and X. Zhou, *2D Mater.* **6**, 015014 (2018).
 - [25] W. Ruan, Y. Chen, S. Tang, J. Hwang, H.-Z. Tsai, R. L. Lee, M. Wu, H. Ryu, S. Kahn, F. Liou, C. Jia, A. Aikawa, C. Hwang, F. Wang, Y. Choi, S. G. Louie, P. A. Lee,

- Z.-X. Shen, S.-K. Mo, and M. F. Crommie, *Nat. Phys.* **17**, 1154 (2021).
- [26] J. Alicea, *Rep. Prog. Phys.* **75**, 076501 (2012).
- [27] K. Sengupta, I. Žutić, H. J. Kwon, V. M. Yakovenko, and S. Das Sarma, *Phys. Rev. B* **63**, 144531 (2001).
- [28] K. T. Law, P. A. Lee, and T. K. Ng, *Phys. Rev. Lett.* **103**, 237001 (2009).
- [29] K. Flensberg, *Phys. Rev. B* **82**, 180516(R) (2010).
- [30] A. Zazunov, R. Egger, and A. Levy Yeyati, *Phys. Rev. B* **94**, 014502 (2016).
- [31] T. Machida, Y. Sun, S. Pyon, S. Takeda, Y. Kohsaka, T. Hanaguri, T. Sasagawa, and T. Tamegai, *Nat. Mater.* **18**, 811 (2019).
- [32] Q. Liu, C. Chen, T. Zhang, R. Peng, Y. J. Yan, C.-H.-P. Wen, X. Lou, Y.-L. Huang, J.-P. Tian, X.-L. Dong, G.-W. Wang, W.-C. Bao, Q.-H. Wang, Z.-P. Yin, Z.-X. Zhao, and D.-L. Feng, *Phys. Rev. X* **8**, 041056 (2018).
- [33] L. Kong, S. Zhu, M. Papaj, H. Chen, L. Cao, H. Isobe, Y. Xing, W. Liu, D. Wang, P. Fan, Y. Sun, S. Du, J. Schneeloch, R. Zhong, G. Gu, L. Fu, H. J. Gao, and H. Ding, *Nat. Phys.* **15**, 1181 (2019).
- [34] S. Zhu, L. Kong, L. Cao, H. Chen, M. Papaj, S. Du, Y. Xing, W. Liu, D. Wang, C. Shen, F. Yang, J. Schneeloch, R. Zhong, G. Gu, L. Fu, Y. Y. Zhang, H. Ding, and H. J. Gao, *Science* **367**, 189 (2020).
- [35] E. Prada, P. San-Jose, M. W. A. de Moor, A. Geresdi, E. J. H. Lee, J. Klinovaja, D. Loss, J. Nygård, R. Aguado, and L. P. Kouwenhoven, *Nat. Rev. Phys.* **2**, 575 (2020).
- [36] J. G. Rau, Eric Kin-Ho Lee, and H.-Y. Kee, *Phys. Rev. Lett.* **112**, 077204 (2014).
- [37] J. G. Rau, E. K.-H. Lee, and H.-Y. Kee, *Annu. Rev. Condens. Matter Phys.* **7**, 195 (2016).
- [38] S. M. Winter, Y. Li, H. O. Jeschke, and R. Valentí, *Phys. Rev. B* **93**, 214431 (2016).
- [39] R. G. Pereira and R. Egger, *Phys. Rev. Lett.* **125**, 227202 (2020).
- [40] J. Fernández-Rossier, *Phys. Rev. Lett.* **102**, 256802 (2009).
- [41] J. Fransson, O. Eriksson, and A. V. Balatsky, *Phys. Rev. B* **81**, 115454 (2010).
- [42] F. Delgado and J. Fernández-Rossier, *Phys. Rev. B* **84**, 045439 (2011).
- [43] J. Feldmeier, W. Natori, M. Knap, and J. Knolle, *Phys. Rev. B* **102**, 134423 (2020).
- [44] E. J. König, M. T. Randeria, and B. Jäck, *Phys. Rev. Lett.* **125**, 267206 (2020).
- [45] M. Carrega, I. J. Vera-Marun, and A. Principi, *Phys. Rev. B* **102**, 085412 (2020).
- [46] G. Chen and J. L. Lado, *Phys. Rev. Res.* **2**, 033466 (2020).
- [47] M. Udagawa, S. Takayoshi, and T. Oka, *Phys. Rev. Lett.* **126**, 127201 (2021).
- [48] G. Baskaran, S. Mandal, and R. Shankar, *Phys. Rev. Lett.* **98**, 247201 (2007).
- [49] F. L. Pedrocchi, S. Chesi, and D. Loss, *Phys. Rev. B* **84**, 165414 (2011).
- [50] J. Knolle, D. L. Kovrizhin, J. T. Chalker, and R. Moessner, *Phys. Rev. Lett.* **112**, 207203 (2014).
- [51] F. Zschöcke and M. Vojta, *Phys. Rev. B* **92**, 014403 (2015).
- [52] X.-Y. Song, Y.-Z. You, and L. Balents, *Phys. Rev. Lett.* **117**, 037209 (2016).
- [53] D. Otten, A. Roy, and F. Hassler, *Phys. Rev. B* **99**, 035137 (2019); however, one can easily take into account such excitations.
- [54] D. Aasen, R. S. K. Mong, B. M. Hunt, D. Mandrus, and J. Alicea, *Phys. Rev. X* **10**, 031014 (2020).
- [55] M. G. Yamada and S. Fujimoto, *Phys. Rev. Lett.* **127**, 047201 (2021).
- [56] R. Chari, R. Moessner, and J. G. Rau, *Phys. Rev. B* **103**, 134444 (2021).
- [57] S. Banerjee and S. Z. Lin, *arXiv:2208.06887*.
- [58] F. Elste and C. Timm, *Phys. Rev. B* **75**, 195341 (2007).
- [59] D. A. S. Kaib, S. Biswas, K. Riedl, S. M. Winter, and R. Valentí, *Phys. Rev. B* **103**, L140402 (2021).
- [60] S. M. Winter, K. Riedl, P. A. Maksimov, A. L. Chernyshev, A. Honecker, and R. Valentí, *Nat. Commun.* **8**, 1152 (2017).
- [61] Y. Sugita, Y. Kato, and Y. Motome, *Phys. Rev. B* **101**, 100410(R) (2020).
- [62] B. Yang, Y. M. Goh, S. H. Sung, G. Ye, S. Biswas, D. A. S. Kaib, R. Dhakal, S. Yan, C. Li, S. Jiang, F. Chen, H. Lei, R. He, R. Valentí, S. M. Winter, R. Hovden, and A. W. Tsen, *Nat. Mater.* **22**, 50 (2023).
- [63] Y. S. Hou, H. J. Xiang, and X. G. Gong, *Phys. Rev. B* **96**, 054410 (2017).
- [64] V. M. Katukuri, S. Nishimoto, V. Yushankhai, A. Stoyanova, H. Kandpal, S. Choi, R. Coldea, I. Rousochatzakis, L. Hozoi, and J. van den Brink, *New J. Phys.* **16**, 013056 (2014).
- [65] Y. Yamaji, Y. Nomura, M. Kurita, R. Arita, and M. Imada, *Phys. Rev. Lett.* **113**, 107201 (2014).
- [66] V. M. Katukuri, S. Nishimoto, I. Rousochatzakis, H. Stoll, J. van den Brink, and L. Hozoi, *Sci. Rep.* **5**, 14718 (2015).
- [67] K. Dhochak, R. Shankar, and V. Tripathi, *Phys. Rev. Lett.* **105**, 117201 (2010).
- [68] A. J. Willans, J. T. Chalker, and R. Moessner, *Phys. Rev. B* **84**, 115146 (2011).
- [69] M. Vojta, A. K. Mitchell, and F. Zschöcke, *Phys. Rev. Lett.* **117**, 037202 (2016).
- [70] J.-P. Blaizot and G. Ripka, *Quantum Theory of Finite Systems*, Vol. 3 (MIT Press, Cambridge, MA, 1986).
- [71] M. Cozzini, P. Giorda, and P. Zanardi, *Phys. Rev. B* **75**, 014439 (2007).
- [72] G. Bertsch, J. Dobaczewski, W. Nazarewicz, and J. Pei, *Phys. Rev. A* **79**, 043602 (2009).
- [73] Some of the relations in Sec. III, in particular, Eqs. (3.22) and (3.23), assume that $|0_a\rangle$ and $|0_b\rangle$ are the respective vacuum states without extra excitations to satisfy the fermion parity constraint. The corresponding expressions in the presence of such excitations follow accordingly.
- [74] J. Knolle, R. Moessner, and N. B. Perkins, *Phys. Rev. Lett.* **122**, 047202 (2019).
- [75] W.-H. Kao, J. Knolle, G. B. Hálasz, R. Moessner, and N. B. Perkins, *Phys. Rev. X* **11**, 011034 (2021).
- [76] V. Dantas and E. C. Andrade, *Phys. Rev. Lett.* **129**, 037204 (2022).
- [77] Y. Imry and S. Ma, *Phys. Rev. Lett.* **35**, 1399 (1975).
- [78] D. Rhodes, S. H. Chae, R. Ribeiro-Palau, and J. Hone, *Nat. Mater.* **18**, 541 (2019).

P4 Local spin-flip transitions induced by magnetic quantum impurities in two-dimensional magnets

The following text is reproduced from the publication

T. Bauer, L. R. D. Freitas, E. C. Andrade, R. Egger, and R. G. Pereira

Local spin-flip transitions induced by magnetic quantum impurities in two-dimensional magnets

Physical Review B, vol. 110, no. 22, p. L220403 (2024).

The supplementary material provided with this publication is attached to the text.

Digital Object Identifier (DOI): [10.1103/PhysRevB.110.L220403](https://doi.org/10.1103/PhysRevB.110.L220403)

Statement of contribution

The idea for this work emerged from discussions between ECA, RGP and me. ECA and RGP proposed the analysis of magnon bound states for inhomogeneous classical spin configurations. RGP and I developed the linear-spin wave theory of quantum impurity spins and identified the spin-flip transition. ECA numerically determined the classical ground state configurations, which I subsequently used for numerical calculations within linear spin-wave theory. RGP and LRDF complemented this approach with results from exact diagonalization. RGP and I derived the continuum theory analytically. I also developed and numerically calculated the differential conductance. RE reviewed and provided input on all calculations. RGP and I prepared the figures for the manuscript, which RE drafted and all authors subsequently finalized.

Copyright and license notice

The copyright for this article is held by the American Physical Society (APS). APS grants authors the right to use their articles or portions of their articles in a dissertation without requesting permission from APS, provided the bibliographic citation and the APS copyright credit line are given on the appropriate pages.

Local spin-flip transitions induced by magnetic quantum impurities in two-dimensional magnetsTim Bauer¹, Lucas R. D. Freitas², Eric C. Andrade³, Reinhold Egger¹, and Rodrigo G. Pereira²¹*Institut für Theoretische Physik, Heinrich-Heine-Universität, D-40225 Düsseldorf, Germany*²*International Institute of Physics and Departamento de Física Teórica e Experimental, Universidade Federal do Rio Grande do Norte, Natal, Rio Grande do Norte, 59078-970, Brazil*³*Instituto de Física, Universidade de São Paulo, 05315-970 São Paulo, São Paulo, Brazil*

(Received 30 May 2024; revised 2 August 2024; accepted 25 November 2024; published 9 December 2024)

We predict a general local spin-flip transition mechanism caused by magnetic quantum impurities in (partially) polarized phases of quantum magnets in the absence of conservation laws. This transition arises when a magnon bound-state crosses zero energy as a function of the magnetic field. As an application, we study two-dimensional (2D) van der Waals magnets described by the Kitaev-Heisenberg honeycomb model which applies to the transition metal trihalides CrI_3 and $\alpha\text{-RuCl}_3$. We consider the adatom and substitutional impurity positions, and show how spin-flip transitions can be detected in scanning tunneling spectroscopy.

DOI: [10.1103/PhysRevB.110.L220403](https://doi.org/10.1103/PhysRevB.110.L220403)

Introduction. Understanding the fascinating properties of the recently discovered two-dimensional (2D) van der Waals magnets is a topic of enormous current interest; for reviews, see Refs. [1–7]. These materials can be directly studied by surface probe techniques. In particular, their local magnetization profile has been mapped out by scanning nitrogen-vacancy magnetometry and by magnetic force microscopy [7]. With the atomic resolution offered by scanning tunneling spectroscopy (STS) [8], one may examine single-atom spin-flip processes and spin excitations localized near impurities in full detail [9,10]. In this Letter, we study magnetic quantum impurities in (partially) polarized phases of 2D magnets in the absence of conservation laws. We uncover a mechanism for local spin-flip transitions tied to subgap magnon bound states induced by magnetic quantum impurities. Whenever the bound-state energy crosses zero as a function of the magnetic field, we predict such a transition to happen. This mechanism differs from a conventional spin-flop transition [11]. We also develop a low-energy continuum approach showing that these spin-flip transitions appear not only in 2D magnets, but also in one-dimensional (1D) spin chains, and possibly even in three-dimensional (3D) magnets.

For concrete calculations, we focus on the Kitaev-Heisenberg (KH) honeycomb model for transition metal trihalides [7]. This material class includes CrI_3 , a celebrated 2D ferromagnet with a small spin gap due to anisotropic exchange interactions [12–17]. A second example is the layered Kitaev material $\alpha\text{-RuCl}_3$ [18–21]. In the latter, the effects of dilute Cr^{3+} magnetic impurities have been linked to the Kondo screening by a Majorana metal phase [22], but magnon bound states may also potentially affect the low-energy spectrum. We note that STS observations of bound states induced by magnetic impurities in the spin-liquid candidate TaSe_2 have been interpreted as spinon-Kondo effect [23,24]. Similar bound states have been studied in the context of the Kondo effect in spin chains [25], a problem of relevance also for nanographene chains [26,27].

For 2D magnets in a magnetic field, nonmagnetic impurities (such as vacancies or bond defects) are generally *not* expected to induce bound states below the magnon gap. For instance, for the 2D KH model [28–34] in a partially polarized phase [35–37], nonmagnetic impurities generate magnon bound states only inside the energy gap between magnon bands of opposite Chern number [38,39]. These bound states are precursors of the chiral edge states in topological magnon phases [36,37,40–42]. However, for a classical magnetic impurity (with spin $S_{\text{imp}} \gg 1$), which is equivalent to a local magnetic field, bound states below the magnon gap were predicted [39]. This effect is independent of the band topology, see the Supplemental Material [43].

We here include quantum fluctuations of the magnetic impurity by using exact diagonalization (ED) for small lattices, linear spin wave (LSW) theory in the thermodynamic limit, and a low-energy continuum theory. Quantum effects are shown to *qualitatively* change the scaling properties of the sub-gap bound-state energy. Depending, in particular, on the values of the bulk (S) and the impurity (S_{imp}) spins and on the impurity position type (e.g., adatom versus substitutional), the bound-state energy can reach zero multiple times as a function of the magnetic field. Whenever this happens, we predict a *discontinuity* in the local magnetization of the impurity and/or its neighboring bulk spins. Such local spin-flip transitions manifest themselves as pronounced steps in the field dependence of the zero-bias STS conductance. By scanning the STS conductance at finite bias voltage, one obtains information about the bound-state energy. Moreover, by performing spatial STS scans, the impurity type can be fully resolved.

General setup. We consider 2D spin Hamiltonians of the form ($\hbar = e = 1$ below)

$$H = \sum_{\langle j,k \rangle} \mathbf{S}_j^T H_{j,k} \mathbf{S}_k - \sum_j \mathbf{h}_j \cdot \mathbf{S}_j, \quad (1)$$

where $\mathbf{S}_j = (S_j^x, S_j^y, S_j^z)^T$ is a spin operator at site j , $\langle j, k \rangle$ denotes a bond between neighboring sites, $H_{j,k}$ are spin-spin

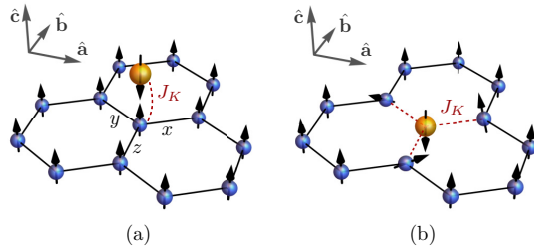
TIM BAUER *et al.*PHYSICAL REVIEW B **110**, L220403 (2024)

FIG. 1. Sketch of a (small part of) a 2D magnet with honeycomb lattice structure (bulk spins are shown in blue) and a single magnetic quantum impurity (yellow). Coordinate unit vectors (\hat{a} , \hat{b} , \hat{c}) and nearest-neighbor bond types (x , y , z) are also indicated. We assume $\mathbf{h} = h\hat{c}$. (a) Adatom position of the impurity with isotropic exchange coupling $J_K > 0$ to a single bulk spin. (b) Substitutional position, where the impurity replaces one bulk spin and interacts through isotropic couplings $J_K > 0$ with the three neighboring bulk spins. Here we schematically illustrate that, in general, the classical spin configuration minimizing the energy can be inhomogeneous due to spin canting in the vicinity of the impurity [43–47].

coupling matrices, and the vector \mathbf{h}_j is proportional to the local magnetic field at site j . For simplicity, we consider a homogeneous field $\mathbf{h} = h\hat{c}$, see Fig. 1. The bulk sites are occupied by spins S , and there is a single magnetic impurity with spin S_{imp} . We denote the impurity site by $j = 0$, which is included in the summations in Eq. (1). The bulk spins reside on a honeycomb lattice, where we consider two types of impurity locations as illustrated in Fig. 1. In the *adatom* case, the magnetic impurity couples to a single bulk spin. In the *substitutional* case, one replaces a single bulk spin by the impurity spin which then couples to the three neighboring bulk spins. For other configurations, e.g., if the impurity is located in the center of a hexagonal plaquette and thus couples to six bulk spins, results can be obtained by adapting our calculations for the cases considered here. For anisotropic exchange interactions, spin-rotational symmetry is absent, but the bulk spin coupling matrix $H_{j,k}$ can be constrained by the space group symmetry of the lattice [48]. As a paradigmatic model for transition metal trihalides, we consider the KH honeycomb model [49] for bulk spin $S = 3/2$ and ferromagnetic bulk exchange coupling $J_b > 0$. For CrI_3 , first-principles calculations and analysis of experimental data [50–52] indicate a subdominant antiferromagnetic Kitaev coupling $K < 0$. However, other studies [15,53] instead reported evidence for a dominant ferromagnetic Kitaev coupling. Below we take the parameters from Ref. [52], but in the SM, we also present results for the idealized ferromagnetic ($K > 0$, $J_b = 0$) Kitaev model with $S = 1/2$ [28]. We note that it is straightforward to generalize our approach to include other couplings, e.g., Dzyaloshinskii-Moriya interactions between next-nearest neighbors.

For the impurity-bulk spin couplings in Fig. 1, we instead consider an isotropic antiferromagnetic exchange coupling, $H_{0,j} = J_K \mathbb{1}_3$ with $J_K > 0$. This is a natural assumption if the impurity atom has no orbital degeneracy [22]. Next, we recall that for a free magnetic ion with spin S , orbital angular momentum L , and total angular momentum J , the Landé

factor is $g_L = \frac{3}{2} + \frac{S(S+1)-L(L+1)}{2J(J+1)}$ [54]. This value is typically a good approximation for $4f$ ions like Yb^{3+} , where crystal field effects are weak and J follows from Hund’s rules. However, for $3d$ ions like Cr^{3+} , L is quenched by crystal field effects and hence $g_L = 2$ for all S . For Ru^{3+} ions in $\alpha\text{-RuCl}_3$, the intricate interplay between orbital degeneracy, crystal field, and spin-orbit coupling [55] implies that g_L is an anisotropic tensor [54], with $g_L \approx 1.3$ for magnetic fields along the \hat{c} direction [56]. Assuming a homogeneous external magnetic field, we absorb the Bohr magneton and the bulk Landé factor into $\mathbf{h}_j = \mathbf{h}$ in Eq. (1) for bulk sites ($j \neq 0$). For the impurity spin ($j = 0$), we set

$$\mathbf{h}_0 = g\mathbf{h}, \quad g = g_L^{\text{imp}}/g_L^{\text{bulk}}, \quad (2)$$

where g is the relative Landé factor of the impurity compared to the bulk spins. For instance, for Ru^{3+} ions and $\mathbf{h} = h\hat{c}$, one finds $g \approx 1.5$ and $S_{\text{imp}} = 1/2$ both for Co adatoms [23] and for Ti^{3+} ions at substitutional sites.

Let us first summarize several key aspects. We assume that, without the impurity, the system is in a gapped (partially) polarized phase with magnons as low-energy excitations, where the magnon gap is basically set by the magnetic field, and study subgap magnon bound states induced by a single magnetic quantum impurity. The impurity coupling J_K now competes with the magnetic field \mathbf{h} . In a classical picture, \mathbf{h} tries to polarize all spins in the same direction, but spins coupled by J_K align in opposite directions if $J_K \gg |\mathbf{h}|$. For the adatom case with $S_{\text{imp}} = S$, the limit $J_K \rightarrow \infty$ corresponds to singlet formation between the impurity and a bulk spin, where both spins are frozen out and can be described as a vacancy. However, for the KH honeycomb model, a vacancy does *not* induce subgap bound states [38,39]. As one varies $J_K/|\mathbf{h}|$ between the weak- and strong-coupling limits, either the impurity or the bulk spin has to flip against the magnetic field. In the adatom case with $S_{\text{imp}} \neq S$ and/or in the substitutional case, the strong-coupling limit may have a residual spin, and thus multiple transitions are possible. Below we describe such discontinuous spin transitions in the quantum case and show how they can be detected in STS. We emphasize that the magnetic-field energy scale characterizing the spin-flip transition is not set by the magnon gap but by the typically much smaller impurity coupling scale J_K .

KH model. The bulk spin couplings $H_{j,k}$ in Eq. (1) include an isotropic ferromagnetic Heisenberg coupling $J_b > 0$, and a bond-dependent Kitaev contribution K . For instance, for a z -bond in Fig. 1, we have $H_{j,k} = -\text{diag}(J_b, J_b, J_b + K)$. Bulk interactions for bonds of type $\gamma \in \{x, y\}$ then follow by cyclic permutation of (α, β, γ) in $H_{j,k}^{\alpha,\beta}$. In CrI_3 , bulk spins (Cr^{3+} ions) have $S = 3/2$ [6]. Magnetic impurities at substitutional sites could be, e.g., V^{3+} ions with $S_{\text{imp}} = 1$ [57] where we obtain $g = 1$ from Eq. (2). However, adatom impurities should be neutral, e.g., Co atoms with $S_{\text{imp}} = 1/2$ [23], again resulting in $g = 1$. *Ab initio* calculations for CrI_3 [58] favor impurity locations in the hexagon center, while for Ni atoms, the adatom location is also possible. However, with a scanning probe tip, one can move around impurities at will [23].

We show ED and LSW results for $S = 3/2$ in Fig. 2. While ED is a numerically exact method, it is limited to small system size. LSW theory instead allows us to treat the thermodynamic

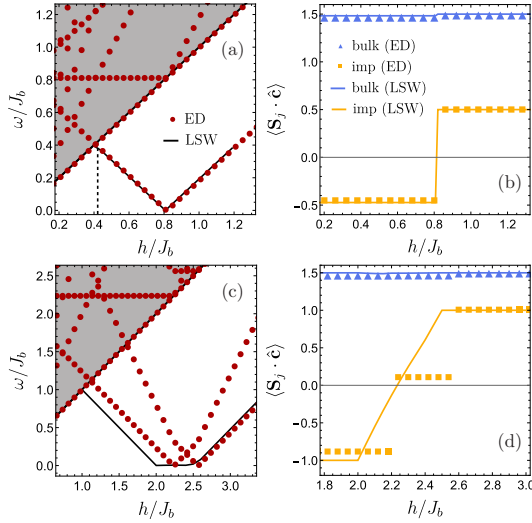


FIG. 2. ED and LSW results for the KH model with $S = 3/2$, $K/J_b = -0.2$, $J_K/J_b = 0.5$, and $\mathbf{h} = h\hat{\mathbf{e}}$. For all cases studied here, $g = 1$ in Eq. (2). The shaded region indicates the magnon continuum $\omega > \omega_g$ in the thermodynamic limit, with the magnon gap $\omega_g = h$. ED results refer to a cluster with 2×2 unit cells (nine sites for the adatom case) and periodic boundary conditions. *Adatom impurity:* (a) Excitation spectrum ω/J_b (relative to the ground state) versus magnetic field h/J_b for $S_{\text{imp}} = 1/2$. ED (LSW) results correspond to red dots (black lines). The dashed vertical line indicates the classical spin flip transition. (b) Spin projections $\langle \mathbf{S}_{0,1} \cdot \hat{\mathbf{e}} \rangle$ vs h/J_b for the case in panel (a). Yellow squares (lines) correspond to ED (LSW) results for the impurity spin. Results for the coupled bulk spin are shown as blue triangles (ED) and blue lines (LSW), respectively. *Substitutional impurity:* (c) ω/J_b vs h/J_b and (d) $\langle \mathbf{S}_{0,1} \cdot \hat{\mathbf{e}} \rangle$ vs h/J_b for $S_{\text{imp}} = 1$.

limit, where the first step is to determine the classical spin configuration that minimizes the energy. In general, there can be spin canting as schematically illustrated in Fig. 1(b). One then performs a Holstein-Primakoff transformation to boson operators describing the magnons. In principle, the linearized theory becomes exact for large S [36,37,39,54]. Since the impurity breaks translation invariance, one diagonalizes the quadratic LSW Hamiltonian in real space. This can be done for fairly large lattices, allowing for an extrapolation to the thermodynamic limit [43].

Remarkably, both methods give almost perfect agreement for an adatom impurity with $S_{\text{imp}} = 1/2$, see Figs. 2(a) and 2(b). Here a subgap magnon bound state appears whose energy vanishes for $h/J_b \approx 0.8$. For $h \ll J_K$, the bound state merges with the magnon continuum as expected from the impurity screening scenario discussed above. As seen in Fig. 2(b), the spin projections $\langle \mathbf{S}_{0,1} \cdot \hat{\mathbf{e}} \rangle$ of the impurity spin and (to much lesser degree) the coupled bulk spin exhibit *discontinuous* jumps at $h/J_b \approx 0.8$. Importantly, the transition obtained within LSW theory is due to quantum fluctuations on top of a uniformly polarized spin configuration. By contrast, a classical transition might be expected when the energy of the

configuration with the flipped impurity spin falls below the energy of the uniform configuration. Calculating these energies within LSW theory up to order S (in the $1/S$ expansion) [43], we find that this semi-classical criterion underestimates the critical magnetic field, see the dashed vertical line in Fig. 2(a).

We next address the *substitutional* case. For $S_{\text{imp}} = 1/2$, we find similar results as for the adatom case above. Below we instead focus on $S_{\text{imp}} = 1$, see Figs. 2(c) and 2(d), where marked differences between ED and LSW results emerge. In particular, ED results indicate *two* spin transitions associated with multiple zeros of the bound-state energy. However, the LSW spectrum calculated for the uniform classical spin configuration (with polarized impurity) captures only one transition. In Figs. 2(c) and 2(d), we show the LSW spectrum and spin projections for a configuration in which the impurity spin is allowed to rotate to minimize the classical energy [43]. This continuous rotation of the impurity spin breaks the exact C_3 lattice symmetry. However, such a spontaneous symmetry breaking is not possible for a single degree of freedom with local interactions since there are only finite energy barriers to other broken-symmetry states and quantum fluctuations can restore the symmetry. In fact, we never observed transverse components of the impurity spin in ED. Another indication of the failure of LSW theory is that the predicted magnon bound-state energy vanishes in the regime where the classical spin rotates (which is where ED identifies multiple transitions). In this case, the putative classical configuration cannot be stable because one can add magnons without energy cost. Given the excellent agreement between ED and LSW results in Figs. 2(a) and 2(b), we believe that ED captures the thermodynamic limit also in Figs. 2(c) and 2(d). The transitions at $h/J_b \approx 2.2$ and $h/J_b \approx 2.55$ are again predominantly due to discontinuities in the local magnetization. They correspond to zeros of the energy for excitations with n magnons in the bound state, where $n \leq 2S_{\text{imp}}$. For higher S_{imp} , one can thus expect more spin transitions.

Low-energy continuum approach. For the adatom case and $\mathbf{h} = h\hat{\mathbf{e}}$, we can analytically determine the scaling of the subgap magnon bound-state energy $E_b < 0$ (relative to the magnon gap ω_g) in the regime $J_K \ll h$, where Eq. (1) affords an effective continuum description [43]. The bulk magnon dispersion can be approximated by $\omega(\mathbf{k}) \approx \omega_g + \frac{\mathbf{k}^2}{2m}$. (For the KH model, $\omega_g = h$ and $m^{-1} = J + \frac{K}{3} - \frac{K^2}{h+3J+K}$, independent of the sign of K .) The low-energy Schrödinger equation for a single magnon described by $\psi(\mathbf{r})$ with $\mathbf{r} = (r_x, r_y)^T$ then contains an attractive δ -function potential due to the impurity

$$-\frac{1}{2m}\nabla^2\psi(\mathbf{r}) - V_{\text{eff}}(E_b)\delta(\mathbf{r})\psi(\mathbf{r}) = E_b\psi(\mathbf{r}), \quad (3)$$

with the energy-dependent coupling strength $V_{\text{eff}}(E_b) = J_K S_{\text{imp}}(1 + \frac{J_K S}{\varepsilon_a + |E_b|})$, where ε_a is an energy scale for the impurity. (For the KH model, $\varepsilon_a = gh - \omega_g - J_K S$.) For a classical magnetic impurity with $S_{\text{imp}} \rightarrow \infty$ at constant $J_K S_{\text{imp}}$ [39,59,60], we obtain the nonperturbative scaling law $E_b \propto -e^{-c_b/(mJ_K)}$ [61], where c_b is of order unity. However, for a quantum impurity, we find a qualitatively different scaling, $E_b \simeq gh - \omega_g - J_K S + \mathcal{O}(J_K^2)$, in accordance with our numerical ED and LSW results. By varying the magnetic field, the

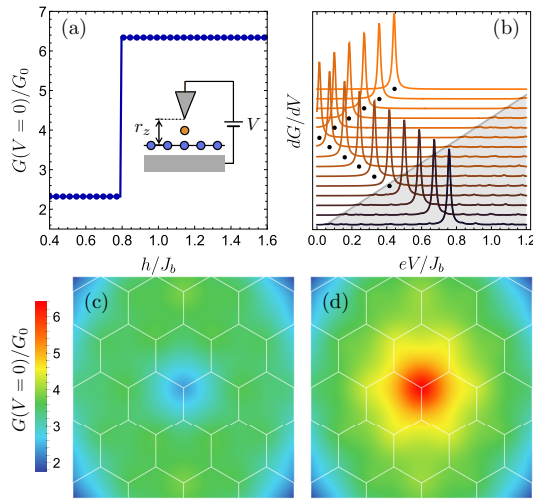


FIG. 3. STS conductance for the KH model with an adatom magnetic impurity from LSW theory, cf. Figs. 2(a) and 2(b), with $K = -0.2J_b$, $J_K = 0.5J_b$, $S = 3/2$, $S_{\text{imp}} = 1/2$, and $g = 1$. The reference conductance $G_0 = 2\pi d_A d_B / \hbar_{\text{bulk}}^2$ involves densities of states d_A and d_B for tip and substrate, and we use cotunneling amplitudes t_{imp} and t_{bulk} for the impurity and bulk spins, respectively. The STM tip and the impurity position are characterized by $l_0 = r_z = 0.5a_0$, $t_{\text{imp}}/\hbar_{\text{bulk}} = 1.5$, and $\mathbf{R}_0 = \mathbf{R}_1 + 0.2a_0\hat{e}$, where a_0 is the lattice constant and l_0 the tip resolution. The bulk spin at site \mathbf{R}_1 is coupled to the impurity at site \mathbf{R}_0 . (a) $V = 0$ conductance versus magnetic field h for a tip above the impurity as schematically depicted in the inset. (b) Conductance derivative dG/dV (in arbitrary units) versus bias voltage. Different curves correspond to uniformly spaced field values ranging from $h = 0.05J_b$ (bottom) to $h = 1.25J_b$ (top curve), shifted vertically to aid visualization. The δ -function peaks are broadened by a Lorentzian of width $0.01J_b$. The dots track the bound-state energy. (c,d) Colorscale plots for the spatial profile of the zero-bias conductance near the magnetic impurity (which is in the center of the respective panel) for two field values: (c) $h = 0.65J_b$ (below the transition) and (d) $h = 1.164J_b$ (above the transition).

bound-state crosses zero energy (i.e., $E_b = -\omega_g$), and a discontinuous local spin-flip transition occurs. The low-energy Eq. (3) is not limited to the KH model but applies to many other 2D magnets as well. With minor modifications, it also describes 1D and 3D magnets, underlining the generality of the found spin-flip mechanism. This mechanism is qualitatively different from a conventional spin flop transition [11]

which involves a first-order transition without magnon gap closing, see Ref. [43].

STS conductance. We next discuss how the above spin transitions can be observed in STS. Known expressions for the zero-temperature STS conductance $G(V, \mathbf{r}_t)$ at bias voltage V and tip position $\mathbf{r}_t = (r_x, r_y, r_z)^T$ [38,39,62–67] are summarized in the SM [43], involving a form factor and the dynamical spin correlation function of the 2D magnet. (Here the z -axis is aligned with \hat{e} .) The zero-bias STS conductance is expressed by the spin expectation values $\langle S_j^z \rangle$, and can thus directly reveal spin transitions. We illustrate the STS conductance in Fig. 3 for an adatom impurity with $S_{\text{imp}} = 1/2$, cf. Figs. 2(a) and 2(b). The step in the field dependence of the zero-bias conductance seen in Fig. 3(a) directly follows from the spin transition in Fig. 2(b). At low but finite bias voltage, Fig. 3(b) illustrates that the conductance derivative dG/dV exhibits a pronounced *peak* whenever the voltage matches the subgap magnon bound-state energy. By varying both the magnetic field and the bias voltage, one can thus map out the field dependence of the bound-state energy. Finally, see Figs. 3(c) and 3(d), in spatial scans of the zero-bias conductance, the conductance switches from a minimum to a maximum near the impurity site when increasing h/J_b across the transition at $h/J_b \approx 0.8$, consistent with Fig. 3(a).

Conclusion. Magnetic impurities in 2D magnets can give rise to magnon bound states at very low energies. Such states can cause similar behavior in STS as fractional excitations such as spinons or \mathbb{Z}_2 vortices in spin liquids. To distinguish such phases, one could characterize magnon bound states by STS by first exposing the system to a strong field. In a second step, one lowers the field to reach the putative spin liquid phase, where detailed STS predictions are available [39,66,67]. In any case, we expect that the predicted spin transitions due to zero-energy magnon bound states will soon be observed.

The data underlying the figures in this paper can be found at the zenodo site [68].

Acknowledgments. We acknowledge funding by the Deutsche Forschungsgemeinschaft (DFG, German Research Foundation), Project No. 277101999 - TRR 183 (project C01) and under Germany's Excellence Strategy - Cluster of Excellence Matter and Light for Quantum Computing (ML4Q) EXC 2004/1 - 390534769, by the Simons Foundation (Grant No. 1023171, R.G.P.), by the Brazilian ministries MEC and MCTI, by the Brazilian agencies CNPq and FAPESP, and by the Coordenação de Aperfeiçoamento de Pessoal de Nível Superior - Brasil (CAPES) - Finance Code 001.

- [1] K. S. Burch, D. Mandrus, and J.-G. Park, Magnetism in two-dimensional van der Waals materials, *Nature (London)* **563**, 47 (2018).
- [2] M. Gibertini, M. Koperski, A. F. Morpurgo, and K. S. Novoselov, Magnetic 2D materials and heterostructures, *Nat. Nanotechnol.* **14**, 408 (2019).
- [3] Y. Khan, S. M. Obaidulla, M. R. Habib, A. Gayen, T. Liang, X. Wang, and M. Xu, Recent breakthroughs in two-dimensional

van der Waals magnetic materials and emerging applications, *Nano Today* **34**, 100902 (2020).

- [4] S. Yang, T. Zhang, and C. Jiang, Van der Waals magnets: Material family, detection and modulation of magnetism, and perspective in spintronics, *Adv. Sci.* **8**, 2002488 (2021).
- [5] H. Kurebayashi, J. H. Garcia, S. Khan, J. Sinova, and S. Roche, Magnetism, symmetry and spin transport in van der Waals layered systems, *Nat. Rev. Phys.* **4**, 150 (2022).

- [6] Q. H. Wang, A. Bedoya-Pinto, M. Blei, A. H. Dismukes, A. Hamo, S. Jenkins, M. Koperski, Y. Liu, Q.-C. Sun, E. J. Telford, H. H. Kim, M. Augustin, U. Vool, J.-X. Yin, L. H. Li, A. Falin, C. R. Dean, F. Casanova, R. F. L. Evans, M. Chshiev *et al.*, The magnetic genome of two-dimensional van der Waals materials, *ACS Nano* **16**, 6960 (2022).
- [7] Y. Ahn, X. Guo, S. Son, Z. Sun, and L. Zhao, Progress and prospects in two-dimensional magnetism of van der Waals materials, *arXiv:2401.13781*.
- [8] J.-X. Yin, S. H. Pan, and M. Z. Hasan, Probing topological quantum matter with scanning tunneling microscopy, *Nat. Rev. Phys.* **3**, 249 (2021).
- [9] A. J. Heinrich, J. A. Gupta, C. P. Lutz, and D. M. Eigler, Single-atom spin-flip spectroscopy, *Science* **306**, 466 (2004).
- [10] R. Wiesendanger, Spin mapping at the nanoscale and atomic scale, *Rev. Mod. Phys.* **81**, 1495 (2009).
- [11] S. Blundell, *Magnetism in Condensed Matter* (Oxford University Press, Oxford, 2001).
- [12] B. Huang, G. Clark, E. Navarro-Moratalla, D. R. Klein, R. Cheng, K. L. Seyler, D. Zhong, E. Schmidgall, M. A. McGuire, D. H. Cobden, W. Yao, D. Xiao, P. Jarillo-Herrero, and X. Xu, Layer-dependent ferromagnetism in a van der Waals crystal down to the monolayer limit, *Nature (London)* **546**, 270 (2017).
- [13] J. L. Lado and J. Fernández-Rossier, On the origin of magnetic anisotropy in two dimensional CrI₃, *2D Mater.* **4**, 035002 (2017).
- [14] L. Chen, J.-H. Chung, T. Chen, C. Duan, A. Schneidewind, I. Radelytskyi, D. J. Voneshen, R. A. Ewings, M. B. Stone, A. I. Kolesnikov, B. Winn, S. Chi, R. A. Mole, D. H. Yu, B. Gao, and P. Dai, Magnetic anisotropy in ferromagnetic CrI₃, *Phys. Rev. B* **101**, 134418 (2020).
- [15] I. Lee, F. G. Utermohlen, D. Weber, K. Hwang, C. Zhang, J. van Tol, J. E. Goldberger, N. Trivedi, and P. C. Hammel, Fundamental spin interactions underlying the magnetic anisotropy in the kitaev ferromagnet CrI₃, *Phys. Rev. Lett.* **124**, 017201 (2020).
- [16] L. Chen, J.-H. Chung, M. B. Stone, A. I. Kolesnikov, B. Winn, V. O. Garlea, D. L. Abernathy, B. Gao, M. Augustin, E. J. G. Santos, and P. Dai, Magnetic field effect on topological spin excitations in CrI₃, *Phys. Rev. X* **11**, 031047 (2021).
- [17] P. P. Stavropoulos, X. Liu, and H.-Y. Kee, Magnetic anisotropy in spin-3/2 with heavy ligand in honeycomb Mott insulators: Application to CrI₃, *Phys. Rev. Res.* **3**, 013216 (2021).
- [18] S. M. Winter, A. A. Tsirlin, M. Daghofer, J. van den Brink, Y. Singh, P. Gegenwart, and R. Valentí, Models and materials for generalized Kitaev magnetism, *J. Phys.: Condens. Matter* **29**, 493002 (2017).
- [19] J. Knolle and R. Moessner, A field guide to spin liquids, *Annu. Rev. Condens. Matter Phys.* **10**, 451 (2019).
- [20] C. Hickey, M. Gohlke, C. Berke, and S. Trebst, Generic field-driven phenomena in Kitaev spin liquids: Canted magnetism and proximate spin liquid physics, *Phys. Rev. B* **103**, 064417 (2021).
- [21] I. Rousochatzakis, N. B. Perkins, Q. Luo, and H.-Y. Kee, Beyond Kitaev physics in strong spin-orbit coupled magnets, *Rep. Prog. Phys.* **87**, 026502 (2024).
- [22] S. Lee, Y. S. Choi, S.-H. Do, W. Lee, C. H. Lee, M. Lee, M. Vojta, C. N. Wang, H. Luetkens, Z. Guguchia, and K.-Y. Choi, Kondo screening in a Majorana metal, *Nat. Commun.* **14**, 7405 (2023).
- [23] Y. Chen, W.-Y. He, W. Ruan, J. Hwang, S. Tang, R. L. Lee, M. Wu, T. Zhu, C. Zhang, H. Ryu, F. Wang, S. G. Louie, Z.-X. Shen, S.-K. Mo, P. A. Lee, and M. F. Crommie, Evidence for a spinon Kondo effect in cobalt atoms on single-layer 1T-TaSe₂, *Nat. Phys.* **18**, 1335 (2022).
- [24] W.-Y. He and P. A. Lee, Magnetic impurity as a local probe of the U(1) quantum spin liquid with spinon Fermi surface, *Phys. Rev. B* **105**, 195156 (2022).
- [25] P. Kattel, P. R. Pasnoori, J. H. Pixley, P. Azaria, and N. Andrei, Kondo effect in the isotropic Heisenberg spin chain, *Phys. Rev. B* **109**, 174416 (2024).
- [26] S. Mishra, G. Catarina, F. Wu, R. Ortiz, D. Jacob, K. Eimre, J. Ma, C. A. Pignedoli, X. Feng, P. Ruffieux, F. Fernández-Rossier, and R. Fasel, Observation of fractional edge excitations in nanographene spin chains, *Nature (London)* **598**, 287 (2021).
- [27] D. Jacob, R. Ortiz, and J. Fernández-Rossier, Renormalization of spin excitations and Kondo effect in open-shell nanographenes, *Phys. Rev. B* **104**, 075404 (2021).
- [28] A. Kitaev, Anyons in an exactly solved model and beyond, *Ann. Phys. (NY)* **321**, 2 (2006).
- [29] L. Savary and L. Balents, Quantum spin liquids: A review, *Rep. Prog. Phys.* **80**, 016502 (2017).
- [30] Y. Zhou, K. Kanoda, and T.-K. Ng, Quantum spin liquid states, *Rev. Mod. Phys.* **89**, 025003 (2017).
- [31] M. Hermanns, I. Kimchi, and J. Knolle, Physics of the Kitaev model: Fractionalization, dynamic correlations, and material connections, *Annu. Rev. Condens. Matter Phys.* **9**, 17 (2018).
- [32] H. Takagi, T. Takayama, G. Jackeli, G. Khaliullin, and S. E. Nagler, Concept and realization of Kitaev quantum spin liquids, *Nat. Rev. Phys.* **1**, 264 (2019).
- [33] Y. Motome and J. Nasu, Hunting Majorana fermions in Kitaev magnets, *J. Phys. Soc. Jpn.* **89**, 012002 (2020).
- [34] S. Trebst and C. Hickey, Kitaev materials, *Phys. Rep.* **950**, 1 (2022).
- [35] P. A. McClarty, X.-Y. Dong, M. Gohlke, J. G. Rau, F. Pollmann, R. Moessner, and K. Penc, Topological magnons in Kitaev magnets at high fields, *Phys. Rev. B* **98**, 060404(R) (2018).
- [36] L. E. Chern, E. Z. Zhang, and Y. B. Kim, Sign structure of thermal Hall conductivity and topological magnons for in-plane field polarized Kitaev magnets, *Phys. Rev. Lett.* **126**, 147201 (2021).
- [37] E. Z. Zhang, L. E. Chern, and Y. B. Kim, Topological magnons for thermal Hall transport in frustrated magnets with bond-dependent interactions, *Phys. Rev. B* **103**, 174402 (2021).
- [38] A. Mitra, A. Corticelli, P. Ribeiro, and P. A. McClarty, Magnon Interference Tunneling Spectroscopy as a Probe of 2D Magnetism, *Phys. Rev. Lett.* **130**, 066701 (2023).
- [39] T. Bauer, L. R. D. Freitas, R. G. Pereira, and R. Egger, Scanning tunneling spectroscopy of Majorana zero modes in a Kitaev spin liquid, *Phys. Rev. B* **107**, 054432 (2023).
- [40] R.-J. Slager, L. Rademaker, J. Zaanen, and L. Balents, Impurity-bound states and Green's function zeros as local signatures of topology, *Phys. Rev. B* **92**, 085126 (2015).
- [41] S.-S. Diop, L. Fritz, M. Vojta, and S. Rachel, Impurity bound states as detectors of topological band structures revisited, *Phys. Rev. B* **101**, 245132 (2020).
- [42] J. Habel, A. Mook, J. Willsher, and J. Knolle, Breakdown of chiral edge modes in topological magnon insulators, *Phys. Rev. B* **109**, 024441 (2024).

TIM BAUER *et al.*PHYSICAL REVIEW B **110**, L220403 (2024)

- [43] See Supplemental Material at <http://link.aps.org/supplemental/10.1103/PhysRevB.110.L220403> for detailed derivations and additional data.
- [44] J. Villain, Insulating spin glasses, *Z. Phys. B* **33**, 31 (1979).
- [45] A. Wollny, L. Fritz, and M. Vojta, Fractional impurity moments in two-dimensional noncollinear magnets, *Phys. Rev. Lett.* **107**, 137204 (2011).
- [46] A. Wollny, E. C. Andrade, and M. Vojta, Singular field response and singular screening of vacancies in antiferromagnets, *Phys. Rev. Lett.* **109**, 177203 (2012).
- [47] V. S. Maryasin and M. E. Zhitomirsky, Triangular antiferromagnet with nonmagnetic impurities, *Phys. Rev. Lett.* **111**, 247201 (2013).
- [48] J. G. Rau and M. J. P. Gingras, Frustration and anisotropic exchange in ytterbium magnets with edge-shared octahedra, *Phys. Rev. B* **98**, 054408 (2018).
- [49] L. Janssen and M. Vojta, Heisenberg-Kitaev physics in magnetic fields, *J. Phys.: Condens. Matter* **31**, 423002 (2019).
- [50] C. Xu, J. Feng, H. Xiang, and L. Bellaiche, Interplay between Kitaev interaction and single ion anisotropy in ferromagnetic CrI_3 and CrGeTe_3 monolayers, *npj Comput. Mater.* **4**, 57 (2018).
- [51] R. Jaeschke-Ubiergo, E. Suárez Morell, and A. S. Nunez, Theory of magnetism in the van der Waals magnet CrI_3 , *Phys. Rev. B* **103**, 174410 (2021).
- [52] J. Cen and H.-Y. Kee, Determining Kitaev interaction in spin- S honeycomb Mott insulators, *Phys. Rev. B* **107**, 014411 (2023).
- [53] V. Brehm, P. Sobieszczyk, J. N. Kløgetvedt, R. F. L. Evans, E. J. G. Santos, and A. Qaiumzadeh, Topological magnon gap engineering in van der Waals CrI_3 ferromagnets, *Phys. Rev. B* **109**, 174425 (2024).
- [54] P. Fazekas, *Lecture Notes on Electron Correlation and Magnetism* (World Scientific, Singapore, 1999).
- [55] G. Jackeli and G. Khaliullin, Mott insulators in the strong spin-orbit coupling limit: From Heisenberg to a quantum compass and Kitaev models, *Phys. Rev. Lett.* **102**, 017205 (2009).
- [56] S. M. Winter, K. Riedl, D. Kaib, R. Coldea, and R. Valentí, Probing α - RuCl_3 beyond magnetic order: Effects of temperature and magnetic field, *Phys. Rev. Lett.* **120**, 077203 (2018).
- [57] S. Son, M. J. Coak, N. Lee, J. Kim, T. Y. Kim, H. Hamidov, H. Cho, C. Liu, D. M. Jarvis, P. A. C. Brown, J. H. Kim, C.-H. Park, D. I. Khomskii, S. S. Saxena, and J.-G. Park, Bulk properties of the van der Waals hard ferromagnet VI_3 , *Phys. Rev. B* **99**, 041402(R) (2019).
- [58] Q. Yang, X. Hu, X. Shen, A. V. Krashenninnikov, Z. Chen, and L. Sun, Enhancing ferromagnetism and tuning electronic properties of CrI_3 monolayers by adsorption of transition-metal atoms, *ACS Appl. Mater. Interfaces* **13**, 21593 (2021).
- [59] H. Shiba, Classical spins in superconductors, *Prog. Theor. Phys.* **40**, 435 (1968).
- [60] Y. Imry and S.-k. Ma, Random-field instability of the ordered state of continuous symmetry, *Phys. Rev. Lett.* **35**, 1399 (1975).
- [61] R. Jackiw, Delta function potentials in two-dimensional and three-dimensional quantum mechanics, in *M.A.B. Bég Memorial Volume*, edited by A. Ali and P. Hoodbhoy (World Scientific, Singapore, 1991).
- [62] J. Fransson, O. Eriksson, and A. V. Balatsky, Theory of spin-polarized scanning tunneling microscopy applied to local spins, *Phys. Rev. B* **81**, 115454 (2010).
- [63] J. Fernández-Rossier, Theory of single-spin inelastic tunneling spectroscopy, *Phys. Rev. Lett.* **102**, 256802 (2009).
- [64] J. Feldmeier, W. Natori, M. Knap, and J. Knolle, Local probes for charge-neutral edge states in two-dimensional quantum magnets, *Phys. Rev. B* **102**, 134423 (2020).
- [65] M. Carrega, I. J. Vera-Marun, and A. Principi, Tunneling spectroscopy as a probe of fractionalization in two-dimensional magnetic heterostructures, *Phys. Rev. B* **102**, 085412 (2020).
- [66] W.-H. Kao, N. B. Perkins, and G. B. Halász, Vacancy Spectroscopy of non-Abelian Kitaev spin liquids, *Phys. Rev. Lett.* **132**, 136503 (2024).
- [67] W.-H. Kao, G. B. Halász, and N. B. Perkins, Dynamics of vacancy-induced modes in the non-Abelian Kitaev spin liquid, *Phys. Rev. B* **109**, 125150 (2024).
- [68] <https://doi.org/10.5281/zenodo.14278500>.

Supplementary Material to “Local spin-flip transitions induced by magnetic quantum impurities in two-dimensional magnets”

Tim Bauer,¹ Lucas R. D. Freitas,² Eric C. Andrade,³ Reinhold Egger,¹ and Rodrigo G. Pereira²

¹*Institut für Theoretische Physik, Heinrich-Heine-Universität, D-40225 Düsseldorf, Germany*

²*International Institute of Physics and Departamento de Física Teórica e Experimental, Universidade Federal do Rio Grande do Norte, Natal, RN, 59078-970, Brazil*

³*Instituto de Física, Universidade de São Paulo, 05315-970 São Paulo, SP, Brazil*

We here provide (i) details about linear spin wave theory in the presence of a single magnetic quantum impurity, (ii) derive analytical results for the sub-gap magnon bound state energy in the weak-coupling limit, (iii) discuss the tunneling conductance expression, and (iv) show data for the idealized Kitaev honeycomb model. Equation (X) in the main text is referred to as Eq. (MX) below.

Below we provide additional details and derivations concerning the results presented in the main text. For concrete results, we focus on a paradigmatic model for 2D van der Waals magnets like CrI_3 , namely the Kitaev-Heisenberg (KH) model on the honeycomb lattice [1–4]. Leaving aside the so-called Γ exchange terms [5], this model is also expected to describe the physics of $\alpha\text{-RuCl}_3$ layers. We discuss in Sec. I our formulation of linear spin wave (LSW) theory in the presence of a magnetic quantum impurity for the Hamiltonian in Eq. (M1). As discussed in the main text, the corresponding results show excellent agreement with exact diagonalization (ED) results for small systems in the adatom case with $S_{\text{imp}} = 1/2$. For the substitutional impurity with $S_{\text{imp}} = 1$, however, we saw in the main text that the continuous rotation of the impurity spin in the classical background of the LSW theory artificially breaks exact symmetries and can lead to spurious results. In Sec. II, we derive analytical results for the sub-gap magnon bound state energy which are valid in certain limits and shown in the main text. Next, in Sec. III, known expressions for the scanning tunneling spectroscopy (STS) conductance are summarized, including a brief outline of their derivation. Finally, we address the idealized Kitaev honeycomb model in Sec. IV.

I. LSW THEORY

As one method for studying partially polarized phases of 2D magnets with a single magnetic quantum impurity, see Eq. (M1), we use LSW theory [6]. One starts by determining the classical spin configuration minimizing the energy, see Sec. IA. After rotating the local spin quantization axis to the corresponding classical spin axis, one performs a Holstein-Primakoff transformation to introduce boson operators for the magnon degrees of freedom. We consider a linear approximation, where the Hamiltonian can be diagonalized by a Bogoliubov transformation, see Sec. IB. In Sec. IC, we briefly describe how one can obtain dynamical spin correlations from this approach, which enter the STS conductance

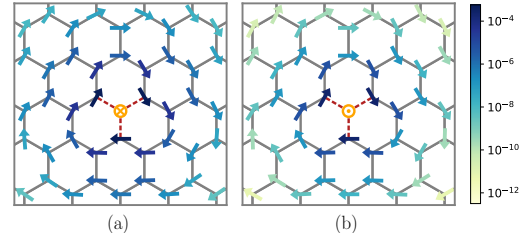


FIG. 1. Examples for classical spin configurations near a magnetic impurity of substitution type in the KH model. Arrows represent spin components in the ab plane, where the color scale indicates the magnitude of the in-plane component. Orange-colored symbols show the out-of-plane components of the impurity spin. Parameters are chosen as in Fig. 2(c) of the main text, i.e., $S = 3/2$, $S_{\text{imp}} = 1/2$, $K/J_b = -0.2$, and $J_K/J_b = 0.5$. Panel (a) shows results for $h/J_b = 1.2$, i.e., below the spin transitions. Panel (b) is for $h/J_b = 3.5$, i.e., above the spin transitions.

in Sec. III. In Sec. ID, we discuss estimates for the regime where discontinuous spin transitions occur based on comparing the energies of the competing classical configurations. Finally, in Sec. IE, we contrast the found spin-flip transition mechanism from conventional spin-flop transitions [7].

A. Classical spin configuration and spin canting

The first step is to find the classical spin configuration that minimizes the energy. In frustrated magnets, inhomogeneities can locally tip the energy balance and disturb the local spin environment, a phenomenon dubbed local relief of frustration [8]. Because a classical adatom magnetic impurity effectively acts as a local field, a local distortion (“spin canting”, schematically illustrated in Fig. 1(b) of the main text) occurs in the neighboring bulk spins with respect to the uniform case. For a substitutional impurity, the situation is similar, as

the bulk spins neighboring the impurity feel an imbalance in their local exchange field. In noncollinear long-ranged ordered phases, such local distortions decay as a power law in space and lead to nontrivial spin textures [9–11]. In polarized phases, magnons are gapped and we expect an exponential decay of the texture, limiting it to the immediate vicinity of the impurity. We numerically determine the classical ground state by sequentially anti-aligning the spins with their local exchange field. To ensure convergence, we start from distinct initial conditions and select as the ground state the spin texture with the lowest energy. This procedure allows us to obtain canted spin texture and gauge the competition between the impurity-bulk exchange coupling $J_K > 0$ and the external magnetic field strength h in determining the local spin configuration.

As an example, we show results for the KH honeycomb model with a substitutional magnetic impurity. Figure 1 illustrates the classical spin configuration for the same parameters as in Fig. 2(c) of the main text. Here we choose two values of the magnetic field along the \hat{c} direction, where the impurity spin in the classical configuration is either antiparallel [Fig. 1(a)] or parallel [Fig. 1(b)] to the field direction. This way, we avoid the regime near the transitions where the classical state incorrectly predicts a smooth rotation of the impurity spin. As shown in Fig. 1, we observe a vortex-like pattern for the bulk spin components in the ab plane, both above and below the transition. In contrast to the spurious rotation of the impurity spin discussed in the main text, the vortex-like pattern for the bulk spins respects the discrete \mathbb{Z}_3 spin-rotation symmetry around the impurity site. A similar pattern has been observed near a vacancy in the KH model [12].

B. Holstein-Primakoff transformation

Given the classical spin configuration, we apply a local rotation that aligns the z -axis with the local spin polarization, $\mathbf{S}_j = R_j \hat{\mathbf{S}}_j$, where R_j is an orthogonal matrix. For polarized phases with a homogeneous spin configuration, $R_j = R$ is site independent and there is no spin canting. For instance, assuming that all spins are polarized by a magnetic field perpendicular to the honeycomb plane, $\mathbf{h} = h\hat{c}$, the spin basis used for representing the KH honeycomb model is rotated according to [13]

$$R = \begin{pmatrix} \frac{1}{\sqrt{6}} & \frac{-1}{\sqrt{2}} & \frac{1}{\sqrt{3}} \\ \frac{1}{\sqrt{6}} & \frac{1}{\sqrt{2}} & \frac{1}{\sqrt{3}} \\ \frac{-2}{\sqrt{6}} & \frac{1}{\sqrt{2}} & \frac{1}{\sqrt{3}} \end{pmatrix}. \quad (1)$$

In any case, given the orthogonal matrices R_j , we next employ a standard Holstein-Primakoff transformation in order to represent spin operators in terms of bosonic

operators b_j and b_j^\dagger describing magnons [6],

$$\begin{aligned} \tilde{S}_j^z &= S_j - n_j, & \tilde{S}_j^+ &= \sqrt{2S_j - n_j} b_j \approx \sqrt{2S_j} b_j, \\ \tilde{S}_j^- &= b_j^\dagger \sqrt{2S_j - n_j} \approx \sqrt{2S_j} b_j^\dagger, \end{aligned} \quad (2)$$

where $n_j = b_j^\dagger b_j$. The polarized impurity spin at $j = 0$ is included in Eq. (2), where $S_0 = S_{\text{imp}}$ generally differs from the value for bulk spins, $S_{j \neq 0} = S$.

To leading order in $1/S$, the Hamiltonian can be written as

$$H = E_{\text{cl}} + H_{\text{sw}} + \mathcal{O}(S^{1/2}), \quad (3)$$

where $E_{\text{cl}} \sim \mathcal{O}(S^2)$ is the classical ground state energy and $H_{\text{sw}} \sim \mathcal{O}(S)$ is the LSW Hamiltonian,

$$H_{\text{sw}} = \sum_{\langle j,k \rangle} \left[t_{j,k} b_j^\dagger b_k + \Delta_{j,k} b_j b_k + \text{h.c.} \right] + \sum_j h_j^{\text{eff}} b_j^\dagger b_j. \quad (4)$$

For $S \rightarrow \infty$, the LSW approach, neglecting all terms beyond H_{sw} in Eq. (3), becomes formally exact (but see below and the main text for subtleties related to the classical reference configuration). The parameters $t_{j,k}$ and $\Delta_{j,k}$ in Eq. (4) follow from the rotated spin-spin interaction matrices, $\tilde{H}_{j,k} = R_j^T H_{j,k} R_k$ with $H_{j,k}$ in Eq. (M1), as

$$\begin{aligned} t_{j,k} &= \frac{\sqrt{S_j S_k}}{2} \left[\left(\tilde{H}_{j,k}^{xx} - i\tilde{H}_{j,k}^{xy} \right) + \left(\tilde{H}_{j,k}^{yy} + i\tilde{H}_{j,k}^{yx} \right) \right], \\ \Delta_{j,k} &= \frac{\sqrt{S_j S_k}}{2} \left[\left(\tilde{H}_{j,k}^{xx} - i\tilde{H}_{j,k}^{xy} \right) - \left(\tilde{H}_{j,k}^{yy} + i\tilde{H}_{j,k}^{yx} \right) \right] \end{aligned} \quad (5)$$

Note that the anomalous couplings $\Delta_{j,k}$ change the total number of magnons. The effective field h_j^{eff} involves both the external field and a contribution from spin interactions. For bulk sites ($j \neq 0$), we find

$$h_j^{\text{eff}} = \tilde{h}^z - \sum_{k \in \mathcal{V}_j} S_k \tilde{H}_{j,k}^{zz}, \quad (6)$$

where \mathcal{V}_j denotes the set of nearest neighbors of j and \tilde{h}^z is the z -component of the rotated field $\tilde{\mathbf{h}} = R_j^T \mathbf{h}$. At the impurity site ($j = 0$), the effective field is given by

$$h_0^{\text{eff}} = g\tilde{h}^z - \sum_{k \in \mathcal{V}_0} S \tilde{H}_{j,k}^{zz} = gh - |\mathcal{V}_0| S J_K, \quad (7)$$

where $|\mathcal{V}_0| = 1$ for an adatom and $|\mathcal{V}_0| = 3$ for a substitutional impurity. The second equality only holds for a polarized uniform spin configuration, where $\tilde{h}^z = h$. The factor g has been defined in Eq. (M2).

The quadratic Hamiltonian (4) can be diagonalized by a Bogoliubov transformation. For a decoupled adatom impurity ($J_K = 0$) and a fully polarized system, we can diagonalize the Hamiltonian in momentum space and obtain analytical expressions for the magnon dispersion relation. The magnon gap is given by $\omega_g = h$ for the

KH model. For $J_K > 0$, we perform a Bogoliubov transformation in real space for a finite system with periodic boundary conditions, and then extrapolate to the thermodynamic limit.

As shown in Fig. 2 of the main text, sub-gap magnon bound states appear for arbitrarily small exchange coupling $J_K > 0$. Within LSW theory, the discontinuous spin transition is well described by calculating $\langle \tilde{S}_j^z \rangle = S_j - \langle b_j^\dagger b_j \rangle$ for the adatom case in the uniform classical configuration. Even without changing the classical state, the discontinuity in the quantum correction to the magnetization is possible because there is a rearrangement of the eigenvectors in the Bogoliubov transformation when the lowest eigenvalue (associated with the magnon bound state) goes through zero.

C. Dynamical spin correlations

Let us briefly sketch how to obtain dynamical spin correlations from this approach. The Bogoliubov transformation yields the single-particle eigenenergies ω_n with bosonic eigenoperators b_n and b_n^\dagger . We can thereby rewrite Eq. (4) as

$$H_{\text{sw}} = \sum_n \omega_n \tilde{b}_n^\dagger \tilde{b}_n + \Delta E, \quad \Delta E = \frac{1}{2} \sum_n \omega_n. \quad (8)$$

The Lehmann representation of the dynamical spin correlations appearing in the STS conductance expression, see Eq. (24) below, is given by

$$C_{jk}^{\alpha\beta}(\omega) = \sum_\nu \langle \Phi_0 | S_j^\alpha | \Phi_\nu \rangle \langle \Phi_\nu | S_k^\beta | \Phi_0 \rangle \delta(\omega + E_0 - E_\nu), \quad (9)$$

where $|\Phi_\nu\rangle$ are many-body eigenstates with energy E_ν , including the ground state $|\Phi_0\rangle$ with energy E_0 . Within LSW theory, the matrix elements $\langle \Phi_0 | S_j^\alpha | \Phi_\nu \rangle$ are finite only for states of the form

$$|\Phi_\nu\rangle \propto |\Phi_0\rangle, |\Phi_\nu\rangle \propto \tilde{b}_n^\dagger |\Phi_0\rangle \text{ or } |\Phi_\nu\rangle \propto \tilde{b}_n^\dagger \tilde{b}_m^\dagger |\Phi_0\rangle. \quad (10)$$

We can thereby rationalize the emergence of zero-, one- and two-magnon contributions in the nonlinear STS conductance. However, we find that the two-magnon contribution of the bound state vanishes within LSW theory. For the pure Heisenberg model ($K = 0$) in a perpendicular magnetic field above the transition, i.e., for $h \gg J_K$, this follows analytically from magnon number conservation, i.e., $\Delta_{j,k} = 0$ in Eq. (5). This fact implies that spin expectation values do not fluctuate for magnetic fields above the spin flip transition within LSW theory. This analytical argument does not hold below the transition or for finite Kitaev interaction, but we here have verified the absence of two-magnon contributions numerically.

D. Classical spin flip

In the main text, we mentioned that LSW theory provides an estimate for a classical spin flip transition. At strong magnetic fields, $h \gg J_K$, the classical ground state is homogeneous and fully polarized. On the other hand, as we decrease the ratio h/J_K , at some point a spin flip will be energetically preferred in the classical ground state configuration. The energy cost of flipping the spin at site j is given by $2S_j h_j^{\text{eff}}$, with the effective field in Eq. (6) for a bulk spin and in Eq. (7) for the impurity. For an adatom impurity, the classical configuration with a flipped spin has lower energy than the uniform classical state if the magnetic field falls below the critical value $h^* = \max(h_{\text{imp}}^*, h_{\text{bulk}}^*)$, where

$$h_{\text{imp}}^* = \frac{S}{g} J_K, \quad h_{\text{bulk}}^* = \sum_{k \in \mathcal{V}_j} S_k \tilde{H}_{j',k}^{zz} \quad (11)$$

correspond to a spin flip of the impurity and the bulk spin $j' \in \mathcal{V}_0$ coupled to the impurity, respectively. Note that for $g \gg 1$, we have $h^* = h_{\text{bulk}}^*$, meaning that in this case we expect the bulk spin to flip against the magnetic field as we decrease h/J_K .

Applying Eq. (11) for an adatom impurity with $S_{\text{imp}} = 1/2$ and the same parameters as in Fig. 2(a,b) of the main text, we obtain the estimate $h^*/J_b \simeq 0.75$ for the classical spin flip transition. However, this estimate is based on comparing the classical energies at order S^2 . If we include quantum corrections to the ground state energy only at order S , the estimate for the classical spin flip shifts to the much smaller value $h^*/J_b \simeq 0.42$, indicated as dashed vertical line in Fig. 2(a) of the main text. Moreover, the latter estimate neglects a possible spin canting in the classical configuration near the flipped spin. (In the adatom case, this can only happen if the bulk spin is flipped.) We stress that, while this semiclassical analysis tells us that a spin flip must occur as we decrease h/J_K , the comparison with ED indicates that the discontinuous spin transition of a $S_{\text{imp}} = 1/2$ magnetic impurity is better described by quantum fluctuations on top of the uniform spin configuration.

E. Difference to spin-flop transitions

We here describe the difference between the spin-flip transitions discovered in this work and the well-known spin-flop transition in an applied field [7]. The “classical” spin-flop mechanism occurs, e.g., for an antiferromagnetic XXZ model in an external field applied along the direction of the sublattice magnetization. For an easy-axis anisotropy, $J_z > J_{x,y}$, the low-field state remains a Néel state along the z -axis. At a critical field h_c , the spin flops to the canted state in which

the spins now have a projection in the x - y plane that spontaneously breaks the spin rotation symmetry along the z -axis. This transition is of first order, and there is no reason for the magnon gap to close due to the anisotropies. In general, one expects a gap closing only at the transition to the polarized phase.

The situation described in our work is very distinct. We are in a (partially) polarized phase, where spin-flip transitions only take place in the vicinity of a magnetic quantum impurity. In the adatom position, for instance, the impurity and the bulk spin that interact antiferromagnetically cannot acquire in-plane components nor rotate continuously toward the polarized state because the local interactions in the quantum impurity problem cannot spontaneously break the (discrete) rotation symmetry along the $\hat{\mathbf{c}}$ direction. In contrast to the mean-field-like argument of the spin-flop transition [7], the local spin-flip transitions described here involve the gap closing of a magnon bound state, which then leads to jumps in the local magnetization.

II. ANALYTICAL RESULTS FOR BOUND STATE ENERGIES

In this section, we consider an adatom impurity position and a perpendicular magnetic field, $\mathbf{h} = \hat{\mathbf{c}}$. We study the KH model in the weak-coupling limit $J_K \ll h$. As shown below, we arrive at a simple structure of the resulting continuum theory describing the magnon bound state and the associated spin-flip transition whenever the bound state energy crosses zero. This continuum argument shows that the predicted spin-flip transitions can occur in general 2D magnets, i.e., not only in van der Waals magnets described by the KH honeycomb model. Moreover, repeating similar arguments for 1D spin chains (and to some extent, even 3D magnets), spin-flip transitions are expected to occur as well. In our example, there is no spin canting and we stay away from spin transitions. Our goal is to obtain analytical results for the sub-gap magnon bound state energy.

Under the above conditions, we can treat the adatom as a weak perturbation to the homogeneous system. We take the continuum limit of the LSW Hamiltonian (4) by expanding the free magnon spectrum about the band minimum at the Γ point. The magnon dispersion is then approximated by $\omega(\mathbf{k}) \approx \omega_g + \frac{\mathbf{k}^2}{2m}$, where ω_g is the magnon gap and the mass term is isotropic. We here consider a partially polarized phase without spontaneous symmetry breaking. While anisotropic exchange interactions such as the Kitaev interaction K may contribute to ω_g in general, in the partially polarized phase of the KH model, the magnon gap increases with the magnetic field according to $\omega_g = h$ without

contributions due to K . Moreover, we find

$$m^{-1} = J + \frac{K}{3} - \frac{K^2}{h + 3J + K}. \quad (12)$$

We recall that for $K \neq 0$, magnon number is not conserved, see Eq. (4). In the unperturbed free-magnon Hamiltonian, this effect is taken care of by the Bogoliubov transformation that gives the magnon dispersion to order k^2 . Next, we take the continuum limit of the impurity contribution, where we expand the bulk modes in terms of momentum eigenstates and neglect terms beyond zeroth order in k . As a result, the Kondo interaction and the Zeeman term for the impurity spin give

$$\begin{aligned} H_{\text{imp}} = & -J_K S_{\text{imp}} b^\dagger(\mathbf{R}_1) b(\mathbf{R}_1) \\ & + J_K \sqrt{S S_{\text{imp}}} [b^\dagger(\mathbf{R}_0) b(\mathbf{R}_1) + \text{h.c.}] \\ & + (gh - S J_K) b^\dagger(\mathbf{R}_0) b(\mathbf{R}_0) + \text{const.}, \end{aligned} \quad (13)$$

where $b(\mathbf{R})$ annihilates a boson at position \mathbf{R} , with \mathbf{R}_0 and \mathbf{R}_1 being the positions of the impurity and the bulk spin coupled to the impurity, respectively. We single out the impurity mode by introducing the notation $a = b(\mathbf{R}_0)$, whereas all the bulk modes are represented by $b(\mathbf{r})$ with $\mathbf{r} \in \mathbb{R}^2$ a vector in the plane that contains the honeycomb lattice. Setting $\mathbf{R}_1 = 0$ and measuring the energies with respect to the lower threshold ω_g of the magnon continuum, we write the effective low-energy Hamiltonian in real space as

$$\begin{aligned} H_{\text{eff}} = & \int d^2r b^\dagger(\mathbf{r}) \left[-\frac{\nabla^2}{2m} - V_0 \delta(\mathbf{r}) \right] b(\mathbf{r}) \\ & + \varepsilon_a a^\dagger a + w [a^\dagger b(\mathbf{r}=0) + b^\dagger(\mathbf{r}=0) a]. \end{aligned} \quad (14)$$

Here, $V_0 = J_K S_{\text{imp}}$ is the strength of an attractive potential for the bulk magnons induced by the magnetization of the impurity. The energy of the bosonic state associated with the impurity (measured from the bulk magnon gap ω_g) is

$$\varepsilon_a = gh - \omega_g - J_K S. \quad (15)$$

Note that the occupation $a^\dagger a$ of this state can change due to quantum fluctuations of the impurity. Finally, $w = J_K \sqrt{S S_{\text{imp}}}$ is an effective hybridization due to the transverse part of the Kondo interaction. The classical magnetic impurity limit [14, 15] corresponds to taking $S_{\text{imp}} \rightarrow \infty$ and $J_K \rightarrow 0$ while keeping the product $V_0 = J_K S_{\text{imp}}$ constant. In this limit, one finds $w \rightarrow 0$, i.e., the a boson decouples from the $b(\mathbf{r})$ bosons. Then the only effect of the impurity is to act as a static local field on the bulk degrees of freedom.

Noting that the effective Hamiltonian (14) conserves the total magnon number, we use an *Ansatz* for a general single-particle state,

$$|\Psi\rangle = \left(\int d^2r \psi(\mathbf{r}) b^\dagger(\mathbf{r}) + \phi_a a^\dagger \right) |0\rangle, \quad (16)$$

where $\psi(\mathbf{r})$ and ϕ_a are wave functions and $|0\rangle$ is the vacuum state, identified with the ground state of the unperturbed Hamiltonian (for $J_K = 0$). The Schrödinger equation, $H_{\text{eff}}|\Psi\rangle = E|\Psi\rangle$, where the energy E is measured relative to ω_g , yields the coupled equations

$$-\frac{1}{2m}\nabla^2\psi(\mathbf{r}) - V_0\delta(\mathbf{r})\psi(\mathbf{r}) + w\phi_a\delta(\mathbf{r}) = E\psi(\mathbf{r}),$$

$$\varepsilon_a\phi_a + w\psi(0) = E\phi_a. \quad (17)$$

From Eq. (17), we observe that a bound state solution with $E = E_b < 0$ satisfies the relation

$$\phi_a = -\frac{w\psi(0)}{\varepsilon_a + |E_b|}. \quad (18)$$

Substituting Eq. (18) into the first equation in Eq. (17), we obtain the Schrödinger equation (M3) for a δ -function potential with a renormalized coupling that depends on the energy itself,

$$V_{\text{eff}}(E_b) = V_0 + \frac{w^2}{\varepsilon_a + |E_b|}. \quad (19)$$

For a *classical* magnetic impurity, $w \rightarrow 0$ implies that $V_{\text{eff}} = V_0$ is constant. Hence Eq. (M3) can be solved after imposing a large-momentum cutoff Λ [16]. The resulting bound state energy is exponentially small at weak coupling but depends on V_0 and m in a nonperturbative manner,

$$E_b \simeq -\frac{\Lambda^2}{2m}e^{-2\pi/(mV_0)}. \quad (20)$$

For a *quantum impurity*, on the other hand, we obtain a qualitatively different scaling of the bound state energy. In this case, $V_{\text{eff}}(E_b)$ becomes large if ε_a is negative and $\varepsilon_a \approx E_b$. In particular, for the KH model with $g = 1$, we have $\omega_g = h$ and then $\varepsilon_a = -J_K S < 0$ for any $J_K > 0$. In general, the binding energy is given by the solution of the equation

$$\frac{2m|E_b|}{\Lambda^2} = \exp\left[-\frac{2\pi}{mV_{\text{eff}}(E_b)}\right], \quad (21)$$

In the regime $|V_{\text{eff}}(E_b)| \gg 1$, we can approximate

$$\frac{2m|E_b|}{\Lambda^2} \approx 1 - \frac{2\pi}{mV_0 + \frac{mw^2}{\varepsilon_a + |E_b|}}, \quad (22)$$

which is a quadratic equation in $|E_b|$. The low-energy solution is

$$E_b = \varepsilon_a + \mathcal{O}(w^2) = gh - \omega_g - J_K S + \mathcal{O}(J_K^2), \quad (23)$$

as quoted in the main text. For $g = 1$, the binding energy vanishes for $J_K \rightarrow 0$ and scales linearly with J_K at weak coupling. The linear dependence predicted by Eq. (23), without any free fitting parameter, is in excellent agreement with our numerical results for the

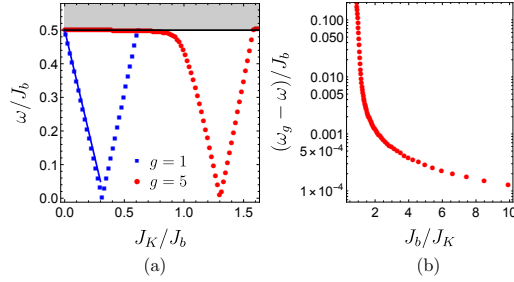


FIG. 2. Magnon spectrum ω for the KH model with an adatom quantum magnetic impurity vs impurity coupling J_K (both ω and J_K are in units of the bulk exchange coupling $J_b > 0$). We set $S = 3/2$, $S_{\text{imp}} = 1/2$, $h/J_b = 0.5$, and $K/J_b = -0.2$, where the field is along the \hat{c} direction. (a) The symbols represent the bound state energy calculated by LSW theory for $g = 1$ (blue squares) and $g = 5$ (red dots). The solid line for $g = 1$ gives the analytical prediction (23). The shaded region represents the magnon continuum $\omega > \omega_g = h$. (b) Binding energy for $g = 5$ in the weak-coupling regime, plotted on a logarithmic scale vs J_b/J_K .

lattice model, see Fig. 2(a). For $g > 1$, the binding energy is exponentially small at weak coupling, see Fig. 2(b), but it crosses over to the linear dependence as one increases J_K . The condition $w^2/\varepsilon_a \sim V_0$, see Eq. (19), gives the estimate $J_K \sim \frac{(g-1)h}{2S}$ for the crossover scale. In the strong-coupling regime, i.e., above the spin transition, the bound state eventually merges with the continuum and disappears for sufficiently large J_K .

III. ON THE STS CONDUCTANCE

In this section, we summarize known results for the STS conductance which have been used for generating Fig. 4 in the main text. For the tip position \mathbf{r} and bias voltage V , the zero-temperature STS conductance can be written as [12, 15, 17–22]

$$G(V) = G_0 \sum_{j,k} \frac{t_j t_k^*}{|t_{\text{bulk}}|^2} F_{j,k}(\mathbf{r}) \sum_{\alpha} \int_0^{eV} d\omega C_{j,k}^{\alpha,\alpha}(\omega), \quad (24)$$

where $t_{j=0} = t_{\text{imp}}$ and $t_{j \neq 0} = t_{\text{bulk}}$ are cotunneling amplitudes discussed below. This expression holds in the weak-coupling limit, where the tip (and the substrate) are kept sufficiently distant from both the impurity and the bulk spins in order to allow for a perturbative treatment of the respective tunneling processes. The conductance reference scale used in Eq. (24) is defined as

$$G_0 = 2\pi d_A d_B |t_{\text{bulk}}|^2, \quad (25)$$

where d_A (d_B) is the density of states of the tip (substrate) at the Fermi level. Moreover, the function

$$F_{j,k}(\mathbf{r}) = \exp\left(-\frac{|\mathbf{R}_j - \mathbf{r}| + |\mathbf{R}_k - \mathbf{r}|}{l_0}\right) \quad (26)$$

encodes the tip position dependence. The spin sites (including the impurity) are denoted by \mathbf{R}_j , and l_0 is a length characterizing the STS resolution. Finally, the dynamical spin correlation function of the magnet (in the absence of tip and substrate) is given by

$$C_{j,k}^{\alpha,\beta}(\omega) = \int dt e^{i\omega t} \langle \Phi_0 | S_j^\alpha(t) S_k^\beta(0) | \Phi_0 \rangle, \quad (27)$$

using the ground state $|\Phi_0\rangle$ of the 2D magnet. We note that on top of the inelastic contribution (24), there is a featureless voltage-independent elastic cotunneling term [15, 19]. For finite bound state energy, the zero-bias conductance obtained from Eq. (24) is expressed in terms of spin expectation values $\langle S_j^\alpha \rangle$ only,

$$G(V=0) = G_0 \sum_\alpha \left| \sum_j \frac{t_j}{|t_{\text{bulk}}|} e^{-|\mathbf{R}_j - \mathbf{r}|/l_0} \langle S_j^\alpha \rangle \right|^2. \quad (28)$$

We conclude that local spin-flip transitions are directly visible as steps in the zero-bias STS conductance.

Let us briefly describe the main ideas behind the derivation of Eq. (24). In order to describe electrical transport through a 2D magnet, one has to start from a model that retains the charge degrees of freedom, e.g., the Hubbard-Kanamori model. By a Schrieffer-Wolff transformation to the low-energy spin sector, one then obtains the Hamiltonian (M1) in terms of the spin operators \mathbf{S}_j . We now include tunneling processes with amplitude $t_A(\mathbf{r} - \mathbf{R}_j)$ connecting a normal-conducting scanning probe tip at position \mathbf{r} , described by noninteracting fermion operators $c_{A,\tau}(\mathbf{r})$ for spin projection $\tau \in \{\uparrow, \downarrow\}$, to lattice site \mathbf{R}_j of the 2D layer. Here we assume that t_A is independent of the momentum and the spin of the tunneling electrons. Similarly, we include tunneling processes with constant amplitude t_B connecting the respective site in the 2D layer to a 2D substrate described by noninteracting fermion operators $c_{B,\tau}(\mathbf{R}_j)$. Below, Pauli matrices $\boldsymbol{\tau} = (\tau_x, \tau_y, \tau_z)$ and the identity τ_0 act in conduction electron spin space. Applying a Schrieffer-Wolff transformation in the presence of these tunneling terms now yields an effective cotunneling Hamiltonian connecting the tip and the substrate via the 2D magnetic layer, see [12, 15, 17–19] for details,

$$H_{\text{cot}} = \sum_j \frac{t_A^*(\mathbf{r} - \mathbf{R}_j) t_B}{U} c_A^\dagger(\mathbf{r}) (\eta_0 \tau_0 \mathbb{1}_j + \eta_1 \boldsymbol{\tau} \cdot \mathbf{S}_j) c_B(\mathbf{R}_j) + \text{H.c.}, \quad (29)$$

where the sum runs over all lattice sites of the 2D magnet in Eq. (M1), including the impurity site. Here, U is a

Coulomb interaction energy scale of the 2D layer, and $c_{A/B}^\dagger = (c_{A/B,\uparrow}^\dagger, c_{A/B,\downarrow}^\dagger)$. The numbers η_0 and η_1 depend, in particular, on the ratio of the Hund's rule coupling J_H and the parameter U , and are of order unity [15]. (In general, they are different for bulk and impurity sites.) We note in passing that in general there is also a spin-rotation-symmetry breaking contribution [15] which we have neglected in Eq. (29). We assume an exponential distance dependence of the tunneling matrix elements, $t_A(\mathbf{r} - \mathbf{R}_j) \propto e^{-|\mathbf{r} - \mathbf{R}_j|/l_0}$, where the length scale l_0 sets the resolution of the scanning probe tip. We also assume a constant and spin-independent (non-polarized) density of states in the relevant energy range for both the tip (d_A) and the substrate (d_B).

A computation of the current $I(V)$ from tip to substrate, and thus of the differential conductance $G(V) = dI/dV$, can now be performed by perturbation theory in H_{cot} . To that end, we proceed along standard steps, see, e.g., Ref. [15]. Within Fermi's golden rule, the squared matrix elements of $\eta_0 \tau_0 \mathbb{1}_j + \eta_1 \boldsymbol{\tau} \cdot \mathbf{S}_j$ appear. The term $G \propto \eta_0^2$ is associated with elastic tunneling processes and gives rise to a background conductance which is independent of voltage and tip position. The term $G \propto \eta_0 \eta_1$ is also independent of voltage but generally depends on the tip position as it involves the spin expectation values $\langle S_j^\alpha \rangle$. However, it vanishes under the above assumption of a non-polarized tip and substrate. Finally, the term $G \propto \eta_1^2$ depends on voltage in a nontrivial manner since it probes the dynamical spin correlations of the 2D magnet. This term is shown in Eq. (24). Accounting for the exponential distance dependence of t_A through the form factors $F_{j,k}$ in Eq. (26), all other microscopic factors in Eq. (29) appear only via the overall scale G_0 in Eq. (25) for the cotunneling conductance, and through cotunneling amplitudes t_j . For the latter, we distinguish between bulk sites (with $t_{j \neq 0} = t_{\text{bulk}}$) and the impurity site (with $t_{j=0} = t_{\text{imp}}$). The ratio $t_{\text{imp}}/t_{\text{bulk}}$ may vary substantially depending on the impurity type (adatom vs substitutional). In Fig. 3 of the main text, we considered $t_{\text{imp}} > t_{\text{bulk}}$, assuming a stronger overlap of the tip wavefunction with Co adatoms than with Cr^{3+} ions in the honeycomb layer. After the above steps, one arrives at Eq. (24).

The conductance is thereby expressed in terms of dynamical spin correlations of the 2D magnet in the absence of tip and substrate, see Sec. IC. These correlations exhibit a peak at the bound state energy which translates to a step in the conductance. As discussed in the main text, one can thereby track the energy of the bound state as a function of the external magnetic field by measuring $G(V)$ or dG/dV . Moreover, $G(V=0)$ can directly monitor atomic-scale spin-flip transitions.

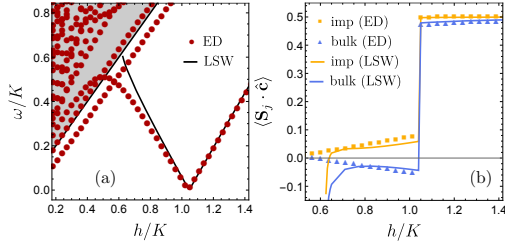


FIG. 3. ED and LSW results for a magnetic quantum impurity in the adatom configuration for the ferromagnetic Kitaev model ($K > 0$, $J_b = 0$) with $S = S_{\text{imp}} = 1/2$, $J_K/K = 1.5$, $g = 1.5$, and $\mathbf{h} = h\hat{c}$. (a) Excitation spectrum vs magnetic field. ED (LSW) results correspond to red dots (black lines). ED results were obtained for a system of 2×2 unit cells with periodic boundary conditions. (b) Spin projections $\langle \mathbf{S}_{0,1} \cdot \hat{c} \rangle$ vs h/J_b . Yellow squares (lines) correspond to ED (LSW) results for the impurity spin. Results for the coupled bulk spin are shown as blue triangles (ED) and blue lines (LSW), respectively.

IV. KITAEV HONEYCOMB MODEL

We here show results for the ferromagnetic 2D Kitaev honeycomb model with $J_b = 0$ and $K > 0$ [13] in the partially polarized phase, which may serve as idealized model for $\alpha\text{-RuCl}_3$ in a strong magnetic field. For the bulk spins (Ru^{3+}), we effectively have $S = 1/2$. Using Co atoms as examples for the adatom magnetic impurities [23], we have $S_{\text{imp}} = 1/2$ with $g \approx 1.5$. In contrast to Fig. 2(b) of the main text, we now find that the discontinuity in the local magnetization at the transition ($h/K \approx 1.05$) is larger for the bulk than for the impurity spin. In fact, the magnetization of the bulk spin becomes slightly negative for magnetic fields just below the transition. While the spin flip of the bulk spin is expected to occur for the large- g limit, we here observe that it can happen already for moderate values of $g > 1$. Despite of the small system size used in the ED calculations, LSW and ED results agree rather well for large magnetic fields. However, Fig. 3 shows that they significantly deviate for $h/K < 0.7$, i.e., once the bound state approaches the continuum. However, since the main emphasis of our work is on spin-flip transitions associated with zero-energy bound states, we do not study this regime here in detail.

In Fig. 4, we show the spatial profile of the STS zero-bias conductance for the Kitaev model near the adatom impurity studied in Fig. 3. Similar to our results for the KH model in Fig. 3 of the main text, the zero-bias conductance is significantly enhanced in the vicinity of the impurity for magnetic fields above the transition. In the present case, however, both the impurity and the coupled bulk spin show positive magnetization. In

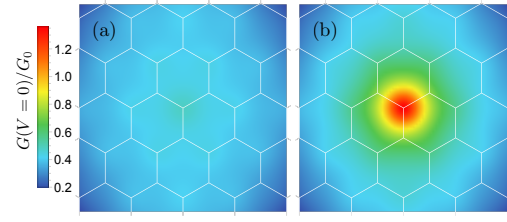


FIG. 4. Spatial profile of the zero-bias STS conductance near an adatom magnetic impurity for the ferromagnetic Kitaev model, with the same parameters as in Fig. 3. Results obtained from LSW theory for two field values: (a) $h = 0.854K$ (below the transition), (b) $h = 1.33K$ (above the transition).

fact, below the critical field, the conductance has a local maximum when the tip is right above the impurity, in contrast to the local minimum observed in Fig. 3(c) of the main text. This difference can be rationalized by noticing that the parameter choice $t_{\text{imp}} > t_{\text{bulk}}$ used in Fig. 4 favors contributions due to cotunneling via the impurity site. The corresponding impurity spin still has a small positive magnetization even below the transition, see Fig. 3(b), in contrast to the negative magnetization observed below the transition in Fig. 2(b) of the main text.

- [1] L. Janssen and M. Vojta, Heisenberg-Kitaev physics in magnetic fields, *J. Phys. Condens. Matter* **31**, 423002 (2019).
- [2] P. P. Stavropoulos, X. Liu, and H.-Y. Kee, Magnetic anisotropy in spin-3/2 with heavy ligand in honeycomb Mott insulators: Application to CrI_3 , *Phys. Rev. Res.* **3**, 013216 (2021).
- [3] Q. H. Wang, A. Bedoya-Pinto, M. Blei, A. H. Dismukes, A. Hamo, S. Jenkins, M. Koperski, Y. Liu, Q.-C. Sun, E. J. Telford, H. H. Kim, M. Augustin, U. Vool, J.-X. Yin, L. H. Li, A. Falin, C. R. Dean, F. Casanova, R. F. L. Evans, M. Chshiev, A. Mishchenko, C. Petrovic, R. He, L. Zhao, A. W. Tsen, B. D. Gerardot, M. Brotons-Gisbert, Z. Guguchia, X. Roy, S. Tongay, Z. Wang, M. Z. Hasan, J. Wrachtrup, A. Yacoby, A. Fert, S. Parkin, K. S. Novoselov, P. Dai, L. Balicas, and E. J. G. Santos, The Magnetic Genome of Two-Dimensional van der Waals Materials, *ACS Nano* **16**, 6960 (2022).
- [4] Y. Ahn, X. Guo, S. Son, Z. Sun, and L. Zhao, Progress and Prospects in Two-Dimensional Magnetism of van der Waals Materials (2024), arXiv:2401.13781 [cond-mat.mtrl-sci].
- [5] S. M. Winter, A. A. Tsirlin, M. Daghofer, J. van den Brink, Y. Singh, P. Gegenwart, and R. Valentí, Models and materials for generalized Kitaev magnetism, *J. Phys.: Condens. Matter* **29**, 493002 (2017).
- [6] P. Fazekas, *Lecture Notes on Electron Correlation and Magnetism* (World Scientific, 1999).

- [7] S. Blundell, *Magnetism in Condensed Matter* (Oxford University Press, Oxford, UK, 2001).
- [8] J. Villain, Insulating spin glasses, *Z. Phys. B* **33**, 31 (1979).
- [9] A. Wollny, L. Fritz, and M. Vojta, Fractional Impurity Moments in Two-Dimensional Noncollinear Magnets, *Phys. Rev. Lett.* **107**, 137204 (2011).
- [10] A. Wollny, E. C. Andrade, and M. Vojta, Singular field response and singular screening of vacancies in antiferromagnets, *Phys. Rev. Lett.* **109**, 177203 (2012).
- [11] V. S. Maryasin and M. E. Zhitomirsky, Triangular antiferromagnet with nonmagnetic impurities, *Phys. Rev. Lett.* **111**, 247201 (2013).
- [12] A. Mitra, A. Corticelli, P. Ribeiro, and P. A. McClarty, Magnon Interference Tunneling Spectroscopy as a Probe of 2D Magnetism, *Phys. Rev. Lett.* **130**, 066701 (2023).
- [13] A. Kitaev, Anyons in an exactly solved model and beyond, *Ann. Phys.* **321**, 2 (2006).
- [14] Y. Imry and S.-k. Ma, Random-Field Instability of the Ordered State of Continuous Symmetry, *Phys. Rev. Lett.* **35**, 1399 (1975).
- [15] T. Bauer, L. R. D. Freitas, R. G. Pereira, and R. Egger, Scanning tunneling spectroscopy of Majorana zero modes in a Kitaev spin liquid, *Phys. Rev. B* **107**, 054432 (2023).
- [16] R. Jackiw, Delta function potentials in two-dimensional and three-dimensional quantum mechanics, in *M.A.B. Bég Memorial Volume*, edited by A. Ali and P. Hoodbhoy (World Scientific, Singapore, 1991).
- [17] J. Fransson, O. Eriksson, and A. Balatsky, Theory of spin-polarized scanning tunneling microscopy applied to local spins, *Phys. Rev. B* **81**, 115454 (2010).
- [18] J. Fernández-Rossier, Theory of single-spin inelastic tunneling spectroscopy, *Phys. Rev. Lett.* **102**, 256802 (2009).
- [19] J. Feldmeier, W. Natori, M. Knap, and J. Knolle, Local probes for charge-neutral edge states in two-dimensional quantum magnets, *Phys. Rev. B* **102**, 134423 (2020).
- [20] M. Carrega, I. J. Vera-Marun, and A. Principi, Tunneling spectroscopy as a probe of fractionalization in two-dimensional magnetic heterostructures, *Phys. Rev. B* **102**, 085412 (2020).
- [21] W.-H. Kao, N. B. Perkins, and G. B. Halász, Vacancy Spectroscopy of Non-Abelian Kitaev Spin Liquids, *Phys. Rev. Lett.* **132**, 136503 (2024).
- [22] W.-H. Kao, G. B. Halász, and N. B. Perkins, Dynamics of vacancy-induced modes in the non-Abelian Kitaev spin liquid, *Phys. Rev. B* **109**, 125150 (2024).
- [23] Y. Chen, W.-Y. He, W. Ruan, J. Hwang, S. Tang, R. L. Lee, M. Wu, T. Zhu, C. Zhang, H. Ryu, F. Wang, S. G. Louie, Z.-X. Shen, S.-K. Mo, P. A. Lee, and M. F. Crommie, Evidence for a spinon Kondo effect in cobalt atoms on single-layer 1T-TaSe₂, *Nat. Phys.* **18**, 1335 (2022).

References

- [1] F. Abdulla, S. Rao, and G. Murthy. Fermi arc reconstruction at the interface of twisted Weyl semimetals. *Physical Review B*, 103(23):235308, 2021. doi:10.1103/PhysRevB.103.235308.
- [2] S. L. Adler. Axial-vector vertex in spinor electrodynamics. *Physical Review*, 177(5):2426, 1969. doi:10.1103/PhysRev.177.2426.
- [3] A. Akhmerov and C. Beenakker. Detection of valley polarization in graphene by a superconducting contact. *Physical Review Letters*, 98(15):157003, 2007. doi:10.1103/PhysRevLett.98.157003.
- [4] A. Akhmerov and C. Beenakker. Boundary conditions for Dirac fermions on a terminated honeycomb lattice. *Physical Review B*, 77(8):085423, 2008. doi:10.1103/PhysRevB.77.085423.
- [5] P. W. Anderson, G. Baskaran, Z. Zou, and T. Hsu. Resonating-valence-bond theory of phase transitions and superconductivity in La_2CuO_4 -based compounds. *Physical Review Letters*, 58(26):2790, 1987. doi:10.1103/PhysRevLett.58.2790.
- [6] N. Armitage, E. Mele, and A. Vishwanath. Weyl and Dirac semimetals in three-dimensional solids. *Reviews of Modern Physics*, 90(1):015001, 2018. doi:10.1103/RevModPhys.90.015001.
- [7] J. E. Avron, R. Seiler, and B. Simon. Homotopy and quantization in condensed matter physics. *Physical Review Letters*, 51(1):51, 1983. doi:10.1103/PhysRevLett.51.51.
- [8] S. Bachus, D. A. Kaib, A. Jesche, V. Tsurkan, A. Loidl, S. M. Winter, A. A. Tsirlin, R. Valenti, and P. Gegenwart. Angle-dependent thermodynamics of α - RuCl_3 . *Physical Review B*, 103(5):054440, 2021. doi:10.1103/PhysRevB.103.054440.
- [9] S. Bachus, D. A. Kaib, Y. Tokiwa, A. Jesche, V. Tsurkan, A. Loidl, S. M. Winter, A. A. Tsirlin, R. Valenti, and P. Gegenwart. Thermodynamic perspective on field-induced behavior of α - RuCl_3 . *Physical Review Letters*, 125(9):097203, 2020. doi:10.1103/PhysRevLett.125.097203.
- [10] S.-H. Baek, S.-H. Do, K.-Y. Choi, Y. S. Kwon, A. Wolter, S. Nishimoto, J. Van Den Brink, and B. Büchner. Evidence for a field-induced quantum spin liquid in α - RuCl_3 . *Physical Review Letters*, 119(3):037201, 2017. doi:10.1103/PhysRevLett.119.037201.
- [11] A. Balatsky, Y. Manassen, and R. Salem. ESR-STM of a single precessing spin: detection of exchange-based spin noise. *Physical Review B*, 66(19):195416, 2002. doi:10.1103/PhysRevB.66.195416.
- [12] C. Balz, L. Janssen, P. Lampen-Kelley, A. Banerjee, Y. Liu, J.-Q. Yan, D. Mandrus, M. Vojta, and S. E. Nagler. Field-induced intermediate ordered phase and anisotropic interlayer interactions in α - RuCl_3 . *Physical Review B*, 103(17):174417, 2021. doi:10.1103/PhysRevB.103.174417.

- [13] A. Banerjee, C. Bridges, J.-Q. Yan, A. Aczel, L. Li, M. Stone, G. Granroth, M. Lumsden, Y. Yiu, J. Knolle, et al. Proximate Kitaev quantum spin liquid behaviour in a honeycomb magnet. *Nature Materials*, 15(7):733–740, 2016. doi:10.1038/nmat4604.
- [14] A. Banerjee, P. Lampen-Kelley, J. Knolle, C. Balz, A. A. Aczel, B. Winn, Y. Liu, D. Pajerowski, J. Yan, C. A. Bridges, et al. Excitations in the field-induced quantum spin liquid state of α -RuCl₃. *npj Quantum Materials*, 3(1):8, 2018. doi:10.1038/s41535-018-0079-2.
- [15] A. Banerjee, J. Yan, J. Knolle, C. A. Bridges, M. B. Stone, M. D. Lumsden, D. G. Mandrus, D. A. Tennant, R. Moessner, and S. E. Nagler. Neutron scattering in the proximate quantum spin liquid α -RuCl₃. *Science*, 356(6342):1055–1059, 2017. doi:10.1126/science.aah6015.
- [16] G. Baskaran, S. Mandal, and R. Shankar. Exact results for spin dynamics and fractionalization in the Kitaev model. *Physical Review Letters*, 98(24):247201, 2007. doi:10.1103/PhysRevLett.98.247201.
- [17] G. Baskaran, D. Sen, and R. Shankar. Spin- S Kitaev model: classical ground states, order from disorder, and exact correlation functions. *Physical Review B*, 78(11):115116, 2008. doi:10.1103/PhysRevB.78.115116.
- [18] Y. Baum, E. Berg, S. Parameswaran, and A. Stern. Current at a distance and resonant transparency in Weyl semimetals. *Physical Review X*, 5(4):041046, 2015. doi:10.1103/PhysRevX.5.041046.
- [19] C. Beenakker. Search for Majorana fermions in superconductors. *Annual Review of Condensed Matter Physics*, 4(1):113–136, 2013. doi:10.1146/annurev-conmatphys-030212-184337.
- [20] J. S. Bell and R. W. Jackiw. A PCAC puzzle: $\pi^0 \rightarrow \gamma\gamma$ in the σ -model. *Nuovo cimento*, 60(CERN-TH-920):47–61, 1969.
- [21] I. Belopolski, K. Manna, D. S. Sanchez, G. Chang, B. Ernst, J. Yin, S. S. Zhang, T. Cochran, N. Shumiya, H. Zheng, et al. Discovery of topological Weyl fermion lines and drumhead surface states in a room temperature magnet. *Science*, 365(6459):1278–1281, 2019. doi:10.1126/science.aav2327.
- [22] B. A. Bernevig, C. Felser, and H. Beidenkopf. Progress and prospects in magnetic topological materials. *Nature*, 603(7899):41–51, 2022. doi:10.1038/s41586-021-04105-x.
- [23] B. A. Bernevig, T. L. Hughes, and S.-C. Zhang. Quantum spin Hall effect and topological phase transition in HgTe quantum wells. *Science*, 314(5806):1757–1761, 2006. doi:10.1126/science.1133734.
- [24] M. V. Berry. Quantal phase factors accompanying adiabatic changes. *Proceedings of the Royal Society of London. A*, 392(1802):45–57, 1984. doi:10.1098/rspa.1984.0023.
- [25] R. Bianco and R. Resta. Mapping topological order in coordinate space. *Physical Review B*, 84(24):241106, 2011. doi:10.1103/PhysRevB.84.241106.
- [26] S. Biswas, Y. Li, S. M. Winter, J. Knolle, and R. Valentí. Electronic properties of α -RuCl₃ in proximity to graphene. *Physical Review Letters*, 123(23):237201, 2019. doi:10.1103/PhysRevLett.123.237201.
- [27] J.-P. Blaizot and G. Ripka. *Quantum theory of finite systems*, volume 3. MIT press Cambridge, MA, 1986.

- [28] N. Bovenzi, M. Breitzkreiz, T. O'Brien, J. Tworzydło, and C. Beenakker. Twisted Fermi surface of a thin-film Weyl semimetal. *New Journal of Physics*, 20(2):023023, 2018. doi:[10.1088/1367-2630/aaaa90](https://doi.org/10.1088/1367-2630/aaaa90).
- [29] B. Bradlyn, L. Elcoro, J. Cano, M. G. Vergniory, Z. Wang, C. Felser, M. I. Aroyo, and B. A. Bernevig. Topological quantum chemistry. *Nature*, 547(7663):298–305, 2017. doi:[10.1038/nature23268](https://doi.org/10.1038/nature23268).
- [30] S. Bramwell, M. Harris, B. Den Hertog, M. Gingras, J. Gardner, D. McMorrow, A. Wildes, A. Cornelius, J. Champion, R. Melko, et al. Spin correlations in $\text{Ho}_2\text{Ti}_2\text{O}_7$ a dipolar spin ice system. *Physical Review Letters*, 87(4):047205, 2001. doi:[10.1103/PhysRevLett.87.047205](https://doi.org/10.1103/PhysRevLett.87.047205).
- [31] F. Bucchieri, R. Egger, and A. De Martino. Transport, refraction, and interface arcs in junctions of Weyl semimetals. *Physical Review B*, 106(4):045413, 2022. doi:[10.1103/PhysRevB.106.045413](https://doi.org/10.1103/PhysRevB.106.045413).
- [32] L. Bulaevskii, C. Batista, M. Mostovoy, and D. Khomskii. Electronic orbital currents and polarization in Mott insulators. *Physical Review B*, 78(2):024402, 2008. doi:[10.1103/PhysRevB.78.024402](https://doi.org/10.1103/PhysRevB.78.024402).
- [33] A. Burkov. Anomalous hall effect in weyl metals. *Physical Review Letters*, 113(18):187202, 2014. doi:[10.1103/PhysRevLett.113.187202](https://doi.org/10.1103/PhysRevLett.113.187202).
- [34] A. Burkov. Chiral anomaly and transport in Weyl metals. *Journal of Physics: Condensed Matter*, 27(11):113201, 2015. doi:[10.1088/0953-8984/27/11/113201](https://doi.org/10.1088/0953-8984/27/11/113201).
- [35] A. Burkov. Weyl metals. *Annual Review of Condensed Matter Physics*, 9(1):359–378, 2018. doi:[10.1146/annurev-conmatphys-033117-054129](https://doi.org/10.1146/annurev-conmatphys-033117-054129).
- [36] M. Burrello, E. Guadagnini, L. Lepori, and M. Mintchev. Field theory approach to the quantum transport in Weyl semimetals. *Physical Review B*, 100(15):155131, 2019. doi:[10.1103/PhysRevB.100.155131](https://doi.org/10.1103/PhysRevB.100.155131).
- [37] C. Castelnovo, R. Moessner, and S. L. Sondhi. Spin ice, fractionalization, and topological order. *Annual Review of Condensed Matter Physics*, 3(1):35–55, 2012. doi:[10.1146/annurev-conmatphys-020911-125058](https://doi.org/10.1146/annurev-conmatphys-020911-125058).
- [38] A. Catuneanu, Y. Yamaji, G. Wachtel, Y. B. Kim, and H.-Y. Kee. Path to stable quantum spin liquids in spin-orbit coupled correlated materials. *npj Quantum Materials*, 3(1):23, 2018. doi:[10.1038/s41535-018-0095-2](https://doi.org/10.1038/s41535-018-0095-2).
- [39] J. T. Chalker. Geometrically frustrated antiferromagnets: statistical mechanics and dynamics. In C. Lacroix, P. Mendels, and F. Mila, editors, *Introduction to frustrated magnetism: materials, experiments, theory*, pages 3–22. Springer, 2010. doi:[10.1007/978-3-642-10589-0_1](https://doi.org/10.1007/978-3-642-10589-0_1).
- [40] J. Chaloupka, G. Jackeli, and G. Khaliullin. Kitaev-Heisenberg model on a honeycomb lattice: possible exotic phases in iridium oxides A_2IrO_3 . *Physical Review Letters*, 105(2):027204, 2010. doi:[10.1103/PhysRevLett.105.027204](https://doi.org/10.1103/PhysRevLett.105.027204).
- [41] P. Chandra and B. Doucot. Possible spin-liquid state at large S for the frustrated square Heisenberg lattice. *Physical Review B*, 38(13):9335, 1988. doi:[10.1103/PhysRevB.38.9335](https://doi.org/10.1103/PhysRevB.38.9335).
- [42] S. Chandra, K. Ramola, and D. Dhar. Classical Heisenberg spins on a hexagonal lattice with Kitaev couplings. *Physical Review E*, 82(3):031113, 2010. doi:[10.1103/PhysRevE.82.031113](https://doi.org/10.1103/PhysRevE.82.031113).

- [43] A. Y. Chaou, V. Dwivedi, and M. Breitzkreiz. Magnetic breakdown and chiral magnetic effect at Weyl-semimetal tunnel junctions. *Physical Review B*, 107(24):L241109, 2023. doi:10.1103/PhysRevB.107.L241109.
- [44] H.-D. Chen and Z. Nussinov. Exact results of the Kitaev model on a hexagonal lattice: spin states, string and brane correlators, and anyonic excitations. *Journal of Physics A*, 41(7):075001, 2008. doi:10.1088/1751-8113/41/7/075001.
- [45] L. Chen, J.-H. Chung, B. Gao, T. Chen, M. B. Stone, A. I. Kolesnikov, Q. Huang, and P. Dai. Topological spin excitations in honeycomb ferromagnet CrI₃. *Physical Review X*, 8(4):041028, 2018. doi:10.1103/PhysRevX.8.041028.
- [46] L. E. Chern and C. Castelnovo. Topological phase diagrams of in-plane field polarized Kitaev magnets. *Physical Review B*, 109(18):L180407, 2024. doi:10.1103/PhysRevB.109.L180407.
- [47] L. E. Chern, E. Z. Zhang, and Y. B. Kim. Sign structure of thermal Hall conductivity and topological magnons for in-plane field polarized Kitaev magnets. *Physical Review Letters*, 126(14):147201, 2021. doi:10.1103/PhysRevLett.126.147201.
- [48] A. Chernyshev, D. Galanakis, P. Phillips, A. Rozhkov, and A.-M. Tremblay. Higher order corrections to effective low-energy theories for strongly correlated electron systems. *Physical Review B*, 70(23):235111, 2004. doi:10.1103/PhysRevB.70.235111.
- [49] S. Choi, R. Coldea, A. Kolmogorov, T. Lancaster, I. Mazin, S. Blundell, P. Radaelli, Y. Singh, P. Gegenwart, K. Choi, et al. Spin waves and revised crystal structure of honeycomb iridate Na₂IrO₃. *Physical Review Letters*, 108(12):127204, 2012. doi:10.1103/PhysRevLett.108.127204.
- [50] R. Comin, G. Levy, B. Ludbrook, Z.-H. Zhu, C. Veenstra, J. Rosen, Y. Singh, P. Gegenwart, D. Stricker, J. N. Hancock, et al. Na₂IrO₃ as a novel relativistic Mott insulator with a 340-meV gap. *Physical Review Letters*, 109(26):266406, 2012. doi:10.1103/PhysRevLett.109.266406.
- [51] T. Cookmeyer and J. E. Moore. Spin-wave analysis of the low-temperature thermal Hall effect in the candidate Kitaev spin liquid α -RuCl₃. *Physical Review B*, 98(6):060412, 2018. doi:10.1103/PhysRevB.98.060412.
- [52] P. Czajka, T. Gao, M. Hirschberger, P. Lampen-Kelley, A. Banerjee, N. Quirk, D. G. Mandrus, S. E. Nagler, and N. P. Ong. Planar thermal Hall effect of topological bosons in the Kitaev magnet α -RuCl₃. *Nature Materials*, 22(1):36–41, 2023. doi:10.1038/s41563-022-01397-w.
- [53] P. Czajka, T. Gao, M. Hirschberger, P. Lampen-Kelley, A. Banerjee, J. Yan, D. G. Mandrus, S. E. Nagler, and N. Ong. Oscillations of the thermal conductivity in the spin-liquid state of α -RuCl₃. *Nature Physics*, 17(8):915–919, 2021. doi:10.1038/s41567-021-01243-x.
- [54] P. A. M. Dirac. The quantum theory of the electron. *Proceedings of the Royal Society of London. Series A, Containing Papers of a Mathematical and Physical Character*, 117(778):610–624, 1928. doi:10.1098/rspa.1928.0023.
- [55] L. Du, Y. Huang, Y. Wang, Q. Wang, R. Yang, J. Tang, M. Liao, D. Shi, Y. Shi, X. Zhou, et al. 2D proximate quantum spin liquid state in atomic-thin α -RuCl₃. *2D Materials*, 6(1):015014, 2018. doi:10.1088/2053-1583/aaee29.
- [56] V. Dwivedi. Fermi arc reconstruction at junctions between Weyl semimetals. *Physical Review B*, 97(6):064201, 2018. doi:10.1103/PhysRevB.97.064201.

- [57] S. R. Elliott and M. Franz. Colloquium: Majorana fermions in nuclear, particle, and solid-state physics. *Reviews of Modern Physics*, 87(1):137–163, 2015. doi:10.1103/RevModPhys.87.137.
- [58] P. Fazekas and P. W. Anderson. On the ground state properties of the anisotropic triangular antiferromagnet. *Philosophical Magazine*, 30(2):423–440, 1974. doi:10.1080/14786439808206568.
- [59] J. Feldmeier, W. Natori, M. Knap, and J. Knolle. Local probes for charge-neutral edge states in two-dimensional quantum magnets. *Physical Review B*, 102(13):134423, 2020. doi:10.1103/PhysRevB.102.134423.
- [60] X.-Y. Feng, G.-M. Zhang, and T. Xiang. Topological characterization of quantum phase transitions in a spin-1/2 model. *Physical Review Letters*, 98(8):087204, 2007. doi:10.1103/PhysRevLett.98.087204.
- [61] T. Fennell, P. Deen, A. Wildes, K. Schmalzl, D. Prabhakaran, A. Boothroyd, R. Aldus, D. McMorrow, and S. Bramwell. Magnetic Coulomb phase in the spin ice $\text{Ho}_2\text{Ti}_2\text{O}_7$. *Science*, 326(5951):415–417, 2009. doi:10.1126/science.1177582.
- [62] J. Fernández-Rossier. Theory of single-spin inelastic tunneling spectroscopy. *Physical Review Letters*, 102(25):256802, 2009. doi:10.1103/PhysRevLett.102.256802.
- [63] J. Fletcher, W. Gardner, A. Fox, and G. Topping. X-ray, infrared, and magnetic studies of α - and β -ruthenium trichloride. *Journal of the Chemical Society A*, pages 1038–1045, 1967. doi:10.1039/J19670001038.
- [64] J. Fransson, O. Eriksson, and A. Balatsky. Theory of spin-polarized scanning tunneling microscopy applied to local spins. *Physical Review B*, 81(11):115454, 2010. doi:10.1103/PhysRevB.81.115454.
- [65] M. Freedman, A. Kitaev, M. Larsen, and Z. Wang. Topological quantum computation. *Bulletin of the American Mathematical Society*, 40(1):31–38, 2003. doi:10.1090/S0273-0979-02-00964-3.
- [66] L. Fu and C. L. Kane. Superconducting proximity effect and majorana fermions at the surface of a topological insulator. *Physical Review Letters*, 100(9):096407, 2008. doi:10.1103/PhysRevLett.100.096407.
- [67] L. Fu, C. L. Kane, and E. J. Mele. Topological insulators in three dimensions. *Physical Review Letters*, 98(10):106803, 2007. doi:10.1103/PhysRevLett.98.106803.
- [68] M. J. Gilbert. Topological electronics. *Communications Physics*, 4(1):70, 2021. doi:10.1038/s42005-021-00569-5.
- [69] M. Gohlke, R. Verresen, R. Moessner, and F. Pollmann. Dynamics of the Kitaev-Heisenberg model. *Physical Review Letters*, 119(15):157203, 2017. doi:10.1103/PhysRevLett.119.157203.
- [70] E. Gorbar, V. Miransky, I. Shovkovy, and P. Sukhachov. Quantum oscillations as a probe of interaction effects in Weyl semimetals in a magnetic field. *Physical Review B*, 90(11):115131, 2014. doi:10.1103/PhysRevB.90.115131.
- [71] J. S. Gordon, A. Catuneanu, E. S. Sørensen, and H.-Y. Kee. Theory of the field-revealed Kitaev spin liquid. *Nature Communications*, 10(1):2470, 2019. doi:10.1038/s41467-019-10405-8.

- [72] P. Goswami and S. Tewari. Axionic field theory of $(3+1)$ -dimensional Weyl semimetals. *Physical Review B*, 88(24):245107, 2013. doi:10.1103/PhysRevB.88.245107.
- [73] H. Gretarsson, J. Clancy, X. Liu, J. Hill, E. Bozin, Y. Singh, S. Manni, P. Gegenwart, J. Kim, A. Said, et al. Crystal-field splitting and correlation effect on the electronic structure of $A_2\text{IrO}_3$. *Physical Review Letters*, 110(7):076402, 2013. doi:10.1103/PhysRevLett.110.076402.
- [74] H. Gretarsson, J. Clancy, Y. Singh, P. Gegenwart, J. Hill, J. Kim, M. Upton, A. Said, D. Casa, T. Gog, et al. Magnetic excitation spectrum of Na_2IrO_3 probed with resonant inelastic x-ray scattering. *Physical Review B*, 87(22):220407, 2013. doi:10.1103/PhysRevB.87.220407.
- [75] A. G. Grushin. Consequences of a condensed matter realization of Lorentz-violating QED in Weyl semi-metals. *Physical Review D*, 86(4):045001, 2012. doi:10.1103/PhysRevD.86.045001.
- [76] G. B. Halász, J. Chalker, and R. Moessner. Doping a topological quantum spin liquid: slow holes in the Kitaev honeycomb model. *Physical Review B*, 90(3):035145, 2014. doi:10.1103/PhysRevB.84.165414.
- [77] F. D. M. Haldane. Model for a quantum Hall effect without Landau levels: condensed-matter realization of the “parity anomaly”. *Physical Review Letters*, 61(18):2015, 1988. doi:10.1103/PhysRevLett.61.2015.
- [78] K. Hashimoto, T. Kimura, and X. Wu. Boundary conditions of Weyl semimetals. *Progress of Theoretical and Experimental Physics*, 2017(5):053101, 2017. doi:10.1093/ptep/ptx053.
- [79] Y. Hatsugai. Chern number and edge states in the integer quantum Hall effect. *Physical Review Letters*, 71(22):3697, 1993. doi:10.1103/PhysRevLett.71.3697.
- [80] C. L. Henley. The “Coulomb phase” in frustrated systems. *Annual Review of Condensed Matter Physics*, 1(1):179–210, 2010. doi:10.1146/annurev-conmatphys-070909-104138.
- [81] M. Hermanns, K. O’Brien, and S. Trebst. Weyl spin liquids. *Physical Review Letters*, 114(15):157202, 2015. doi:10.1103/PhysRevLett.114.157202.
- [82] C. Herring. Accidental degeneracy in the energy bands of crystals. *Physical Review*, 52(4):365, 1937. doi:10.1103/PhysRev.52.365.
- [83] D. R. Hofstadter. Energy levels and wave functions of Bloch electrons in rational and irrational magnetic fields. *Physical review B*, 14(6):2239, 1976. doi:10.1103/PhysRevB.14.2239.
- [84] P. Hosur and X. Qi. Recent developments in transport phenomena in Weyl semimetals. *Comptes Rendus. Physique*, 14(9-10):857–870, 2013. doi:10.1016/j.crhy.2013.10.010.
- [85] Y. Hou, H. Xiang, and X. Gong. Unveiling magnetic interactions of ruthenium trichloride via constraining direction of orbital moments: potential routes to realize a quantum spin liquid. *Physical Review B*, 96(5):054410, 2017. doi:10.1103/PhysRevB.96.054410.
- [86] Z. Hou and Q.-F. Sun. Nonlocal correlation mediated by Weyl orbits. *Physical Review Research*, 2(2):023236, 2020. doi:10.1103/PhysRevResearch.2.023236.
- [87] D. Hsieh, D. Qian, L. Wray, Y. Xia, Y. S. Hor, R. J. Cava, and M. Z. Hasan. A topological Dirac insulator in a quantum spin Hall phase. *Nature*, 452(7190):970–974, 2008. doi:10.1038/nature06843.

- [88] S.-M. Huang, S.-Y. Xu, I. Belopolski, C.-C. Lee, G. Chang, B. Wang, N. Alidoust, G. Bian, M. Neupane, C. Zhang, et al. A Weyl Fermion semimetal with surface Fermi arcs in the transition metal monophnictide TaAs class. *Nature Communications*, 6(1):7373, 2015. doi:10.1038/ncomms8373.
- [89] S. Hwan Chun, J.-W. Kim, J. Kim, H. Zheng, C. C. Stoumpos, C. Malliakas, J. Mitchell, K. Mehlawat, Y. Singh, Y. Choi, et al. Direct evidence for dominant bond-directional interactions in a honeycomb lattice iridate Na_2IrO_3 . *Nature Physics*, 11(6):462–466, 2015. doi:10.1038/nphys3322.
- [90] K. Imamura, S. Suetsugu, Y. Mizukami, Y. Yoshida, K. Hashimoto, K. Ohtsuka, Y. Kasahara, N. Kurita, H. Tanaka, P. Noh, et al. Majorana-fermion origin of the planar thermal Hall effect in the Kitaev magnet $\alpha\text{-RuCl}_3$. *Science advances*, 10(11):eadk3539, 2024. doi:10.1038/s41563-022-01397-w.
- [91] D. Ivanov. Vortexlike elementary excitations in the Rokhsar-Kivelson dimer model on the triangular lattice. *Physical Review B*, 70(9):094430, 2004. doi:10.1103/PhysRevB.70.094430.
- [92] D. A. Ivanov. Non-abelian statistics of half-quantum vortices in p -wave superconductors. *Physical Review Letters*, 86(2):268, 2001. doi:10.1103/PhysRevLett.86.268.
- [93] G. Jackeli and G. Khaliullin. Mott Insulators in the Strong Spin-Orbit Coupling Limit: from Heisenberg to a quantum compass and Kitaev Models. *Physical Review Letters*, 102(1):017205, 2009. doi:10.1103/PhysRevLett.102.017205.
- [94] S.-H. Jang and Y. Motome. Exploring rare-earth Kitaev magnets by massive-scale computational analysis. *Communications Materials*, 5(1):192, 2024. doi:10.1038/s43246-024-00634-w.
- [95] H.-C. Jiang, Z.-C. Gu, X.-L. Qi, and S. Trebst. Possible proximity of the Mott insulating iridate Na_2IrO_3 to a topological phase: phase diagram of the Heisenberg-Kitaev model in a magnetic field. *Physical Review B*, 83(24):245104, 2011. doi:10.1103/PhysRevB.83.245104.
- [96] R. D. Johnson, S. Williams, A. Haghighirad, J. Singleton, V. Zapf, P. Manuel, I. Mazin, Y. Li, H. O. Jeschke, R. Valentí, et al. Monoclinic crystal structure of $\alpha\text{-RuCl}_3$ and the zigzag antiferromagnetic ground state. *Physical Review B*, 92(23):235119, 2015. doi:10.1103/PhysRevB.92.235119.
- [97] D. G. Joshi. Topological excitations in the ferromagnetic Kitaev-Heisenberg model. *Physical Review B*, 98(6):060405, 2018. doi:10.1103/PhysRevB.98.060405.
- [98] A. P. Joy and A. Rosch. Dynamics of visons and thermal Hall effect in perturbed Kitaev models. *Physical Review X*, 12(4):041004, 2022. doi:10.1103/PhysRevLett.98.247201.
- [99] J. Kanamori. Superexchange interaction and symmetry properties of electron orbitals. *Journal of Physics and Chemistry of Solids*, 10(2-3):87–98, 1959. doi:10.1016/0022-3697(59)90061-7.
- [100] C. Kane and M. P. Fisher. Quantized thermal transport in the fractional quantum Hall effect. *Physical Review B*, 55(23):15832, 1997. doi:10.1103/PhysRevB.55.15832.
- [101] C. L. Kane and E. J. Mele. Quantum spin Hall effect in graphene. *Physical Review Letters*, 95(22):226801, 2005. doi:10.1103/PhysRevLett.95.226801.
- [102] C. L. Kane and E. J. Mele. \mathbb{Z}_2 topological order and the quantum spin Hall effect. *Physical Review Letters*, 95(14):146802, 2005. doi:10.1103/PhysRevLett.95.146802.
- [103] W.-H. Kao and N. B. Perkins. Disorder upon disorder: localization effects in the Kitaev spin liquid. *Annals of Physics*, 435:168506, 2021. doi:10.1016/j.aop.2021.168506.

- [104] Y. Kasahara, T. Ohnishi, Y. Mizukami, O. Tanaka, S. Ma, K. Sugii, N. Kurita, H. Tanaka, J. Nasu, Y. Motome, et al. Majorana quantization and half-integer thermal quantum Hall effect in a Kitaev spin liquid. *Nature*, 559(7713):227–231, 2018. doi:10.1038/s41586-018-0274-0.
- [105] Y. Kasahara, K. Sugii, T. Ohnishi, M. Shimozawa, M. Yamashita, N. Kurita, H. Tanaka, J. Nasu, Y. Motome, T. Shibauchi, et al. Unusual thermal Hall effect in a Kitaev spin liquid candidate α -RuCl₃. *Physical Review Letters*, 120(21):217205, 2018. doi:10.1103/PhysRevLett.120.217205.
- [106] G. Kells, D. Meidan, and P. Brouwer. Near-zero-energy end states in topologically trivial spin-orbit coupled superconducting nanowires with a smooth confinement. *Physical Review B*, 86(10):100503, 2012. doi:10.1103/PhysRevB.86.100503.
- [107] G. Khaliullin. Orbital order and fluctuations in Mott insulators. *Progress of Theoretical Physics Supplement*, 160:155–202, 2005. doi:10.1143/PTPS.160.155.
- [108] D. Khomskii. Spin chirality and nontrivial charge dynamics in frustrated Mott insulators: spontaneous currents and charge redistribution. *Journal of Physics: Condensed Matter*, 22(16):164209, 2010. doi:10.1088/0953-8984/22/16/164209.
- [109] D. I. Khomskii. *Transition metal compounds*. Cambridge University Press, 2014. doi:10.1017/CB09781139096782.
- [110] B. Kim, H. Jin, S. Moon, J.-Y. Kim, B.-G. Park, C. Leem, J. Yu, T. Noh, C. Kim, S.-J. Oh, et al. Novel $J_{\text{eff}} = 1/2$ Mott state induced by relativistic spin-orbit coupling in Sr₂IrO₄. *Physical Review Letters*, 101(7):076402, 2008. doi:10.1103/PhysRevLett.101.076402.
- [111] B. Kim, H. Ohsumi, T. Komesu, S. Sakai, T. Morita, H. Takagi, and T.-h. Arima. Phase-sensitive observation of a spin-orbital Mott state in Sr₂IrO₄. *Science*, 323(5919):1329–1332, 2009. doi:10.1126/science.1167106.
- [112] A. Kitaev. Anyons in an exactly solved model and beyond. *Annals of Physics*, 321(1):2–111, 2006. doi:10.1016/j.aop.2005.10.005.
- [113] A. Y. Kitaev. Unpaired Majorana fermions in quantum wires. *Physics-uspekhi*, 44(10S):131, 2001. doi:10.1070/1063-7869/44/10S/S29.
- [114] A. Y. Kitaev. Fault-tolerant quantum computation by anyons. *Annals of physics*, 303(1):2–30, 2003. doi:10.1016/S0003-4916(02)00018-0.
- [115] S. Kivelson. Statistics of holons in the quantum hard-core dimer gas. *Physical Review B*, 39(1):259, 1989. doi:10.1103/PhysRevB.39.259.
- [116] K. v. Klitzing, G. Dorda, and M. Pepper. New method for high-accuracy determination of the fine-structure constant based on quantized Hall resistance. *Physical Review Letters*, 45(6):494, 1980. doi:10.1103/PhysRevLett.45.494.
- [117] K. Klocke, Y. Liu, G. B. Halász, and J. Alicea. Spin-liquid-based topological qubits, 2024. arXiv:2411.08093.
- [118] J. Knolle. *Dynamics of a Quantum Spin Liquid*. Springer, 2016. doi:10.1007/978-3-319-23953-8.
- [119] J. Knolle, D. Kovrizhin, J. Chalker, and R. Moessner. Dynamics of a two-dimensional quantum spin liquid: signatures of emergent Majorana fermions and fluxes. *Physical Review Letters*, 112(20):207203, 2014. doi:10.1103/PhysRevLett.112.207203.

- [120] Y. Kobayashi, T. Okada, K. Asai, M. Katada, H. Sano, and F. Ambe. Moessbauer spectroscopy and magnetization studies of α - and β -ruthenium trichloride. *Inorganic Chemistry*, 31(22):4570–4574, 1992. doi:10.1021/ic00048a025.
- [121] Y. Kohsaka, S. Akutagawa, S. Omachi, Y. Iwamichi, T. Ono, I. Tanaka, S. Tateishi, H. Murayama, S. Suetsugu, K. Hashimoto, et al. Imaging quantum interference in a monolayer Kitaev quantum spin liquid candidate. *Physical Review X*, 14(4):041026, 2024. doi:10.1103/PhysRevX.14.041026.
- [122] A. Koitzsch, C. Habenicht, E. Müller, M. Knupfer, B. Büchner, H. C. Kandpal, J. Van Den Brink, D. Nowak, A. Isaeva, and T. Doert. J_{eff} description of the honeycomb Mott insulator α -RuCl₃. *Physical Review Letters*, 117(12):126403, 2016. doi:10.1103/PhysRevLett.117.126403.
- [123] M. König, S. Wiedmann, C. Brune, A. Roth, H. Buhmann, L. W. Molenkamp, X.-L. Qi, and S.-C. Zhang. Quantum spin Hall insulator state in HgTe quantum wells. *Science*, 318(5851):766–770, 2007. doi:10.1126/science.1148047.
- [124] Y. Kubota, H. Tanaka, T. Ono, Y. Narumi, and K. Kindo. Successive magnetic phase transitions in α -RuCl₃: XY-like frustrated magnet on the honeycomb lattice. *Physical Review B*, 91(9):094422, 2015. doi:10.1103/PhysRevB.91.094422.
- [125] V. Lahtinen, A. W. Ludwig, and S. Trebst. Perturbed vortex lattices and the stability of nucleated topological phases. *Physical Review B*, 89(8):085121, 2014. doi:10.1103/PhysRevB.89.085121.
- [126] L. D. Landau. On the theory of phase transitions. *Zh. eksp. teor. Fiz*, 7(19-32):926, 1937.
- [127] R. B. Laughlin. Anomalous quantum Hall effect: an incompressible quantum fluid with fractionally charged excitations. *Physical Review Letters*, 50(18):1395, 1983. doi:10.1103/PhysRevLett.50.1395.
- [128] F.-Y. Li, Y.-D. Li, Y. Yu, A. Paramakanti, and G. Chen. Kitaev materials beyond iridates: order by quantum disorder and Weyl magnons in rare-earth double perovskites. *Physical Review B*, 95(8):085132, 2017. doi:10.1103/PhysRevB.95.085132.
- [129] P. Li, Y. Wen, X. He, Q. Zhang, C. Xia, Z.-M. Yu, S. A. Yang, Z. Zhu, H. N. Alshareef, and X.-X. Zhang. Evidence for topological type-II Weyl semimetal WTe₂. *Nature Communications*, 8(1):2150, 2017. doi:10.1038/s41467-017-02237-1.
- [130] E. H. Lieb. Flux phase of the half-filled band. *Physical Review Letters*, 73(16):2158, 1994. doi:10.1103/PhysRevLett.73.2158.
- [131] D. Liu, A. Liang, E. Liu, Q. Xu, Y. Li, C. Chen, D. Pei, W. Shi, S. Mo, P. Dudin, et al. Magnetic Weyl semimetal phase in a Kagomé crystal. *Science*, 365(6459):1282–1285, 2019. doi:10.1126/science.aav2873.
- [132] X. Liu, T. Berlijn, W.-G. Yin, W. Ku, A. Tsvelik, Y.-J. Kim, H. Gretarsson, Y. Singh, P. Gegenwart, and J. Hill. Long-range magnetic ordering in Na₂IrO₃. *Physical Review B*, 83(22):220403, 2011. doi:10.1103/PhysRevB.83.220403.
- [133] Z. Liu, B. Zhou, Y. Zhang, Z. Wang, H. Weng, D. Prabhakaran, S.-K. Mo, Z. Shen, Z. Fang, X. Dai, et al. Discovery of a three-dimensional topological Dirac semimetal, Na₃Bi. *Science*, 343(6173):864–867, 2014. doi:10.1126/science.124508.

- [134] R. M. Lutchyn, J. D. Sau, and S. Das Sarma. Majorana fermions and a topological phase transition in semiconductor-superconductor heterostructures. *Physical Review Letters*, 105(7):077001, 2010. doi:10.1103/PhysRevLett.105.077001.
- [135] B. Lv, H. Weng, B. Fu, X. P. Wang, H. Miao, J. Ma, P. Richard, X. Huang, L. Zhao, G. Chen, et al. Experimental discovery of Weyl semimetal TaAs. *Physical Review X*, 5(3):031013, 2015. doi:10.1103/PhysRevX.5.031013.
- [136] A. H. MacDonald, S. M. Girvin, and D. t. Yoshioka. $\frac{t}{U}$ expansion for the Hubbard model. *Physical Review B*, 37(16):9753, 1988. doi:10.1103/PhysRevB.37.9753.
- [137] M. Majumder, M. Schmidt, H. Rosner, A. Tsirlin, H. Yasuoka, and M. Baenitz. Anisotropic $\text{Ru}^{3+}4d^5$ magnetism in the $\alpha\text{-RuCl}_3$ honeycomb system: susceptibility, specific heat, and zero-field NMR. *Physical Review B*, 91(18):180401, 2015. doi:10.1103/PhysRevB.91.180401.
- [138] S. Mandal and N. Surendran. Exactly solvable Kitaev model in three dimensions. *Physical Review B*, 79(2):024426, 2009. doi:10.1103/PhysRevB.79.024426.
- [139] R. Matsumoto and S. Murakami. Rotational motion of magnons and the thermal Hall effect. *Physical Review B*, 84(18):184406, 2011. doi:10.1103/PhysRevB.84.184406.
- [140] R. Matsumoto, R. Shindou, and S. Murakami. Thermal Hall effect of magnons in magnets with dipolar interaction. *Physical Review B*, 89(5):054420, 2014. doi:10.1103/PhysRevB.89.054420.
- [141] P. McClarty, X.-Y. Dong, M. Gohlke, J. Rau, F. Pollmann, R. Moessner, and K. Penc. Topological magnons in Kitaev magnets at high fields. *Physical Review B*, 98(6):060404, 2018. doi:10.1103/PhysRevB.98.060404.
- [142] P. A. McClarty. Topological magnons: a review. *Annual Review of Condensed Matter Physics*, 13(1):171–190, 2022. doi:10.1146/annurev-conmatphys-031620-104715.
- [143] G. Misguich, D. Serban, and V. Pasquier. Quantum dimer model on the kagome lattice: solvable dimer-liquid and Ising gauge theory. *Physical Review Letters*, 89(13):137202, 2002. doi:10.1103/PhysRevLett.89.137202.
- [144] A. Mitra, A. Corticelli, P. Ribeiro, and P. A. McClarty. Magnon interference tunneling spectroscopy as a probe of 2d magnetism. *Physical Review Letters*, 130(6):066701, 2023. doi:10.1103/PhysRevLett.130.066701.
- [145] K. A. Modic, R. D. McDonald, J. Ruff, M. D. Bachmann, Y. Lai, J. C. Palmstrom, D. Graf, M. K. Chan, F. Balakirev, J. Betts, et al. Scale-invariant magnetic anisotropy in RuCl_3 at high magnetic fields. *Nature Physics*, 17(2):240–244, 2021. doi:10.1038/s41567-020-1028-0.
- [146] K. A. Modic, T. E. Smidt, I. Kimchi, N. P. Breznay, A. Biffin, S. Choi, R. D. Johnson, R. Coldea, P. Watkins-Curry, G. T. McCandless, et al. Realization of a three-dimensional spin-anisotropic harmonic honeycomb iridate. *Nature Communications*, 5(1):4203, 2014. doi:10.1038/ncomms5203.
- [147] R. Moessner and J. E. Moore. *Topological phases of matter*. Cambridge University Press, 2021. doi:10.1017/9781316226308.
- [148] R. Moessner and K. S. Raman. Quantum dimer models. In C. Lacroix, P. Mendels, and F. Mila, editors, *Introduction to frustrated magnetism: materials, experiments, theory*, pages 3–22. Springer, 2010. doi:10.1007/978-3-642-10589-0_17.

- [149] R. Moessner and S. L. Sondhi. Ising models of quantum frustration. *Physical Review B*, 63(22):224401, 2001. doi:10.1103/PhysRevB.63.224401.
- [150] R. Moessner and S. L. Sondhi. Resonating valence bond phase in the triangular lattice quantum dimer model. *Physical Review Letters*, 86(9):1881, 2001. doi:10.1103/PhysRevLett.86.1881.
- [151] R. Moessner, S. L. Sondhi, and P. Chandra. Two-dimensional periodic frustrated Ising models in a transverse field. *Physical Review Letters*, 84(19):4457, 2000. doi:10.1103/PhysRevLett.84.4457.
- [152] P. J. Moll, N. L. Nair, T. Helm, A. C. Potter, I. Kimchi, A. Vishwanath, and J. G. Analytis. Transport evidence for Fermi-arc-mediated chirality transfer in the Dirac semimetal Cd_3As_2 . *Nature*, 535(7611):266–270, 2016. doi:10.1038/nature18276.
- [153] G. Moore and N. Read. Nonabelions in the fractional quantum Hall effect. *Nuclear Physics B*, 360(2-3):362–396, 1991. doi:10.1016/0550-3213(91)90407-0.
- [154] J. E. Moore and L. Balents. Topological invariants of time-reversal-invariant band structures. *Physical Review B*, 75(12):121306, 2007. doi:10.1103/PhysRevB.75.121306.
- [155] N. Morali, R. Batabyal, P. K. Nag, E. Liu, Q. Xu, Y. Sun, B. Yan, C. Felser, N. Avraham, and H. Beidenkopf. Fermi-arc diversity on surface terminations of the magnetic Weyl semimetal $\text{Co}_3\text{Sn}_2\text{S}_2$. *Science*, 365(6459):1286–1291, 2019. doi:10.1126/science.aav2334.
- [156] N. Nagaosa, J. Sinova, S. Onoda, A. H. MacDonald, and N. P. Ong. Anomalous Hall effect. *Reviews of modern physics*, 82(2):1539–1592, 2010. doi:10.1103/RevModPhys.82.1539.
- [157] N. L. Nair, M.-E. Boulanger, F. Laliberté, S. Griffin, S. Channa, A. Legros, W. Tabis, C. Proust, J. Neaton, L. Taillefer, et al. Signatures of possible surface states in TaAs. *Physical Review B*, 102(7):075402, 2020. doi:10.1103/PhysRevB.102.075402.
- [158] C. Nayak, S. H. Simon, A. Stern, M. Freedman, and S. Das Sarma. Non-Abelian anyons and topological quantum computation. *Reviews of Modern Physics*, 80(3):1083–1159, 2008. doi:10.1103/RevModPhys.80.1083.
- [159] M. Neupane, S.-Y. Xu, R. Sankar, N. Alidoust, G. Bian, C. Liu, I. Belopolski, T.-R. Chang, H.-T. Jeng, H. Lin, et al. Observation of a three-dimensional topological Dirac semimetal phase in high-mobility Cd_3As_2 . *Nature Communications*, 5(1):3786, 2014. doi:10.1038/ncomms4786.
- [160] D.-H.-M. Nguyen, K. Kobayashi, J.-E. R. Wichmann, and K. Nomura. Quantum Hall effect induced by chiral Landau levels in topological semimetal films. *Physical Review B*, 104(4):045302, 2021. doi:10.1103/PhysRevB.104.045302.
- [161] H. B. Nielsen and M. Ninomiya. Absence of neutrinos on a lattice: (I). Proof by homotopy theory. *Nuclear Physics B*, 185(1):20–40, 1981. doi:10.1016/0550-3213(81)90361-8.
- [162] H. B. Nielsen and M. Ninomiya. The Adler-Bell-Jackiw anomaly and Weyl fermions in a crystal. *Physics Letters B*, 130(6):389–396, 1983. doi:10.1016/0370-2693(83)91529-0.
- [163] K. O’Brien, M. Hermanns, and S. Trebst. Classification of gapless \mathbb{Z}_2 spin liquids in three-dimensional Kitaev models. *Physical Review B*, 93(8):085101, 2016. doi:10.1103/PhysRevB.93.085101.
- [164] N. Ong and S. Liang. Experimental signatures of the chiral anomaly in Dirac–Weyl semimetals. *Nature Reviews Physics*, 3(6):394–404, 2021. doi:10.1038/s42254-021-00310-9.

- [165] Y. Oreg, G. Refael, and F. Von Oppen. Helical liquids and Majorana bound states in quantum wires. *Physical Review Letters*, 105(17):177002, 2010. doi:[10.1103/PhysRevLett.105.177002](https://doi.org/10.1103/PhysRevLett.105.177002).
- [166] D. Otten, A. Roy, and F. Hassler. Dynamical structure factor in the non-Abelian phase of the Kitaev honeycomb model in the presence of quenched disorder. *Physical Review B*, 99(3):035137, 2019. doi:[10.1103/PhysRevB.99.035137](https://doi.org/10.1103/PhysRevB.99.035137).
- [167] S. Parameswaran, T. Grover, D. Abanin, D. Pesin, and A. Vishwanath. Probing the chiral anomaly with nonlocal transport in three-dimensional topological semimetals. *Physical Review X*, 4(3):031035, 2014. doi:[10.1103/PhysRevX.4.031035](https://doi.org/10.1103/PhysRevX.4.031035).
- [168] F. L. Pedrocchi, S. Chesi, and D. Loss. Physical solutions of the Kitaev honeycomb model. *Physical Review B*, 84(16):165414, 2011. doi:[10.1103/PhysRevB.84.165414](https://doi.org/10.1103/PhysRevB.84.165414).
- [169] R. G. Pereira and R. Egger. Electrical access to Ising anyons in Kitaev spin liquids. *Physical Review Letters*, 125(22):227202, 2020. doi:[10.1103/PhysRevLett.125.227202](https://doi.org/10.1103/PhysRevLett.125.227202).
- [170] D. Pesin and A. H. MacDonald. Spintronics and pseudospintronics in graphene and topological insulators. *Nature materials*, 11(5):409–416, 2012. doi:[10.1038/nmat3305](https://doi.org/10.1038/nmat3305).
- [171] A. S. T. Pires. *Theoretical tools for spin models in magnetic systems*. IOP Publishing, 2021. doi:[10.1088/978-0-7503-3879-0](https://doi.org/10.1088/978-0-7503-3879-0).
- [172] K. Plumb, J. Clancy, L. Sandilands, V. V. Shankar, Y. Hu, K. Burch, H.-Y. Kee, and Y.-J. Kim. α -RuCl₃: a spin-orbit assisted Mott insulator on a honeycomb lattice. *Physical Review B*, 90(4):041112, 2014. doi:[10.1103/PhysRevB.90.041112](https://doi.org/10.1103/PhysRevB.90.041112).
- [173] I. Pollini. Electronic properties of the narrow-band material α -RuCl₃. *Physical Review B*, 53(19):12769, 1996. doi:[10.1103/PhysRevB.53.12769](https://doi.org/10.1103/PhysRevB.53.12769).
- [174] A. C. Potter, I. Kimchi, and A. Vishwanath. Quantum oscillations from surface Fermi arcs in Weyl and Dirac semimetals. *Nature Communications*, 5(1):5161, 2014. doi:[10.1038/ncomms6161](https://doi.org/10.1038/ncomms6161).
- [175] E. Prodan, T. L. Hughes, and B. A. Bernevig. Entanglement spectrum of a disordered topological Chern insulator. *Physical Review Letters*, 105(11):115501, 2010. doi:[10.1103/PhysRevLett.105.115501](https://doi.org/10.1103/PhysRevLett.105.115501).
- [176] S. Rachel, L. Fritz, and M. Vojta. Landau levels of Majorana fermions in a spin liquid. *Physical Review Letters*, 116(16):167201, 2016. doi:[10.1103/PhysRevLett.116.167201](https://doi.org/10.1103/PhysRevLett.116.167201).
- [177] A. Ralko, M. Ferrero, F. Becca, D. Ivanov, and F. Mila. Zero-temperature properties of the quantum dimer model on the triangular lattice. *Physical Review B*, 71(22):224109, 2005. doi:[10.1103/PhysRevB.71.224109](https://doi.org/10.1103/PhysRevB.71.224109).
- [178] J. G. Rau, E. K.-H. Lee, and H.-Y. Kee. Generic spin model for the honeycomb iridates beyond the Kitaev limit. *Physical Review Letters*, 112(7):077204, 2014. doi:[10.1103/PhysRevLett.112.077204](https://doi.org/10.1103/PhysRevLett.112.077204).
- [179] J. Reuther, P. Wölfle, R. Darradi, W. Brenig, M. Arlego, and J. Richter. Quantum phases of the planar antiferromagnetic J_1 - J_2 - J_3 Heisenberg model. *Physical Review B*, 83(6):064416, 2011. doi:[10.1103/PhysRevB.83.064416](https://doi.org/10.1103/PhysRevB.83.064416).
- [180] A. Revelli, M. Moretti Sala, G. Monaco, C. Hickey, P. Becker, F. Freund, A. Jesche, P. Gegenwart, T. Eschmann, F. Buessen, et al. Fingerprints of Kitaev physics in the magnetic excitations of honeycomb iridates. *Physical Review Research*, 2(4):043094, 2020. doi:[10.1103/PhysRevResearch.2.043094](https://doi.org/10.1103/PhysRevResearch.2.043094).

- [181] D. S. Rokhsar and S. A. Kivelson. Superconductivity and the quantum hard-core dimer gas. *Physical Review Letters*, 61(20):2376, 1988. doi:[10.1103/PhysRevLett.61.2376](https://doi.org/10.1103/PhysRevLett.61.2376).
- [182] A. Sahasrabudhe, D. Kaib, S. Reschke, R. German, T. Koethe, J. Buhot, D. Kamenskyi, C. Hickey, P. Becker, V. Tsurkan, et al. High-field quantum disordered state in α -RuCl₃: spin flips, bound states, and multiparticle continuum. *Physical Review B*, 101(14):140410, 2020. doi:[10.1103/PhysRevB.101.140410](https://doi.org/10.1103/PhysRevB.101.140410).
- [183] A. M. Samarakoon, A. Banerjee, S.-S. Zhang, Y. Kamiya, S. Nagler, D. Tennant, S.-H. Lee, and C. Batista. Comprehensive study of the dynamics of a classical Kitaev spin liquid. *Physical Review B*, 96(13):134408, 2017. doi:[10.1103/PhysRevB.96.134408](https://doi.org/10.1103/PhysRevB.96.134408).
- [184] L. Saminadayar, D. Glatli, Y. Jin, and B. Etienne. Observation of the $e/3$ fractionally charged Laughlin quasiparticle. *Physical Review Letters*, 79(13):2526, 1997. doi:[10.1103/PhysRevLett.79.2526](https://doi.org/10.1103/PhysRevLett.79.2526).
- [185] L. J. Sandilands, Y. Tian, K. W. Plumb, Y.-J. Kim, and K. S. Burch. Scattering continuum and possible fractionalized excitations in α -RuCl₃. *Physical Review Letters*, 114(14):147201, 2015. doi:[10.1103/PhysRevLett.114.147201](https://doi.org/10.1103/PhysRevLett.114.147201).
- [186] L. J. Sandilands, Y. Tian, A. A. Reijnders, H.-S. Kim, K. W. Plumb, Y.-J. Kim, H.-Y. Kee, and K. S. Burch. Spin-orbit excitations and electronic structure of the putative Kitaev magnet α -RuCl₃. *Physical Review B*, 93(7):075144, 2016. doi:[10.1103/PhysRevB.93.075144](https://doi.org/10.1103/PhysRevB.93.075144).
- [187] L. Savary and L. Balents. Quantum spin liquids: a review. *Reports on Progress in Physics*, 80(1):016502, 2016. doi:[10.1088/0034-4885/80/1/016502](https://doi.org/10.1088/0034-4885/80/1/016502).
- [188] J. A. Sears, Y. Zhao, Z. Xu, J. W. Lynn, and Y.-J. Kim. Phase diagram of α -RuCl₃ in an in-plane magnetic field. *Physical Review B*, 95(18):180411, 2017. doi:[10.1103/PhysRevB.95.180411](https://doi.org/10.1103/PhysRevB.95.180411).
- [189] E. Sela, H.-C. Jiang, M. H. Gerlach, and S. Trebst. Order-by-disorder and spin-orbital liquids in a distorted Heisenberg-Kitaev model. *Physical Review B*, 90(3):035113, 2014. doi:[10.1103/PhysRevB.90.035113](https://doi.org/10.1103/PhysRevB.90.035113).
- [190] E. Shender. Anti-ferromagnetic garnets with fluctuation-like interacting sub-lattices. *Zhurnal Eksperimentalnoi I Teoreticheskoi Fiziki*, 83(1):326–337, 1982.
- [191] Y. Singh and P. Gegenwart. Antiferromagnetic Mott insulating state in single crystals of the honeycomb lattice material Na₂IrO₃. *Physical Review B*, 82(6):064412, 2010. doi:[10.1103/PhysRevB.82.064412](https://doi.org/10.1103/PhysRevB.82.064412).
- [192] Y. Singh, S. Manni, J. Reuther, T. Berlijn, R. Thomale, W. Ku, S. Trebst, and P. Gegenwart. Relevance of the Heisenberg-Kitaev model for the honeycomb lattice iridates A₂IrO₃. *Physical Review Letters*, 108(12):127203, 2012. doi:[10.1103/PhysRevB.88.085125](https://doi.org/10.1103/PhysRevB.88.085125).
- [193] S. Sinn, C. H. Kim, B. H. Kim, K. D. Lee, C. J. Won, J. S. Oh, M. Han, Y. J. Chang, N. Hur, H. Sato, et al. Electronic structure of the Kitaev material α -RuCl₃ probed by photoemission and inverse photoemission spectroscopies. *Scientific Reports*, 6(1):39544, 2016. doi:[10.1038/srep39544](https://doi.org/10.1038/srep39544).
- [194] C. H. Sohn, H.-S. Kim, T. F. Qi, D. W. Jeong, H. J. Park, H. K. Yoo, H.-H. Kim, J.-Y. Kim, T. D. Kang, D.-Y. Cho, et al. Mixing between $J_{\text{eff}} = \frac{1}{2}$ and $\frac{3}{2}$ orbitals in Na₂IrO₃: a spectroscopic and density functional calculation study. *Physical Review B*, 88(8):085125, 2013. doi:[10.1103/PhysRevB.88.085125](https://doi.org/10.1103/PhysRevB.88.085125).

- [195] D. T. Son and N. Yamamoto. Berry curvature, triangle anomalies, and the chiral magnetic effect in Fermi liquids. *Physical Review Letters*, 109(18):181602, 2012. doi:10.1103/PhysRevLett.109.181602.
- [196] A. Stern. Anyons and the quantum Hall effect—A pedagogical review. *Annals of Physics*, 323(1):204–249, 2008. doi:10.1016/j.aop.2007.10.008.
- [197] S. Sugano. *Multiplets of transition-metal ions in crystals*. Elsevier, 2012.
- [198] Y. Sugita, Y. Kato, and Y. Motome. Antiferromagnetic Kitaev interactions in polar spin-orbit Mott insulators. *Physical Review B*, 101(10):100410, 2020. doi:10.1103/PhysRevB.101.100410.
- [199] G. Sundaram and Q. Niu. Wave-packet dynamics in slowly perturbed crystals: gradient corrections and Berry-phase effects. *Physical Review B*, 59(23):14915, 1999. doi:10.1103/PhysRevB.59.14915.
- [200] M. Takahashi. Half-filled Hubbard model at low temperature. *Journal of Physics C*, 10(8):1289, 1977. doi:10.1088/0022-3719/10/8/031.
- [201] T. Takayama, A. Kato, R. Dinnebier, J. Nuss, H. Kono, L. Veiga, G. Fabbri, D. Haskel, and H. Takagi. Hyperhoneycomb iridate β -Li₂IrO₃ as a platform for Kitaev magnetism. *Physical Review Letters*, 114(7):077202, 2015. doi:10.1103/PhysRevLett.114.077202.
- [202] F. Tang, H. C. Po, A. Vishwanath, and X. Wan. Comprehensive search for topological materials using symmetry indicators. *Nature*, 566(7745):486–489, 2019. doi:10.1038/s41586-019-0937-5.
- [203] G. C. Thiang. On spectral flow and Fermi arcs. *Communications in Mathematical Physics*, 385(1):465–493, 2021. doi:10.1007/s00220-021-04007-z.
- [204] D. J. Thouless, M. Kohmoto, M. P. Nightingale, and M. den Nijs. Quantized Hall conductance in a two-dimensional periodic potential. *Physical Review Letters*, 49(6):405, 1982. doi:10.1103/PhysRevLett.49.405.
- [205] S. Trebst. Kitaev magnets. In E. Pavarini and E. Koch, editors, *Orbital Physics in Correlated Matter*, pages 338–364. Forschungszentrum Jülich GmbH Institute for Advanced Simulation, 2023. doi:10.34734/FZJ-2023-03329.
- [206] S. Trebst and C. Hickey. Kitaev materials. *Physics Reports*, 950:1–37, 2022. doi:10.1016/j.physrep.2021.11.003.
- [207] D. C. Tsui, H. L. Stormer, and A. C. Gossard. Two-dimensional magnetotransport in the extreme quantum limit. *Physical Review Letters*, 48(22):1559, 1982.
- [208] M. Vazifeh and M. Franz. Electromagnetic response of Weyl semimetals. *Physical Review Letters*, 111(2):027201, 2013. doi:10.1103/PhysRevLett.111.027201.
- [209] M. Vergniory, L. Elcoro, C. Felser, N. Regnault, B. A. Bernevig, and Z. Wang. A complete catalogue of high-quality topological materials. *Nature*, 566(7745):480–485, 2019. doi:10.1038/s41586-019-0954-4.
- [210] J. Villain. Insulating spin glasses. *Zeitschrift für Physik B*, 33(1):31–42, 1979. doi:10.1007/BF01325811.

- [211] J. Villain, R. Bidaux, J.-P. Carton, and R. Conte. Order as an effect of disorder. *Journal de Physique*, 41(11):1263–1272, 1980. doi:10.1051/jphys:0198000410110126300.
- [212] Y. Vinkler-Aviv and A. Rosch. Approximately quantized thermal Hall effect of chiral liquids coupled to phonons. *Physical Review X*, 8(3):031032, 2018. doi:10.1103/PhysRevX.8.031032.
- [213] M. Vojta. Orbitals, frustration and quantum criticality. In E. Pavarini and E. Koch, editors, *Orbital Physics in Correlated Matter*, pages 272–302. Forschungszentrum Jülich GmbH Institute for Advanced Simulation, 2023. doi:10.34734/FZJ-2023-03329.
- [214] J. Wang, B. Normand, and Z.-X. Liu. One proximate Kitaev spin liquid in the K - J - Γ model on the honeycomb lattice. *Physical Review Letters*, 123(19):197201, 2019. doi:10.1103/PhysRevLett.123.197201.
- [215] G. Wannier. Antiferromagnetism. The triangular Ising net. *Physical Review*, 79(2):357, 1950. doi:10.1103/PhysRev.79.357.
- [216] X.-G. Wen. *Quantum field theory of many-body systems: from the origin of sound to an origin of light and electrons*. Oxford university press, 2004.
- [217] X.-G. Wen and Q. Niu. Ground-state degeneracy of the fractional quantum Hall states in the presence of a random potential and on high-genus Riemann surfaces. *Physical Review B*, 41(13):9377, 1990. doi:10.1103/PhysRevB.41.9377.
- [218] H. Weng, C. Fang, Z. Fang, B. A. Bernevig, and X. Dai. Weyl semimetal phase in noncentrosymmetric transition-metal monophosphides. *Physical Review X*, 5(1):011029, 2015. doi:10.1103/PhysRevX.5.011029.
- [219] H. Weyl. Gravitation and the electron. *Proceedings of the National Academy of Sciences*, 15(4):323–334, 1929. doi:10.1073/pnas.15.4.323.
- [220] A. Willans, J. Chalker, and R. Moessner. Disorder in a quantum spin liquid: flux binding and local moment formation. *Physical Review Letters*, 104(23):237203, 2010. doi:10.1103/PhysRevLett.104.237203.
- [221] A. Willans, J. Chalker, and R. Moessner. Site dilution in the Kitaev honeycomb model. *Physical Review B*, 84(11):115146, 2011. doi:10.1103/PhysRevB.84.115146.
- [222] S. M. Winter, Y. Li, H. O. Jeschke, and R. Valentí. Challenges in design of Kitaev materials: magnetic interactions from competing energy scales. *Physical Review B*, 93(21):214431, 2016. doi:10.1103/PhysRevB.93.214431.
- [223] S. M. Winter, K. Riedl, P. A. Maksimov, A. L. Chernyshev, A. Honecker, and R. Valentí. Breakdown of magnons in a strongly spin-orbital coupled magnet. *Nature Communications*, 8(1):1152, 2017. doi:10.1038/s41467-017-01177-0.
- [224] S. M. Winter, A. A. Tsirlin, M. Daghofer, J. van den Brink, Y. Singh, P. Gegenwart, and R. Valentí. Models and materials for generalized Kitaev magnetism. *Journal of Physics: Condensed Matter*, 29(49):493002, 2017. doi:10.1088/1361-648X/aa8cf5.
- [225] E. Witten. Three lectures on topological phases of matter. *La Rivista del Nuovo Cimento*, 39:313–370, 2016. doi:10.1393/ncr/i2016-10125-3.

- [226] A. Wollny, E. C. Andrade, and M. Vojta. Singular field response and singular screening of vacancies in antiferromagnets. *Physical Review Letters*, 109(17):177203, 2012. doi:10.1103/PhysRevLett.109.177203.
- [227] A. Wollny, L. Fritz, and M. Vojta. Fractional impurity moments in two-dimensional noncollinear magnets. *Physical Review Letters*, 107(13):137204, 2011. doi:10.1103/PhysRevLett.107.137204.
- [228] A. Wolter, L. Corredor, L. Janssen, K. Nenkov, S. Schönecker, S.-H. Do, K.-Y. Choi, R. Albrecht, J. Hunger, T. Doert, et al. Field-induced quantum criticality in the Kitaev system α -RuCl₃. *Physical Review B*, 96(4):041405, 2017. doi:10.1103/PhysRevB.96.041405.
- [229] D. Wulferding, Y. Choi, S.-H. Do, C. H. Lee, P. Lemmens, C. Faurgas, Y. Gallais, and K.-Y. Choi. Magnon bound states versus anyonic Majorana excitations in the Kitaev honeycomb magnet α -RuCl₃. *Nature Communications*, 11(1):1603, 2020. doi:10.1038/s41467-020-15370-1.
- [230] D. Xiao, M.-C. Chang, and Q. Niu. Berry phase effects on electronic properties. *Reviews of modern physics*, 82(3):1959–2007, 2010. doi:10.1103/RevModPhys.82.1959.
- [231] S.-Y. Xu, I. Belopolski, N. Alidoust, M. Neupane, G. Bian, C. Zhang, R. Sankar, G. Chang, Z. Yuan, C.-C. Lee, et al. Discovery of a Weyl fermion semimetal and topological Fermi arcs. *Science*, 349(6248):613–617, 2015. doi:10.1126/science.aaa9297.
- [232] Y. Xu, L. Elcoro, Z.-D. Song, B. J. Wieder, M. Vergniory, N. Regnault, Y. Chen, C. Felser, and B. A. Bernevig. High-throughput calculations of magnetic topological materials. *Nature*, 586(7831):702–707, 2020. doi:10.1038/s41586-020-2837-0.
- [233] R. Yadav, N. A. Bogdanov, V. M. Katukuri, S. Nishimoto, J. Van Den Brink, and L. Hozoi. Kitaev exchange and field-induced quantum spin-liquid states in honeycomb α -RuCl₃. *Scientific Reports*, 6(1):37925, 2016. doi:10.1038/srep37925.
- [234] Y. Yamaji, T. Suzuki, T. Yamada, S.-i. Suga, N. Kawashima, and M. Imada. Clues and criteria for designing a Kitaev spin liquid revealed by thermal and spin excitations of the honeycomb iridate Na₂IrO₃. *Physical Review B*, 93(17):174425, 2016. doi:10.1103/PhysRevB.93.174425.
- [235] B. Yang, Y. M. Goh, S. H. Sung, G. Ye, S. Biswas, D. A. Kaib, R. Dhakal, S. Yan, C. Li, S. Jiang, et al. Magnetic anisotropy reversal driven by structural symmetry-breaking in monolayer α -RuCl₃. *Nature Materials*, 22(1):50–57, 2023. doi:10.1038/s41563-022-01401-3.
- [236] H. Yao and S. A. Kivelson. Exact chiral spin liquid with non-Abelian anyons. *Physical Review Letters*, 99(24):247203, 2007. doi:10.1103/PhysRevLett.102.217202.
- [237] F. Ye, S. Chi, H. Cao, B. C. Chakoumakos, J. A. Fernandez-Baca, R. Custelcean, T. Qi, O. Korneta, and G. Cao. Direct evidence of a zigzag spin-chain structure in the honeycomb lattice: a neutron and x-ray diffraction investigation of single-crystal Na₂IrO₃. *Physical Review B*, 85(18):180403, 2012. doi:10.1103/PhysRevB.85.180403.
- [238] M. Ye, G. B. Halász, L. Savary, and L. Balents. Quantization of the thermal Hall conductivity at small Hall angles. *Physical Review Letters*, 121(14):147201, 2018. doi:10.1103/PhysRevLett.121.147201.
- [239] T. Yokoi, S. Ma, Y. Kasahara, S. Kasahara, T. Shibauchi, N. Kurita, H. Tanaka, J. Nasu, Y. Motome, C. Hickey, et al. Half-integer quantized anomalous thermal Hall effect in the Kitaev material candidate α -RuCl₃. *Science*, 373(6554):568–572, 2021. doi:10.1126/science.aay5551.

- [240] A. Zazunov, R. Egger, and A. Levy Yeyati. Low-energy theory of transport in Majorana wire junctions. *Physical Review B*, 94(1):014502, 2016. doi:10.1103/PhysRevB.94.014502.
- [241] C. Zhang, A. Narayan, S. Lu, J. Zhang, H. Zhang, Z. Ni, X. Yuan, Y. Liu, J.-H. Park, E. Zhang, et al. Evolution of Weyl orbit and quantum Hall effect in Dirac semimetal Cd_3As_2 . *Nature Communications*, 8(1):1272, 2017. doi:10.1038/s41467-017-01438-y.
- [242] C. Zhang, Z. Ni, J. Zhang, X. Yuan, Y. Liu, Y. Zou, Z. Liao, Y. Du, A. Narayan, H. Zhang, et al. Ultrahigh conductivity in Weyl semimetal NbAs nanobelts. *Nature Materials*, 18(5):482–488, 2019. doi:10.1038/s41563-019-0320-9.
- [243] C. Zhang, Y. Zhang, H.-Z. Lu, X. Xie, and F. Xiu. Cycling Fermi arc electrons with Weyl orbits. *Nature Reviews Physics*, 3(9):660–670, 2021. doi:10.1038/s42254-021-00344-z.
- [244] C.-L. Zhang, S.-Y. Xu, I. Belopolski, Z. Yuan, Z. Lin, B. Tong, G. Bian, N. Alidoust, C.-C. Lee, S.-M. Huang, et al. Signatures of the Adler–Bell–Jackiw chiral anomaly in a Weyl fermion semimetal. *Nature Communications*, 7(1):1–9, 2016. doi:10.1038/ncomms10735.
- [245] C.-L. Zhang, S.-Y. Xu, C. Wang, Z. Lin, Z. Du, C. Guo, C.-C. Lee, H. Lu, Y. Feng, S.-M. Huang, et al. Magnetic-tunnelling-induced Weyl node annihilation in TaP. *Nature Physics*, 13(10):979–986, 2017. doi:10.1038/nphys4183.
- [246] E. Z. Zhang, L. E. Chern, and Y. B. Kim. Topological magnons for thermal Hall transport in frustrated magnets with bond-dependent interactions. *Physical Review B*, 103(17):174402, 2021. doi:10.1103/PhysRevB.103.174402.
- [247] H. Zhang, H. Miao, T. Z. Ward, D. G. Mandrus, S. E. Nagler, M. A. McGuire, and J. Yan. Anisotropic thermal conductivity oscillations in relation to the putative Kitaev spin liquid phase of $\alpha\text{-RuCl}_3$. *Physical Review Letters*, 133(20):206603, 2024. doi:10.1103/PhysRevLett.133.206603.
- [248] L. Zhang and Y. Motome. Possible Realization of Kitaev Spin Liquids in van der Waals Heterostructures of $\alpha\text{-RuCl}_3$ and CrX_3 ($X=\text{Cl}$ and I), 2023. arXiv:2310.01075.
- [249] S.-S. Zhang, G. B. Halász, W. Zhu, and C. D. Batista. Variational study of the Kitaev-Heisenberg-Gamma model. *Physical Review B*, 104(1):014411, 2021. doi:10.1103/PhysRevB.104.014411.
- [250] T. Zhang, Y. Jiang, Z. Song, H. Huang, Y. He, Z. Fang, H. Weng, and C. Fang. Catalogue of topological electronic materials. *Nature*, 566(7745):475–479, 2019. doi:10.1038/s41586-019-0944-6.
- [251] Y. Zhang, D. Bulmash, P. Hosur, A. C. Potter, and A. Vishwanath. Quantum oscillations from generic surface Fermi arcs and bulk chiral modes in Weyl semimetals. *Scientific Reports*, 6(1):23741, 2016. doi:10.1038/srep23741.
- [252] Y.-F. Zhao, S.-H. Jang, and Y. Motome. Spin-orbit coupled insulators and metals on the verge of Kitaev spin liquids in ilmenite heterostructures, 2024. arXiv:2403.09112.
- [253] G. Zheng, M. Wu, H. Zhang, W. Chu, W. Gao, J. Lu, Y. Han, J. Yang, H. Du, W. Ning, et al. Recognition of Fermi-arc states through the magnetoresistance quantum oscillations in Dirac semimetal Cd_3As_2 nanoplates. *Physical Review B*, 96(12):121407, 2017. doi:10.1103/PhysRevB.96.121407.
- [254] X. Zheng, K. Jia, J. Ren, C. Yang, X. Wu, Y. Shi, K. Tanigaki, and R.-R. Du. Tunneling spectroscopic signatures of charge doping and associated Mott transition in $\alpha\text{-RuCl}_3$ in proximity to graphite. *Physical Review B*, 107(19):195107, 2023. doi:10.1103/PhysRevB.107.195107.

- [255] X. Zheng, O. Takuma, H. Zhou, C. Yang, X. Han, G. Wang, J. Ren, Y. Shi, K. Tanigaki, and R.-R. Du. Insulator-to-metal Mott transition facilitated by lattice deformation in monolayer α -RuCl₃ on graphite. *Physical Review B*, 109(3):035106, 2024. doi:10.1103/PhysRevB.109.035106.
- [256] X. Zhou, H. Li, J. Waugh, S. Parham, H.-S. Kim, J. Sears, A. Gomes, H.-Y. Kee, Y.-J. Kim, and D. Dessau. Angle-resolved photoemission study of the Kitaev candidate α -RuCl₃. *Physical Review B*, 94(16):161106, 2016. doi:10.1103/PhysRevB.94.161106.
- [257] F. Zschöcke and M. Vojta. Physical states and finite-size effects in Kitaev’s honeycomb model: bond disorder, spin excitations, and NMR line shape. *Physical Review B*, 92(1):014403, 2015. doi:10.1103/PhysRevB.92.014403.
- [258] M. Zubkov. Weyl orbits as probe of chiral separation effect in magnetic Weyl semimetals. *Journal of Physics: Condensed Matter*, 36(41):415501, 2024. doi:10.1088/1361-648X/ad5d36.
- [259] A. Zyuzin and A. Burkov. Topological response in Weyl semimetals and the chiral anomaly. *Physical Review B*, 86(11):115133, 2012. doi:10.1103/PhysRevB.86.115133.

Eidesstattliche Versicherung

Ich versichere an Eides Statt, dass die Dissertation von mir selbstständig und ohne unzulässige fremde Hilfe unter Beachtung der *“Grundsätze zur Sicherung guter wissenschaftlicher Praxis an der Heinrich-Heine-Universität Düsseldorf”* erstellt worden ist.

Düsseldorf, 11. Dezember 2024

Tim Yannik Bauer